



**Politecnico
di Torino**

Tesi di Laurea Magistrale in Ingegneria Meccanica - Progettazione meccanica LM-33
(DM270)

**Thermo-structural analysis and associated experimental
characterization of an innovative metal-matrix-composite
copper-steel material for a new Liquid Rocket Engine (LRE)
thrust chamber geometry processed by SLM Additive
Manufacturing**

Autore:

Matteo Crachi

Relatrice:

Professoressa Sesana Raffaella

Correlatori:

Professoressa Delprete Cristiana, Politecnico di Torino

PhD. Marco Pizzarelli, Italian Space Agency (ASI) Researcher,

PhD. Domenico Borrelli, Sophia High Tech s.r.l.

Politecnico di Torino

2022

Declaration

I hereby declare that, the contents and organization of this dissertation constitute my own original work and does not compromise in any way the rights of third parties, including those relating to the security of personal data.

Matteo Crachi
2022

L'unione, se correlata alla dedizione ed al sacrificio, porta sempre a grandi risultati.

Acknowledgements

I ringraziamenti spesso vengono visti come un semplice atto formale e doveroso. In questo caso ci tengo a precisare che tutte le persone, gli enti pubblici e le istituzioni sotto citate meritano realmente un caloroso e concreto ringraziamento.

Da dove cominciare? Il presente progetto mi ha permesso di conoscere persone fantastiche, che hanno creduto nell'idea comune di migliorare, anche se in piccolo, un settore estremamente importante per il futuro: la propulsione spaziale. Gli sforzi che ognuno degli attori partecipanti al progetto ha compiuto è stato fondamentale in ogni suo aspetto, emotivo, tecnico, teorico.

In primo luogo vorrei ringraziare mio Cugino Andrea. Sì con la C maiuscola. In questo ultimo anno di studi è stata la persona che più mi ha fatto da esempio. Un vero modello di uomo. Uomo che ha affrontato grandi sfide con una calma che solo un matto poteva riuscire ad avere. Ecco quella forza e quella calma mi hanno insegnato qualcosa che nessun libro, laurea, corso potrà mai trasmettere: il calore della famiglia. Come grande esempio si aggiungono anche mia cugina Alexia, mia zia Marina e mio zio Jean. Quest'ultimo ha portato ancora più in alto i valori della famiglia: il modo in cui è riuscito nell'impresa lo conosce solo Lui. Sono sicuro che Nonno e Nonna, dà la su, sono orgogliosi. Missione compiuta.

La cosa più bella che ho è la mia famiglia. Mio padre e mia madre durante gli anni di studio mi hanno sempre sostenuto, supportato e motivato. Ho la fortuna di avere due genitori che non mi hanno mai fatto mancare nulla. Grazie. Grazie per la pazienza che avete dimostrato, anche quando il 'piccolo diavolo' che è in me ha predominato. Grazie Vittoria, cara sorella, per esserti sempre sentita in dovere di aiutarmi, proteggermi, motivarmi e consolarmi: a volte sembravi tu la grande di famiglia, e non io. Continua così, hai un futuro ricco di soddisfazioni davanti. Grazie Nonna per i saggi consigli e l'amore che da quando sono piccolo mi hai trasmesso, l'amore per la scienza, l'amore per le persone ed il rispetto per la natura. Oggi sono arrivato qui grazie a te. Grazie zio Vincenzo per essere sempre stato al mio fianco come solo un secondo padre può fare. Sono molto fiero di te e della persona che sei. Per me sei, e sarai sempre un grandissimo esempio di uomo da seguire.

Caro Nonno Tico, come vedi ci avevi preso, tuo nipote è finalmente Dottore Magistrale in Ingegneria meccanica. Spero che da la su tu sia fiero di me.

E poi c'è Lei, Alessia, mia complice in tutto. Ogni giorno mi rendi sempre più orgoglioso della persona che sei. Mi hai trasmesso fiducia e soprattutto forza, forza in quei momenti complicati che io e te conosciamo. Senza di te non sarei mai riuscito a

finire gli studi come ho fatto, nei tempi e nel modo che ho raggiunto. La tua presenza accanto a me mi fa sentire sempre più fiero di quello che insieme stiamo costruendo. Un particolare ringraziamento va alla tua spendita famiglia, che ogni giorno, in un modo o nell'altro, mi rende ancora più fiero di te. Grazie Felice, Gabriella, Tina, Renato, Luca, Simona e Paola per avermi accolto, fin dall'inizio, con calore e affetto come solo voi sapete fare.

Vorrei ringraziare uno dei miei più cari amici, Daniele Arcangeli. Durante il mio percorso di studi mi ha sempre supportato, nonostante la distanza. Persona sensibile e sempre disponibile per gli altri, prima ancora che per se stesso. Grande uomo prima ancora di essere un grande amico. Sono molto orgoglioso della persona che sei e del percorso che hai intrapreso. Grazie.

Vorrei ringraziare il Politecnico di Torino per le nozioni che mi ha trasmesso durante i due anni di Laurea Magistrale in Ingegneria Meccanica - Progettazione Meccanica. Ringrazio in particolare la Professoressa Sesana, mia relatrice, per avermi dato la possibilità di entrare in diretto contatto con la vera ricerca sperimentale accademica, per aver creato contatti che mi hanno permesso di trascorrere del tempo presso l'università di Tous in Francia, per avermi presentato il team dell'università di Bratislava con cui abbiamo collaborato, per la pazienza che ha avuto nei momenti più complicati e per aver sempre messo avanti gli interessi degli studenti ai propri personali. Ringrazio la professoressa Delprete per il supporto tecnico e per la grande fiducia trasmessa fin dall'inizio del progetto.

Il progetto è nato grazie ad una persona che durante la mia esperienza presso l'Agenzia Spaziale Europea (ESA) è stata capace di trasmettermi la passione per il mondo spazio, Marco Pizzarelli, mio correlatore. Grazie Marco per il tempo, le nozioni tecniche e soprattutto per la fiducia che hai sempre avuto in me. Grazie per quello che hai fatto e stai facendo per il mio futuro. Sei un grande esmpio, sono fortunato ad averti avuto accanto in questi anni.

Senza il supporto tecnico di Sophia High tech s.r.l. questo progetto non sarebbe mai potuto partire. Ricordo perfettamente la prima conversazione telefonica durante i periodo di pandemica con Antonella Allocca. Grazie alla persona appena citata sono riuscito ad entrare in contatto con il CEO Antonio Caraviello ed il responsabile ricerca e sviluppo Domenico Borrelli. Grazie Antonio per aver creduto nella mia persona e nel progetto pioneristico. Un particolare ringraziamento è indirizzato a Domenico Borrelli, il quale con pazienza e molto impegno, ha reso possibile la presente collaborazione. Ho avuto la possibilità di passare un breve periodo presso Sophia High Tech s.r.l. e conoscervi di persona, siete persone fantastiche, disponibili e tecnicamente molto preparate. Complimenti! Ringrazio anche Nicola Sicignano per la pazienza ed il supporto al progetto, importante e sempre sostanzioso.

Durante il periodo passato in Francia alcuni problemi tecnici hanno messo a rischio parte del progetto. I problemi sono stati risolti grazie al supporto tecnico e soprattutto morale di tutti i dipendenti dell'azienda AAMS. In particolare vorrei ringraziare Damien per l'enorme disponibilità che ha mostrato tutti i gironi, Régis per la pazienza con cui ha realizzato parte delle attrezzature necessarie a svolgere alcuni test, Anotoine per avermi

insegnato ad affrontare problemi tecnici con una mentalità professionale e scientifica, Achref, Marwa, Aurore, Paul e Loic per avermi fatto divertire e per aver contribuito tecnicamente a raggiungere i risultati attesi dal progetto. In particolare vorrei ringraziare una persona, Renè: grazie per aver dedicato intere giornate per risolvere problemi tecnici insieme a me. Un doveroso ringraziamento è rivolto a Arnold e Roger che hanno permesso la mia permanenza al CEROC. Vorrei ringraziare anche tutti i professionisti del centro di ricerca CERMEL.

Vorrei ringraziare tutti i tecnici e gli ingegneri del Politecnico di Torino che mi hanno aiutato durante il progetto. In particolare il Prof. Daniele Camatti, per la pazienza e l'aiuto fornito anche a distanza, per la quotidiana simpatia ed armonia che trasmette e per l'enorme disponibilità, Frediano De Marco, per aver passato gratuitamente fino a sera inoltrata del tempo all'intorno dei laboratori del Politecnico di Torino, il Prof. Matteo pavese e Luca Lavagna per avermi guidato nella caratterizzazione termo-chimica del materiale. Grazie.

Infine, vorrei rivolgere un particolare ringraziamento allo splendido gruppo di amici di Torino: Marco, Luca, Sebastiano, Simone, Andrea, Delio, Melania, Bianca, Antonella. Senza di voi al mio fianco il percorso di laurea magistrale sarebbe stato molto meno affascinante. Grazie del tempo che avete speso con me. Sono orgoglioso di ognuno di voi.

Abstract

Thrust chamber of high performance bi-propellant liquid rocket engines is a critical component of the launch vehicles because it is designed to operate in some of the most severe conditions seen in engineering practice. The requirement of reducing the temperature of the walls exposed to the hot gas can be met with high-thermal-conductivity copper alloys while the mechanical stiffness is achieved by using high-strength steel or nickel alloys. Because the stress–strain behaviour of a regeneratively cooled thrust chamber is directly correlated with its temperature behaviour, it is of primary importance to select the correct alloy.

Nowadays manufacturing processes are playing an important role in the global space industry, with particular emphasis respect to space propulsion. Thanks to Sophia High Tech s.r.l. advanced studies a new patented copper-steel composite, processed by SLM Additive Manufacturing process, is proposed for a Liquid Rocket Engine (LRE) application. A patented additive manufacturing powders mixing process developed by Sophia High Tech srl is used: it consists in a powder mixing new technology developed in order to mix two or more additive manufacturing powders.

A deep thermal and mechanical characterization of the new composite is presented, with particular reference to high temperature Low Cycle Fatigue, Differential scanning calorimetry (DSC), Thermal conductivity, micrography analysis, EDS chemical composition analysis, digital tomography analysis, thermomechanical analysis (TMA), Hardness, optical and SEM fracture analysis, high temperature traction tensile test, high temperature creep test.

Analytical models have been employed in order to replicate the correct new composite's behaviour. Ramberg–Osgood and Coffin-Manson have shown excellent results. A new material's behavior has been discovered. The 'local hill softening-hardening phenomenon' is a time dependent activated damage which occurs during cycling and quasi static tests at very high temperature.

The composite cu174PH shows an overall good behavior for liquid rocket engine application, however a heat treatment is strictly necessary in order to improve the elongation to fracture and the thermal conductivity.

Contents

List of Figures	xiv
------------------------	------------

List of Tables	xxvii
-----------------------	--------------

1 A New Space Economy Project	1
1.1 Aims of The Project	2
1.1.1 Technical Aims	2
1.1.2 Social Aims	2
1.2 The Project	4
1.2.1 Main Partners	4
1.2.2 Project Organization	6
1.2.3 Project Progress Logic	6
1.3 The New Space Economy	9
2 Introduction: Additive Manufacturing in the Space Liquid Rocket Engine (LRE) Industry	13
2.1 Metal Additive Manufacturing Technology	13
2.1.1 Selective Laser Melting (SLM)	16
2.2 Metal Additive Manufacturing in the aerospace sector	21
2.2.1 Additive Manufacturing of liquid rocket engine thrust chamber assembly	23
2.3 Materials for Liquid Rocket Engine (LRE) Thrust Chambers	27
2.3.1 Common Materials for Liquid Rocket Engine (LRE)	28
2.3.2 The role of Inconel alloys in AM LRE thrust chambers	31
2.3.3 From Inconel to Copper: modern AM LRE thrust chambers	35
3 Introduction: Liquid Rocket Engine (LRE)	37

3.1	Cooling Techniques for Rocket Engines	37
3.2	LRE Regenerative Cooling	39
3.2.1	Additive Manufacturing unconventional and innovative geometries for Liquid Rocket Engine (LRE) cooling channels	42
3.3	LRE Regenerative Cooling Fracture Mechanism	43
3.3.1	Thermally induced deformations of regenerative thrust chambers	44
3.3.2	Low Cycle Fatigue VS Creep-Fatigue Fracture	46
4	LRE thrust chambers predictable life methods	50
4.1	LRE thrust chambers physical test methodologies	50
4.1.1	Cylindrical thrust chambers	50
4.1.2	TMF panel	52
4.2	LRE thrust chambers numerical test methodologies	53
4.2.1	Algebraic models	54
4.2.2	Numerical models	55
5	Cu-17 4PH: a new innovative metal-matrix-composite material	57
5.1	Powders Data	57
5.1.1	Pure Copper by Legor Powmet	57
5.1.2	17-4 PH by Carpenter Additive	58
5.2	Powder Mixing Process	59
5.3	Additive Manufacturing Process Parameters	63
5.3.1	Platform Calibration Strategy	68
5.4	Printing Jobs and Cost Analysis	69
6	Experimental Set-Up: Materials and Method	73
6.1	Technological Tests	76
6.2	Physical/Chemical Properties Analysis	76
6.2.1	Roughness	76
6.2.2	Optical Micrography and Porosity analysis	77
6.2.3	SEM Micrography and Chemical Composition	78
6.2.4	Void distribution	78
6.3	Thermal Properties Analysis	79
6.3.1	Thermal conductivity	79

6.3.2	Linear Thermal Expansion Coefficient	83
6.3.3	Thermal Capacity	85
6.4	Mechanical Analysis	87
6.4.1	Hardness and Micro Hardness	87
6.4.2	Traction	89
6.4.3	Compression	93
6.4.4	Low Cycle Fatigue	94
6.4.5	Machine troubleshooting	105
6.4.6	Creep	107
6.5	Fracture Surface Analysis	108
7	Experimental Results: Technological Tests	109
7.1	Cooling channels	109
7.2	Channels angle	111
7.3	Lattice Structure	113
8	Experimental Results: Physical/Chemical Properties Tests	114
8.1	Roughness	114
8.2	Optical Micrography	116
8.2.1	XY plane	116
8.2.2	ZX/ZY plane	121
8.2.3	Defects	126
8.3	SEM Micrography	129
8.4	Chemical Composition	130
8.4.1	Overall material chemical composition	130
8.4.2	17-4PH phase chemical composition	132
8.4.3	Copper phase chemical composition	135
8.4.4	Hypothetical explanation of the mismatch between pre-custom Cu-174PH powder % composition and the experimental % powder composition	138
8.5	Porosity analysis	142
8.6	Void distribution	144
9	Experimental Results: Thermal Properties Tests	148

9.1	Thermal Conductivity - Hot Disk	148
9.1.1	Z direction thermal conductivity	148
9.1.2	XY direction thermal conductivity	151
9.1.3	Z direction thermal conductivity: 700° C heat treatment	152
9.1.4	Thermal conductivity comparison	153
9.2	Specific Heat Capacity - DSC	155
9.2.1	Specific Heat Capacity comparison	156
9.3	Coefficient of Linear Thermal Dilatation - TMA	157
10	Experimental Results: Mechanical Properties Tests	159
10.1	Hardness and Micro-hardness	159
10.1.1	Indentation Size Effect Evaluation	160
10.1.2	HV20 hardness results	161
10.1.3	HV0.2 micro-hardness results	164
10.1.4	Yield strength-Hardness relation	166
10.2	Tensile Traction	168
10.2.1	Poisson Ration	168
10.2.2	Young Module	170
10.2.3	Tensile Traction test	171
10.2.4	Ramberg Osgood Model	173
10.2.5	Comparison with competitors	174
10.2.6	Z direction estimated tensile properties	177
10.3	Compression	180
10.3.1	Compression Young Module	180
10.3.2	Compression test	183
10.3.3	Lattice structure Compression test	184
11	Experimental Results: Low Cycle Fatigue Tests	186
11.1	LCF Results: Room temperature	187
11.2	LCF Results: 150°C	190
11.3	LCF Results: 350°C	191
11.4	LCF Results: 550°C	193
11.5	LCF Results: Deformation VS Temperature Analysis	197

11.6 LCF Results: Cyclic Curve	198
11.7 LCF Results: Coffin Manson Model	200
11.8 Ratcheting tests result	203
12 Experimental Results: Creep Tests	207
12.1 Creep tests	207
12.1.1 Breakdown Limit Effect	209
12.2 Creep Model	211
12.3 Creep (traction) Relaxation tests	213
13 Experimental Results: Fracture surface analysis	215
13.1 Tensile traction tests	215
13.1.1 Tensile test - Room temperature (SEM)	217
13.1.2 Tensile test - 150°C (SEM)	219
13.1.3 Tensile test - 550°C (SEM)	222
13.2 Low Cycle Fatigue tests	224
13.2.1 Room temperature fracture surfaces	226
13.2.2 150°C fracture surfaces	228
14 Conclusion	230
References	233
Appendix A LCF specimen buckling instability analysis	241
Appendix B Roughness test	242
Appendix C Molten pool dynamics: AM SLM Conduction and Keyhole mode	243
Appendix D Transient Plane Source technique (ISO 22007-2)	245
Appendix E Energy Density DoE of Additive Manufacturing Inocnel 718 for Space Rocket application	249
E.1 Introduction	249
E.2 Background - VICKERS test	249
E.3 Materials and methods	251
E.4 Hardness testing	256

E.5	Results	257
E.5.1	Density measurements	257
E.5.2	Preliminary hardness measurements	258
E.5.3	Hardness results: as built specimens	259
E.5.4	Hardness results: heat treated specimens	261
E.6	Discussion	263
E.6.1	As build specimens	263
E.6.2	Heat treated specimens	265
Appendix F	Hardness and Micro-hardness full results	268
Appendix G	Tensile Test full results	270
G.1	Tensile Traction test - Room Temperature	270
G.2	Tensile Traction test - 150°C	272
G.3	Tensile Traction test - 350°C	274
G.4	Tensile Traction test - 550°C	276
G.5	Tensile Traction test - 650°C	278
Appendix H	Tensile Test Ramberg-Osgood relationship calculation procedure	279
H.1	Ramberg-Osgood model VS real deformation-real stress curve	280
H.2	Log-Log Ramberg-Osgood relationship chart	282
Appendix I	Compression Test Young Module calculation procedure	284
Appendix J	Ramberg - Osgood Cycling curve relationship	286
Appendix K	Coffin - Manson parameters	288

List of Figures

1.1	Project Main Partners	4
1.2	Project schematic organization	6
1.3	Project Progress Logic	8
1.4	Private industry space race by ISPI (Italian Institute for International Political Studies)	9
1.5	ESA investment in 2021	11
1.6	Measuring Space Power	12
1.7	Space Power Matrix by ESPI	12
2.1	Additive Manufacturing (AM) VS Traditional Methodologies (TM), from [1]	15
2.2	Schematics of additive manufacturing (AM) by Selective Laser Melting (SLM) process	16
2.3	Example of large-scale NASA GRCop-42 chambers fabricated by SLM	18
2.4	Illustration of Selective Laser Melting main process parameters	19
2.5	Examples of fully and partially blocked internal channels shown in Computed Tomography, from [2]	20
2.6	Comparison of traditional manufacturing to additive manufacturing evolution (cost in US\$, 2020 equivalent), from [2]	22
2.7	Additive Manufacturing imitated scale machine technologies respect to common size liquid rocket engine, from [3]	23
2.8	Additive Manufacturing used across all components on liquid rocket engines, from [3]	23
2.9	Full-scale manufacturing demonstrator for liquid rocket engine application, from [4]	24
2.10	Tubular-wall design used on relatively low chamber pressure thrust chambers or nozzle extensions	25

2.11	Typical fabrication procedure is shown, where the laying of a thermal barrier coating, usually composed by Yttria-stabilized Zirconia[5], and a Nichrome layer, to protect from oxidation, are included , from [5]	26
2.12	Conventional rocket thrust chambers manufacturing technologies, from [6]	27
2.13	Summary of Additive Combustion Chamber Hot-fire Testing by NASA MSFC (Marshall Space Flight Center) from 2013 to 2018, from [7]	29
2.14	Right: SpaceX AM built Superdraco rocket engine. Left: SuperDraco Test Fire by SpaceX, from [8]	32
2.15	Orion Crew Module RCS engine nozzles, from [9]	32
2.16	AM power to reduction a component from 162 parts to 2 parts, from [10]	33
2.17	Hyperganic prototype rocket nozzle featuring internal cooling channels and an external lattice, from [8]	35
2.18	The damage of a common SM SLM optical mirror, from [11]	35
3.1	RS-68 rocket engine: two different cooling system	39
3.2	Schematic representation of the SSME (Space Shuttle Main Engine) global system	40
3.3	Schematic representation of the VULCAN Engine global system, from [12]	40
3.4	Schematic of a regenerative thrust chamber cross section nomenclature, from [13]	41
3.6	LRE cooling channels filled with copper metal foam, from [14]	42
3.7	AVIO s.p.a. United States Patent Application Publication No.: US 2017/0122258 A1	43
3.8	Regenerative thrust chamber strain behavior	44
3.9	Throat section of SSME - MCC showing channel rupture, from [15]	45
3.10	'Dog House' effect Examples	46
3.11	Liquid rocket engine (left), schematic of the combustion chamber (middle) and crack at the combustion chamber wall (right), from [16]	47
3.12	Results of 3D-FEM simulation for one engine-combustion cycle: (a) temperature–time profile and (b) strain/stress–time profiles, from [16]	48
3.13	(First image) Comparison between the accumulative creep curve of the creep–fatigue test and the creep curve of the simple creep test; (Second image) comparison between the maximum and minimum stresses in each cycle in the creep–fatigue test and the simple fatigue test, from [16]	49
3.14	LCF-Creep fracture mechanism, from ([16])	49

4.1	Cylindrical thrust chambers system facility	51
4.2	Convergent-divergent typical test thrust chamber [17]	52
4.3	Thermo Mechanical Pannel facility	53
4.4	SSME life analysis logic, from [18]	54
4.5	Sketch of the thrust chamber structure and its structural modelling (circular symmetry is not shown), from [13]	55
5.1	Scanning electron microscopy (SEM) image of the Legor Powmet pure Copper Powder, from [19]	58
5.2	<i>Carpenter Additive</i> 17-4 PH Powder Chemical Composition, from [19] .	58
5.3	Scanning electron microscopy (SEM) image of the Carpenter Additive 17-4 PH Powder, from official <i>Carpenter Additive</i> 17-4 PH Data Sheet .	59
5.4	Patented powder mixing process logic	60
5.5	Powder Mixing Process	61
5.6	Powder Mixing Process	63
5.7	Laser Spot Overlap (Hatch Overlap), from [20]	64
5.8	Layer random island strategy	65
5.9	Island strategy	65
5.10	Random island algorithm: study Job 1	66
5.11	Two different supports strategies adopted	67
5.12	Step A) (left) pre-melting and Step B) (right) Melting process	67
5.13	Logical scheme of the Concept Laser M2 power coating system	68
5.14	Platform Calibration Strategy	69
5.15	Job 1 and Job 2	70
5.16	Printing platform removing procedures	71
5.17	Example of manual supports removing procedure	71
5.18	Hand made machine cleaning procedure	72
6.1	Typical LRE z-axisymmetric plane fracture, from [12]	74
6.2	LRE fracture mechanism and uni-axial Low Cycle Fatigue specimen replication. Orange Arrows: uni-axial Low Cycle Fatigue test loading displacement direction; Blue lightning: spacemen XY plane in where uni-axial fracture occur	74
6.3	Roughness test facilities	77

6.4	Micrography analysis of the CEROC Laboratory of Université de Tours, France	78
6.5	CT scan test, Laboratory of Université de Tours, France	79
6.6	Hot Disk machine and sensor	80
6.7	Hot Disk - Minimum distance from sensor to boundary surface	81
6.8	Hot Disk - Temperature drift example	82
6.9	Hot Disk - Transient measure example	82
6.10	Hot Disk - Calculated fitting curve example	82
6.11	Hot Disk - Residual example	83
6.12	CT scan test, Laboratory of Université de Tours, France	83
6.13	TMA specimen orientation respect	84
6.14	DSC set up	86
6.15	DSC test	87
6.16	Hardness testing machines, DIMEAS Laboratory at Politecnico di Torino	88
6.17	Common cuboid specimen skin schematic representation	89
6.18	INSTRON 8801 machine, DIMEAS Laboratory, Politecnico di Torino .	90
6.19	Room and high temperature tensile test specimens geometry	91
6.20	550°C traction test specimen temperature profile	92
6.21	High temperature tensile test facilities	93
6.22	Compression test facilities	93
6.23	INSTRON Electro-Thermal Mechanical Testing II of CEROC Laboratory, Université de Tours, France	94
6.24	Second LVDT possible configurations	95
6.25	ETMT II system components	96
6.26	ETMT II water cooling system	96
6.27	Second thermocouple system facilities	97
6.28	LCF specimen's grips and custom hexagonal screws	97
6.29	Custom M6 hexagonal screws system	98
6.30	LCF specimen	98
6.31	LCF specimen's roughness: 3D profile reconstruction and optical magnification	99
6.32	Spot welding machine	100
6.33	First thermocouple system	100

6.34	Second thermocouple system (the one from which the result are used)	101
6.35	Second thermocouple system facilities	101
6.36	Temperature VS Current Calibration	102
6.37	Temperature VS Current Calibration	102
6.38	Software used for the set up of all LCF tests	104
6.39	Sinusoidal LCF curve	105
6.40	LVDT1 (left) and Load (right) signal problem	106
6.41	INSTRON ETMT II disassembly procedure	107
6.42	Ball screw damage	107
6.43	Creep machine, Slovak University of Technology, Slovakia	108
6.44	SEM at DIMEAS Laboratoy, Politecnico di Torino	108
7.1	Island scanning algorithm	109
7.2	Cooling channel replica specimens	110
7.3	2mm z-direction material removed specimen followed by a coarse surface polishing	111
7.4	Sloping specimens on the building platform	112
7.5	Sloping specimens surface quality	112
7.6	Schematic illustration of the SLM manufacturing process of the angular z-direction build, from [21].	113
7.7	Lattice Structure	113
8.1	Roughness tests	114
8.2	Roughness tests results	115
8.3	Re-coating method	116
8.4	Copper-Iron phase diagram	116
8.5	Optical micrography	117
8.6	Optical micrography with acid attack	117
8.7	Cu174PH microstructure	118
8.8	Optical micrography of a common low rate 17-4PH spherical spots area	118
8.9	Optical micrography of a common very high rate 17-4PH spherical spots area	119
8.10	Laser Track of a custom Inocnel718-Cu%20, from [22]. Same scanning strategy of the under study Cu-174PH composite material.	120
8.11	Very rare Laser tracks	121

8.12 Z plane microstructure	122
8.13 Complex melting pool: top image shows a copper base melting pool, bottom image shows a more 17-4PH base melting pool	123
8.14 Z plane melting pools	124
8.15 Rare key-hole melting pool	125
8.16 Optical micrograph of a rare columnar grain	126
8.17 Island inside Island example	126
8.18 Lack of fusion porosity example	127
8.19 Gas captured porosity example	127
8.20 No melted powder example	128
8.21 SEM Z building direction micrography.	129
8.22 Chemical composition specimen location	130
8.23 EDS spectrum of XY plane (one example out of three tests)	131
8.24 EDS spectrum of Z plane	132
8.25 17-4PH XY plane phase EDS analysis	134
8.26 17-4PH Z plane phase EDS analysis	135
8.27 Z plane EDS SEM map chemical composition map analysis	137
8.28 Gradient concentration along the Z axe of the powder supplier tank . . .	138
8.29 Gradient concentration along the Z axe of the printing platform	138
8.30 Powders distribution on the platform	139
8.31 Chemical composition specimen location on the printing platform . . .	139
8.32 Chemical composition gradient analysis - specimen location on the printing platform	140
8.33 Chemical composition map analysis - Start location on traction specimen - XY direction	141
8.34 Chemical composition map analysis - End location on traction specimen - XY direction	141
8.35 XY plane porosity highlighting	142
8.36 Z plane porosity highlighting	143
8.37 CT scan Z direction images	145
8.38 CT scan XY plane images	146
9.1 Thermal Conductivity specimens location - Job 1	148
9.2 Z direction thermal conductivity test - 4.5 mm Probing Depth - 10 tests .	149

9.3	Z direction thermal conductivity test - 4.0 mm Probing Depth - 10 tests .	150
9.4	XY direction thermal conductivity test - 5.0 mm Probing Depth - 1 test out of 6	151
9.5	Z direction thermal conductivity Heat Treated test - 4.9 mm Probing Depth - 5 tests	152
9.6	Cu-174PH Thermal Conductivity comparison with LRE historical NASA materials, data from [23]	154
9.7	Cu-174PH Thermal Conductivity comparison with modern LRE AM NASA materials, data from [24]	154
9.8	Cu-174PH Thermal Conductivity comparison with AM C18150 copper alloy, data from [25]	155
9.9	Cu-174PH Specific Heat Capacity vs Temperature	155
9.10	Delta heat power evaluation example	156
9.11	Cu-174PH specific heat capacity comparison with LRE historical NASA materials, data from [23]	157
9.12	Cu-174PH specific heat capacity comparison with AM C18150 copper alloy, data from [25]	157
9.13	Linear displacement vs temperature test results	158
9.14	Cu-174PH Coefficient of Linear Thermal Dilatation vs Temperature . .	158
10.1	Roughness analysis	160
10.2	Indentation Size Effect Evaluation - Cu-174PH	160
10.3	Indentation Size Effect Evaluation - Inconel718	161
10.4	HV20 Hardness Tests - Specimen A	162
10.5	HV20 Hardness Tests - Specimen B	163
10.6	HV20 Hardness Tests - footprint magnifications.	164
10.7	Specimen A micro-hardness	165
10.8	Specimen B micro-hardness	165
10.9	HV0.2 Micro-hardness Tests - footprint magnifications.NOTE: Images are not in proportion to real scale	165
10.10	Traction tensile test direction	168
10.11	Poisson Ration - Room Temperature	169
10.12	Young Module non-linearity - Traction test 150°C n.1	171
10.13	Traction tensile test - engineering % deformation	171
10.14	Engineering Traction properties VS Temperature	173

10.15 Traction tensile test - real % deformation	173
10.16 Ramberg - Osgood model - Test 1 T350	174
10.17 NASA historical [23] and modern [24] Copper alloy VS Cu174PH - yield strength (respect to temperature)	175
10.18 NASA historical Copper alloy [23] VS Cu174PH - Young Module (respect to temperature)	175
10.19 NASA modern Copper alloy [24] VS Cu174PH - Elongation to fracture (respect to temperature)	176
10.20 Hypothetical dislocation block mechanism	176
10.21 Hardness-Tensile direction relation	179
10.22 Color scale-based hardness representation for as-build Inconels 718 specimens: a) x-y plane; b) x-z or y-z plane	180
10.23 As-build traction tensile tests - Inconel 718	180
10.24 Pre-yield elastic region	181
10.25 Compression Young Module	181
10.26 Compression Young Module at high temperature	182
10.27 Compression Tests	183
10.28 Schematic compression behavior	184
10.29 Lattice Compression Test fractures	185
10.30 Lattice Compression Tests - Room temperature	185
11.1 LCF room temperature $\Delta\epsilon = 0.5\%$	187
11.2 Local hill phenomenon	188
11.3 LCF room temperature $\Delta\epsilon = 1.4\%$	188
11.4 LCF room temperature $\Delta\epsilon = 2.0\%$	189
11.5 LCF room temperature $\Delta\epsilon = 2.8\%$	189
11.6 LCF room temperature $\Delta\epsilon = 3.6\%$	189
11.7 LCF 150°C $\Delta\epsilon = 2.0\%$	190
11.8 LCF 150°C $\Delta\epsilon = 2.8\%$	190
11.9 LCF 150°C $\Delta\epsilon = 3.6\%$	191
11.10 LCF 350°C $\Delta\epsilon = 2.0\%$	191
11.11 Double stress breakdown	192
11.12 LCF 350°C $\Delta\epsilon = 2.8\%$	192
11.13 LCF 350°C $\Delta\epsilon = 3.6\%$	192

11.14LCF 550°C $\Delta\epsilon = 1.0\%$	193
11.15Stress breakdown phenomenon	194
11.16LCF 550°C $\Delta\epsilon = 1.4\%$	194
11.17NASA Narloy-z copper alloy LCF R-24-17 test at 538°C - Cusp behavior after N cycle	195
11.18Cu174PH $\Delta\epsilon = 1.4\%$ LCF test at 538°C - Cusp behavior after the 539th cycle out of 546 total cycle to failure	195
11.19LCF 550°C $\Delta\epsilon = 2.0\%$	196
11.20LCF 550°C $\Delta\epsilon = 2.8\%$	196
11.21LCF 550°C $\Delta\epsilon = 3.6\%$	196
11.22LCF $\Delta\epsilon = 2.0\%$ vs temperatures	197
11.23LCF $\Delta\epsilon = 2.8\%$ vs temperatures	197
11.24LCF $\Delta\epsilon = 3.6\%$ vs temperatures	198
11.25LCF Cyclic Curve	199
11.26R.-O. Cyclic Curve	199
11.27Cyclic Curves and Tensile Traction Curves	200
11.28LCF life	201
11.29Cu174PH and historical NASA's copper alloys life comparison, NASA's data from [26], [24] and [27].	202
11.30Cu174PH Coffin Manson Model vs Experiments results	203
11.31Ratcheting tests - 550°C 130 MPa	204
11.32Ratcheting tests - 550°C 160 MPa	205
11.33Ratcheting tests - 550°C 200 MPa	205
11.34Cu174PH ratcheting analysis	206
12.1 Cu174PH Creep tests results	208
12.2 Cu174PH Creep tests results in a Log-Log representation	208
12.3 Cu174PH Creep Strain rate	209
12.4 Cu174PH and modern bulk NASA's copper alloys Creep strain rates VS stress and temperature dependence	209
12.5 Cu174PH Breakdown phenomenon	210
12.6 Cu174PH Creep 300°C@270MPa and 500°C@117MPa tests loads . . .	210
12.7 Cu174PH Creep tests loads magnification	211
12.8 Cu174PH Breakdown Limit	211

12.9 Arrhenius's creep activation energy determination	212
12.10 Norton's creep exponent determination	212
12.11 Norton's creep exponent	213
12.12 Cu174PH Creep Relaxation tests	213
12.13 Cu174PH Creep Relaxation tests history	214
13.1 Optic images of the tensile traction fracture surfaces - part A	215
13.2 Optic images of the tensile traction fracture surfaces - part B	216
13.3 Optic images of the tensile traction fracture surfaces - Top side of the 550°C traction specimen	216
13.4 Optic images of the tensile traction fracture surfaces - Bottom side of the 550°C traction specimen	217
13.5 SEM image of the tensile traction crack propagation - Room temperature test	217
13.6 SEM image of the tensile traction fracture surface - Room temperature test	218
13.7 SEM magnification of the tensile different material's traction fracture - Room temperature test	218
13.8 SEM image of the tensile traction fracture surface - 150°C test	219
13.9 SEM magnification of the tensile traction fracture surface - 150°C test .	219
13.10 Copper vs 174PH fracture mechanism at 150°C	220
13.11 Porosity fracture	221
13.12 Circumnavigation fracture	221
13.13 SEM image of the tensile traction fracture surface - 550°C test	222
13.14 SEM image of the tensile traction fracture surface - 550°C test	223
13.15 SEM image of the broken copper-174PH interface - 550°C test	223
13.16 SEM image of the broken copper-174PH spherical interface - 550°C test	224
13.17 LCF transverse magnification of the fracture surface - general room temperature test	224
13.18 LCF circumnavigation fracture	225
13.19 Trans-copper general Low Cycle Fatigue fracture	225
13.20 174PH circumnavigation general Low Cycle Fatigue fracture	225
13.21 LCF $\Delta\epsilon = 1.0\%$ room temperature test fracture surface	226
13.22 LCF $\Delta\epsilon = 1.0\%$ room temperature test fracture surface	226
13.23 SEM LCF $\Delta\epsilon = 1.0\%$ room temperature test fracture surface	227

13.24	LCF $\Delta\epsilon = 1.8\%$ room temperature test fracture surface	227
13.25	LCF $\Delta\epsilon = 1.8\%$ room temperature test fracture surface	227
13.26	SEM LCF $\Delta\epsilon = 1.8\%$ room temperature test fracture surface	228
13.27	LCF $\Delta\epsilon = 1.4\%$ 150°C test fracture surface	228
13.28	LCF $\Delta\epsilon = 1.4\%$ 150°C test angle of fracture surface	229
B.1	Roughness tests results - part A	242
B.2	Roughness tests results - part b	242
C.1	Different molten pool dynamics, from [22]	243
D.1	Transient recording of the thermal transport properties of the material surrounding the sensor.	246
D.2	Sensor and sample temperature increase curves	247
E.1	Powder Chemical composition	252
E.2	Powder properties	252
E.3	Building platform and coordinate system	253
E.4	Main body and contour process parameters	253
E.5	DoE process parameters	253
E.6	Island scanning strategy	254
E.7	ED parameters	254
E.8	Thermal treatment furnace with specimens	255
E.9	Thermal treatment cycle	255
E.10	Sample preparation	256
E.11	Example of indentation print	256
E.12	Measured surface	257
E.13	Relative density vs ED	257
E.14	Relative density vs ED	258
E.15	Preliminary hardness testing results	258
E.16	Color scale-based hardness representation for as-build specimens: 1a) x-y plane; 1b) x-z or y-z plane	259
E.17	Specimens isotropy: as-build samples	260
E.18	Similitude between different quadrants: as-build specimens	261

E.19 Color scale-based hardness representation for heat treated specimens: 1a) x-y plane; 1b) x-z or y-z plane	261
E.20 Specimens isotropy: heat treated samples	262
E.21 Similitude between different quadrants: heat treated specimens	263
E.22 Hardness vs Energy Density - Specimens A	264
E.23 Hardness vs Energy Density - Specimens B	265
E.24 Hardness vs Energy Density - Specimens C	265
E.25 Hardness vs Energy Density - Specimens D	265
E.26 Hardness vs Energy Density - Specimens heat treated A	266
E.27 Hardness vs Energy Density - Specimens heat treated B	267
E.28 Hardness vs Energy Density - Specimens heat treated C	267
E.29 Hardness vs Energy Density - Specimens heat treated D	267
F.1 Hardness full results - Specimen A	268
F.2 Hardness full results - Specimen B	268
F.3 Micro-hardness full results - Specimen A	269
F.4 Micro-hardness full results - Specimen B	269
G.1 Traction Test 1 - Room Temp	270
G.2 Young Module Traction Test 1 - Room Temp	271
G.3 Traction Test 2 - Room Temp	271
G.4 Young Module Traction Test 2 - Room Temp	272
G.5 Traction Test 1 - 150°C	272
G.6 Young Module Traction Test 1 - 150°C	273
G.7 Traction Test 2 - 150°C	273
G.8 Young Module Traction Test 2 - 150°C	274
G.9 Traction Test 1 - 350°C	274
G.10 Young Module Traction Test 1 - 350°C	275
G.11 Traction Test 2 - 350°C	275
G.12 Young Module Traction Test 2 - 350°C	276
G.13 Traction Test 1 - 550°C	276
G.14 Young Module Traction Test 1 - 550°C	277
G.15 Traction Test 2 - 550°C	277
G.16 Young Module Traction Test 2 - 550°C	277

G.17 Traction Test 1 - 650°C	278
G.18 Young Module Traction Test 1 - 650°C	278
H.1 Ramberg - Osgood model - Test 1 Troom	280
H.2 Ramberg - Osgood model - Test 1 T150	280
H.3 Ramberg - Osgood model - Test 1 T350	281
H.4 Ramberg - Osgood model - Test 1 T550	281
H.5 Ramberg - Osgood model - Test 1 T650	281
H.6 Ramberg-Osgood relationship - T room	282
H.7 Ramberg-Osgood relationship - T 150°C	282
H.8 Ramberg-Osgood relationship - T 350°C	282
H.9 Ramberg-Osgood relationship - T 550°C	283
H.10 Ramberg-Osgood relationship - T 650°C	283
I.1 Young Module XY - test 1	284
I.2 Young Module XY - test 2	284
I.3 Young Module Z - test 1	285
I.4 Young Module Z - test 2	285
J.1 Ramberg - Osgood cycling model - First parameters attempt	286
K.1 Coffin - Manson Log-log parameters	288

List of Tables

5.1	<i>Carpenter Additive</i> 17-4 PH as-build and heat treated mechanical properties, from [19]	59
5.2	Concept Laser M2 Specifications	63
5.3	Job 1 and Job 2 parameters: nomenclature from Figure 2.4	64
5.4	Job 1 and Job 2 additional in formations	64
5.5	72
6.1	Test Planning	75
6.2	PID controller parameters	105
8.1	Material XY and Z pale SEM EDS chemical composition	131
8.2	Material overall SEM EDS chemical composition	132
8.3	17-4PH phase chemical composition - XY plane	133
8.4	17-4PH phase chemical composition - Z plane	134
8.5	17-4PH islands chemical composition: Start powder VS Melted powder	135
8.6	Pre-custom Cu-174PH powder % composition and the experimental % powder composition	136
8.7	Copper islands chemical composition	136
8.8	Chemical composition X-direction gradient analysis	140
8.9	Porosity analysis	144
9.1	Z direction thermal conductivity results - 4.5 mm Probing Depth	149
9.2	Z direction thermal conductivity results - 4.0 mm Probing Depth	150
9.3	XY direction thermal conductivity results - 5 mm Probing Depth	152
9.4	Z direction thermal conductivity Heat Treated results - 4.9 mm Probing Depth	153
9.5	Cu-174PH Thermal Conductivity	153
9.6	Cooperation of different materials coefficient of linear thermal dilatation	158

10.1 HV20 Hardness Tests	164
10.2 HV0.2 Micro-hardness Tests	166
10.3 Hardness/Micro-hardness VS Sigma estimation	167
10.4 Poisson's Ration Cu174PH (Room T.)	170
10.5 Young Modules VS Temperature - Cu174PH	170
10.6 Tensile Properties VS Temperature - Cu174PH	172
10.7 Ramberg Osgood Parameters - Cu174PH	174
10.8 NASA AM Copper alloy VS Cu174PH (Room T.), from [28] and [24] .	177
10.9 Estimated Cu174PH Z direction tensile properties	178
10.10 Compression Young Module	182
10.11 Compression Properties - Room Temperature	184
11.1 LCF high temperature and room temperatures Tests	186
11.2 Ramberg - Osgood Cycling curve relationship	200
11.3 Coffin-Manson equation Parameters	203
11.4 Ratcheting test - 550°C	204
J.1 Ramberg - Osgood Cycling curve relationship - First attempt Parameters	287
J.2 Ramberg - Osgood Cycling curve relationship - Correct Parameters . . .	287

Chapter 1

A New Space Economy Project

The potential of space exploration for Italy, Europe and the world is enormous. Europe and the world are facing major global challenges which require equally global responses and imply responsibilities.

The European economy depends on space infrastructures from the point of view of national benefits, social and economic impact of public space incentives on GDP (Gross Domestic Product), on innovation and on the environment.

The space sector needs innovation: reusing space components, such as engines and launcher stages, is the only way to limit space pollution. This requires a major effort by the scientific community to find new manufacturing technologies that, together with new materials, can extend the life of space components.

1.1 Aims of The Project

The present work has different social and technical main goal.

1.1.1 Technical Aims

- **New Composite Material for Space Rocket Application:** The main technical objective of this study is to investigate if the new Copper-Steel composite-metal-matrix alloy, developed by Sophia High Tech s.r.l., has an interesting behavior which purpose is to manufacture a general rocket liquid thrust engine chamber;
- **Test the Patented Powers Mixing Process @Sophia High Tech s.r.l.:** Sophia High Tech s.r.l. developed an innovative Powder Mixing Process able to mix two or more different powder in order make a starting mixed powder for the Additive Manufacturing SLM process. This study provide a indirect technical analysis of the Powder Mixing machine since the material has been printed with a starting mixed powder;
- **Material Characterization:** In the present work, due to the aim of simulating the thermomechanical behavior of a rocket liquid engine thrust chamber, a physical, chemical, thermal and mechanical characterization was mandatory. A massive test campaign was implemented and organize to provide all properties required for a non linear high temperature time dependent FEM simulation. Different international laboratories have been involved because of the requirement of complex facilities (such as High Temperature Low Cycle Fatigue testing machine);
- **New fields of research:** This first and brief Master Thesis Final Project could be a starting point for the implementation of particular composite material in the space liquid rocket engine recherche fields;

1.1.2 Social Aims

- **Science Innovation:** The present work shows a new pioneering patented technologies which could be used for future works and research fields. Furthermore, the main core of the work is a new composite-metal-matrix material processed by Additive Manufacturing SLM technology;
- **The key role of international research:** The cooperation of multiple nation, different international research centers and to work with people from various counties is a perfect way to achieve remarkable result;
- **Team Work:** The present study is a good example of team working. Several different experts have been involved in order to perform the thermal and mechanical tests and to discuss how the physics behind a complex new materials could works;

- **International recherche Cooperation:** This recherche activity has a strong Italian-French partnership and it proves the remarkable importance of international cooperation;
- **Students' Power:** The project has been created from the author of this manuscript. Students are the backbone of the University system and have to be more active, more propositional. Students should have more power face to the decision of their Final Project Thesis subject;
- **Covid-19 Emergency:** This work cloud be an example of resilience face to external not preventable problems. Covid-19 pandemic was declared in May 2020 and just 2 month later this project started. The have been problems and difficulties due to the pandemic state of emergency, but the team achieve all started expectations;
- **Italian Recovery Found (PNRR):** Studying, researching and developing new technologies, materials, manufactures (such as new space engine cooling channels geometry) is a good start to a near future research project that could benefit of the new European Recovery Found. This possibility could improve Italian National space knowledge and know-how in the domain of space material and methodologies to improve rocket engines life;
- **Space 4.0:** Nowadays we are in a new age for venture capital in space sector. It is know that the Space 4.0 is a real opportunity for all national industry to improve their scientific power. One of the goal of this research is to perform analysis with a modern methodology that match with the new space sector's mentality. This study is a good way to start surfing the Space 4.0 weave;

1.2 The Project

This pioneering project was born after several attempts to find an innovative industry ready to invest time and finance in an R&D program with a university partnership. In may 2021, after a amazing web meeting with Sophia High Tech CEO Antonio Caraviello and the R&D chief Domanico Borrelli, we decided to start the project by using a new just processed material.

This material has never been tested, especially for rocket engine application. Due to the high cost of Additive Manufacturing process both partners, SHT s.r.l. and University, found a balanced agreement: SHT s.r.l. provided two printing jobs for the recherche and the Politenico di Torino charged all testing costs.

1.2.1 Main Partners

In order to manage this R&D activity a team of different public and private institution was build up (Figure1.1). In particular the project involve three different Universities, five recherche centers, one french start up one Italian Industry and one Italian National Agency:

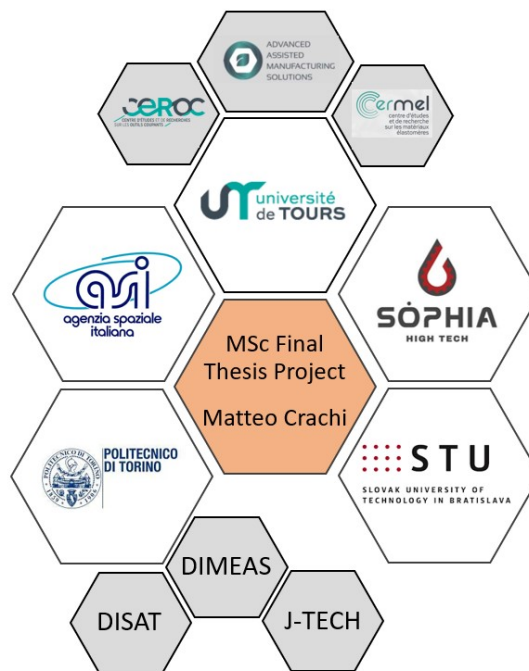


Fig. 1.1 Project Main Partners

- **Politecnico di Torino:** First public University involved in the project;
 - DIMEAS (Department of Mechanical and Aerospace Engineering) Laboratory;
 - DISAT (Department of Applied Science and Technology) Laboratory;
 - J-TECH (Advanced Joining Technologies) Laboratory;
- **Sophia High Tech s.r.l.:** Italian industry specialised in advanced manufacturing and R&D technologies for space and aerospace sector.
- **Université de Tours:** Second public University involved in the project;
 - CEROC (Study and Research Centre for Cutting Tools) Laboratory: Created in 2005, it brings together researchers from the Mechanics and Rheology Laboratory of François-Rabelais University and Sandvik Coromant's RD engineers to work on collaborative research projects. CEROC is an R&D tool open to regional companies, and an innovative training centre, at the interface between university and business. Combining the mastery of production conditions in industrial companies with the laboratory's expertise in characterising and modelling the behaviour of materials and surfaces, the center is a place to optimise its machining concepts and achieve productivity gains.;
 - CERMEL (Centre for Study and Research on Elastomeric Materials) Laboratory: Mainly specialised on the characterization of polymeric materials its missions range from fundamental and applied research (in support of the University of Tours' laboratories), to accompanying and supporting companies in their development and innovation projects. CERMEL is a technological and scientific platform dedicated to collaborative research on polymer and composite materials. Its main activities include: characterisation and modelling of the thermomechanical behaviour of materials, fatigue behaviour, adhesion problems, rheology and polymer ageing;
 - AAMS (Advanced Assisted Manufacturing Solutions): The startup was created by three experts, former employees of the world leader industry in cutting tools, in November 2019. AAMS provides solutions adapted to the various cases of industrial applications, while promoting environmentally friendly strategies, in compliance with your productivity and quality objectives. The company's purpose, in France and abroad, is to private and independent industrial research specialising in technological innovation and the realization and sale of technical studies and various services in these fields of activity, particularly for industry and training organizations.
 - Slovak University of Technology: Third public University involved in the project;

1.2.2 Project Organization

During the first project activity, Sohia High Tech s.r.l. and Politecnico di Torino, decided to start a parallel secondary sub-project: the main goal of the study was to understand the SLM Additive Manufactured Inconel718 behavior by changing the energy density. A DoE (Design of Experiment) has been programmed and several different tests have been performed in order to provide the propriety distribution respect to different process parameters and platform position. A BSc. student was tutored and supervised by Matteo Crachi during the experimental campaign and the numerical simulation activity.

A better schematic representation of both, Master thesis and sub-project is presented in Figure 1.2.

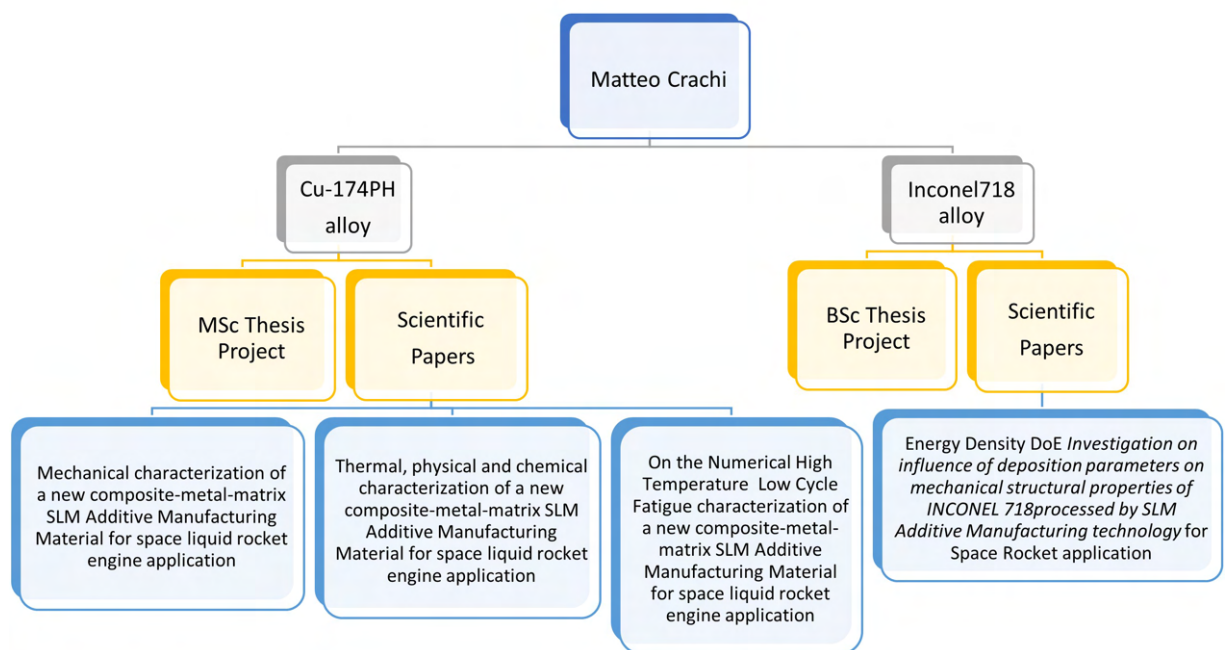


Fig. 1.2 Project schematic organization

1.2.3 Project Progress Logic

The project logical flux implemented in order to achieve all technical goals presented in Subsection 1.1.1 is presented in Figure 1.3. The project has been divided into two main core:

1. Testing Campaign: This first activate was needed in order to know all basic mechanical, physical chemical and thermal properties of new printed alloy and implement those into a Commercial FEM Software;
2. Numerical Simulation of the thrust chamber: Via numerical simulation it has been possible to evaluate the effective real benefits of using an innovative composite-metal-matrix material for the particular understudy application. In addition, if

the target life of the thrust chamber is not reached, it is possible to understand which properties should be enhanced and improved;

3. Geometrical optimization: The final process proposed in this study is an iterative geometrical optimization of the engine cooling channels. Additive Manufacturing has huge advantages for re-design and re-engineering engine cooling channels by providing complex structure in order to improve life and performances;

Due to the high cost of the printing Additive Manufacturing SLM activities, the majority mechanical properties of the new alloy have been tested only in the X-Y direction. However it is important to underline that for fracture mechanism that mainly reduce engine's life, which will be presented in subsequent Chapters, can be characterized by the X-Y direction specimens orientation respect to the printing platform.

Because of the main objective of the present final thesis project is to understand if a new complex additive manufactured material can be used for a new era liquid rocket engine the starting thrust chamber geometry has been taken from the SSME (Space Shuttle Main Engine) project available on literature (NASA archive). Both, the convergent-divergent shape and the cooling channels geometries, for these first-study activities, have been fixed and not more modified. After the massive test campaign and the standard SSME geometrical implementation, numerical simulations start. For the engine cycle profile (heat flux and pressure profile) a classic NASA's test has been used. After reaching all the time dependent profile mapping the same temperature profile has been used for all mechanical cycling simulation. Every mechanical engine's cycle has the same temperature profile. The difference between cycles is the damage that the structure experiences because of the plastic-creep deformation.

The last step of the project logic is to achieve a better engine life by an iterative procedure whose main goal is to use the benefits of the Additive Manufacturing process to implement new structural shapes inside engine cooling channels.

1.3 The New Space Economy

Space has become an important vehicle for achieving objectives in key policy areas including environment, security, economic development, mobility and resource management [29].

According with ESA definitions¹ the first era of space, Space 1.0, can be considered to be the early study of astronomy (and even astrology). The next era, Space 2.0, came about with space faring nations engaging in a space race that led to the Apollo moon landings. The third era, Space 3.0, with the conception of the International Space Station, showed that we understood and valued space as the next frontier for cooperation and exploitation. Space 4.0 era is a time when space is evolving from being the preserve of the governments of a few Spacefaring nations to a situation in which there is the increased number of diverse space actors around the world, including the emergence of private companies (Figure 1.4 shows the growing of private authorised launches in USA from 1989 to 2021), participation with academia, industry and citizens, digitisation and global interaction.

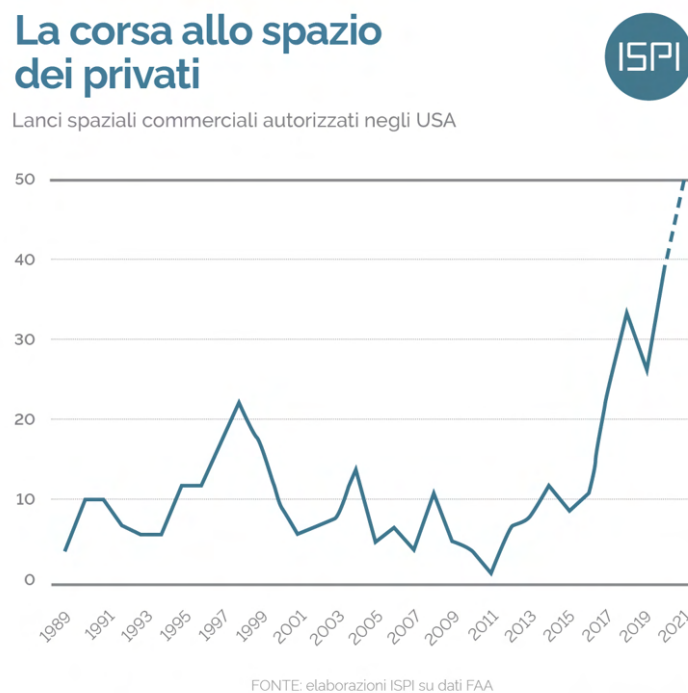


Fig. 1.4 Private industry space race by ISPI (Italian Institute for International Political Studies)

The Organization for Security and Co-operation in Europe (OCSE) provides us with a definition of Space Economy meaning: *"The whole range of activities and use of resources that create and provide value and benefits to human beings in the course of exploration, understanding, management and use of space"*.

¹<https://www.esa.int/AboutUs/MinisterialCouncil2016/WhatIsSpace4.0>

The Space Economy comprises public and private actors involved in the development, supply and use of space products and services such as R&D, manufacturing and use of space infrastructures in order to enable applications, as well as enabling the scientific research generated by them. It follows that the Space Economy goes beyond the space sector itself as it encompasses the continuous and increasing the space sector itself as it encompasses the continuing and growing impacts of space.

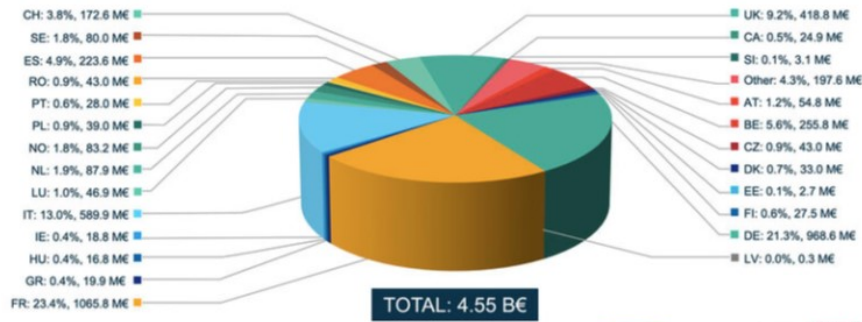
The present work is directly linked to the New Space Economy age, now days also called Space 4.0. Thanks to the new space venture capitals and world wide international incentive to the space sector new technologies, such as the Powder Mixing Machine developed by Sophia High tech s.r.l. and AVIO s.p.a. used in the present study to process the starting powder for the SLM printing activities, are under investigations and provide important new recherche paths.

Europe is developing new investment strategies in order to promote space innovation: an interesting example is the ESA² Business Applications offers funding and support to businesses from any sector who intend to use space (satellite navigation, earth observation, satellite telecommunication, space weather, space technologies) to develop new commercial services.

Figure2.12 shows ESA investment in space divided by domains and by member state contribution in 2021. This pie-chart visualization prove a clearly representation of the most important European nations involved in the spec sector: France (first fort investment in 2021) and Italy (second for investment in 2021) take the lead. It is not a coincidence if the present Master Thesis Final Project work involve Italian and French recherche centers.

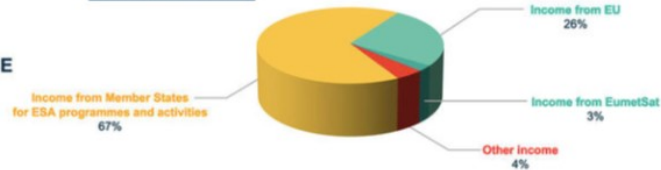
²European Space Agency

BUDGET 2021 ESA Activities and Programmes



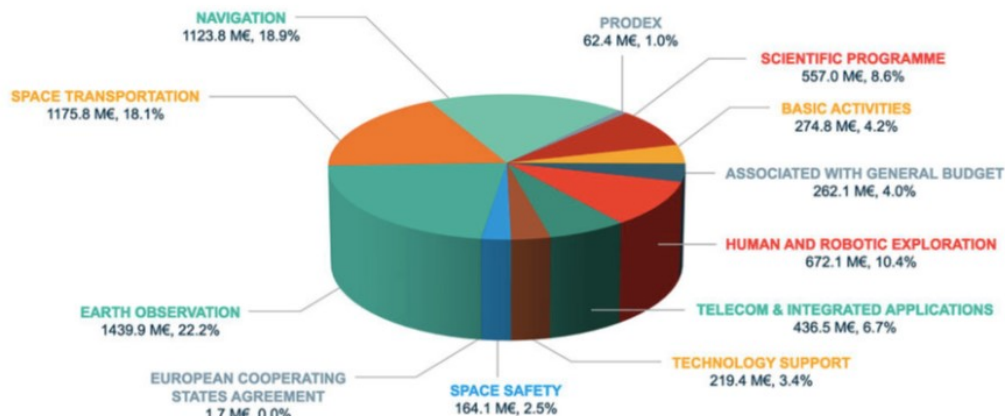
BUDGET 2021 BY FUNDING SOURCE

TOTAL: 6.49 B€



(a) ESA member states investments

ESA BUDGET BY DOMAIN FOR 2021: 6.49 B€*



(b) ESA domain investments

Fig. 1.5 ESA investment in 2021

Space sector generates knowledge and innovation contributes to Europe's identity and capabilities. Europe requires perspectives on how to manage mid- and long-term challenges in exploiting the full potential that space holds for society. The European Space Policy Institute (ESPI) responds to these needs through analyses and advices, with the aim of supporting space as a strategic policy area for Europe by providing different strategic document. Requirements for considering a country a space power can be found in a Measuring Space Power Map proposed by the ESPI³ in Figure 1.6.

³European Space Policy Institute

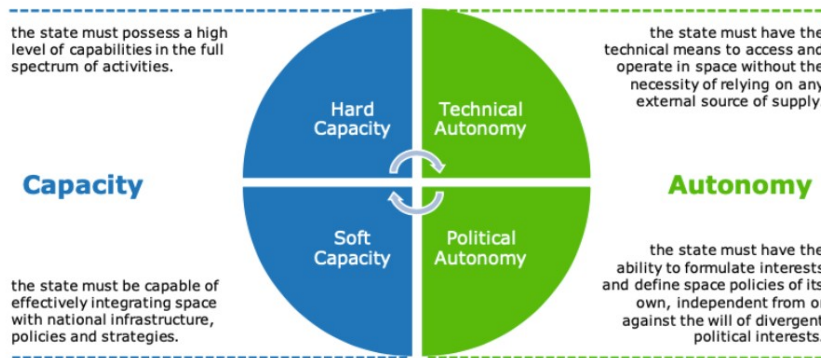


Fig. 1.6 Measuring Space Power

Today, if we use the definition of Space Power proposed by the ESPI, Europe can be classified as a Spacefaring Nation inside a Space Power Matrix: significant capacity but limited autonomy (Figure 1.7).

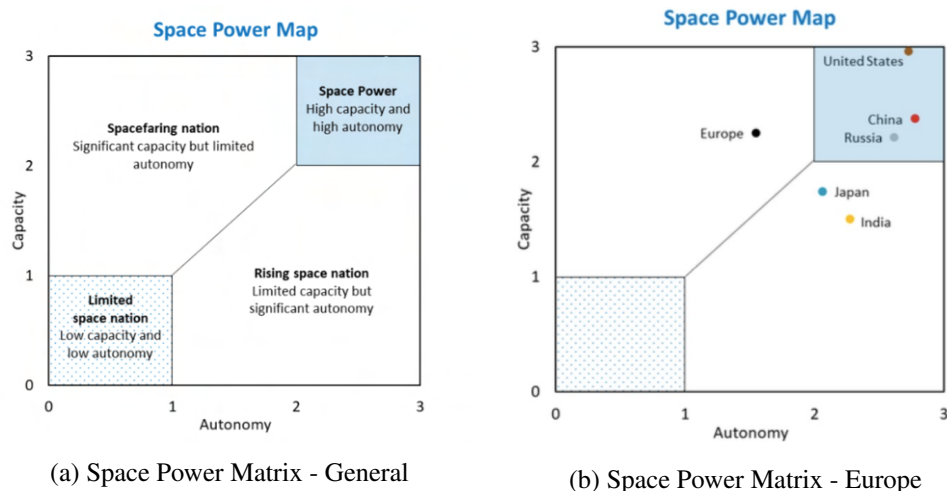


Fig. 1.7 Space Power Matrix by ESPI

Space 4.0 represents the evolution of the space sector into a new era, characterised by a new playing field. This era is unfolding through interaction between governments, private sector, society and politics. Space 4.0 is analogous to, and is intertwined with, Industry 4.0, which is considered as the unfolding fourth industrial revolution of manufacturing and services. To meet the challenges and to proactively develop the different aspects of Space 4.0, the European space sector can become globally competitive only by fully integrating into European society and economy. This requires a sustainable space sector closely connected with the fabric of society and economy. For this to happen, space must be safe, secure and easily and readily accessible, and built on a foundation of excellence in science and technology – broadly and continuously over time.

Chapter 2

Introduction: Additive Manufacturing in the Space Liquid Rocket Engine (LRE) Industry

2.1 Metal Additive Manufacturing Technology

The American Society of Testing and Materials (ASTM) has defined the Additive Manufacturing (AM), sometimes also called as 3D printing, as a process of joining materials to make objects from 3D model data, usually layer by layer, as opposed to subtracting manufacturing technologies [30].

This definition applies to a broad range of materials, such as polymers, ceramics, and metals. The interest here, however, is devoted only to metallic materials. Subtracting manufacturing, also referred as conventional or traditional manufacturing, often begins with a solid billet of material which is machined down to finished size whereas in AM the material is deposited layer by layer to form a solid part. AM components generally require a final machining stage to achieve the desired dimensions, tolerances, and surface finish [31].

AM's main strength is removing a lot of the limitations present with traditional manufacturing techniques and allowing unparalleled design freedom. In particular, AM designs provide great opportunities for new materials, weight optimization, as well as to realize complex and customized shapes and geometries that are impossible or too expensive to create with traditional production techniques [2]. Part consolidation is another prominent benefit of AM production techniques. Part consolidation is the act of consolidating multiple components into one piece without assembly operations. Part consolidation has the primary benefits of reducing the assembly operations and minimising the usage of joining methods such as bolting, welding, brazing, soldering and chemical bonding methods. Minimising these operations in the production process drastically decreases the need for skilled labor throughout resulting in cost reductions. The tooling necessary to manufacture components through traditional manufacturing methods is also reduced by using part consolidation through AM techniques. Another

advantage is the reduced number of components requiring certification and associated documentation, leading to cost time and cost reduction. Risk mitigation is inherent in component consolidation as fewer joins and fewer processes are involved in the manufacturing process [8]. However, compared to parts made with conventional manufacturing, additive manufacturing requires a higher level of inspection in order to detect any potential material flaws like pores or areas of insufficient bonding, which may have a deteriorating effect on the material properties [32]]

Differently from conventional manufacturing, applying metal additive manufacturing requires to address the entire manufacturing process chain, not just the printing of the component. The manufacturing starts with the selection and quality control of the feed-stock material which is used for the manufacturing process. After the printing, several processes are available to improve the surface quality of functional surfaces where needed. Machining steps like the cutting of threads or the milling of sealing surfaces may need to be adapted. Finally, non-destructive testing of the manufactured part needs to be performed [33]. Moreover, the layer-by-layer process that characterize the AM inherently means that not all geometries can be printed in any orientation.

Figure 2.1 shows a unit cost versus production volume and production complexity identifying economically and technically optimal scenarios further developed in this monograph [8, 1]. The AM technology can be easily applied to LRE thrust chambers fabrication process because of the high-complexity and low-production volume of the component: this scenario is especially valuable.

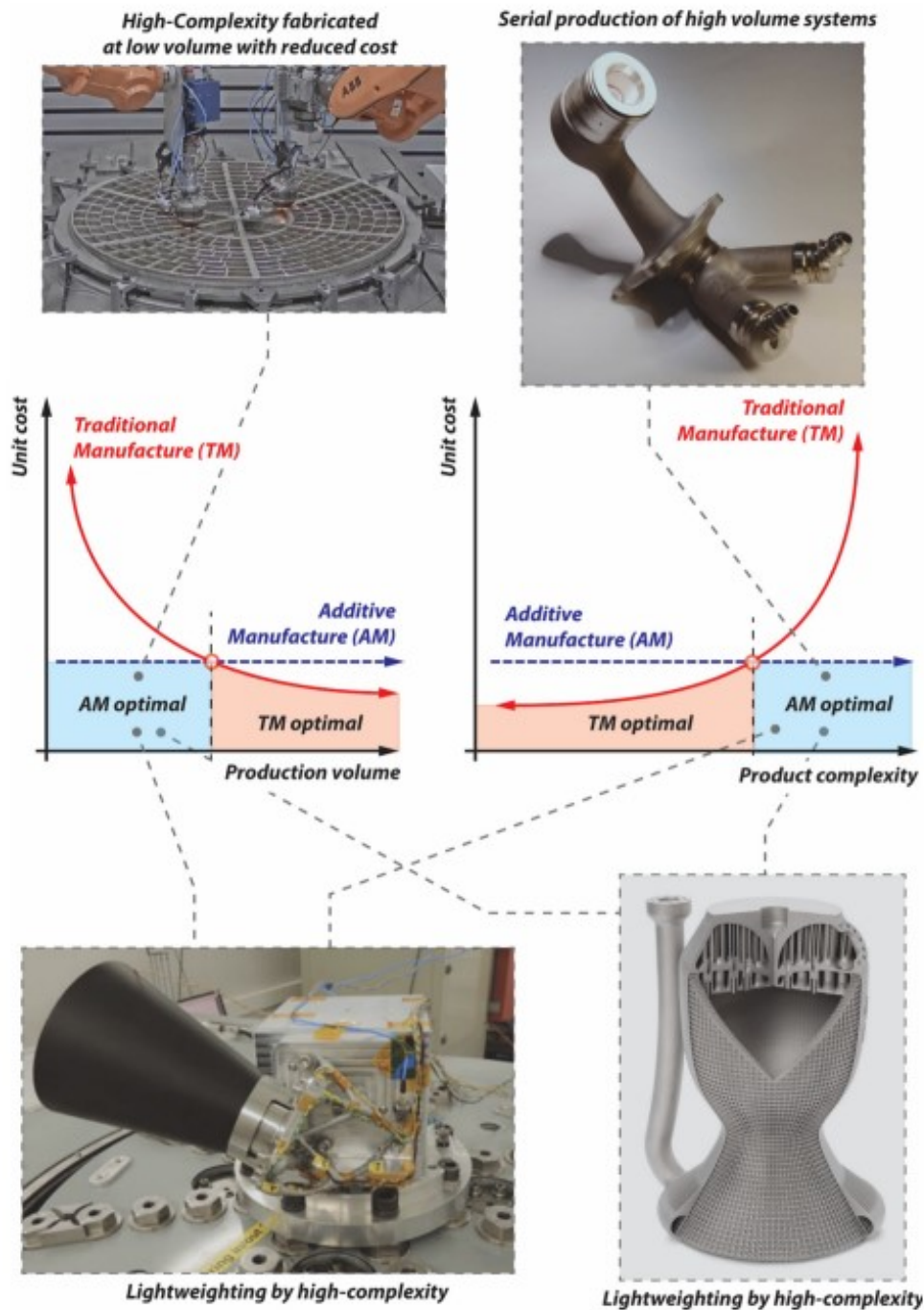


Fig. 2.1 Additive Manufacturing (AM) VS Traditional Methodologies (TM), from [1]

In conclusion, AM is still an emerging technology that will not replace conventional manufacturing methods also because of its increased energy consumption, higher raw material cost, and initial capital investment. Rather, the two technologies will coexist [31].

2.1.1 Selective Laser Melting (SLM)

Selective Laser Melting (SLM), also known under the trade names "Laser Powder Bed Fusion (L-PBF)" or "Direct Metal Laser Sintering", among others, is one of the most commonly used metal AM techniques. The feed stock is provided in powder form which is deposited and melted layer-by-layer on a build plate. The entire SLM process cycle consists of a series of steps from CAD data preparation until the removal of the printed component from the building platform. Before the data are uploaded to the SLM printer, the STereoLithography (.STL) files have to be processed by a 3D printing software, (e.g. Materialize Magics, nTopology, Autofab) to provide support structures for any overhanging features, inspect the geometry of the part, and generate slice data for laser scanning of individual layers. A high-density laser, directed by a scanning mirror, is used to melt selectively regions of metal powder spread across the fabrication bead. Providing the necessary energy at micro-scale focus, the powder absorbs this energy creating local melting. After one layer is finished the build plate is lowered, re-coated with a blade or re-coater arm, and the melting process go on, until a three-dimensional final shape is achieved (Figure 2.2, from [11]). The subsequent removal of the un-melted powder particles and the support structures can be achieved by different methodologies (e.g. band saw, EDM¹). The deposited layer has a typical height in the range of 20–100 μm . To prevent excessive oxidation of the metal in the melt pool, the SLM process occurs in an inert environment [2].

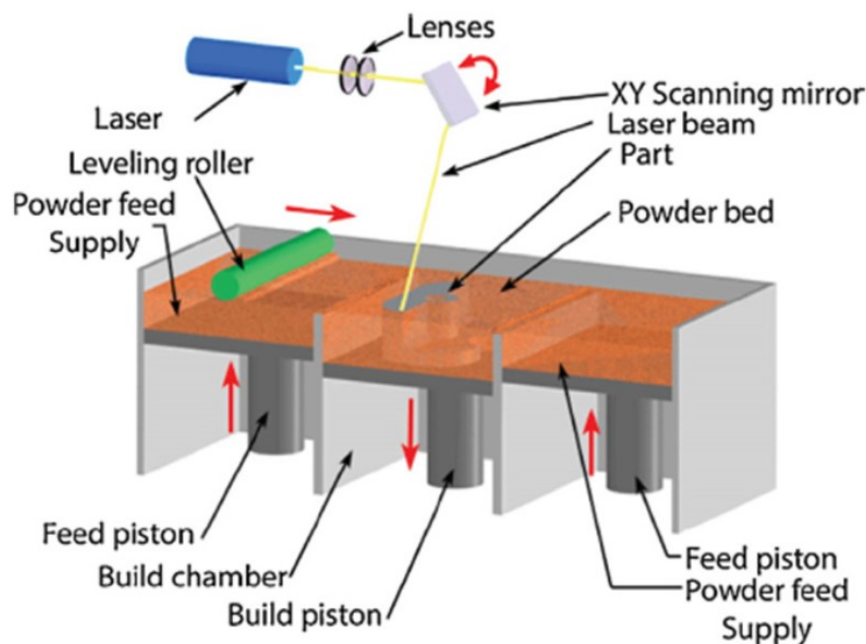


Fig. 2.2 Schematics of additive manufacturing (AM) by Selective Laser Melting (SLM) process

The SLM process is the most mature metal AM technology with the ability to produce complex structures with high resolution. However, besides the great advantages of metal AM and of L-PBF in particular, a number of issues must be taken into consideration

¹Electrical Discharge Machining (electroerosion)

when choosing this technique. In fact, some of the main drawbacks of SLM are as follows:

- Variability of the mechanical properties depending of the starting powders, process parameters, post-processing, size of the build volume, spatial location within the build volume, scanning strategy [34], etc. This implies that material characterisation is often lacking and hard to be achieved in sort time and with imitated cost;
- The as-built parts show a relevant degree of anisotropy in mechanical material properties ([35],[36]). The object is generally (but not necessarily) weaker in the direction perpendicular to the build plate;
- Excess porosity and defects often occurs due to unmelted/partially melted powder particles, lack of fusion between layers, key holes, cracking/delamination, and gas entrapment;
- Rapid cooling of the molten material (in the vicinity of 10^{-5} °C/s due to the highly localized heat input [31] may induce non-uniform precipitate microstructure phases and consequently unintended residual stresses. In order to eliminate the non-ideal material microstructure and the residual stresses, post-printing heat treatment is necessary;
- Relatively high surface roughness that often require post-printing surface finishing; furthermore, the orientation of surfaces also influences the roughness. This is a result of the stair-casing shape of the exposed surfaces induced by the selected layer thickness;
- The design must be adapted to the layered manufacturing process. Consequently, design is typically constrained by no overhangs with inclination larger than about 45° with respect to the build direction and by holes with a minimum feasible size;
- Conventional machining of critical surfaces (interfaces, sealing surfaces, tight fits) is still required;
- Build envelope size of the current largest printers is limited to less than 1 cubic meter;
- Large amounts of powder material to fill the powder bed are required, even if a small part is being built;
- Produces significant waste: spent powder, build plates, failed builds;
- Long build time (that implies low production rate);
- Internal passages cannot be fully inspected;
- Removing powder from small internal passages is not always easy;

- May not be cheaper than traditional manufacturing;
- Particular materials (especially Copper-based alloy) have important laser reflection and local optical lens damage can occur [11];

Among the drawbacks mentioned, the inherent variability of SLM material properties is one of the most important aspects. Consequently, any modification of process parameters, of the material's supplier ², or of the printer used requires a new characterization of the material properties. However NASA's studies show that the same machine with the same powder batch has a job good reproducibility on the platform [38]. Another important aspect is the number of remixing process of the not used previous job powders : a new batch of material will have different properties respect to a first recycled one, which behaves different from, for example, a third recycled one[39]. This characterization, consisting mainly of tensile properties, low and high cycle fatigue life, creep, thermal conductivity, hardness and microstructure (the characterization is typically evaluated by destructive and non-destructive tests on suitable printed samples). Material characterization is devoted also to assessing the anisotropy with respect to the build direction, the variability within the build position, and the effect of the post-printing heat treatments. The criticality related to this issue is further confirmed by the fact that each print job is accompanied by a minimum set of samples that are tested to confirm the expected material properties (in Figure 2.3 it is clearly possible to see printed z-direction traction specimens [7]).



Fig. 2.3 Example of large-scale NASA GRCop-42 chambers fabricated by SLM

Often, in the initial stage of a new material or new component definition, the L-PBF process parameters that optimize the mechanical properties, and possibly the surface

²Same material can be provided by the powder supplier with different atomization process from one batch to another (the supplier could change the atomization process for several different reason). By changing the atomization process the material behavior could completely changes [37]

quality, are assessed by proper preliminary studies. The main process parameters that impact the material properties are: the laser power, the laser spot size, the laser timing, the laser scan strategy, the scan speed, the layer height, the hatch spacing/overlap, the contour spacing/overlap (Figure 2.4, from [40]), the type of re-coater arm, the placement of parts on the build plate, and the build chamber environment [2]. An optimal set of parameters and machine configuration exists to achieve minimal porosity and the most favourable mechanical properties for the core material. In addition, a different set of parameters for contouring can be found to optimize the surface finish [2]. It is worth noting that minimization of porosity reduces the associated stress concentration and thus the possibility of crack propagation while minimization of the surface roughness improves the fatigue behavior. Further minimization of the porosity can be achieved by post-printing heat treatments while further minimization of the surface roughness can be achieved by post-printing surface treatments. However, minimization of the surface roughness by proper selection of process parameters is important for parts with inaccessible internal surfaces, where post-printing surface treatments cannot be applied.

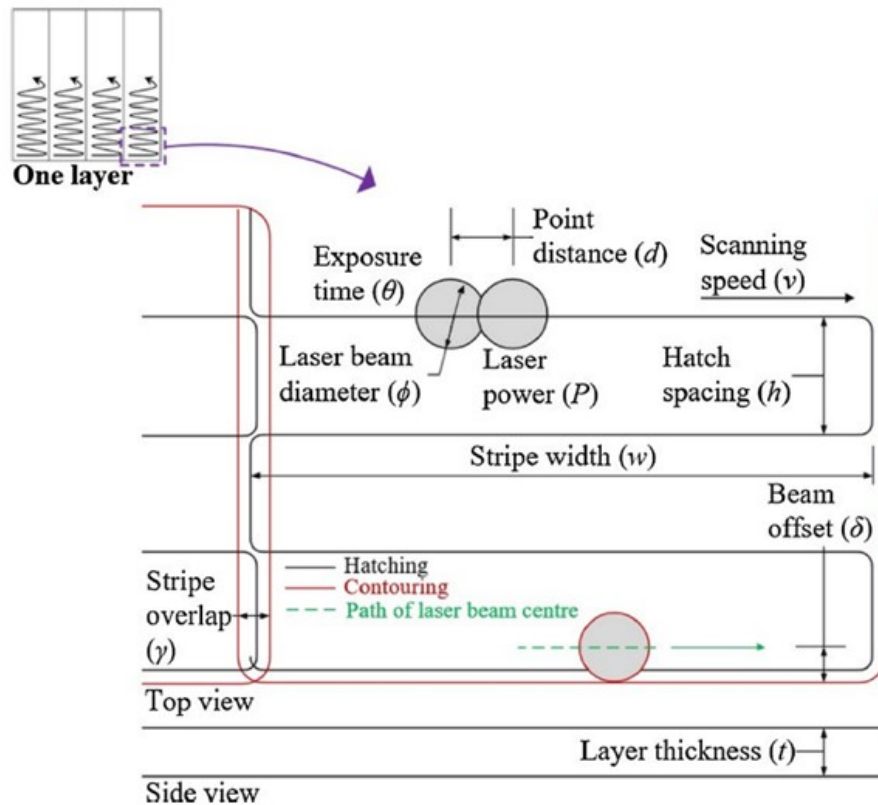


Fig. 2.4 Illustration of Selective Laser Melting main process parameters

Heat treatments play an important role in modifying the microstructure and mechanical properties of SLM parts, particularly when made of heat-treatable alloys. In fact, a post-printing thermal treatment is often required, including stress relief, homogenization and hardening, and hot isostatic pressing (HIP) [31]. During HIP, the part is placed in a chamber and gradually heated to a specified temperature, whilst being subjected to high pressure which is isostatically applied. Besides acting as a stress relief treatment, it strongly reduces the number and size of the internal pores, bringing to near 100%

density. The HIP process further aids with homogeneity of the AM material [2]. Since heat treatment operations such as HIP can sinter powder, a proper removal of the excess powder from the internal cavities (Figure 2.5) is an essential post-build procedure[2].

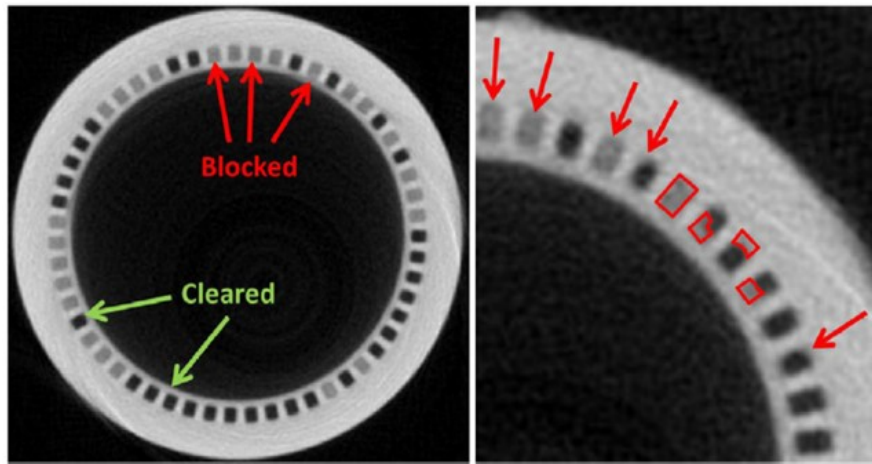


Fig. 2.5 Examples of fully and partially blocked internal channels shown in Computed Tomography, from [2]

Surface treatments should be considered for L-PBF produced parts because they are susceptible to a high surface roughness compared to machined alternatives. This can reduce fatigue life due to crack initiation locations in addition to a negative impact, in case of fluid-dynamic components, on fluid pressure drop [2]. The surface roughness resulting from L-PBF printing is highly dependent on the material, geometry, post-processes, and machine selected. In particular, there is a strong dependency on the build angle on surface finish. The best surface finish is typically found parallel and perpendicular to the build plate, whereas over-hang structures result in a significant increase in roughness [2].

The verification of the requirements of the SLM components is obtained, as well as by sample tests for the evaluation of the material properties, by means of non-destructive tests on the built component. Several non-destructive techniques exist that can be applied to the AM components. One of the most common evaluation techniques is the Computed Tomography (CT) scanning, which determines changes in density to highlight subsurface defects/pores and can be used to verify that the internal volumes are clear of excess powder. This technique has the advantage of revealing defects, even when surfaces are not physically accessible. An alternative technique to reveal subsurface defects for well-accessible surfaces is ultrasonic testing. Other techniques may include traditional or digital X-rays, borescope inspections, in-situ monitoring, and infrared flash thermography. Moreover, to verify dimensional accuracy, the method of structured light or 3D laser scanning may be used [2].

2.2 Metal Additive Manufacturing in the aerospace sector

The aerospace sector relies heavily on machined forged and billet structures. This conventional manufacturing methodology provides high certainty in final component quality, as billet materials are readily certified for porosity and microstructure, but adds substantial direct manufacturing costs and induced costs due to high production lead times. Forging requires the expensive design, manufacture and trialling of preforming dies and billet machining is inherently expensive with typical buy-to-fly ratios estimated at 20:1 [8].

The fundamental opportunities for metal additive manufacturing in aerospace applications include: significant cost and production-time reductions, novel materials, unique design solutions with high degree of geometrical complexity, mass reduction, and minimization of traditional joining processes. A further advantage of the additive manufacturing applied in the aerospace sector is the possibility to improve the design process of a new component. In fact, due to the high cost and complexity of aerospace hardware, it is often common practice to delay the procurement and testing of components when applying conventional manufacturing processes. This reduces the risk of a redesign or costly failure during test. Also, for parts that were traditionally cast the time invested to develop the casting often does not allow for multiple design iterations. Additive manufacturing, thanks to its low cost and quick turnaround times, allows the construction and testing of hardware from the earliest stages of a project development. This positively affects the design and analysis of a new system [41].

At present, AM has a limited role in the production of aerospace parts mainly because of the difficulty in modeling the manufacturing process and predicting the properties of printed parts. This leads to a lack of standardization and therefore limited use of AM in the aerospace industry [42]. Concerning the sole space sector, the design freedom afforded by AM, as well as the potential mass and time savings, is ideal for the space industry, where part production is low volume and highly customized. Consequently, there is a strong push to research these new manufacturing technologies. However, massive use of AM in the space industry has not occurred yet though [42].

The described opportunities of metal-AM are being applied in a range of high-profile aerospace applications, the most notable being heat exchangers, turbomachinery, and liquid-propellant rocket engines. Concerning the heat exchangers, they are characterized by complex designs and internal features. Manufacturing these devices through AM allows for vast improvements in part count reduction, lead time reduction, light weighting and cost reduction [8].

As the AM technology has evolved and AM machines have increased in scale, additional cost and schedule savings are realized moving from two-piece welded to single piece chambers. The possible cost reduction with AM technologies is about 1/3 [2] respect to traditional processes (Figure 2.6).



Fig. 2.6 Comparison of traditional manufacturing to additive manufacturing evolution (cost in US\$, 2020 equivalent), from [2]

Concerning the turbomachinery of both aircraft and rocket engines, they are composed of static and rotational components that are subject to both extreme performance requirements and harsh environments such as elevated pressures, temperatures, and corrosive or embrittlement conditions. These performance requirements often lead to highly complex geometries and special materials being used. Since components such as compressor blades, turbine blades, inducers and impellers have highly complex geometries, AM can be used to increase their performance. In fact, AM technology enables more designer freedom from geometric constraints commonly found using traditional manufacturing techniques allowing for more intricate final components. However, there are limitations of the AM process in producing some of these geometries in build angles and also rougher surfaces than traditional machining [8].

Finally, although there are only very few certified-for-flight AM rocket engines, additive manufacturing of such devices, with particular emphasis on the thrust chamber assembly, is one of the main areas of research and development in the aerospace industry.

2.2.1 Additive Manufacturing of liquid rocket engine thrust chamber assembly

The size of a typical rocket engine is much bigger than the now days available maximum printing volume of common SLM machines (Figure 2.7).

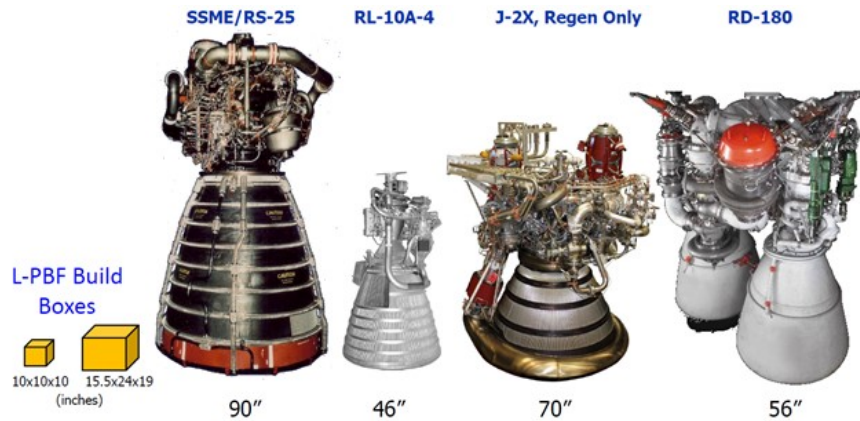


Fig. 2.7 Additive Manufacturing imitated scale machine technologies respect to common size liquid rocket engine, from [3]

Due to this technological limitation it is possible to only produce separate main engine components. Figure 2.8 shows NASA's use of Additive Manufacturing respect to almost 80% of the entire engine (it is important to know that not all highlight components are processed by SLM AM: the nozzle is a DED³ example).

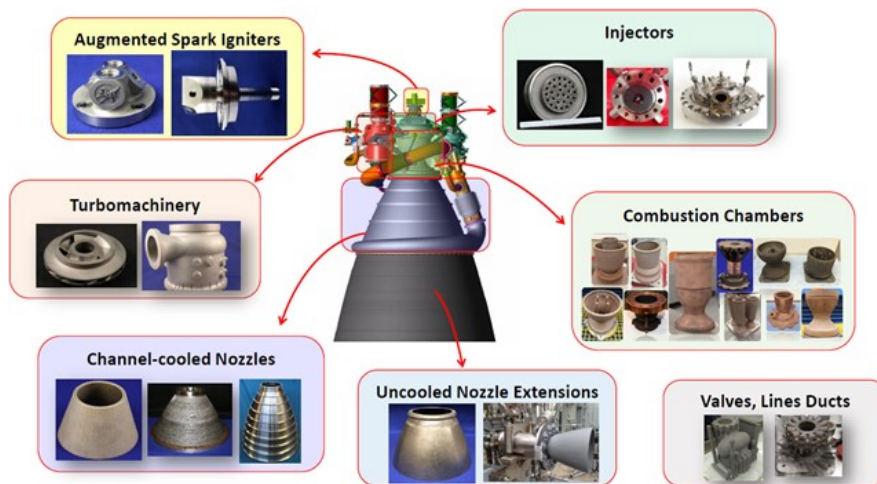


Fig. 2.8 Additive Manufacturing used across all components on liquid rocket engines, from [3]

The thrust chamber assembly of a liquid rocket engine is composed of two main components: the injector and the thrust chamber. The injector, having the aim to inject the propellants within the thrust chamber, is composed of propellant manifolds and a proper number of injector elements that are designed and distributed in such a manner to guarantee homogeneous propellant flow from the injector manifolds to the thrust

³Direct Energy Deposition

chamber, with the desired mass flow rate. The thrust chamber, being the component where the propellant is mixed, burnt, and accelerated, has a convergent-divergent shape and is often composed of suitable cooling channels.

From a design and manufacturing point of view, a liquid rocket engine's injector is one of the most demanding subsystems of a liquid rocket engine. The injector is subjected to extreme temperature and pressure gradients: during startup, in many applications the propellant manifolds of the injector cool down to cryogenic temperatures within seconds, whereas the injector face plate has to withstand the thermomechanical load induced by the combustion, which takes place at temperatures above 3000 K and a pressure level of up to 200 bar [4]. In today's rocket engines, an injector typically consists of hundreds of individually manufactured components with precise tolerances that must be joined together by welding or brazing. The integration process is characterized by numerous manual working steps, inspections and checks and thus significantly contributes to the overall manufacturing cost of a rocket engine [4]. The injectors are particularly attractive devices to additively manufacture due to their complex geometries and intensive fabrication. AM can greatly reduce part count and joints associated with multi-element injectors, as they may be composed of very few AM parts.

A good example of a AM injector head is the AVIO S.p.A. effort to develop new concept for the new cryogenic engines development for Vega-E application. The research activity was born to exploits the new benefits coming from the new manufacturing technology, overcoming some of the limits that have been always met in the past history of rocket engine development [43].

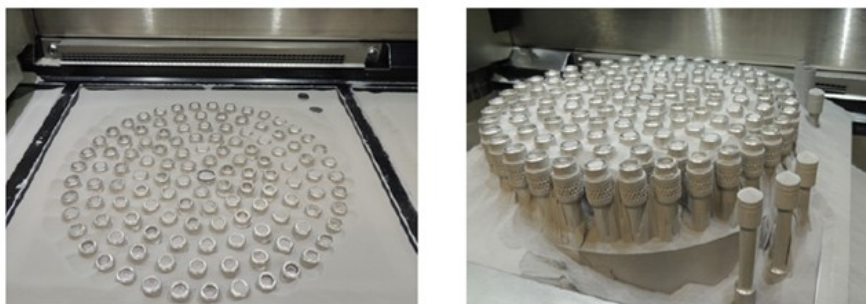


Fig. 2.9 Full-scale manufacturing demonstrator for liquid rocket engine application, from [4]

The reduction in part count also increases the reliability of the component. Fewer parts and assembly steps reduce the likelihood for error during assembly and streamlines the fabrication and assembly procedures. Eliminating welds and braze operations by combining parts, also eliminates the required inspections after the processes are performed [41]. Additionally, additive manufacturing allows to optimize the design of the injector's reducing the weight of the component. In fact, a conventional injector is typically milled from a cast raw part and the manufacturing steps to minimize the wall thickness or locally remove material where it is not needed are skipped, as the potential weight savings cannot balance the additional cost of manufacturing [4]. Some of the specific disadvantages of using AM for injector fabrication, such as poor size resolution and excessive surface roughness, are an active area of development within the

industry and their influence has diminished over time and can be expected to diminish further. Another current disadvantage in injector manufacture, that applies when using AM processes based on powder feed stock, is the necessity to remove residual powder from internal passages where the part may have limited access. Removing all the powder prior to any heat treatment (even stress relief) is necessary because trapped powder can become sintered, making it difficult or impossible to remove later [7].

Thrust chambers of liquid rocket engines are conventionally fabricated using numerous manufacturing methods. The most common methods for chamber fabrication include tube-wall design and channel wall design. In any case, for efficient cooling the wall structures in contact with the hot gas in thrust chambers should have minimal wall thickness (0.25mm - 1mm range. Figure 2.10 from [6]) and require materials that can withstand the high thermal stresses that occur during hot-fire operations.

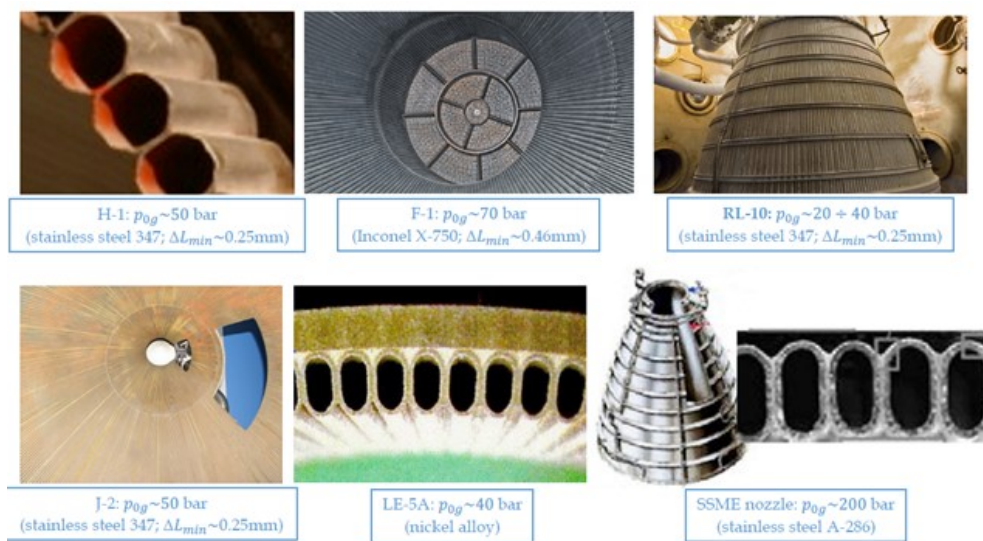


Fig. 2.10 Tubular-wall design used on relatively low chamber pressure thrust chambers or nozzle extensions

Copper alloys have a high thermal conductivity and therefore a relatively low wall temperature for a given heat flux, but they lose mechanical strength at a relatively low temperature. Nickel or iron superalloys have a much lower thermal conductivity, and therefore a high wall temperature for a given heat flux, but are able to maintain mechanical strength at higher temperatures than copper alloys [44].

With conventional approaches, the thrust chambers are manufactured using a series of wrought forming and assembly methods that include forging, machining (Figure 2.12a), electroplating or electrodeposition (Figure 2.12b), welding, brazing (Figure 2.12c), and casting, among several other techniques. Despite being well-established in the industry, these production techniques often prove to be labor-intensive, costly and result in components and subsequent systems with a high part count [2]. Figure 2.11 shows a schematic representation of one of the most common thrust chamber fabrication procedure.

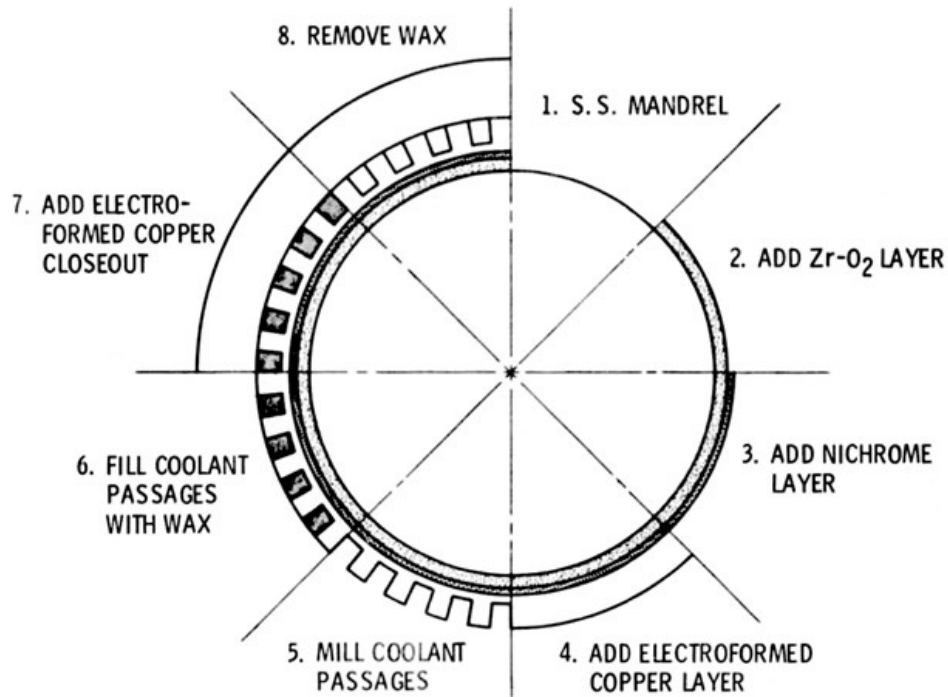


Fig. 2.11 Typical fabrication procedure is shown, where the laying of a thermal barrier coating, usually composed by Yttria-stabilized Zirconia[5], and a Nichrome layer, to protect from oxidation, are included, from [5]

Also in this case, metal additive manufacturing opens new opportunities from both a technical and economical perspective, thanks to greatly reduced production time and more competitive thrust chamber designs that are not feasible by conventional methods [2]. For example, an AM thrust chamber can integrate both the coolant manifolds and the cooling channels in a single component. However, the selection of the material is a critical choice. In fact, while copper alloys are preferred from a thermo-mechanical point of view, especially for thrust chambers operating at high combustion pressure (that is, with high heat flux to the chamber wall), AM is more mature with other materials, like nickel-based or iron-based alloys. These latter materials, being capable of withstanding extreme temperatures while maintaining a good mechanical strength, can be considered acceptable for an AM thrust chamber, as long as the combustion pressure is not too high. Of course, AM production of thrust chambers has the same drawback described for the injector, like poor size resolution, excessive surface roughness, and powder removal from internal passages.

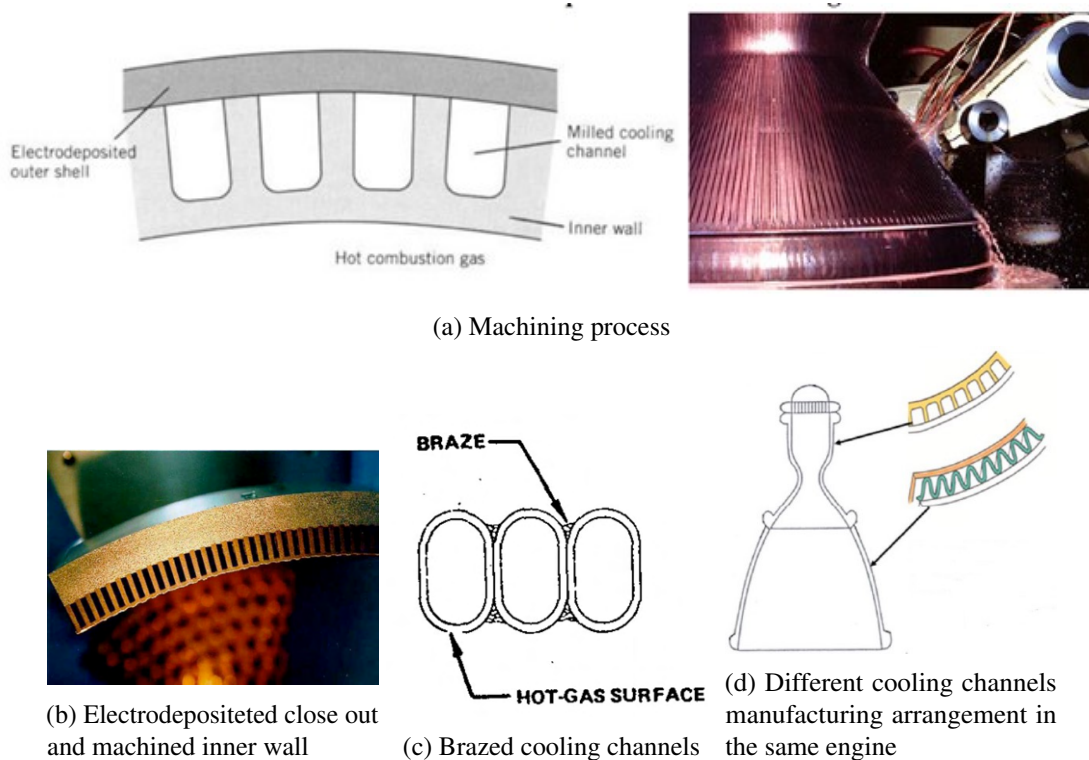


Fig. 2.12 Conventional rocket thrust chambers manufacturing technologies, from [6]

2.3 Materials for Liquid Rocket Engine (LRE) Thrust Chambers

The extreme High-pressure, high-temperature and high-oxidation operating environment of Liquid Rocket Engine components can be defines as a challenging recherc domain for material science. Due to this complex condition a regeneratively-cooled LRE thrust chambers and nozzles require very thin-walls for the channels. LRE has key requirements that must be considered for material selection [45]:

- **Thermal Conductivity:** The primary driver of wall temperature in regenerative-cooling is conduction through ribs and the hot-side wall. A higher thermal conductivity allows use of higher hot-side wall thickness to achieve same hot-side wall temperature. From a different point of view: the higher is the conductivity the higher is the heat flux (by assuming constant wall thickness), therefore we can achieve hot-side wall lower temperature;
- **Low Cycle Fatigue (LCF):** The most frequently observed failure mechanism is the Low Cycle Fatigue rupture. A common thrust chamber goes through cycles including start-up and shutdown transients that stress the structure by mainly loading the hot-side wall. A good material for LRE application needs an excellent high/low temperature Low Cycle Fatigue behavior. NOTE:In the past, regeneratively cooled rocket engine thrust chambers have been required to sustain one, or in some instances only several, hot operating cycles. However,

the current requirements of reusability for standard cycle applications such as the Space Shuttle or the Space Tug engines have introduced the problem of low cycle thermal fatigue [26];

- **Yield Strength:** The entire thrust chamber is not only exposed to cycling stress. The static pressure is terribly high, therefore a material with a remarkable strength is required to react loads from internal pressures, transient side loads, and thrust chamber assembly thrust loads;
- **Elongation:** Because the cycling behavior of the engine is not elastic, but primarily plastic, ductility is very important. Both locally (hotwall, channels, backside walls) and globally: a common to high fragile material has not compatible Low Cycle fatigue endurance;
- **Hydrogen Embrittlement:** The high-pressure hydrogen environment is a ordinary coolant cryogenic fluid in nozzle. A Hydrogen embrittlement material is necessary;

2.3.1 Common Materials for Liquid Rocket Engine (LRE)

The historical advent of the Space Shuttle has brought a new era in the design and fabrication of rocket nozzles. The requirement of re-usability and high-performance coupled with weight and volume limitations have led to the development of several new candidate materials. For example, the SSME nozzle had the requirement that it be capable of operating for 300 major thermal cycles for a total duration of 10 hours.

Due to the restricted material requirements for LRE application, two main historical alloys have been employed in order to make rocket engines:

- * Copper Alloys: Excellent thermal conductivity, excellent elongation, good LCF life, low high temperature resistance, low resistance to oxidation, very-low yield strength;
- * Nickel-base Alloys: Excellent yield strength, excellent high temperature resistance, good LCF life, good resistance to oxidation, low elongation, very-low thermal conductivity;

In order to support the aforementioned data, Figure 2.16 shows recent AM combustion chambers hot-fire testing activities by NASA MSFC. Is it possible to see that the AM SLM is the main process and that Copper and Nickel Alloys are the only material used for thrust chambers fabrication.

Chamber Component Description	Propellants	Additive Process	Material	Starts	Hot-fire Time (sec)
1,000 lbf SLM Chamber Demonstrator, PD061	LOX/GH2	SLM	Inco 625	3	17
4,000 lbf LOX-Methane Regen Thruster, PF037-1	LOX/LCH4	SLM	Inco 718	5	16
4,000 lbf LOX-Methane Regen Thruster, PF037-2	LOX/LCH4	SLM	GRCop-84	3	11
1.2K lbf Slip Jacket Liner Cyclic SLM Chamber, PG034	LOX/GH2	SLM	GRCop-84	25	2365
Methane Engine Thrust Assembly 4K (META4), PG055	LOX/LCH4	SLM	GRCop-84	4	26
Methane Engine Thruster for 1K lbf (MET1), PH127	LOX/LCH4	SLM	GRCop-84	5	30
1.2K Slip Liner for Channel Wall Nozzle, PH034	LOX/GH2	SLM	GRCop-84	19	1805
C-18150 Slip Jacket 1.2K Liner, PH171	LOX/GH2	SLM	C-18150	10	1443
Low Cost Upper Stage Propulsion 35K, PF086	LOX/GH2	SLM/DED	GRCop-84 / Inco 625	12	147
META4 4K lbf #2, PH135	LOX/LCH4	SLM	GRCop-84	17	141
META4x4, PI051 [Ref 34]	LOX/LCH4	SLM	GRCop-84	9	116
TOTAL				112	6117

Fig. 2.13 Summary of Additive Combustion Chamber Hot-fire Testing by NASA MSFC (Marshall Space Flight Center) from 2013 to 2018, from [7]

Various L-PBF thrust chambers across the propulsion industry have been demonstrated in a variety of materials. A generally observed trend is that most companies rely on either a Nickel-superalloy or a highly conductive copper-alloy chamber design. Nickel-superalloy were common prior to 2015 before the copper alloys were fully developed and characterized using L-PBF.

Examples of Traditional Processed Copper-based alloy for LRE thrust chambers

- **OFHC Copper:** It is a oxygen free grade of essentially pure copper. The material has very high electrical and thermal conductivity combined with a high melting point. The material is readily hot or cold worked and the strength of the material increases with the amount of working. In the annealed condition the material has a relatively low strength. Also at cryogenic temperatures the material exhibits high ductility [23];
- **Electroformed Copper:** Electroformed copper is essentially pure copper obtained from an electro-chemical process. The technique involves the deposition of copper ions from a sulfate electrolyte onto a mandrel. The copper deposits may be bonded to or sandwiched between other deposits to provide integral heat sinks. The material can be joined to other materials using the same methods that would be employed for wrought copper. The electroformed copper has very high electrical and thermal conductivity, relatively low strengths, and is non-magnetic [23];
- **Amzirc:** It is a copper base alloy containing a nominal 0.15 percent zirconium. This zirconiumcopper alloy combines high electrical and thermal conductivity with good strength retention at high temperatures. The alloy is readily cold worked in the solution-annealed condition. The strength of the material increases with the amount of cold working without sacrificing ductility or conductivity [23];
- **NARloy Z:** It is a copper base alloy containing a nominal 3-percent silver and 0.5 percent zirconium. The silver-zirconium-copper alloy combines high electrical

and thermal conductivity with moderate strength retention at high temperatures. The alloy is strengthened by heat treatment and is normally used in the solution annealed and aged condition [23];

- Cu-Cr-Nb Alloys: This alloys possessed exceptional high temperature strength and creep resistance while maintaining good electrical and thermal conductivity. Common Cu-Cr-Nb NASA's Alloys were GRCo-84, GRCo-84 Zr and GRCo-42;

Examples of Traditional Processed Nickel-based alloy for LRE thrust chambers

- Electroformed Nickel: It is obtained from an electro-chemical process involving the deposition of nickel ions from an electrolyte onto a mandrel. A sulfamate bath is used to obtain nickel deposits with low internal stresses. The nickel deposits can be bonded to or sandwiched between other material deposits to provide integral heat sinks in an almost unlimited range of regular and irregular configurations. Mechanical properties of electroformed nickel can be varied over a wide range by the methods of deposition and by the composition of the plating bath. The metallurgical structure is characterized by high-purity, needle-like crystals aligned perpendicular to the mandrel.
- NASA HR-1: It is a high-strength Fe-Ni superalloy designed to resist high pressure, hydrogen environment embrittlement, oxidation, and corrosion. NASA HR-1 was originally developed at NASA in the 1990's and derived to increase strength and ductility in high-pressure environments. The NASA HR-1 chemistry was formulated to meet requirements for liquid rocket engine applications, specifically components used in a hydrogen environment [45];

Examples of Additive Manufacturing Copper-based alloy for LRE thrust chambers

- Cu-Cr-Nb Alloys: The focus of these alloys developments is for high heat flux applications such as combustion chambers with complex internal coolant passages that would otherwise require difficult and expensive manufacturing operations, if they were even possible to produce. NASA has observed the growing need for AM, specifically SLM, fabrication of copper-alloys for liquid rocket engine components. Because of excellent performance of Cu-Cr-Nb NASA's Alloys, such as GRCo-84 and GRCo-42, the same materials is used for the AM processes. GRCo-84 (Cu-8 at.% Cr-4 at.% Nb) is the most common alloy having completed substantial process and property development using SLM under the Low Cost Upper Stage Propulsion (LCUSP) program started in 2014. In particular GRCo is a preferred material for use in combustion chambers due to [24]:

- * Oxidation and blanching resistance with thermal and oxidation-reduction cycling;

- * High use temperatures to above approximately 760 °C, depending upon strength and creep requirements, for sustained duration;
- * Material strength at high use temperatures;
- * Established powder supply chain;
- * Mature AM process that meets property minimums

Examples of Additive Manufacturing Nickel-based alloy for LRE thrust chambers

- Inconel 718: This Nickel-based alloys are popular for their high temperature corrosion resistance, excellent mechanical strength at elevated temperature and excellent weldable nickel superalloy, when compared to the nickel-base super alloys hardened by aluminum and titanium. It is able to improve its strength and creep-rupture properties mainly by precipitation hardening phases and solid-solution hardening effect of the refractory metal elements as niobium (Nb) and molybdenum (Mo) in a nickel-chromium based matrix;
- HR-1: Recent developments using additive manufacturing (AM) have made this material an attractive option for channel-cooled nozzles under the Rapid Analysis and Manufacturing Propulsion Technology (RAMPT) NASA's program and other liquid rocket engine component applications [45];

2.3.2 The role of Inconel alloys in AM LRE thrust chambers

L-PBF additive manufacture of aerospace components has been demonstrated using several nickel alloys, most commonly with Inconel 625 and 718. Nickel alloys are often selected because of their capability of withstanding extreme temperatures while maintaining good mechanical strength. Further strengths of these materials are the ability to resist to creep and corrosive environments. The processing of nickel alloys using L-PBF is now a consolidated technology that allows obtaining components of more than acceptable quality in terms of dimensional and mechanical characteristics.

However, only few examples of aerospace components realized in such a way are operative in flight while many examples under research and development are under study for possible use in the future. This apparent slowness of penetration of additive manufacturing in the aerospace sector is mainly due to the intrinsic long time required to introduce new technologies in this sector, where caution is exercised in replacing critical components and new systems or missions become operational only after long phases of design, development, and qualification. Among the few examples of operational fling components realized in nickel alloy with SLM, it is worth mentioning the following examples:

- The SpaceX's SuperDraco (Figure 2.14) rocket engine entered service in 2013 [31]. The SuperDraco engines are used for the mission-critical launch escape system designed to carry astronauts to safety if an emergency occurs during the launch

sequence of the Dragon spacecraft. Featuring an AM built engine chamber made of Inconel 718 that includes integral cooling channels, the SuperDraco is one of the earliest applications of crucial AM built components aboard human-occupied spacecraft [8];

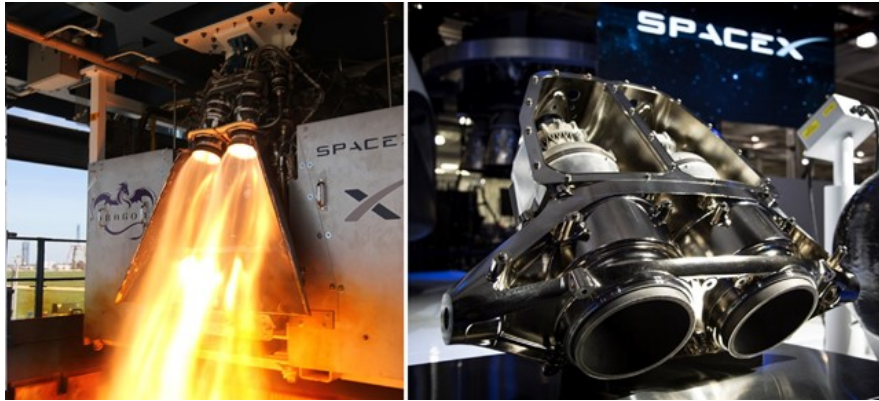


Fig. 2.14 Right: SpaceX AM built Superdraco rocket engine. Left: SuperDraco Test Fire by SpaceX, from [8]

- SpaceX have successfully developed and launched a main oxidizer valve used in the Falcon 9 rocket engines [42].
- The Orion Crew Module RCS engine nozzles (Figure 2.15) utilize nozzle extensions made of Inconel 625, which are welded onto wrought nozzles. AM design incorporated features that can't be conventionally produced [9];



Fig. 2.15 Orion Crew Module RCS engine nozzles, from [9]

- The NASA rover Perseverance, which is currently operative on Mars, carries 11 components fabricated using metal AM techniques. Of these 11 components, 6 are AM built heat exchangers used in the Mars Oxygen In-Situ Resource Utilization Experiment, or MOXIE. These heat exchangers are exposed to the Martian atmosphere and must withstand temperatures of over 800 °C for extended

periods of time. This resulted in nickel-based superalloys being used for the heat exchanger structures which simplified and improved the capabilities of the MOXIE system compared to if they were built using conventional techniques [9].

Concerning the many research and development activities that are based on the consolidation of the L-PBF technology for aerospace components in nickel alloys, here we focus on those related to rocket engines. Indeed, the scientific and technical literature shows that the most promising efforts are focusing on this application. This is the result of the great opportunities that additive manufacturing can offer to the improvement and production of rocket engines, whose high development costs and time justify the introduction of new disruptive technologies. The most notable activities and projects made by space agencies and large private companies are presented below:

- One of the first rocket engine component realized in AM and successfully hot-fire tested is a gas generator discharge duct of the engine J-2X. Such component was manufactured in Inconel 625 by NASA Marshall Space Flight Center (MSFC) [46]. Because of the inherent complexity of the conventional manufacturing in realizing a component that is characterized by a relatively high ratio of the wall thickness to bending radius of the duct, AM resulted a very promising alternative. In fact, the conventional component required the welding 3 separate 60-degree duct sections;
- NASA demonstrated multiple applications of AM to rocket engine injectors made of nickel alloys (Inconel 625, 718, and Monel K-500) since 2013 that significantly reduce part count and lead time. One such example demonstrates a reduction from 162 parts to 2 parts (Figure ??) and tested at full operational conditions with high performance equivalent to traditional manufacturing [10]. NASA completed several injector hot-fire test programs and accumulated thousands of seconds of time, including a sub-scale injector with over 7,200 seconds [7];

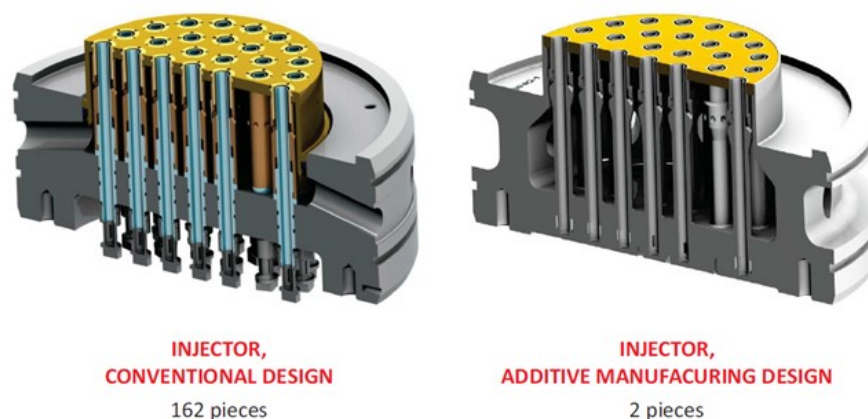


Fig. 2.16 AM power to reduction a component from 162 parts to 2 parts, from [10]

- NASA realized and hot-fire tested a thrust chamber made of Inconel alloy in 2015 [7]. Such demonstrator component had fully integrated cooling channels eliminating the need of a separate inner layer with outer close-out. However, because the

operative conditions that NASA foresees for such component require larger heat transfer capability, Inconel has not been considered for the subsequent realized thrust chambers. Copper alloys, having a much larger thermal conductivity than nickel, is now considered by NASA for the thrust chamber realized in AM [7];

- NASA and Aerojet Rocketdyne partnered to perform hot-fire testing of a sub-scale rocket engine thrust chamber with features of the full-scale rocket engine RL10 [47]. The injector was made of AM nickel alloy and the thrust chamber out of AM copper alloy. Nineteen tests were performed in total with four different engine configurations;
- NASA realized and tested nozzle extensions made of Inconel 625 with L-PBF technology [7]. One of such nozzles has a complex design characterized by integrated cooling channels and a film cooling ring. However, because of the typical large dimension of the nozzle extensions, NASA is developing new additive manufacturing techniques to help solve the scale issues. In particular, a technology based on Direct-Energy-Deposition is selected because it provides sufficiently large build volume;
- AVIO selected L-PBF additive manufacturing of Inconel 718 for the injector and thrust chamber of the engine M10 that will thrust the upper stage of the launcher Vega-E that is under development for the European Space Agency. A sub-scale and a full-scale engine have been tested successfully [44, 48];
- The injector of the gas generator of the engine Vulcain 2 for the first stage of the European launcher Ariane 6 is a fully integrated piece made of Inconel 718, including feeding pipes, manifolds, cavities, and injection elements. The single piece AM injector replaces 150 individually machined components assembled with multiple conventional manufacturing and joining processes and associated inspections [49]. Associated to the injector, the gas generator chamber is also realized in Inconel 718 with SLM. Such assembled gas generator (injector and chamber) was successfully hot fire tested;
- The injector of the engine Vinci for the second stage of the European launcher Ariane 6 is manufactured in Inconel 718 as a single component instead of 248 traditional single components, all while reducing the mass of the injector head [33];

One of the merits of additive manufacturing is the easy access of this technology by realities such as start-up companies or universities that typically do not have the manufacturing capability required by traditional methods due to financial limits or institutional purposes, respectively. Focusing on the L-PBF technology of nickel alloy components for aerospace applications, a number promising projects is carried-out by such entities. Some examples are described below:

- Two different start-up companies, Cellcore and Hyperganic, have demonstrated the ability to produce a complex thrust chamber assembly in Inconel 718. Both

implemented non-conventional cooling system: Cellcore opted for integrated lattice internal cooling channels, while Hyperganic (Figure 2.17) opted for multi-layer cooling channels [8];



Fig. 2.17 Hyperganic prototype rocket nozzle featuring internal cooling channels and an external lattice, from [8]

- The Airborne Engineering company has used a nickel alloy that has been specifically developed for LPBF manufacturing. Such alloy is particularly suited for rocket engine thrust chambers because it maintains strength up to 900 °C, demonstrating an increase in temperature capability over Inconel 718 of about 100°C [44]. A small thrust chamber demonstrator made of such alloy and characterized by helical cooling channels and integrated coolant inlet and outlet manifolds has been hot-fire tested successfully;

2.3.3 From Inconel to Copper: modern AM LRE thrust chambers

A copper alloy, mainly because of the super high conductivity, is the best material for facing the thermal high stressing condition of a LRE regenerative thrust chamber. The main problem of such materials is the low Young module and the very low Yell strength. In addition to this intrinsic material behaviour, in order to process copper by Additive Manufacturing, the laser beam mirrors suffer of optical damage (Figure 2.18) due to the high reflectivity on laser in molten state and liquid state [11].

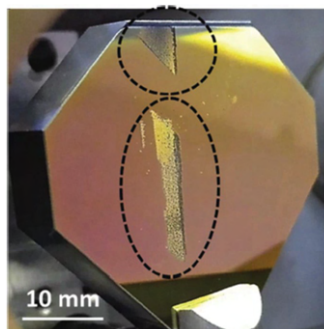


Fig. 2.18 The damage of a common SM SLM optical mirror, from [11]

In general, in order to achieve a mature knowledge of best process parameters for a new AM interesting material for a specific industrial sector, a high number of DoE ⁴

⁴Design of Experiment

test activities have to be performed. This long and high-cost necessary procedure lead the Additive LRE thrust chamber manufacturing to use Inconel alloys, mainly because AM Inconel alloys have been developed much more then copper alloy because of their more interesting versatility (e.g. aerospace applications: impellers, turbines, turbojet engines, oil and gas valves, ecc). Therefore a higher number of recherc project had allowed a very high level awareness respect to the process parameter: Inconel alloys were already mature when the space rocket industry decided to use AM for build LRE thrust chambers;

However, thanks to daily reduction of AM R&D activities, now day copper alloy are beginning to be more considered and the scientific community are focusing much more recherc programs on this subject, respect to the past. A good example is the NASA Low Cost Upper Stage Propulsion (LCUSP) project: GRCop-84 has been an ideal material suited for the SLM processing. This NASA-led project has matured the process significantly and also made process parameters and characterization data available to industry to enable commercial supply chains. Through a variety of complementary projects to the LCUSP program, NASA has designed, developed and tested combustion chambers using the SLM process.

The goal of the present study is to follow this modern research path and envelop a new high performing copper-based alloy processed by AM SLM technologies for LRE thrust chambers instead of using a heavy and low conductivity materials, such as Inconel alloy.

Chapter 3

Introduction: Liquid Rocket Engine (LRE)

A thrust chamber has a key role inside a Liquid Rocket Engine system. This complex component is reasonable for the injection, atomization, mixing, and burning the liquid propellants in order to generate hot gaseous reaction products and thus thrust. Inside the typical De Laval convergent-divergent geometry all combustion products are accelerated to achieve supersonic velocities.

3.1 Cooling Techniques for Rocket Engines

The high temperature produced by the heat coming from the engine hot exhaust gases make metal materials impossible to use without a proper cooling system design. Several different cooling systems have been developed and successfully tested. The severe temperature conditions (2500 K to 3600 K [50]) and the high heat transfer rates from the hot-gas to the chamber wall (1 MW/m² to over 160 MW/m² [50]) of the under study component lead to a properer cooling system design. The primary objective of a cooling system is to prevent the chamber and nozzle walls from reaching such temperature that they will no longer be able to withstand the imposed loads or stresses, thus causing the chamber or nozzle to fail. Therefore the cooling thus reduces the wall temperatures to an acceptable value, which depends on the material used [51].

In order to chose the correct cooling system for a rocket engine, more than a single criteria have to be evaluated: there are many considerations that have to be under investigation. As for every new pioneering component design there are no particular rules. However, a shortlist of main factors that influence the selected design approaches can be identified as [50]: propellants, chamber pressure, propellant feed system, thrust-chamber construction material.

A shortlist of must employed cooling systems is presented [52]:

- **Heat sink cooling:** The most straightforward technique to limit the internal surface temperature is to create a thick enough chamber or nozzle wall with enough heat

capacity to absorb the heat transferred during the firing time. The thrust chamber never reaches thermal equilibrium, and temperatures continue to rise as time goes on. The maximum duration of the hardware is determined by its heat absorption capacity. The rocket's combustion must be halted just when any of the exposed walls reaches a critical temperature that could cause it to fail. The materials with the highest specific heat, thermal conductivity and density values are the best for this sort of cooling. In any instance, as the needed running period for an uncooled motor increases, the required motor weight increases to the point that it is no longer practicable to use. As a result, even though the heat-sink method has the advantages of simplicity and low cost of manufacture, it results in a weight penalty for duration higher than 10 to 20 seconds [53]. It's typically used with low chamber pressures and poor heat transfer rates.

- **Regenerative cooling and dump cooling:** The most extensively used approach is regenerative cooling, which involves injecting cryogenic propellants into the combustion chamber through openings in the thrust chamber wall. This cooling mechanism enables combustion chambers and nozzles to be made of light, thin metal. The "dump cooling" approach is a variation of this method in which a small amount of the propellant, like as hydrogen in a LO₂/LH₂ engine, is delivered via tunnels in the thrust chamber wall for cooling before being thrown overboard through apertures in the nozzle skirt. This approach has only limited utility due to inherent issues such as performance losses [50];
- **Film cooling and transpiration cooling:** Film cooling is an effective strategy for ensuring long-term safe operation of liquid rocket engines with increased heat flux densities. Film cooling and transpiration cooling are supplemental cooling techniques that are occasionally employed in conjunction with regenerative cooling to improve its cooling capacity locally. A thin film of coolant or propellant supplied through orifices around the injector perimeter or through manifolded orifices in the chamber wall near the injector (and sometimes in several more planes toward the throat) protects the wall surfaces from excessive heat in the film cooling method [54]. Transpiration cooling is essentially a sort of film cooling in which a coolant (either gaseous or liquid propellant) is delivered through porous chamber walls at a pace adequate to keep the combustion-gas-side chamber wall at the required temperature;
- **Ablative cooling:** To dissipate heat, the combustion-gas-side wall material is sacrificed through melting, vaporization, and chemical reactions. As a result, comparatively cool gases flow across the wall surface, lowering the temperature of the boundary layer and contributing in the cooling process. Furthermore, the ablative substance is usually a good thermal insulator, reducing heat transfer to the exterior structure to a minimum. Ablative cooling has been effectively used in a variety of designs, primarily for solid-propellant systems, but also for short-duration and/or low-pressure liquid systems[50];
- **Radiation cooling:** Heat is radiated away from the surface of the outer thrust chamber wall using this mechanism. It has been effectively applied to very small,

high-temperature material combustion chambers as well as low-heat-flux portions like nozzle extensions (i.e. diverging nozzle exhaust sections beyond an area ratio of around 6 to 10) [50]);

All the presented advanced cooling systems can be employed separately or together (Figure 3.1).

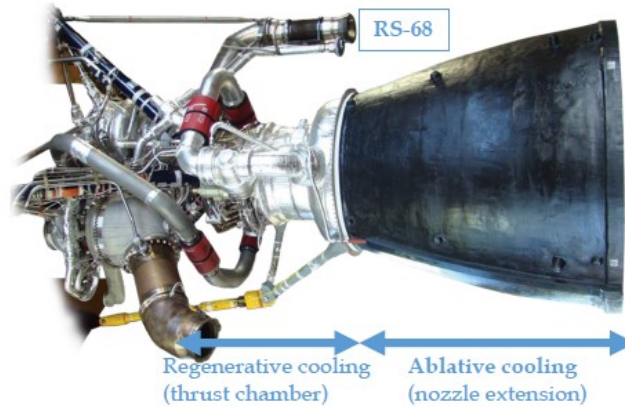


Fig. 3.1 RS-68 rocket engine: two different cooling system

3.2 LRE Regenerative Cooling

The term "regenerative cooling" refers to the fact that the heat collected by the coolant propellant is not squandered, but rather adds to the propellant's starting temperature and energy level prior to injection. Regenerative cooling is the most prevalent cooling mechanism in large liquid rocket engines. One or both of the propellants used in the rocket engine are pushed via a jacket around the combustion chamber and/or nozzle. The heated coolant can then be utilized to power the turbine or fed straight into the combustion chamber, resulting in a more efficient combustion due to the propellant's increased initial energy content prior to injection (Figure 3.2 and Figure 3.3).

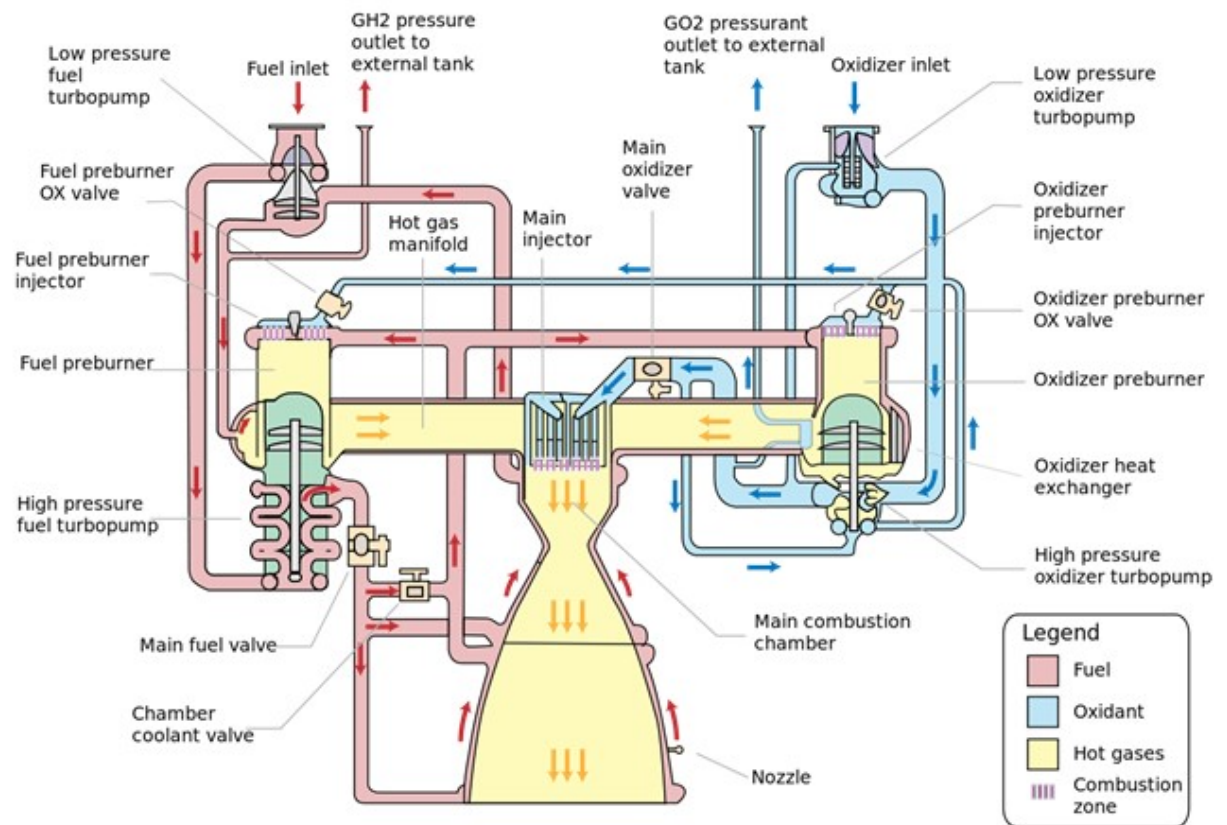


Fig. 3.2 Schematic representation of the SSME (Space Shuttle Main Engine) global system

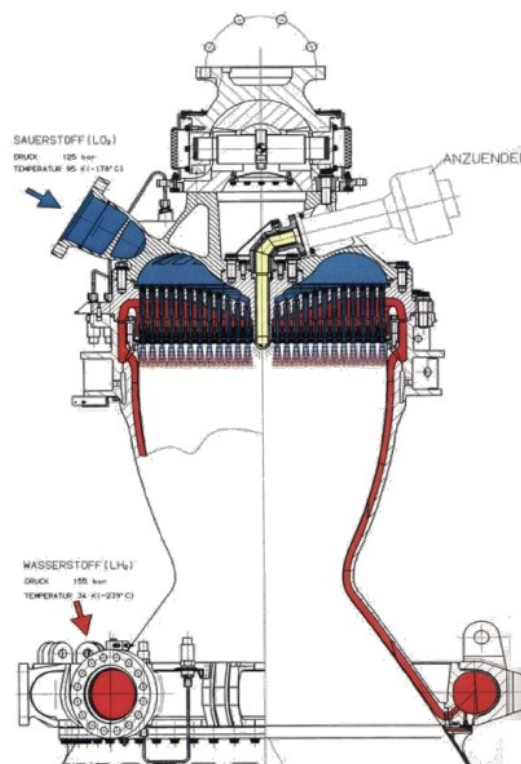


Fig. 3.3 Schematic representation of the VULCAN Engine global system, from [12]

The feed pressure of the fuel must be equal to the sum of the chamber pressure, the injector pressure drop, the cooling channel pressure drop, and any other pressure losses inherent in the system, which is a drawback of regenerative cooling. In large liquid propellant rocket engines, typically turbopump-fed engines, a surprisingly substantial pressure drop is frequently available for chamber cooling.

A material with excellent thermal conductivity and a thin wall design will reduce thermal strains in regeneratively cooled thrust chambers with high performance and high heat transfer. Extended surfaces, known as fins or ribs (Figure 3.4), can be used to reduce the wall temperature on the hot side of the cooling channels in a regeneratively cooled combustion chamber by increasing the coolant side surface area compared to the hot-gas side surface.

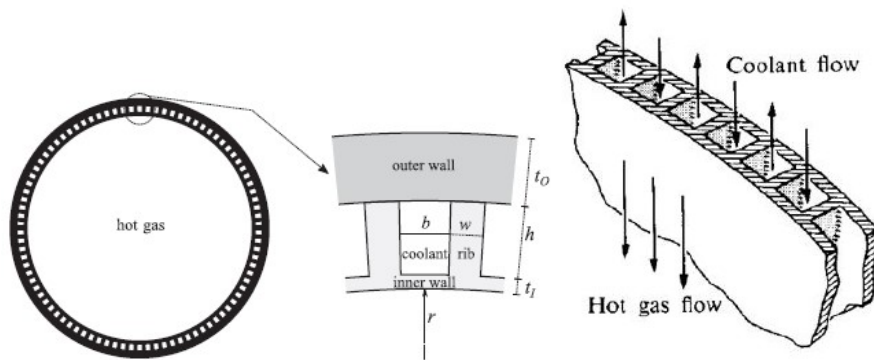
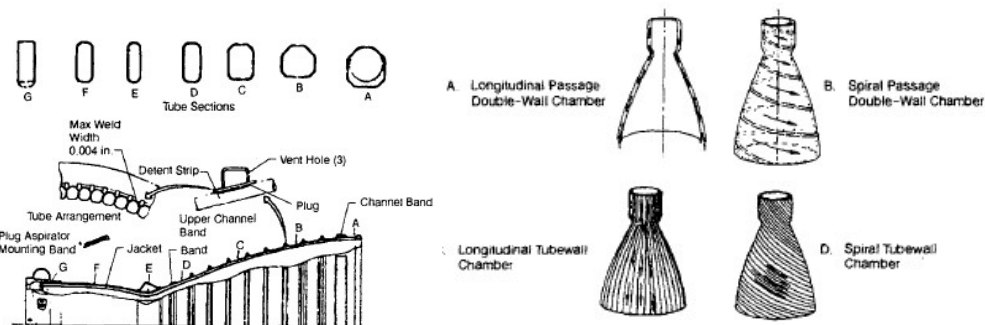


Fig. 3.4 Schematic of a regenerative thrust chamber cross section nomenclature, from [13]

Cooling channels can have different arrangement along the combustion convergent-divergent chamber (Figure 3.5a). In addition to this, cooling channels shape, usually, is not constant respect to the axisymmetric axis and could change both geometry or dimension (Figure 3.5b). An increase in the number of passages, and therefore the surface area of the passages that circumferentially line the outer wall of a combustion chamber, necessarily increases their aspect ratio [52]. High aspect ratio cooling channels (HARCC) have demonstrated a high potential for influencing both the temperature field and pressure loss in a beneficial way [55]. This intriguing and practical geometry is not found in round tubes [56].



(a) LRE cooling channel typical arrangement-(b) LRE cooling channel possible shape variation, ment, from [50] from [50]

3.2.1 Additive Manufacturing unconventional and innovative geometries for Liquid Rocket Engine (LRE) cooling channels

Additive Manufacturing allows designer to achieve complex and unconventional geometries. A modern trend way to perform a new component via AM is to use generative and bio-inspired generative design ([57]) in stead of optimization algorithms: these are typically used for weight optimizations conventional components. Generative design algorithm, in stead, are able to build links and structures by assuming only base constraints bodies of the target structure[58]. With this new design mindset future LRE cooling channels could better perform in terms of heat transfer and structural resistance.

AM has created a world of opportunity to redesign heat exchangers in pioneering forms, shapes, and sizes [59]. From this scientific recherche area regenerative cooled LRE can take advantage of different studies: the cooling channels can be considered ad a cryogenic liquid complex heat exchanger. Indeed there are already interesting tested LRE cooling channels characterized by particular lattice or foam structure inside the channels [14, 60]. However this innovative design has a remarkable disadvantage: the pressure drop rise up (Figure 3.6) and this could be an important problem for LRE applications [14].

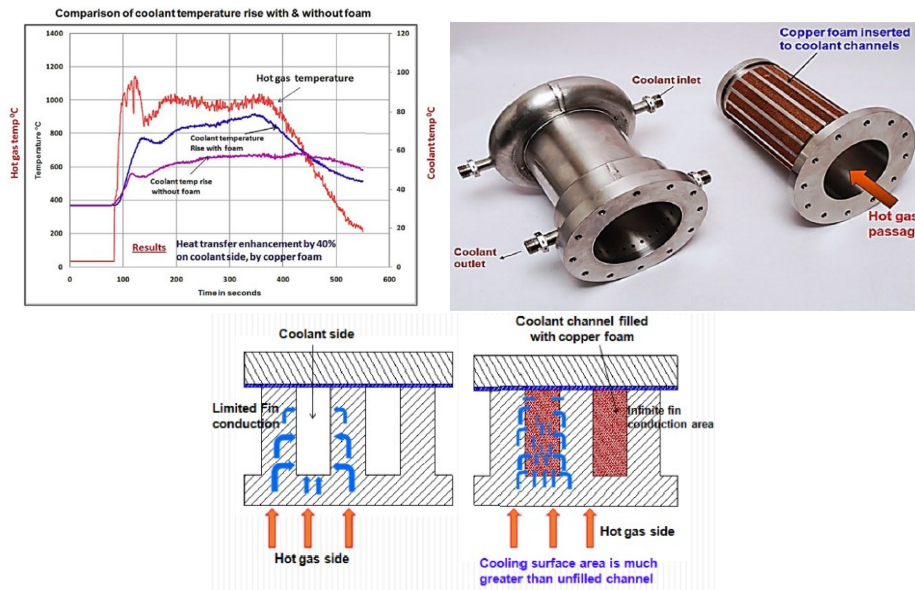


Fig. 3.6 LRE cooling channels filled with copper metal foam, from [14]

In conclusion, in order to proof that AM lattice structure inside LRE cooling channels are under study, Figure 3.7 show the particular structure arrangement proposed by AVIO s.r.p.. The patented geometry has *"the inner and outer walls being spaced apart from each other in radial direction and delimiting at least one guiding conduit of a cooling fluid therebetween; a plurality of bar-shaped elements extending into the guiding conduit, which form a grid for perturbing the cooling fluid, stiffening the casing and increasing the heat exchange Surface; the grid being part of a body made in one piece and of a single material along with the inner and outer walls"* (quotation from [61]).

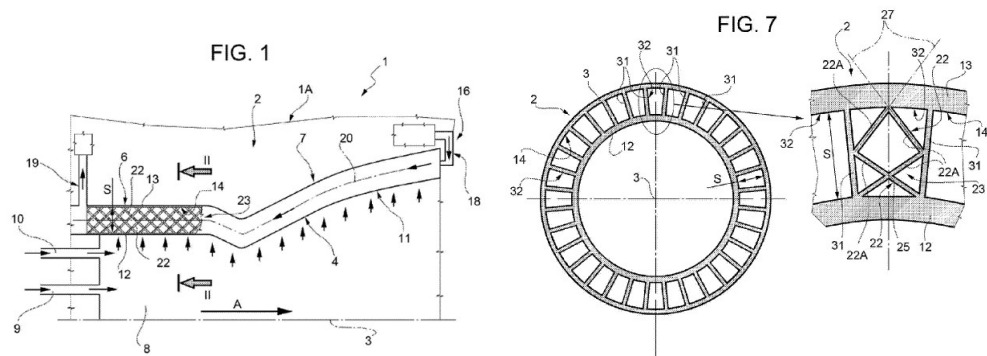


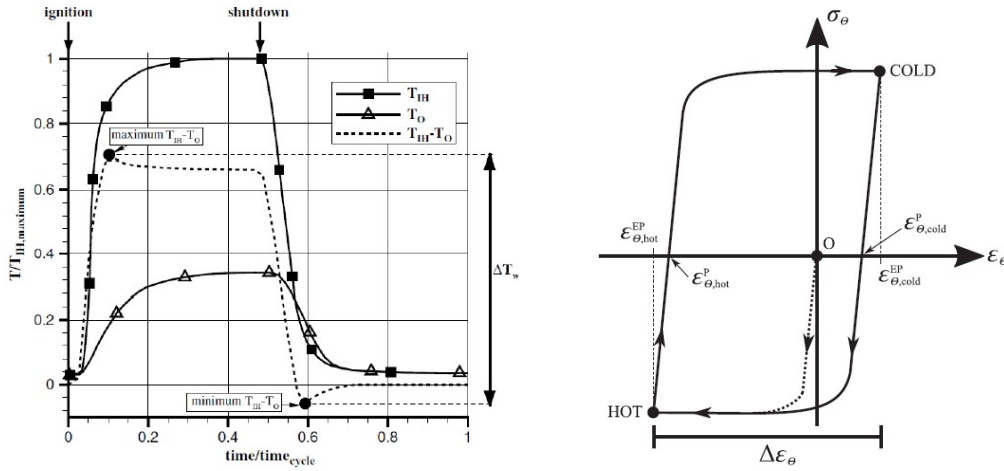
Fig. 3.7 AVIO s.p.a. United States Patent Application Publication No.: US 2017/0122258 A1

3.3 LRE Regenerative Cooling Fracture Mechanism

The modern demand for high performance and re-usability rocket engines has created major design problems. One of the critical aspects of the nozzle design is the fatigue life analysis. This has become a major design problem since a portion of the nozzle, particularly the throat section, is subjected to cyclic plastic strain due to the high temperature differential between the hot inner wall and the relatively cool outer shell during the engine start-stop transients as well as during steady state operation. This has a major impact on nozzle life and creates the need to accurately predict when an engine may fail.

As already explained, to contain chamber pressure and transmit thrust load, the liner is normally closed out with a nickel jacket. To disperse heat more efficiently, a higher-conductive material is utilized for the inner wall sacrificing strength and resistance. This common material difference between inner and close out wall is reflected to different thermal expansion properties. In addition, the different thickness of the inner wall respect to the close out wall leads to very different thermo-structural behaviour: the inner wall, more conductive, with low thickness and with a high thermal dilatation, can rapidly achieve a major volume respect to the close out which has a higher resistance but a low thermal conduction and therefore a lower thermal dilatation.

The outer wall constrains the inner wall through the ribs. In particular when the inner wall is hotter than the outer wall during engine start-up and continuous firing, compressive plastic strains of the order of a few (up to 3%) percent are induced in the inner wall as the hot inner wall wants to expand but is restricted by the cold outer wall. On the other side, when the engine is turned off, the inner wall cools faster than the outer wall, causing tensile plastic strains in the inner wall (Figure 3.8). The largest and minimum temperature discrepancies occurs during the start-up and shut-down transient phases. In fact, because the inner wall is thinner than the outer wall, which is also farther away from the hot gas and often constructed of a less thermally conductive material, the inner wall is more thermally conductive and therefore it is able to cool down quicker the the outer wall.



(a) Typical behavior of the hot-gas-side and backside (b) Typical cyclic stress–strain behavior of the wall temperatures and their difference for a regenera-hot-gas-side wall for a regeneratively cooled thrust chamber, from [13] thrust chamber, from [13]

Fig. 3.8 Regenerative thrust chamber strain behavior

When the engine is fired repeatedly, the plastic deformations in the inner wall accumulate cyclically, and the thrust chamber's life is determined by low cycle fatigue behavior. The consequent strain range $\Delta\epsilon_{tot}$ accumulated in a duty cycle has a significant impact on thrust chamber life, since the larger the strain range, the shorter the cyclic life. If the strain range is roughly estimated as $\Delta\epsilon = 2\alpha\Delta T_{total\ wall\ range}$ it is possible to state that the high is the difference between inlet and close out wall temperature, the lower is the engine life [5].

The main combustion chamber (MCC) of the SSME is a typical state-of-the-art regeneratively cooled thrust chamber. The hot-gas-side wall is nominally at 867 K during steady-state operation in the most thermally solicited portion near the engine throat, and the resultant heat flux is 160 MWm², whereas the outside wall is at 172 K. The total structure reaches roughly 33 K before and after the engine starts and stops. Furthermore, the internal pressure of the coolant hydrogen in the throat region during engine firing is 434 bar, which is roughly 300 bar higher than the hotgas pressure of 145 bar [15]. This is a clear example of the harsh thermomechanical environment in which a high-performance liquid rocket engine's thrust chamber operates.

3.3.1 Thermally induced deformations of regenerative thrust chambers

The main fracture mechanism is due to thermal induced deformation of the cooling channels. Therefore the main problems is not the prefer difference between hot-gases and cooling system, but the temperature difference of cooling channels.

The estimated strain range value, assuming a nominal and fixed chamber geometry, is used in conjunction with results from uniaxial, isothermal fatigue tests done in a laboratory to determine chamber life. Typically, this method fails because the chamber

material degrades sooner than intended. The SSME-MCC is a good illustration of how the engine's actual life has reduced its reusability and, as a result, its ongoing cost. In fact, the need was reduced to 50 missions [5] from an earlier aim of 100 missions with an overall run duration of around 8 hours [18] due to inappropriate life design and prediction criteria (Figure 3.9). After experiencing a different life behavior than planned, the main injector's design was updated to include film cooling to protect the chamber wall from overheating [15]. In practice, none of the 46 SSMEs constructed has flown more than 20 times (on average nine times), and the SSME-MCC liners have been polished to minimize hot-gas-side roughened areas as a result of the effect of degradation of the inner wall finishing [62].

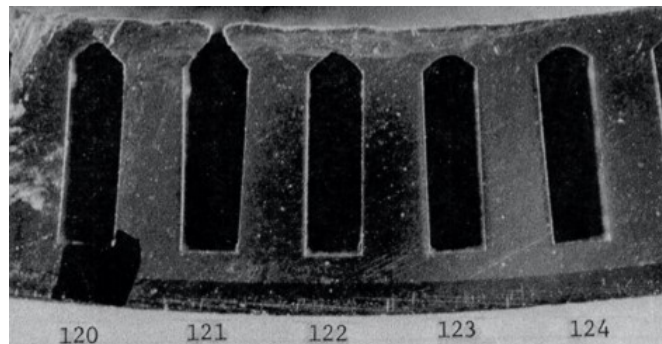


Fig. 3.9 Throat section of SSME - MCC showing channel rupture, from [15]

In general, experimental data reveal that as the cycles accumulate, the inner wall thins and bulges incrementally throughout the heating and cooling cycles associated with each firing, eventually failing [5]. As a result, channel wall thinning is the most important element in determining how long regeneratively cooled thrust chambers may be reused. The analysis and comprehension of such phenomena is further complicated by the fact that a detailed analysis of the failure site reveals that roughening of the hot-gas side wall may occur [5], that the hot-gas wall surface may be subjected to oxidation¹ (i.e., the blanching effect² [64]), and that a rupture may occur via low-cycle fatigue (crack rupture) or plastic instability (tensile ductile rupture), depending primarily on the time-dependent³ behavior of the material.

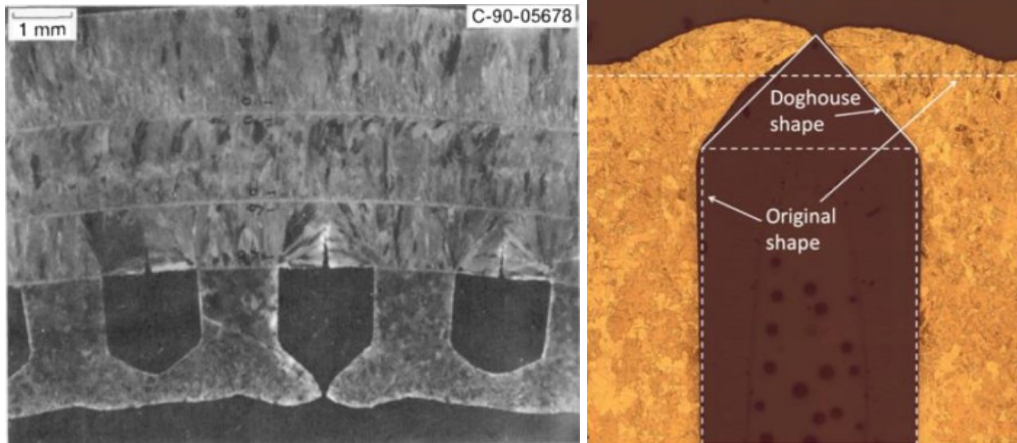
Figure 3.10a shows a detailed shot of a typical failure site of a cyclically fired thrust chamber tested at NASA in the 1970s [65]. This phenomenon is known as the "doghouse effect" because of the shape of such a deformed building. Another clear example is presented in Figure 3.10b [66]. The thinning and bulging of the inner wall can be seen clearly at these types of failure locations. The considerable, thermally induced plastic strains that develop in the hot-gas-side wall during cyclic firing, as well as the biasing

¹ Japan Aerospace Exploration Agency develop an interesting replica oxidation method that employs a rapid setting silicone rubber molding agent [63]

² Blanching is caused by a cyclic oxidation and reduction of copper. The ensuing surface layer becomes white and flaky. Blanching combined with abrasion increases surface roughness and reduces the thickness of the hot-gas wall. Because of combustion instabilities, strong blanching has been seen. The local species concentration varies dramatically during a combustion instability. As a result, an oxidizing and deoxidizing atmosphere alternates.

³ visoplastic phenomenon, as creep for instance, are relevant only for long faring

coolant-to-hot-gas pressure differential across the wall, are related to the deformation of the inner wall [5]. It is important to remake that, because compressive stress cannot generate the cracks seen in the studies (Figure 3.10a and 3.10b), the chambers normally do not break during engine firing, but rather near the conclusion of the cycle, when the tension becomes tensile.



(a) Typical thrust chamber tested at NASA in the 1970s, (b) Standard 'Dog House' fatigue failure in OFHC copper liner, from [66]

Fig. 3.10 'Dog House' effect Examples

Generally, in case of coolant leakage due to fracture, different prevention method are used:

- **High coolant pressure:** Because coolant is fed into the combustion chamber in regenerative thrust chambers, coolant pressure is higher than hot gas pressure. This also ensures that in the event of a channel rupture, hot gas does not enter the cooling circuit, and coolant leakage shields the chamber wall via a film cooling effect;
- **Coolant counter flow:** Coolant and hot-gas flows are typically counter-flow because of the reduced required tubing (i.e., the coolant outlet manifold is closer to the injector). The co-flow configuration, on the other hand, is safer in the event of a channel rupture because the coolant leakage can protect the area of the chamber wall where there is no cooling channel flow;
- **Fuel as coolant:** Because of the risk of tube wall oxidization or even ignite if an oxidizer is employed as a coolant, fuel is usually used. Furthermore, oxidant leakage into the generally fuel-rich combustion gas can be disastrous;

3.3.2 Low Cycle Fatigue VS Creep-Fatigue Fracture

Very low cycle life of LRE thrust chambers has long been considered the critical points for such engines [5]. However, the unmatched between estimated life by assuming only Low Cycle Fatigue as fracture mechanism and the real tested engines life is leading

researchers to a new, still under study now days, particular fracture mechanism: creep-fatigue.

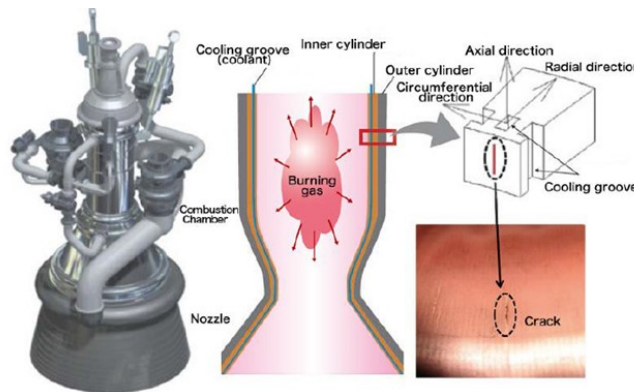


Fig. 3.11 Liquid rocket engine (left), schematic of the combustion chamber (middle) and crack at the combustion chamber wall (right), from [16]

JAXA⁴ has been working on the LE-9 engine for the H3 Rocket (Figure 3.11), which requires excellent reliability and cheap costs. It has a double shell structure with an inner cylinder made of copper (Cu)-chromium (Cr)-zirconium (Zr) alloy and an exterior cylinder built of a heat-resistant nickel alloy. Cooling channels for liquid hydrogen can be found in the inner cylinder (LH2). During start-up and shut-down processes, the groove wall is exposed to 3000°C burning gas and -250°C LH2, resulting in massive temperature swings and considerable thermal strain (Figure 3.12).

⁴Japan Aerospace Exploration Agency

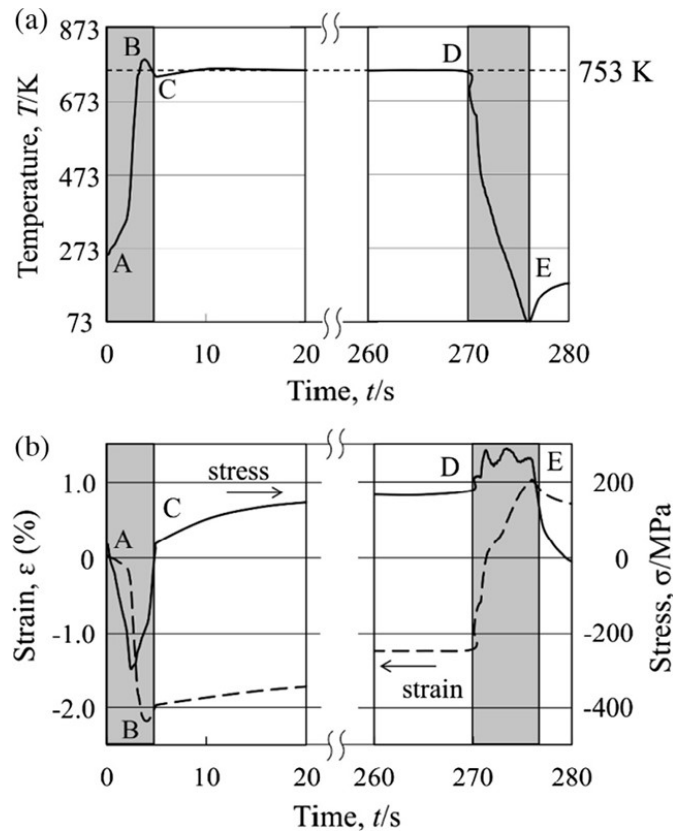


Fig. 3.12 Results of 3D-FEM simulation for one engine-combustion cycle: (a) temperature–time profile and (b) strain/stress–time profiles, from [16]

Around the crack on the combustion chamber wall, the JAXA Engineering Digital Innovation Center performed a three-dimensional finite element study. It was discovered that the temperature of the combustion chamber rapidly rises to over 500°C shortly after start-up, then stabilizes for 270 seconds before rapidly dropping after shut-down. During the start-up and shut-down processes, the chamber wall would be subjected to compressive and tensile deformation reaching the plastic region, as well as extremely low speed tensile deformation (tensile creep deformation) due to the slowly rising temperature of the outer cylinder during stable combustion (Figure 3.12).

According to the results of the 3D-FEM analyses shown, the conditions of the engine thrust chamber were determined with a combined creep-fatigue tests. The engine cycle condition was replaced with creep-fatigue consisting of strain-controlled fatigue and a stress-holding creep in tension under a constant temperature equal to that during the steady-state combustion (753 K). However, in order to have a benchmark, also independent creep and fatigue test have been done. Results shows that creep-fatigue life of the specimen is much lower than the simple fatigue life (Figure 3.13).

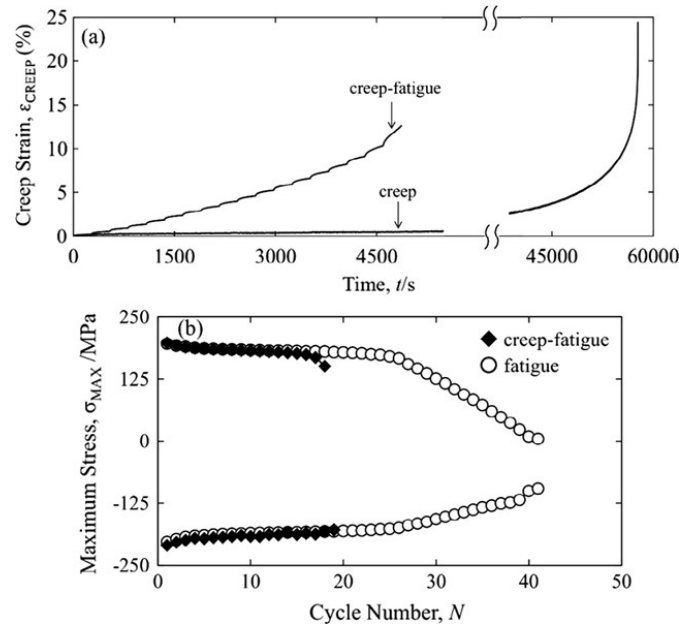


Fig. 3.13 (Fist image) Comparison between the accumulative creep curve of the creep–fatigue test and the creep curve of the simple creep test; (Second image) comparison between the maximum and minimum stresses in each cycle in the creep–fatigue test and the simple fatigue test, from [16]

The study shows that the fracture mechanism is a complex combining of Low Cycle Fatigue cracking, stated from the external surface, and a creep void mechanism far away from the surfaces (Figure 3.14).

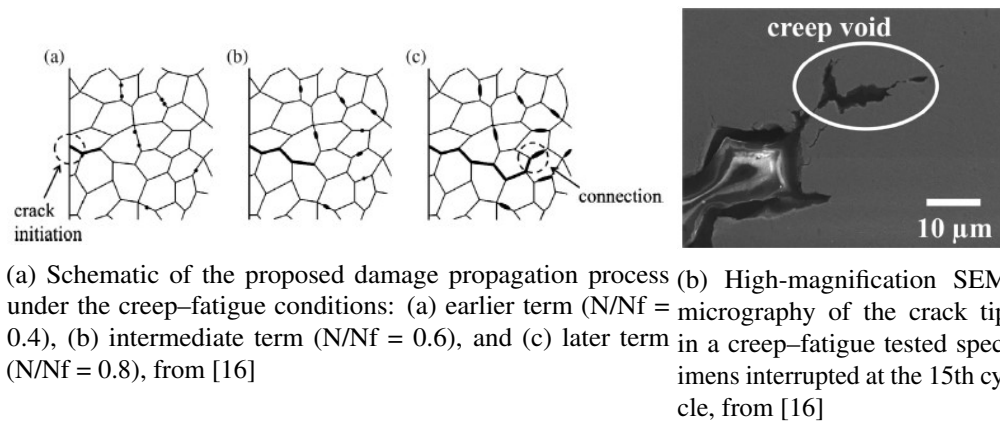


Fig. 3.14 LCF-Creep fracture mechanism, from ([16])

Chapter 4

LRE thrust chambers predictable life methods

4.1 LRE thrust chambers physical test methodologies

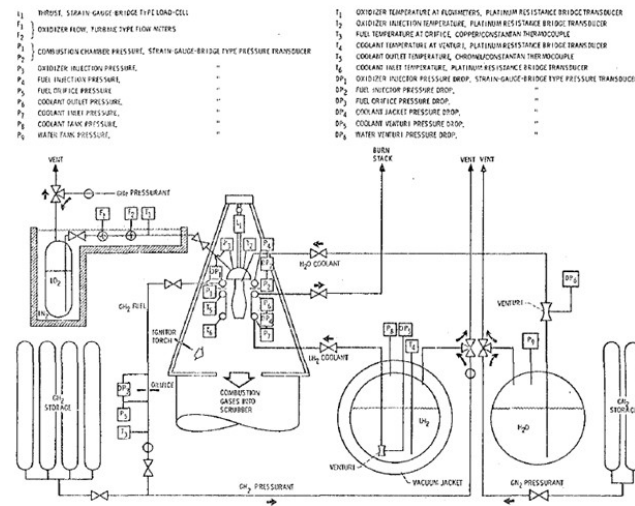
Very few experimental investigations on combustion chamber life and associated failure mechanisms have been carried out. The reason for this is due to the high cost associated with such investigations. During history several different real physical test methodologies have been developed in order to achieve the desired life cycles LRE thrust chambers. It is possible to present two different main test typologies which are different each other for costs, quality of real phenomenon representation and complexity.

4.1.1 Cylindrical thrust chambers

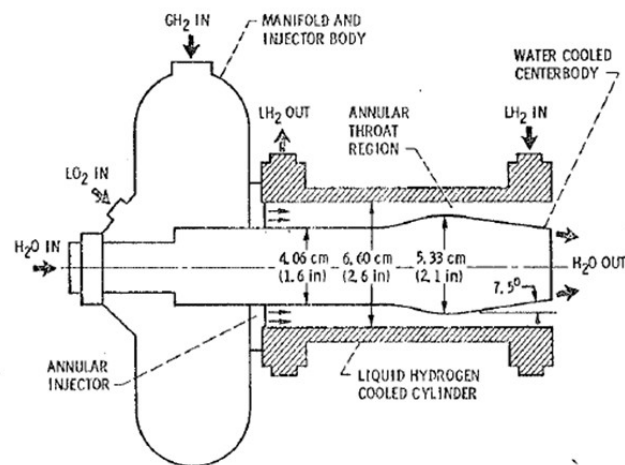
The NASA actions documented by Hannum and Quentmeyer [67] in the development and characterisation of the SSME-MCC still provide a unique and available experimental library of thrust chambers cyclically tested up to failure.

At NASA's Lewis Research Center, a low-cost, sub scale rocket engine test apparatus was developed to screen materials, provide data for model creation, and assess innovative design concepts (LeRC). The schematic for this device is shown in Figure 4.1b. An injector, a test portion in the outer cylindrical chamber¹ and a water-cooled center-body make up the device. The particular chamber is normal cooled with liquid hydrogen separately and is perfect for cyclic life tests since it can be thermally cycled from 28 K to 800 K throat wall temperature and back to liquid hydrogen temperature in about 3.5 seconds. Figure 4.1a shows the complexity of the entire cryogenic system.

¹NOTE: this is not a scaled convergent-divergent chamber



(a) Schematic of cylindrical thrust chamber assembly, from [67]



(b) Schematic of test facility, from [67]

Fig. 4.1 Cylindrical thrust chambers system facility

There are also University project such as Beihang University [68] and Purdue University [69] that use similar NASA's test facilities with cylindrical thrust chambers.

However, NASA also developed more real convergent-divergent test thrust chambers (Figure 4.2) in order to validate different FEM or algebraic models, such as the one implemented by Hannum [70] or Miller [17]. The system facility was approximately the same used for the cylindrical thrust chambers but with a difference in the geometry tested component.

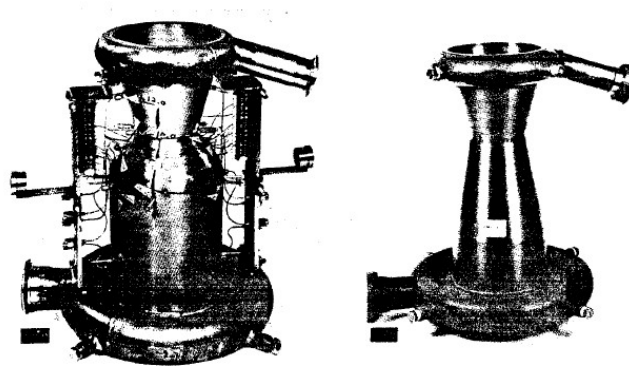
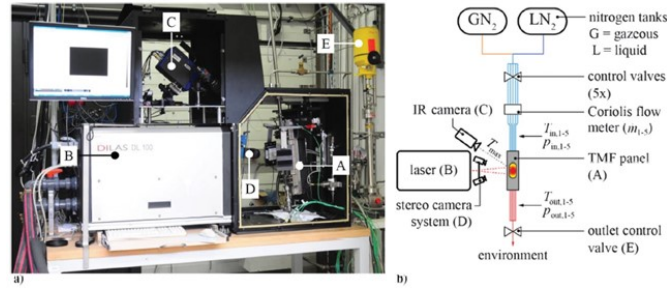


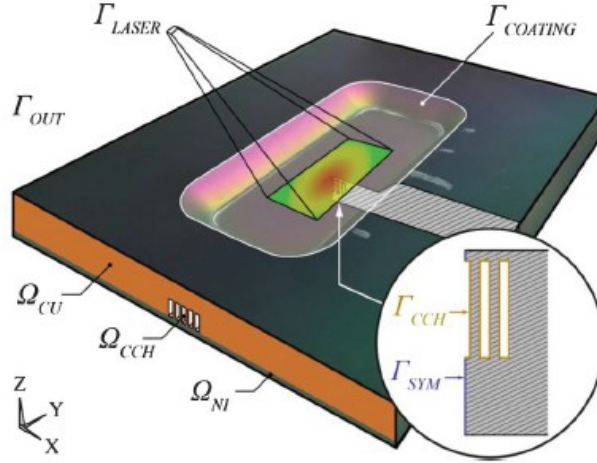
Fig. 4.2 Convergent-divergent typical test thrust chamber [17]

4.1.2 TMF panel

Small actively cooled parts of the hot-gas wall of a regeneratively cooled liquid rocket engine are represented by thermomechanical fatigue panels. The panels are used in conjunction with cyclic laser heating to evaluate fatigue life as well as thinning and bulging phenomena (the so-called doghouse effect) without the requirement to test a full-scale engine (Figure 4.3). This type of gadget is utilized to imitate real-world thrust chamber circumstances at a minimal cost while maintaining exact and repeatable operative settings. Some issues regarding the relation to actual thrust chambers can be raised since the wall temperature distribution on the panel surface is not uniform. Indeed, both the computational forecasts and the one experimental test case provided reveal that the rupture that occurred was not typical of those seen in cyclically tested thrust chambers.



(a) Photograph of a) the TMF test cell and b) schematics of the TMF test bench, from [71]



(b) TMF panel with five cooling channels, laser-heated area, and critical cross section (shaded), from [71]

Fig. 4.3 Thermo Mechanical Pannel facility

DLR, the German Aerospace Center, recently designed and tested a tiny, actively cooled panel heated cyclically by a laser [71]. Another example is the TMP developed by [66], with interesting results.

4.2 LRE thrust chambers numerical test methodologies

Numerical predictions of combustion chambers life and structural behavior have been performed since the very beginning of the concept design of the SSME-MCC by using simplified algebraic models [15] or more accurate Finite Elements Analyses (FEA) [70].

In any case, because the role and the importance of the wall deformation that accumulates cycle after cycle were not fully comprehended at that time (and thus material viscoplastic effects were not included in the models), the chamber life was largely over predicted. Basically the first NASA approach (Figure 4.4) to the problem, by assuming a linearity summable Low Cycle Fatigue and Creep damage [18], was not correct. Deguchi [16] studies show that the creep-fatigue life is much shorter than that predicted by the linear cumulative damage rule: the common model where material fractures occur when summation of the creep damage (Φ_{creep}) and fatigue damage

($\Phi_{LowCycleFatigue}$) reaches unity ($\Phi_{creep} + \Phi_{LowCycleFatigue} = 1$) shows an approximately the double of the value tested with the creep-fatigue experiment.

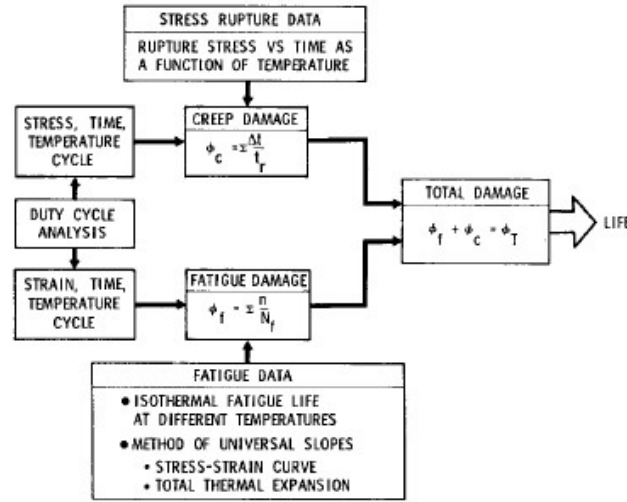


Fig. 4.4 SSME life analysis logic, from [18]

However, more recently, FEM including increasingly accurate viscoplastic models of the inner-wall material (basically, including the yield criterion, the flow rule, the hardening model, and the time-dependent phenomena as creep) has been proposed since the 1990s.

4.2.1 Algebraic models

Because of the inherent complexity of finite element approaches, simple methods for quickly estimating structural behavior and the resulting expected life of regeneratively cooled thrust chambers are critical, particularly at the stage of engine design and optimization when a massive analysis with variable parameters (such as geometric configurations, material properties, pressures, and temperatures) is required. Even though the comparison to experimental data was limited, algebraic models with simplified viscoplastic material behavior were proposed to account for inner-wall deformation (thinning and bulging) to improve the predictions [72, 73].

A great modern examples of algebraic model (sketch presented in Figure 4.5) is the one proposed by Pizzarelli [13]: a procedure based on simplified algebraic models for the estimation of the stresses and strains that affect the thrust chamber as well as the resultant cyclic life. Life is assessed using appropriate models culled from the literature and rearranged. It's worth noting that such models account for the accumulation of inner wall deformation over time (the life-limiting doghouse effect). Low-cycle fatigue and tensile ductile rupture by plastic instability are also thought to be plausible failure mechanisms. The proposed simplified approach has a good agreement with the experimental life data, showing that it may be used to predict the thrust chamber's life without doing a comprehensive finite element study. However, analyzing examples that are notably different from the simulated ones may necessitate additional parameter calibration. The

few predictions that have been made have been shown to be 15–25% correct. This isn't much better than what the proposed Pizzarelli's algebraic model achieves (for the vast majority of the reproduced data). In fact, the average prediction error for thrust chamber life is less than 20%.

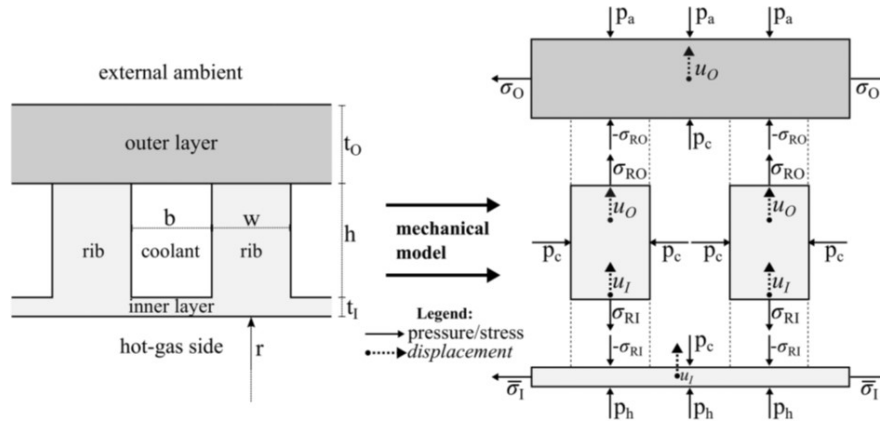


Fig. 4.5 Sketch of the thrust chamber structure and its structural modelling (circular symmetry is not shown), from [13]

4.2.2 Numerical models

The typical performed analysis, which can be assessed for the most solicited chamber section using two-dimensional or for the whole chamber using three-dimensional formulations, includes an evaluation of the hot-gas and coolant heat transfer coefficients during the steady-state hot-run phase, which are eventually assessed by the use of the computational fluid dynamics analysis, a transient heat transfer analysis in the solid structure during one duty cycle and, finally, a structural analysis during one or more duty cycles by means of quasi-static FEA computations.

First LRE numerical analysis generally considered the proposed method reliable if they were able to qualitatively reproduce the doghouse effect. Arya and Arnold [74] are generally considered to have first introduced the use of unified viscoplastic models - into a LRE thrust chamber numerical analysis - that is, simultaneously accounting for all the inelastic strains (i.e., plastic, relaxation, and creep) and their interactions.

Khul et al. used the maximum deformation accumulated after one cycle to determine the longevity in Ref. [75]. This method allows them to quickly estimate the life of the product and is consequently utilized for design optimization. Unfortunately, a one-cycle simulation does not reveal the dog-house effect. In fact, the greatest deformation is identified incorrectly beneath the rib on the hot-gas side, rather than under the cooling channel, where the crack actually occurs.

Schwarz et al. [76] later shown that, cycle after cycle, the inner wall deforms in such a way that the maximum damage flows from the coolant/rib corner to the hot-gas side under the cooling channel, employing the notion of continuum damage mechanics.

More recently, Song and Sun [77], using a nonlinear kinematic hardening model, numerically demonstrated that the failure of the thrust chamber may be dominated

by low-cycle fatigue or tensile ductile rupture, depending on the material viscoplastic behavior. This is in line with the experimental evidence of Refs. [[5],[17]], which showed that pure copper chambers generally exhibit tensile ductile rupture, while chambers made of reinforced copper alloys are more prone to fail under low-cycle fatigue.

Chapter 5

Cu-17 4PH: a new innovative metal-matrix-composite material

The new innovative composite-metal-matrix material have never been characterised. This study provide a fist thermo mechanical characterization of the material in order to understand if the design idea made from Sophia High tech s.r.l. can be proposed for a future re-usable rocket engine design.

The idea is to achieve a good thermal conductivity while having an excellent tensile resistant. These two properties have been taken over by pure copper and a stainless common processed steel in the world of additive manufacturing: maraging 17 4 PH steel.

5.1 Powders Data

5.1.1 Pure Copper by Legor Powmet

PM-CU101P is a gas atomized copper powder, specifically developed for laser melting applications. *Legor Powmet* declare that the material *is carefully prepared by using a special atomizing process, that guarantees spherical powder particle geometry and maximizing the powder quality* and that the *'composition and size distribution have been designed to maximize energetic absorption from laser beam during the laser melting process'*. The as build mechanical properties are not available. The declared chemical composition is 99.9% copper.

Powder particles size (Figure 5.1) is: $D_{10}=5\mu m$, $D_{50}=10\mu m$ and $D_{90}=17\mu m$. The nominal size declared range is $5\mu m-25\mu m$ [78].

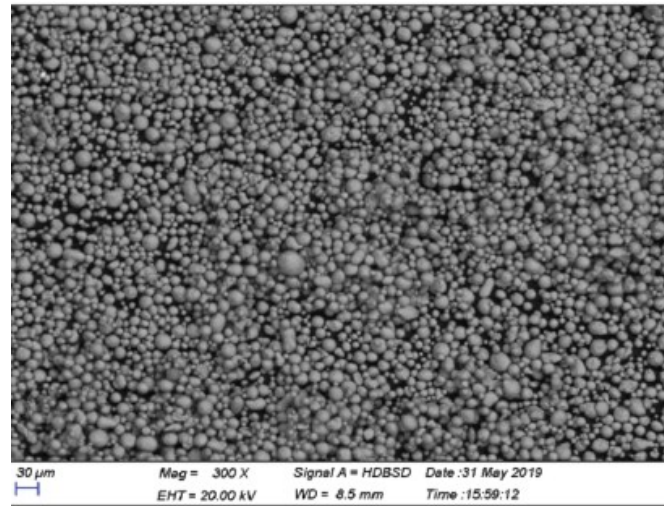


Fig. 5.1 Scanning electron microscopy (SEM) image of the Legor Powmet pure Copper Powder, from [19]

5.1.2 17-4 PH by Carpenter Additive

PowderRange 17-4 AR (17 4PH named from Carpenter Additive) stainless steel is a martensite precipitation/age-hardening stainless-steel offering high strength and hardness, along with excellent corrosion resistance, up to 600°F (316°C) [19]. It has good fabricating characteristics and can be age-hardened by a single-step, low-temperature treatment, which can be chosen to achieve specific strength and toughness combinations. The chemical composition provided by the powder supplier is presented in Figure 5.2. The powder atomization process is a: Vacuum Induction Melted with Argon Gas.

Fe	C	Mg	P	S	Si	Cr	Ni	Cu
Balance	0-0,07	0-1,00	0-0,04	0-0,03	0-1,00	15,00-17,50	3,00-5,00	3,00-5,00

Fig. 5.2 Carpenter Additive 17-4 PH Powder Chemical Composition, from [19]

Due to this balanced combination of performance and ease of use in AM, PowderRange 17-4 PH has been chose from Shpia High Tech s.r.l. as a perfect material for achieve a high yield strength. Mechanical as-built and heat treated mechanical properties provided by the powder supplier are presented in Figure 5.1. The powder supply define an overall *Good* corrosion residence of the powder. This aspect is particular relevant because of the oxidation provided by the LRE combustion hot gas.

	Orientation	0.2% Teld Strength [MPa]	Ultimate Strength [MPa]	Elongation %	Hardness [HRB]
As-Build	X and Y	758	1136	15	35
	Z	747	1145	15	
Sol	X and Y	1209	1342	17	42
	Z	1208	1343	15	
HIP/Sol	X and Y	1207	1338	18	42
	Z	1207	1340	17	

Table 5.1 *Carpenter Additive 17-4 PH* as-build and heat treated mechanical properties, from [19]

The spherical powders have average dimension is not available from official *Carpenter Additive 17-4 PH* Data Sheet: however from Figure 5.3 is it possible to evaluate a minimum size of $15\ \mu\text{m}$ and a maximum size of $45\ \mu\text{m}$.

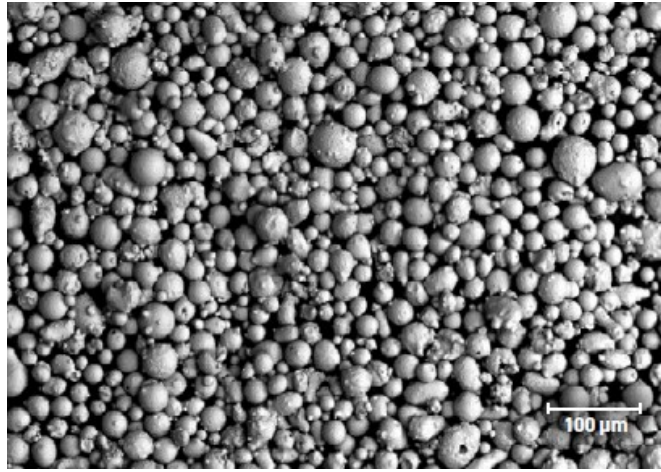


Fig. 5.3 Scanning electron microscopy (SEM) image of the *Carpenter Additive 17-4 PH* Powder, from official *Carpenter Additive 17-4 PH* Data Sheet

5.2 Powder Mixing Process

The experimental activities started with the innovative patented Additive Manufacturing powder mixer developed by Sophia High Tech srl: it consist in a new technology developed in order to mix two or more additive manufacturing powder with an inert gas (Figure 5.4). Because of the possibility of density instability during mixing an acoustic field is used to break all electrostatic forces to ensure a stochastic distribution of the mixed powder composed by the different starting powders on the printing machine platform.

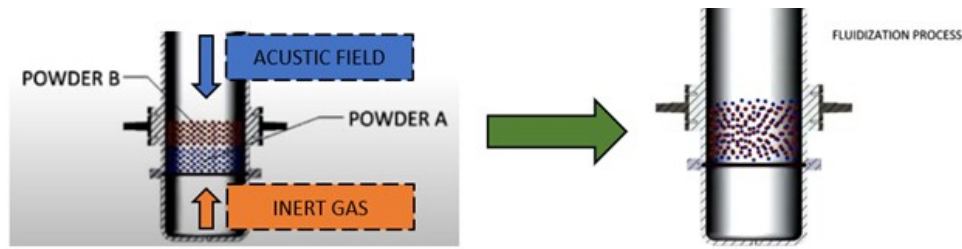


Fig. 5.4 Patented powder mixing process logic

With the goal of a industrialisation of advanced metal powder mixing process for the additive manufacturing sector (Cold Spray, SLM, etc.) the POWMIX project is a program co-funded by the Region CAMPANIA¹.

The acoustic field-assisted mixing technique consists of the dual action of a pressurised gas and a sound pressure field. These actions mix and amalgamate mixtures of metal powders to be used for the production of objects, characterised by a high level of customisation in terms of both shape and material, using additive technologies such as Cold Spray and 3D printing. The final objective of the POWMIX project was to design and produce an industrial-scale mixer capable of producing homogeneous mixes (on a micrometric scale) of metal powders defined by customer's requirements and the operating specifications of the component to be manufactured.

The mixing system integrates the fluid bed mixing technique with that of the acoustic field, which acts as a forcer supplying energy to the fluid phase in order to allow and/or optimise the separation and aggregation between the different powder clusters, thus guaranteeing the homogeneity of the mixture created.

The advanced pulse mixing plant consists of:

- **Reactor:** It is the main element of the entire plant, inside which are the elemental powders to be mixed;
- **Support structure:** It constitutes the frame of the plant and guarantees the movement of the reactor for loading/unloading the powders;
- **Acoustic field generation and propagation system:** It supplies the bed of powders with the acoustic waves (forcing) to carry out the process;
- **Management and monitoring system:** The interface of the plant and allows continuous quality control over the process;

Figure 5.5a shows the machine with the control unit on the right side. On the bottom of the structure a inert gas system provide the mechanical kinetic energy to the powders. The powders movement can be described by a 'random-boiling' mixing process (Figure 5.5b).

¹FESR 2014-2020 - DECREE N°225 of 07/08/2018 - CUP: B32C18000070007 - SURF: 17048BP0000024 - EUROPEAN UNION | European Regional Development Fund



(a) POWMIX mixing machine



(b) Instant photo of the 'random-boiling' mixing process of the custom Cu17-4PH powder

Fig. 5.5 Powder Mixing Process

To carry out the fluidisation and mixing of the powders, nitrogen is insufflated from below into the fluidisation reactor. The flow rate of the process fluid is continuously monitored by an MFC (Mass Flow Controller) sensor. The pressure drop of the nitrogen flow is measured by pressure transducers placed upstream and downstream of the bed.

The acoustic field generation and propagation system consists of:

- **Wave generator:** It is able to produce a signal of the desired shape, amplitude and frequency;
- **Signal amplifier:** Is can provide a signal of about 150 dB intensity;
- **Loudspeaker:** It is installed on the head of the reactor to reproduce the acoustic signal;
- **Microphone:** Via this object it is possible to monitor the sound field supplied to the dust bed;

Feedback on the composition of the clusters (homogenisation of the mixture) is obtained by means of optical sensors located inside the fluidisation chamber. The plant designed in this way can process more than 100 kg of metal powders for the production of custom blends.

One of the most intriguing and recent research fields in metal AM concern the aforementioned powder-based mixing processes to generate parts with custom materials [79]. This is due for two main reasons: take advantage of the enhanced properties of the resulting material, trying to maximize the sum of the benefits of the individual materials and, on the other side, combine the previous aspect with the complexity-for-free-design of AM.

The machine was used in a 36 months project (started in January 2017). AMMEP [Additive Manufacturing by Mixing Elemental Powders] was a research and development project co-financed by the Italian Ministry of Economic Development² which objective was the production of the combustion chamber for the VEGA-E space launcher, by means of the Additive Layer Manufacturing process, using advanced mixing technologies to obtain a custom metal powder.

During the aforementioned activity the process of mixing Inocel 718 and Copper powders was successfully tested [80]. Different DoEs test campaign have been performed in order to better understand the mixing process parameters [81].

In this scenario, the research contributions are still poor. Some authors investigated the mixing of IN718 with Cu for critical application such as hot components for gas turbine engines [57]. More specifically, the most notable scientific contributions were provided by B. Oniuke [82], who studied the LENS³ process to develop a IN718-Cu bimetallic structure, and by A. El Hassanin that investigated the feasibility of pre-mixed IN718-Cu powders[22].

²Prog. n. F/050320/02/X32 - CUP: B38I17000430008 - COR: 309480

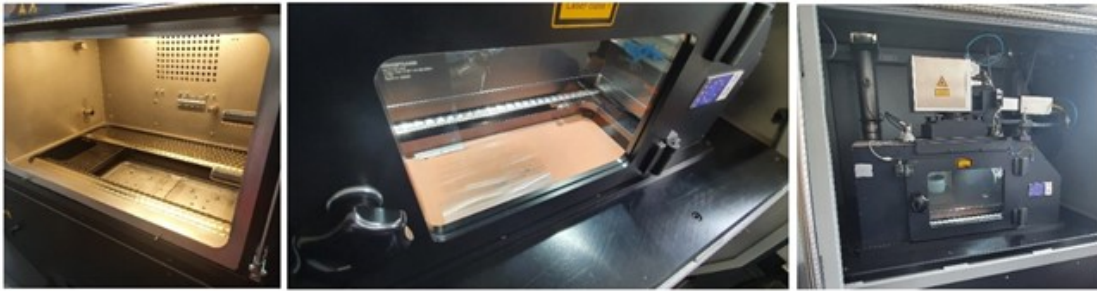
³Laser Engineered Net Shaping

5.3 Additive Manufacturing Process Parameters

The custom powder mixed by the POWMIX machine is a 65% copper - 35% 17-4 PH. The Additive Manufacturing machine is a Concept Laser M2 presented in Figure 5.6 (specification in Table 5.2).



(a) Concept Laser M2 machine



(b) Left: powder charging chamber, Middle: laser printing chamber, Right: laser chamber system

Fig. 5.6 Powder Mixing Process

	Value	Unit
Working Volume	250 x 250 x 250	mm (X,Y,Z)
Layer Thickness	20 - 80	μm
Accuracy	+/- 0.05	mm
Building Velocity	2 - 20	cm/h
Scanning Velocity	Max 7	m/s
Power	200 - 400	w
Spot Laser Diameter	50 - 200	μm
Laser System	Fibre laser	0.7
Atmosphere	nitrogen or argon	

Table 5.2 Concept Laser M2 Specifications

The process parameters are presented in Table 5.3. Because the pre-mixed material is a new one for the industry no Design of Experiment have been done in order to optimize the process parameters. Sophia High Tech s.r.l. decide to adopt this parameters

based by the internal know-how in Additive Manufacturing and by the previous work on Inconel718-Cu pre-mixed recherche project.

	General	Body	Contour
Fusion Strategy	Island (5mm length)		
Layer Thickness t [mm]	0.03		
Hatch Distance h [mm]	0.105		
Spot Size ϕ [mm]	0.15		
Velocity v [mm/s]		253	400
Power P [W]		200	180
Beam Compensation δ [mm]			0.075
Overlap Factor $A1$		0.7	

Table 5.3 Job 1 and Job 2 parameters: nomenclature from Figure 2.4

Note that the Overlap Factor $A1$ is the overlapping between two parallel laser traces (Figure 5.8): Laser Spot Overlap (Hatch Overlap) = Overlap Factor $A1$ x Spot Diameter = $0.7 \times 0.150 \text{ mm} = 0.105 \text{ mm}$; the Beam Compensation is the distance between the trace of the laser and the CAD contour of the object.

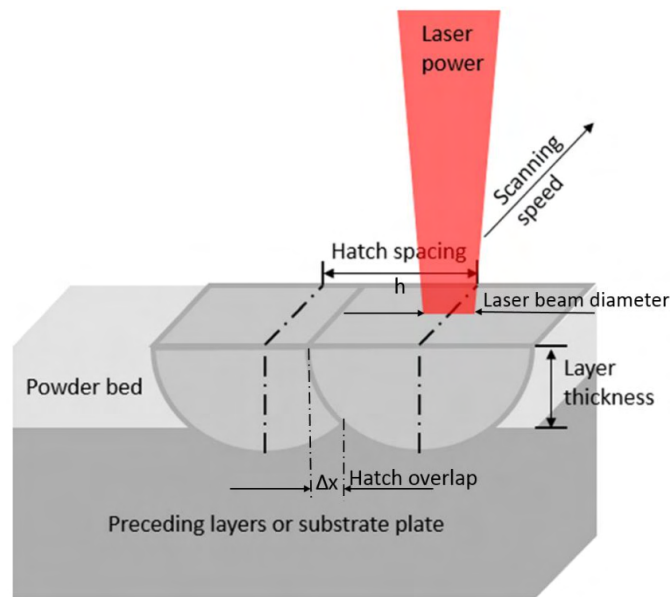


Fig. 5.7 Laser Spot Overlap (Hatch Overlap), from [20]

More details about printing time and number of layers are presented in Table 5.4.

	Job 1	Job2
Layers Number	833	433
Printing time t [days]	5days 4h 45min	2days 2h 13min

Table 5.4 Job 1 and Job 2 additional in formations

The island scanning strategy has been employed in the present study. This strategy divides each layer into smaller islands that are scanned in a random order, maintaining perpendicular the scanning vectors of the neighboring islands. While printing subsequent layers, the islands are shifted with a random θ_i angle (Figure 5.8) in both x and y directions [83]. A scheme of the strategy can be seen in Figure 5.9.

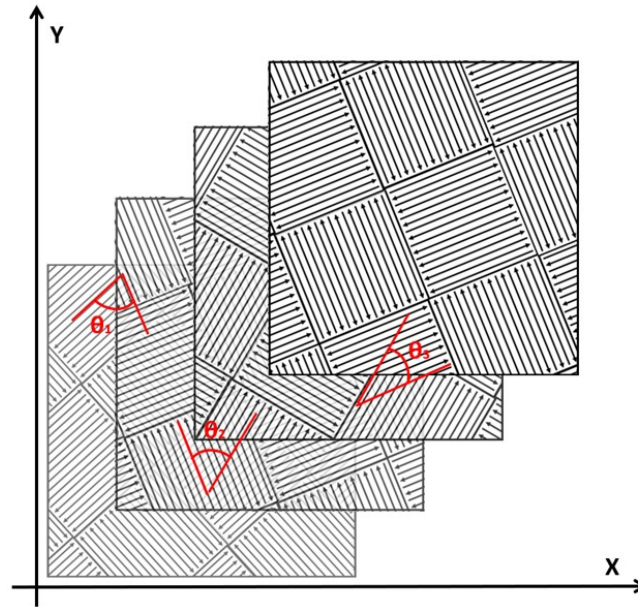


Fig. 5.8 Layer random island strategy

In particular the random algorithm implemented inside the machine controller chose an arbitrarily region to start melting the first island and do not goes on in a precise order but randomly (Figure 5.10). In addition, this random strategy do not perform the same printing islands order layer by layer: every new powder layer have a random melted island path. The advantages of this strategy can be identified in the capability to shorten the scan vector and to reduce the residual stress [84, 85, 83, 86, 87].

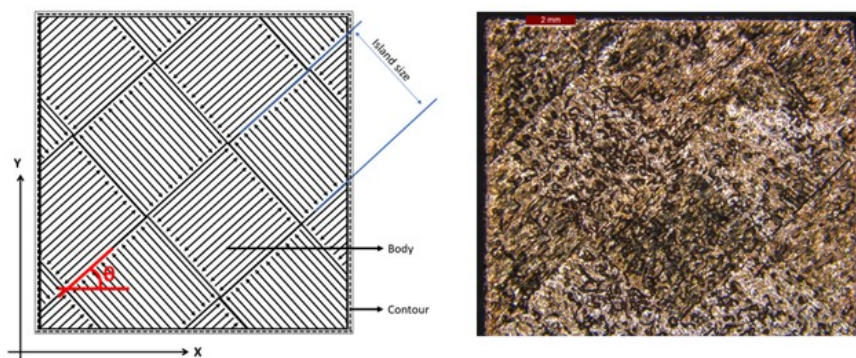


Fig. 5.9 Island strategy

The main reason of this advantages is the better cooling dissipation: the intrinsic random way islands are melted allows a random heat cooling that statistically do not make particular and repetitive thermal gradient with a consequent microstructure gradient. An

homogeneous microstructure is not simple to achieve in Additive Manufacturing but it allows a very good repetitively of mechanical properties.

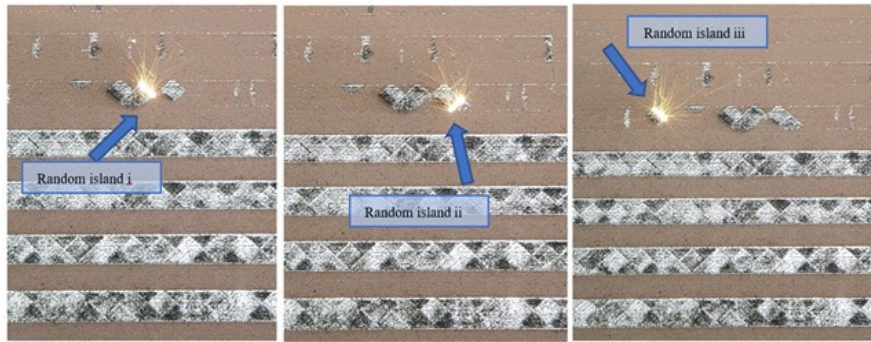


Fig. 5.10 Random island algorithm: study Job 1

As already decided for the process parameters, also object' supports do not have been optimised. Different studies show the different impact of typology, dimension, number and height of Additive Manufacturing supports [88]. However no optical evident strain gradients have been observed. In the same printed job it is possible to see two different support strategies (Figure 5.11):

- **Laid down cylindrical specimens' support:** The strategy is a filling vertical 0.3 diameter cylindrical columnar supports, adopted in order to have a better cylindrical shape of the cylindrical specimens: this was necessary because of the better fit in the CNC⁴ machining post process. The disadvantage of this method is that requires more time (respect to a direct printing strategy) because it has two main steps (Figure 5.12): Step A) pre-melting every single circular support; Step B) Melting process.;
- **Square specimens' supports:** The strategy is a full material filling support. No particular supports are printed between the platform and the component. This strategy is used because these specimens do not require particular lathe mechanical machining. In addition, this strategy requires less time respect to the 0.3 diameter cylindrical columnar supports;

⁴Computer Numerical Controlled milling machine,

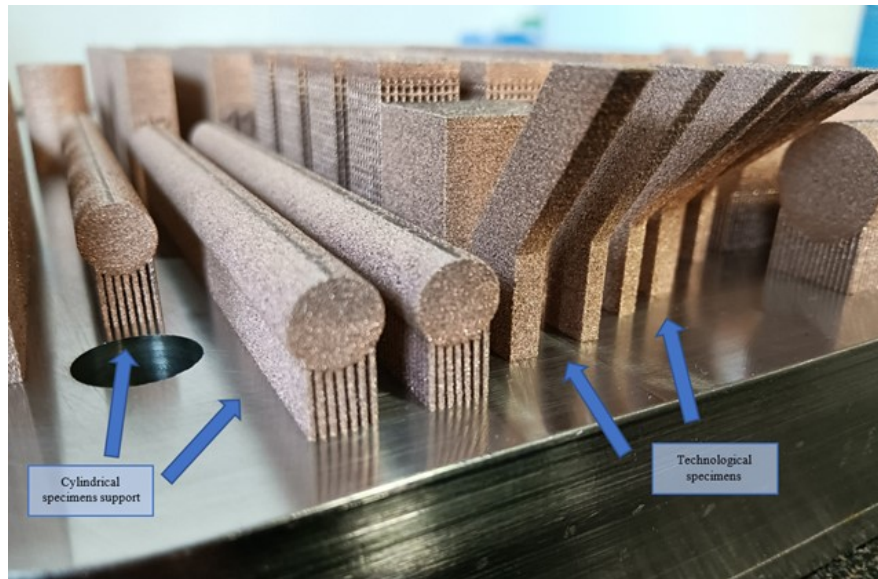


Fig. 5.11 Two different supports strategies adopted



Fig. 5.12 Step A) (left) pre-melting and Step B) (right) Melting process

On the same way, not blade material optimization have been done. A common silicon blade have been employed. The available literature shows that the material and the shape of the blade coating system can change the powder distribution on the printing platform.

The coder system employed in the present study has a right to left side movement (Figure 5.13): i) the powder system moves the storage platform up in order to supply the correct amount of powder to the blade⁵; ii) the blade system moves from right to left: this path allows the blade to collect the powder from the storage platform and spread it to the printing platform; iii) the blade stops its motion and the surplus powder fell into a re-cycle storage tank; iv) the laser melt the powder in order to solidify the layer; v) the printing platform moves down by the amount equal to the height of the layer; vi) the blade system moves to the right and start again the process.

⁵NOTE: the amount of power that the blade spread to the printing platform is twice the building layer height parameters. This is due to a conservative methodology used by Sophia High Tech s.r.l.. The powder surplus is re used for future jobs.

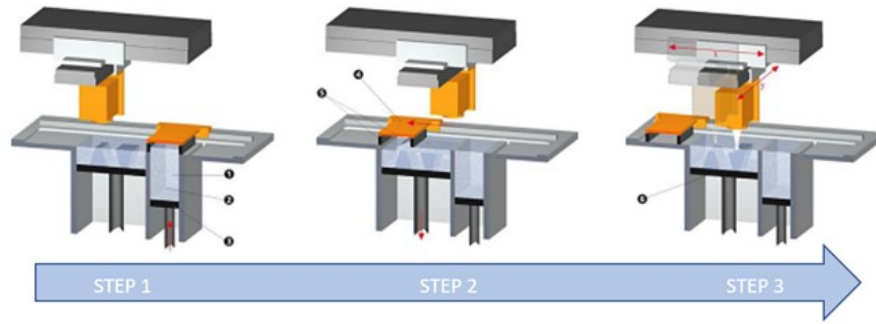


Fig. 5.13 Logical scheme of the Concept Laser M2 power coating system

5.3.1 Platform Calibration Strategy

The printing 250 x 250 mm platform is CNC machined in order to achieve a perfect plenary, however due to machine wearing the system responsible for the up and down movement of the platform can be slightly offset. Sophia High tech s.r.l. bypass the problem using a simple strategy. When the first few layers of powder are dropped on the platform it is possible to see (Figure 5.14a) that not all the area receive the same mount of powder: therefore the first layer is replicated for few times and used to flatten the main printing surface. The result is a starting base for the job better aligned, ready to star the real job printing process (Figure 5.14b).

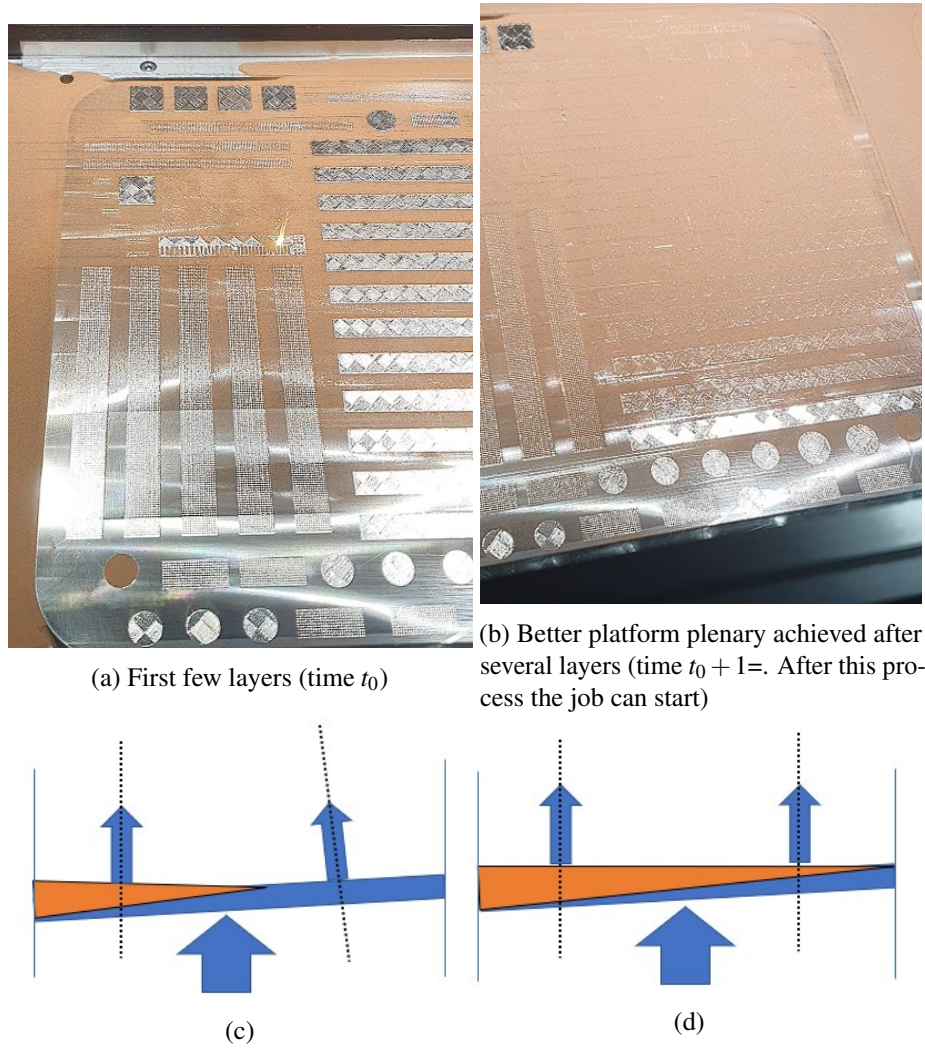


Fig. 5.14 Platform Calibration Strategy

5.4 Printing Jobs and Cost Analysis

The Additive Manufacturing printing process has been divided in two main jobs (Figure 5.15). This is due to the high number of specimens required to characterize the mechanical and thermal material properties. In particular the Low Cycle Fatigue test campaign, because of the time dependent life behavior, required more than 35 specimens, thus all printing platform.

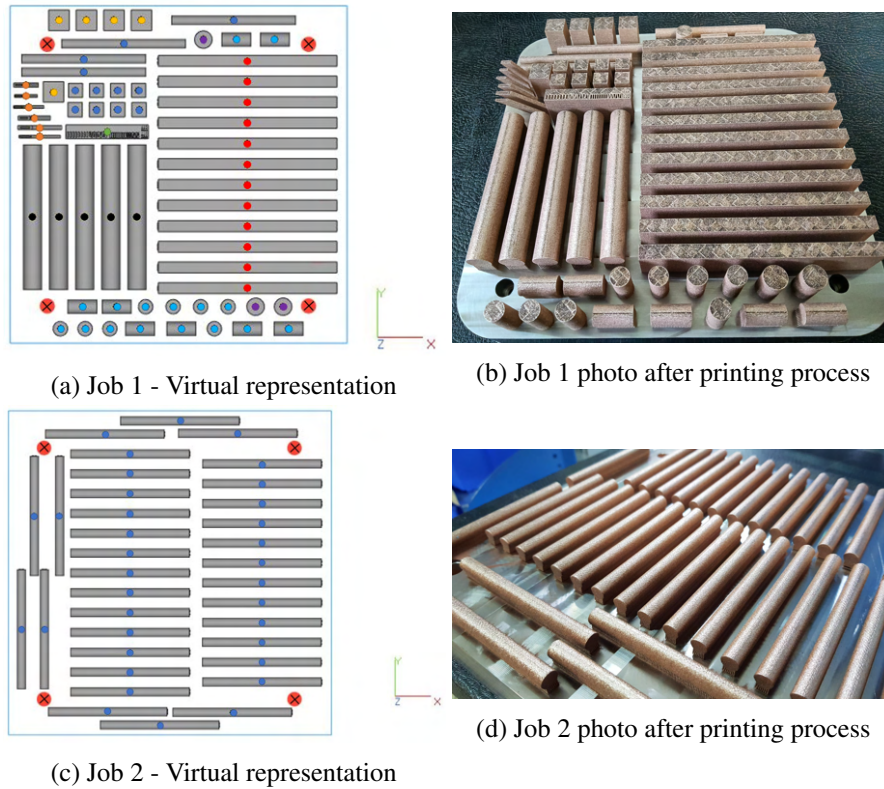


Fig. 5.15 Job 1 and Job 2

All technological specimens inside Job 1 (Figure 5.15a, yellow dots: specimens to investigate the maximum angle achievable for the engine cooling channels; green dot: specimen printed in order to investigate different achievable cooling channels shapes) have been printed at the end of the platform. The powder coating blade moves from right to left respect to the X-axe of the plan view in Figure 5.15a, therefore if the machine would not be able to print the component (e.g. because of a not achievable angle) the other platform specimens would not have been damaged from unmelted particles/rejects.

Another important technique for failing to a successful printing job have been performed: the two columns of cylindrical specimens (Figure 5.15c) have been shifted each other respect to the moving blade axe. This technique, on a similar way the one adopted for the technological specimens, avoids unintentional wrong-melted particles to destroy other specimen's integrity.

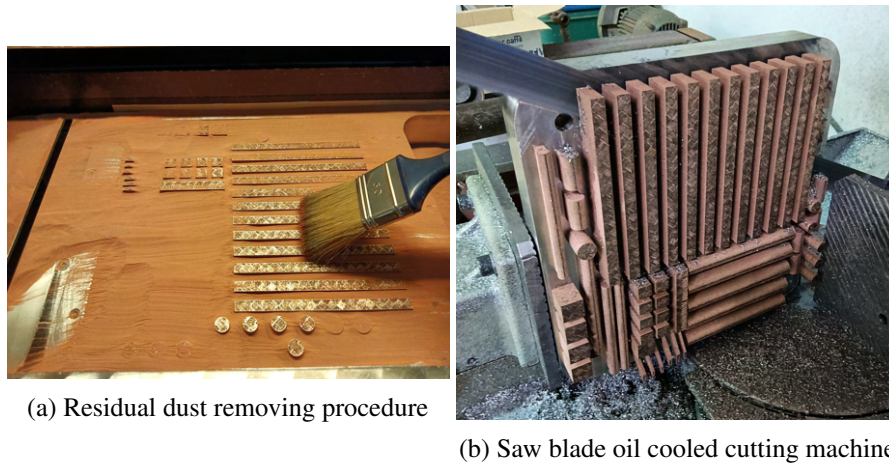


Fig. 5.16 Printing platform removing procedures

After cleaning the platform from residual dust (Figure 5.16a) the cutting process uses a saw blade oil cooled cutting machine (Figure 5.16b). After this procedure all cylindrical columnar supports have been manually removed before starting the CNC machine operations (Figure 5.17).

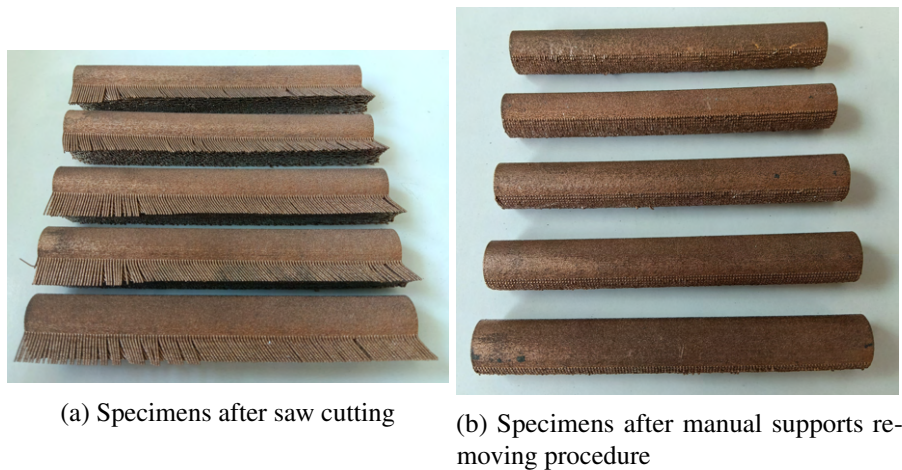


Fig. 5.17 Example of manual supports removing procedure

A brief cost analysis is presented in Table 5.5.

	JOB 1	JOB 2	Additional Informations
Height	25	13	mm
Printed Volume	1562500	812500	mm^3
Powder overdosing	200%	200%	
Custom POWMIX powder	16.659	8.662	Kg
Nitrogen	3	2	Standard 50 liters tank
Cutting procedure	1	1	
Man working hours	12	12	h
Specimens number	54	35	
TOTAL COST	7518.73	4777.34	Euro
Average Specimen cost	138		

Table 5.5

Before the printing process a very careful hand made machine cleaning procedure has been performed in order to avoid particles contamination from previous different materials jobs.



(a)



(b)

Fig. 5.18 Hand made machine cleaning procedure

Chapter 6

Experimental Set-Up: Materials and Method

Typically asymmetric geometry are processed by Additive Manufacturing in a vertical way: the axisymmetric axis is parallel to the building direction (frequently the Z-axis). The LRE thrust chamber is a perfect example of an axisymmetric object almost always processed in a vertical way. This is due to two main reasons: first of all, because of the thermal gradient between the first layer and the last one (the first layer material spent the entire building process time inside the chamber while the last layer just few seconds) it is not recommended to lay down an axisymmetric component. This could produce microstructural remarkable difference around the structure. It is preferable to have a Z-direction mechanical inhomogeneity instead of a fraction of the axisymmetric part. Secondly the support and the powder arrangement on the edge of the circular object is not optimal if the component is laid down. For these reasons LRE thrust chambers are frequently manufactured in a vertical orientation (Figure 2.3).

The fracture mechanism of LRE regenerative cooling thrust chambers (Section 3.3) is a combination of LCF and plastic instability induced by thermal compression-tensile behavior because of the temperature difference during start-up and shut-down operation of the engine. Therefore the cracks opening mechanism (Figure 6.1) do not show up in the XY plane, but in the z-axisymmetric plane (ZX or ZY plane).

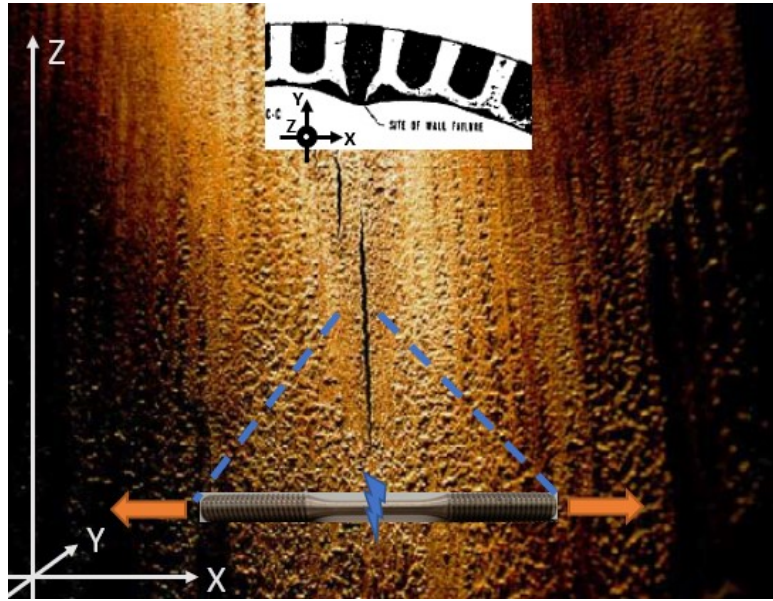


Fig. 6.1 Typical LRE z-axisymmetric plane fracture, from [12]

Because of the exposed scientific evidences the present study has analysed all mechanical properties (except for the hardness tests and the compression test) only in the X or Y direction. This choice have been done in order to better replicate the fracture mechanic 6.2. An AM material can be defined as a transversely isotropic material: X and Y direction behave in the same way, this is not true for the Z-direction. By testing tensile and Low Cycle Fatigue specimens printed in the XY plane we are able to perform a more representative analysis.

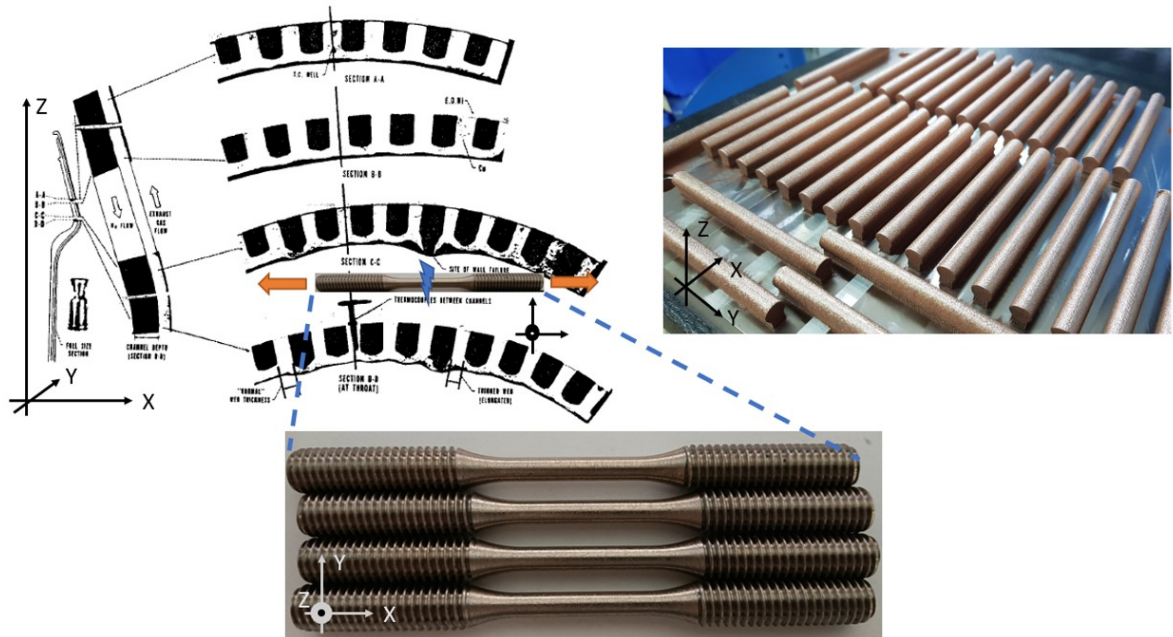


Fig. 6.2 LRE fracture mechanism and uni-axial Low Cycle Fatigue specimen replication. Orange Arrows: uni-axial Low Cycle Fatigue test loading displacement direction; Blue lightning: spacemen XY plane in where uni-axial fracture occur

In addition, because AM costs are relevant and the present project is a first R&D characterisation of the new material, by limiting the overall printing high to a 25 [mmm], a more manageable costs is achieved.

Table 6.1 shows the overall test plane.

	Z Direction	X/Y Direction	High Temperature	Heat Treatment	Additional Notes
Technological Tests					
Technological shapes	V				
Technological maximum angle	V				
Lattice Structure	V				
Physical/Chemical Properties Analysis					
Roughness	V	V			
Optical Micrography	V	V		V	Optical Microscope
SEM Micrography	V	V			SEM Microscope
Chemical Composition (SEM)	V	V			EDS (SEM Microscope)
Porosity analysis	V	V			Image Post Process
Void distribution	V	V			CT scan
Thermal Properties Analysis					
Thermal conductivity	V	V		V	Hot Disch
Linear Thermal Expansion Coefficient	V	HP			TMA
Thermal Capacity	V	HP			DSC
Mechanical Analysis					
Hardness	V	V			Vickert Indentation
Micro Hardness	V	V			Vickert Indentation
Traction	V	HP	V		Traction Machine
Compression	V	V	V		Compressione/ Traction Machine
Lattice Structure Compression	V				
Low Cycle Fatigue		V	V		ETMA Machine
Creep		V	V		Creep Machine
Ratcheting		V	V		ETMA Machine
Fracture Surface Analysis					
Traction		V	V		SEM Microscope
Low Cycle Fatigue		V			SEM Microscope
Low Cycle Fatigue 3D Morphology		V	V		3D Optical Reconstruction
Low Cycle Fatigue Micrography		V			Optical Microscope
Lattice	V				Optical Microscope Qualitative Analysis

Table 6.1 Test Planning

6.1 Technological Tests

All technological tests are not performed with a particular methodology. The only important criteria was to not damage accidental miss-printed areas of the particulars specimens on the printing platform, as already described in Chapter 5.

A low magnification microscope is used in order to identify miss-printed areas or technological problems. However a better analysis could be done by CT scan by a proper comparison between CAD file and 3D reconstruction: this analysis in a common non destructive methodology which allows researchers to understand if dimensional and geometrical tolerances are observed [2, 89].

6.2 Physical/Chemical Properties Analysis

6.2.1 Roughness

The external surface quality is directly linked to the contour process parameters of the Additive Manufacturing Process (Table 5.3). Because the surface contour parameter are the same for both, internal and external surfaces, in order to analyse the surface roughness only external surface have been tested. With this assumption the technological specimens do not have been cut neither transversely nor longitudinally.

No particular polishing have been done on the surface. A basic hand soft brush process for powder removing after the printing jobs followed by a hand compressed air procedure.

The machine is a linear one-direction RPT-80 rugosimeter composed by the diamond head touch probe and the control unit located in DIMEAS laboratory of Politecnico di Torino, Italy. The machine has been calibrated with the recommend plate before using (Figure 6.3a,6.3b). The specimen has been constrained on a specific platform and the test is performed.

Another machine has been employed to analysis the roughness of the Low Cycle Fatigue specimens after CNC machining. The standard linear rugosimeter do not perform acceptable results when a high curvature component is analysed. Therefore, in CEROC laboratory of Univesità de Tours, France, a Veeco Wyko NT1100 Optical Profiling System (Figure 6.3c) have been used for acquiring the 3-Dimensional profile, thus the roughness, only for the Low Cycle Fatigue specimens. This particular machine is provides non-contact surface topography thanks to the Wyko Vision32 analysis Software.

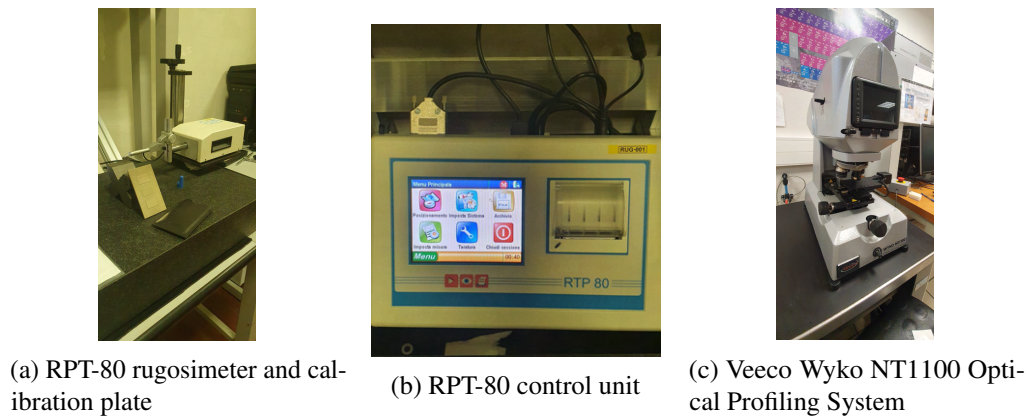


Fig. 6.3 Roughness test facilities

6.2.2 Optical Micrography and Porosity analysis

A specific metal-analysed optical vertical reversed microscope is the main machine employed in order to analyse the metal micrography located in the DISAT laboratory of Politecnico di Torino, Italy. Another more general-use optical microscope has also been used: It is a Keyence VHX located in the CEROC laboratory of Université de Tours, France.

The procedure adopted for analysis the metal micrography is similar for every samples. For specimens analysed in CEROC laboratory (one random specimen from the vertical cylinders, marked with a Blu Cyan dot in Figure 5.15a from Job 1) the cutting procedure is performed by the professional Struers cutting tool from CEROC laboratory (Figure 6.4a), the encapsulation by the Struers LaboPress-3 in Figure 6.4b (no specific resins are used, depends on the availability of the laboratory stocks at the moment) and the final surface polishing with the automatic Struers TegraPol-11 (Figure 6.4c) with a Struers precis grinding procedure recommend for Copper-base alloys. No chemical attacks have been done.

On the other side, for the specimens analysed in the DISAT laboratory of Politecnico di Torino (one random specimen from the cube marked with a Yellow dot in Figure 5.15a from Job 1), the cutting process is performed by hand, the surface polishing with different granulometry sandpapers, from 300 to 2500, a Leco PR-36 encapsulating machine (no specific resins are used, depends on the availability of the laboratory stocks at the moment) and finally a 5 seconds acid attack with ferric nitrate ($Fe(NO_3)_3$) in order to corrode copper.



(a) Struers cutting tool



(b) Struers LaboPress-3



(c) Struers TegraPol-11

Fig. 6.4 Micrography analysis of the CEROC Laboratory of Université de Tours, France

The optical Keyence VHX microscope has a powerful post processing software which has allowed a clear porosity analysis: a contrast path is proposed by the software and the operator can manually change parameters in order to include/exclude fake porosity identification. It is important to highlight that this porosity analysis, as the majority porosity analysis available in literature, is manual and it is highly dependent from the operator choices.

6.2.3 SEM Micrography and Chemical Composition

The sample analysed for the optical micrography have been analysed for a SEM micrography characterization, therefore the method adopted is exactly the same on already presented. The machine is located in the DISAT laboratory of Politenico di Torino, Italy.

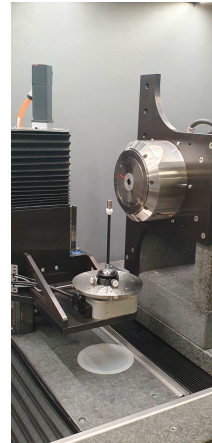
In addition to this, a SEM-EDS chemical analysis has been done on the specimens. It is a non-destructive analytical technique which requires a polished sample. Electrons are irradiated into the sample material, and the energy emissions are converted into varying-intensity spectral peaks, yielding in a spectrum profile that identifies the various inorganic components contained in the sample. The research is qualitative rather than quantitative. The X-ray intensity (the size of the spectrum peaks) is related to the element concentration in the sample. The SEM-EDS machine report provides: a visual representation of the chemical composition, the spectra and a resuming tabular data. This EDS can characterize a surface area (so called map-analysis) or a 1x1x1 micron cube on the surface (so called spot-analysis), allowing for very precise and specific investigation of specific areas of interest: both analysis strategies results will be presented in this study.

Note that the EDS analysis is not reliable for elements position under sodium: an element such as carbon is not very well detected via EDS.

6.2.4 Void distribution

The void distribution is a different analysis from the one of porosities. This analysis is a computational tomography which allows to understand the specific location of the

macro voids. While by the evaluation of a micrography we are able to study a random local scale Additive Manufacturing process quality, with a CT scan it is possible to map the macro voids inside a component. The “computed tomography”, or CT, refers to a computerized x-ray imaging procedure in which a narrow beam of x-rays is aimed at the specimen, producing signals that are processed by the machine’s software to generate cross-sectional images. The study has been used a RX Solution EasyTom machine (Figure 6.5a) is a CT system with in 3D X-ray which can test sample from X, Y, and Z direction, located at CERMEL Laboratory of Université de Tours, France.



(a) RX Solution EasyTom machine, CERMEL Laboratory of Université de Tours, France (b) Placement of the specimen for the CT scan

Fig. 6.5 CT scan test, Laboratory of Université de Tours, France

Both transversely and longitudinally cross section results will be presented. The specimen is a vertical cylinder one marked with a Blu Cyan dot in Figure 5.15a. It has been laid on the machine vertical support and grabbed to it with a non metallic glue 6.5b.

Because of low time available, the high test time and the heavy computational time for images post processing a proper optimization of image quality, unfortunately, do not have been performed. However the images quality is high enough to identify macro porosity location among the analysed specimen.

6.3 Thermal Properties Analysis

6.3.1 Thermal conductivity

The thermal conductivity test facility is a Hot Disk Thermal Constants Analyser located in the DISAT Laboratory of Politecnico di Torino.

When performing a measurement, a plane Hot Disk sensor is fitted between two pieces of the sample, each one with a plane surface facing the sensor (Figure 6.6). By running an electrical current, strong enough to increase the temperature of the sensor between a fraction of a degree up to several degrees, and at the same time recording the resistance (temperature) increase as a function of time. The Hot Disk sensor is used

both as a heat source and as a dynamic temperature sensor. The all structure in merged in a thermostatic 23° C pool and after thermal equilibrium the test is started.

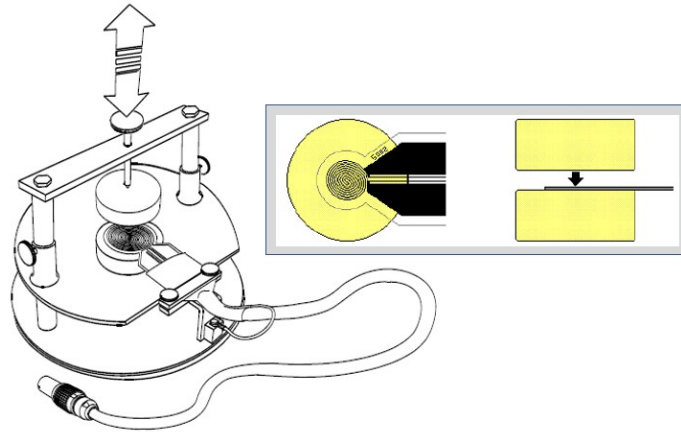


Fig. 6.6 Hot Disk machine and sensor

The Hot Disk sensors is a TPS¹ 2500 with Kapton insulation. The TPS 2500 system is based on a specially designed Wheatstone bridge with the Hot Disk sensor in one of the arms. A DC power supply unit generates a constant voltage across the bridge. Before the measurement, the bridge is automatically balanced and as the resistance of the sensor increases the bridge becomes increasingly un-balanced. A digital voltmeter equipped with a scanner or multiplexing card records the un-balance voltage. From these recorded voltages it is possible to determine the temperature increase of the sensor and consequently the thermal transport properties of the material under test.

Hot Disk TPS 7 software has been employed for experimental data post processing. The specimen is a cylinder according with normative UNI 22007-2 which specify that the thickness of a sample should preferably not be less than the radius of the hot disk sensor: 5 mm height 1 inch diameter. It has been cut from the 1 inch diameter vertical and horizontal printed specimens in the Job 1 (violet dots, Figure 5.15a). The simple preparation has only one peculiarity: the two planes with respect to which, in the nominal direction the thermal conductivity is calculated, have to be planar otherwise the sensor is not able to touch the surface in the correct way. In order to achieve this result a surface polishing has been performed.

The basic assumption in the calculations is a relation between diffusivity, measurement time and radius of the sensor. The sampling rate of the Hot Disk TPS2500 is such that the minimum experimental time has been set to 1 second. However, in order to get good conductivity and diffusivity values for high conducting materials, the measuring time should not be less than 5 seconds using the isotropic method.

The solution of the thermal conductivity equation is based on the assumption that the sensor is located in an infinite material, which means that the total time of the transient recording is limited by the presence of the outside boundaries or the limited size of the sample. In other words, the “thermal wave” or “thermal penetration depth” generated in

¹Transient Plane Source

an experiment must not reach the outside boundaries of the sample pieces during the transient recording. An estimation of how far this thermal wave has proceeded in the sample during a recording is the so-called probing depth, defined as:

$$\Delta_p = 2\sqrt{k\tau} \quad (6.1)$$

Where K is the thermal diffusivity and t is the measuring time of the experiment and the constant 2 has been determined so that the influence of external sample boundaries on the temperature of the sensor cannot be detected when the probing depth is limited to within the sample boundaries. A consequence of this equation is that the distance from any point of the sensor to any point on the surface of the two sample pieces must exceed if the total measuring time is.

The relation between the probing depth and the total measuring time of the experiment indicates that it is easier to make measurements on larger samples. In order to determine both the thermal conductivity and thermal diffusivity with good accuracy, the thickness of a flat sample should not be less than the radius of the hot disk sensor. It is important to realise that the shortest distance from the sensor to the outside sample surface defines the available probing depth. Examples are presented in Figure 6.7 regarding two different scenarios.

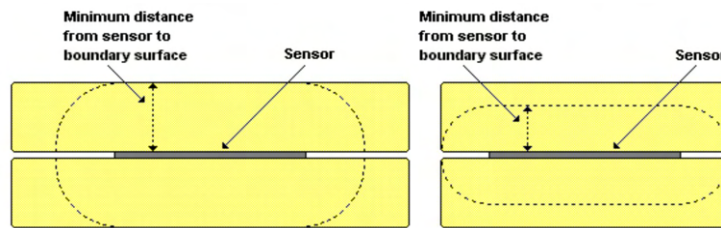


Fig. 6.7 Hot Disk - Minimum distance from sensor to boundary surface

Theoretically, it has been shown that an optimal measurement time of between one third and one whole characteristic time gives best stability in both thermal conductivity and thermal diffusivity results. The aim is to acquire a suitable total temperature increase, typically 2-5 K when using a TPS 2500 S.

The experiment gives back 4 different chart. All of them are important and have to be well interpret in order to have a physically significant result:

- **Temperature drift:** The temperature stability is normally recorded for 40 s immediately before the transient measurement is performed. The temperature drift recorded is automatically adjusted by the software with a subtraction post procedure. If the drift is very small the software automatically do not perform the post processing procedure. The lower the drift is the better the measures are;

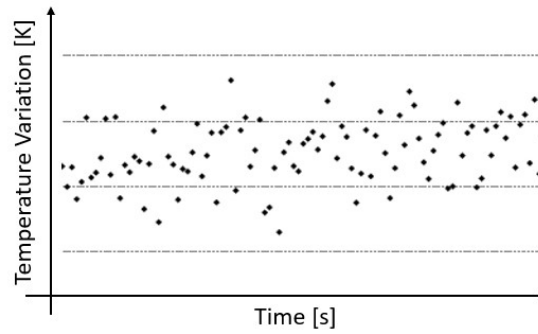


Fig. 6.8 Hot Disk - Temperature drift example

- **Transient measure:** The transient curve must show a continuous temperature increase, and should be free of sudden jumps or discontinuities. The curve depends on the power choice by the operator in order to achieve the 2-5 degrees increment;

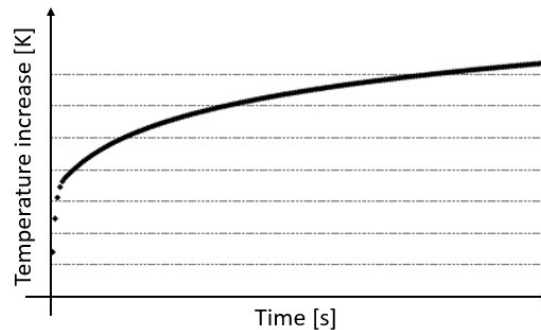


Fig. 6.9 Hot Disk - Transient measure example

- **Calculated fitting curve:** It is a temperature vs. $F(\tau)$ graph showing the line fitting. From this curve, via an automatic software post processing (Appendix D), the thermal conductivity is calculated. This graph should show a straight line if the calculation is good;

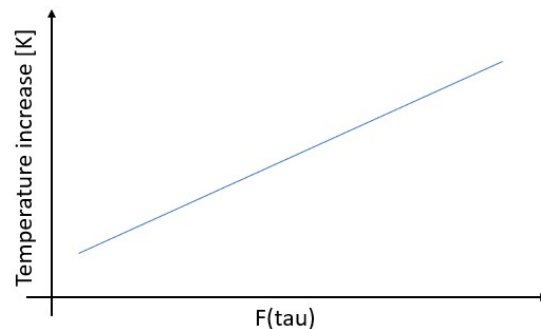


Fig. 6.10 Hot Disk - Calculated fitting curve example

- **Residual:** The chart shows the residual between calculated and measured data. A successful measurement and calculation will yield a random scatter. The residual graph presents the difference between the measurement data and the fitted data. In the ideal case the residual plot should be a random scatter around a horizontal line.

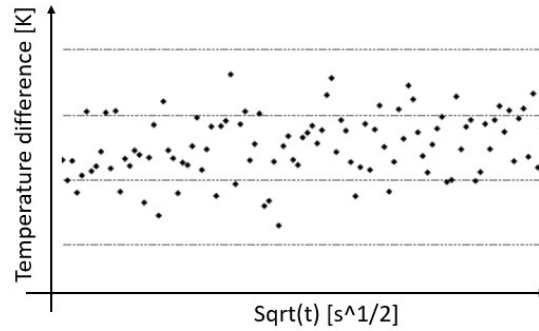


Fig. 6.11 Hot Disk - Residual example

The thermal conductivity is calculated by the program following the steps presented in Appendix D. Briefly, the thermal conductivity is given by the slope of the line in the graph presented in Figure 6.10.

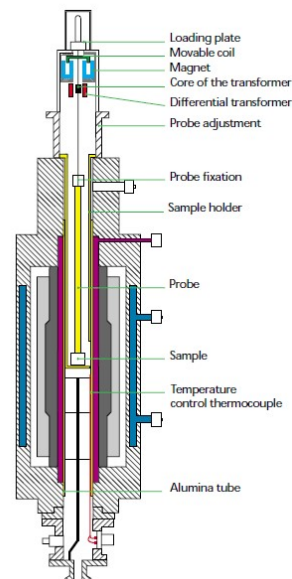
Because the thermal conductivity is not highly depend from the building direction of the specimens the isotropic method has been used for this experiment. However evidence from comparing Z thermal conductivity and the XY one has proved that the assumption of testing both Z and XY thermal conductivity by assuming a isotopic behavior was correct.

6.3.2 Linear Thermal Expansion Coefficient

Linear Thermal Expansion Coefficient has been calculated with a SETSYS Evolution Thermo Mechanical Analysis (TMA) machine (Figure 6.12a) at DISAT Laboratory of Politecnico di Torno, Italy.



(a) SETSYS Evolution TMA machine



(b) SETSYS Evolution TMA schematic working system

Fig. 6.12 CT scan test, Laboratory of Université de Tours, France

Thermomechanic analysis is a technique that measures the deformation of a sample free from stress when subjected to a temperature program in a controlled atmosphere. The displacement transducer on the SETSYS Evolution TMA model (Figure 6.12b) has an accuracy variations in movement as small as 0.01 micron which can be detected with such a transducer. The temperature is measured by a thermocouple near the sample.

A Specific SETSYS software has been used in order to provide accurate measurement of the coefficient of expansion in the materials. A calibration curve, in the form of a polynomial, introduced into the computer, guarantees the accuracy of the coefficient of expansion measured. With such software the SETSYS Evolution TMA can be used as a dilatometer.

Before testing the target specimen a Blank test has been done without any specimens in the machine. This procedure gives the base dilatation the instrument displacement kinemantism: the curve will be substrate form the one obtained from the Cu174PH simple.

A cuboid 5mm x 5mm section size and 10.35 mm height has been cut from a random not-tested² traction specimen and polished in order to obtain a plenary between the two planes respect to the X direction in Figure 6.13. The linear thermal expansion coefficient of the material has been tested respect to the same direction of all traction and Low Cycle Fatigue tests, thus respect to the 10.35 mm height (Figure 6.13).

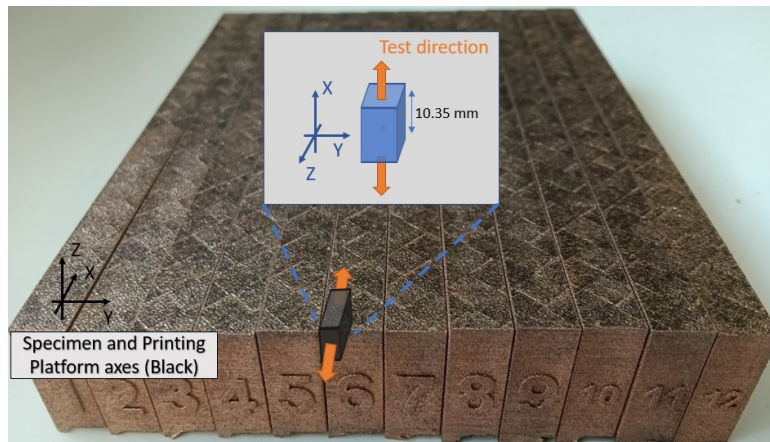


Fig. 6.13 TMA specimen orientation respect

This choice has been done since the most important dilatation/compression thermal behavior of a common LRE thrust chamber is the one respect to the circumferential direction, which is responsible for the fracture of the cooling channels (Figure 6.1).

²2 traction specimens out of 12 do not have been tested because of CNC machine errors

6.3.3 Thermal Capacity

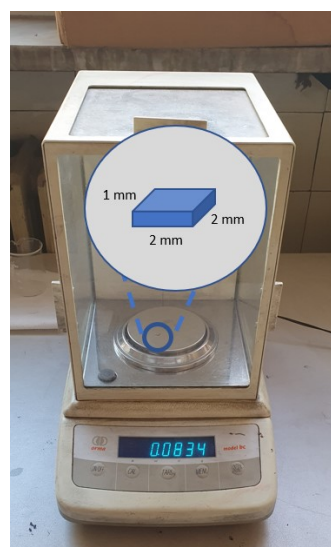
The apparatus used in this study for differential scanning calorimetry (DSC) is a Perkin-Elmer Pyris 1 Heat-Flux differential scanning calorimeter (Figure 6.14a).

Differential Scanning Calorimetry, or DSC, is a thermal analysis technique that looks at how a material's heat capacity (C_p) is changed by temperature. A sample of known mass is heated or cooled and the changes in its heat capacity are tracked as changes in the heat flow.

A 0.083 [g] specimen from a foil sheet 2 [mm] x 2 [mm] plane section and about 1 [mm] of high has been used. The DSC simple has the same cutting and orientation procedure of the TMA specimen. After weighting procedure (Figure 6.14b) the simple is pressed inside the specific aluminium melting pot (Figure 6.14c) and entered in the machine (Figure 6.14d). The same test process has been done for a pure copper and pure steel specimens in order to have a benchmark. Also for this experiment a Blank curve has been performed for subtract the aluminium melting pot thermal capacity from the final result. This is a standard operation build in the test process: every time a new test is performed both, the empty aluminium melting pot and the aluminium melting pot with in the material under study are simultaneously tested.



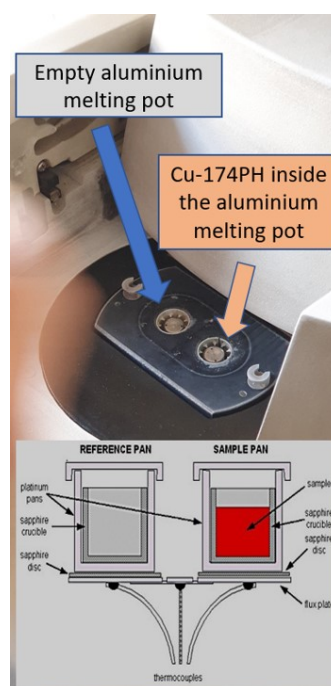
(a) Perkin-Elmer Pyris 1 Heat-Flux differential scanning calorimeter



(b) Weighting procedure



(c) Weighting procedure



(d)

Fig. 6.14 DSC set up

In order to have reference value both, pure copper and pure iron have been tested with the same set up used for the Cu-174PH material. In particular a heating step ramping of 10° [C/s] has been employed and a 1 [min] waiting time for each steps is performed (Figure 6.15). The machine has been set up with a waiting time of 1 [min] at an isothermal temperature of -50° [C] before starting the test.

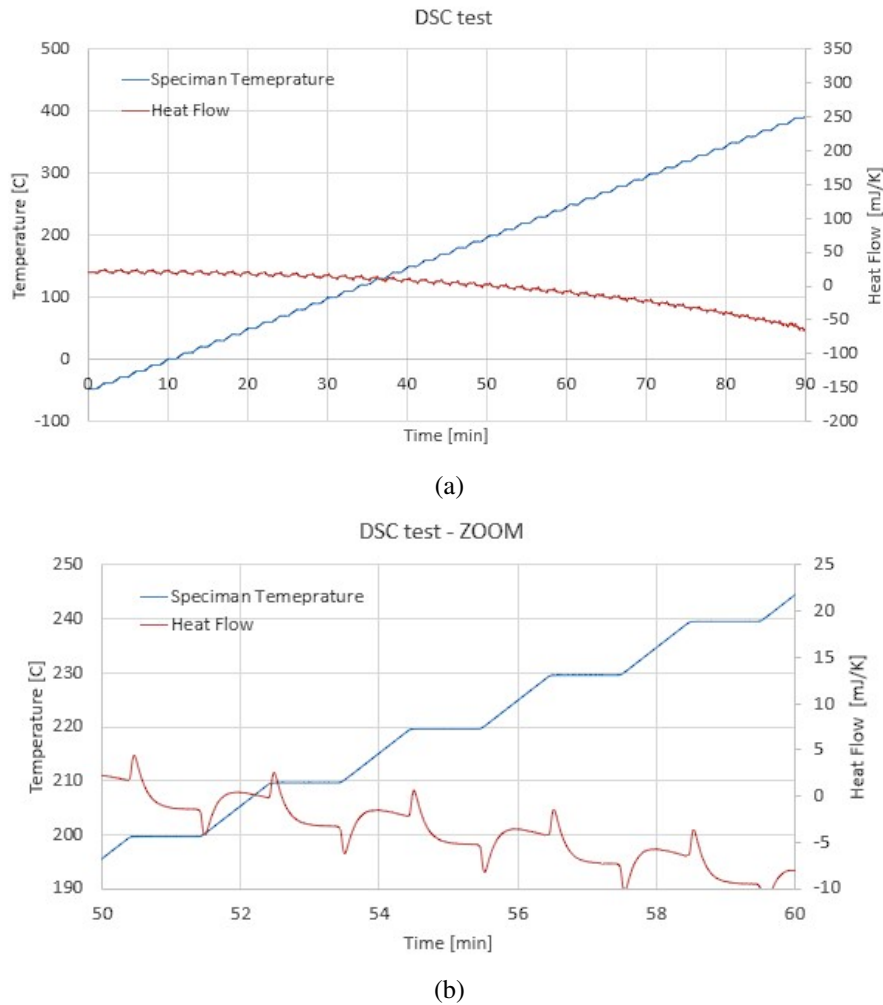


Fig. 6.15 DSC test

6.4 Mechanical Analysis

6.4.1 Hardness and Micro Hardness

Known as an extrinsic material property, hardness can be defined as the resistance presented by a material respect to plastic deformation due to the penetration of an indenter tool [90, 91].

Hardness and micro-hardness have been evaluated at the DIMEAS Laboratory of Politecnico di Torino. The used durometer is an INOVATEST NEMESIS 9000 (Figure 6.16a) integrated with the IMPRESSIONS™ tester control and workflow software. The used micro-durometer is an INNOVATEST NOVA 130 (Figure 6.16b) also integrated with the IMPRESSIONS™ tester control and workflow software.

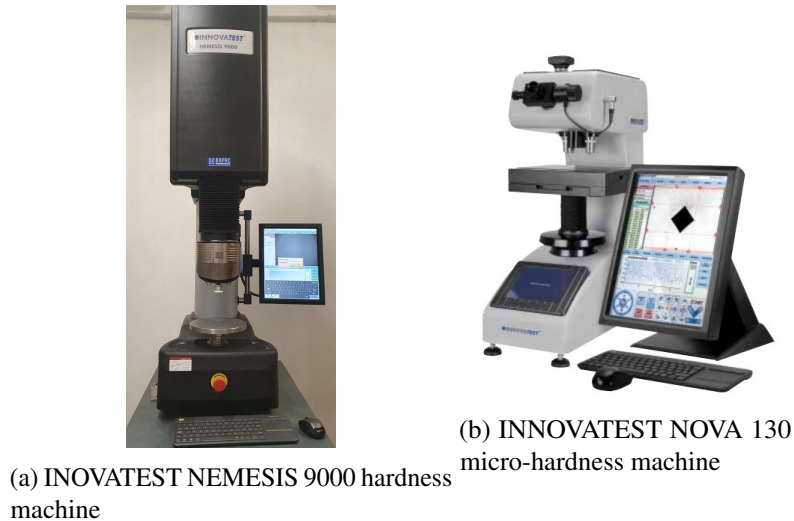


Fig. 6.16 Hardness testing machines, DIMEAS Laboratory at Politecnico di Torino

Vickers test was chosen. Vickers hardness is related to the measure of the diagonal of the square plastic indentation obtained by a diamond pyramid indenter pressed against the investigated surface with a given load L , after elastic recovery. A preliminary study has been performed to choose a correct load able to perform the lower possible standard deviation linked to the largest available plastic deformation.

Data acquisition is obtained according to Standard EN ISO 6507. Two different surfaces of every sample were tested and 10 repetition for each measuring configuration were acquired at room temperature; the average of the 10 measures was assumed as the hardness value. Indent sizes were measured using the machine implemented software (impressions©) with a manual selection of 4 vertices. Two random 20x20x20 mm cube specimens have been tested (yellow dots in Figure 5.15a).

Additive Manufacturing processes provide different mechanical properties between the printing base plane (xy plane) and the building job direction (z). Then, hardness and micro-hardness were evaluated in both planes: horizontal slices (xy-plane) and vertical cross-sections (xz or yz plane). Difference between bottom, centre and top location of the plane analysed respect to X, Y or Z axe has not been considered: for XY plane only the top one, far away from the support that links the specimens to the platform, has been tested. For YZ/XZ plane a random one has been selected.

The Standard applied to perform hardness was designed for standard fabrication processes. Currently no Standards describe procedures dedicated to Additive Manufactured surface hardness measurements. J. Slotwinski [92] prove that standard procedures to measure the material properties of a bulk materials can be applied also to additive manufacturing materials. Keist and Palmer [93] demonstrated that Vickers test hardness procedure can be applied for Additive Manufacturing SLM processed materials as Ti-6Al-4V alloys but it results in a large result scattering due to different phase orientation because of the AM manufacturing process.

For reliable hardness measures, the surface finish state is critical. A flat surface is indicated and for accurate penetration the surface roughness must be minimized

according to BS EN ISO 6507. The applicability of ISO 6507 for testing AM materials is linked to the requirements ‘to meet surface finish specification’. Surfaces obtained by means of Additive Manufacturing present a rough surface, and surface roughness changes according to the investigated (side or front with respect to growth direction) surface. In addition to this, the contour layer are not representative of material mechanical properties because of different process parameters. This remarkable difference could cause a high porosity that makes indentation test difficult and measure unreliable. Polishing surfaces allows avoiding this influence from the hardness measurement.

Once fabricated, each coupon was removed from build plate. The sample preparation was performed by means of machining removal, for XY plane tests, of the down-skin and, for the XZ/YZ plane, of the Contour Layer skin (Figure 6.17). Mechanical polishing with a sander machine (Grit size 320, 800) and water coolant.

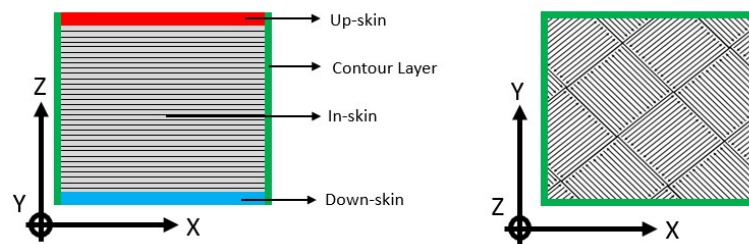
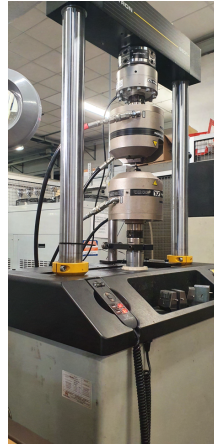


Fig. 6.17 Common cuboid specimen skin schematic representation

6.4.2 Traction

INSTRON 8801 hydraulic 100 kN machine located at DIMEAS Laboratory of Politecnico di Torino has performed all room temperate tensile test. The machine is equipped with a bi-axial INSTRON extensometer: this tool will provide the Poisson ration. A general test velocity of 2mm/min is used. Room temperature test have been performed with a vertically 25mm gauge length, and a traversal 6 mm gauge length (specimen width). High temperature test have been performed with a 25mm vertically gauge length.



(a)



(b)



(c) Hydraulic power supply (right side)

Fig. 6.18 INSTRON 8801 machine, DIMEAS Laboratory, Politecnico di Torino

The specimen geometry was imposed by the unique particular grips for the high temperate machine. Sample geometry is presented in Figure 6.19, according with ISO 6892, ASTM E8 and ASTM E21. The starting geometry is a parallelepiped with a of 18mm + 5mm of direct full support. The specimen thickness have been selected after an optimization study in order to have a good compromise between CNC machining available grips and a maximum filling on the Job 1 platform.

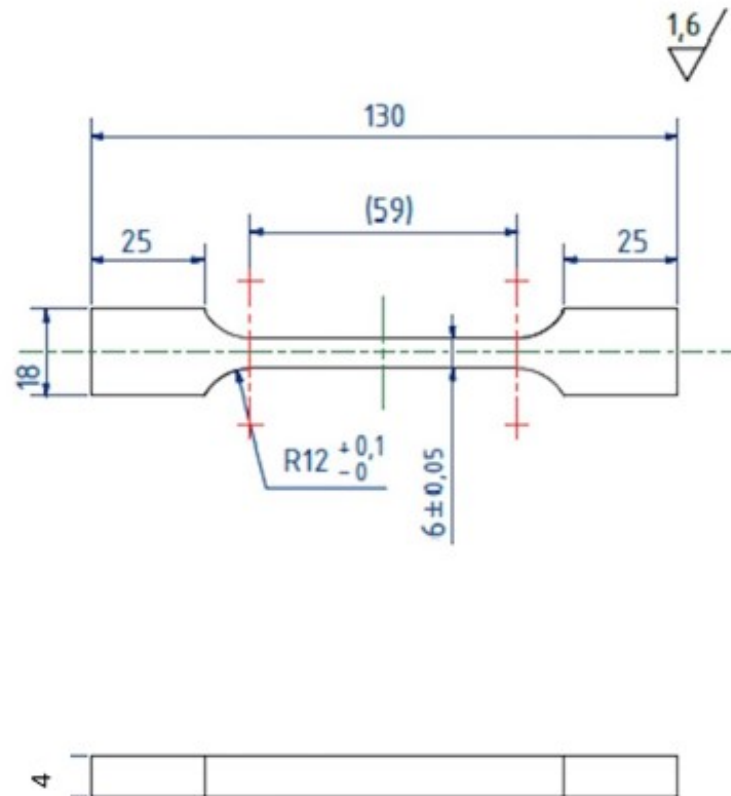
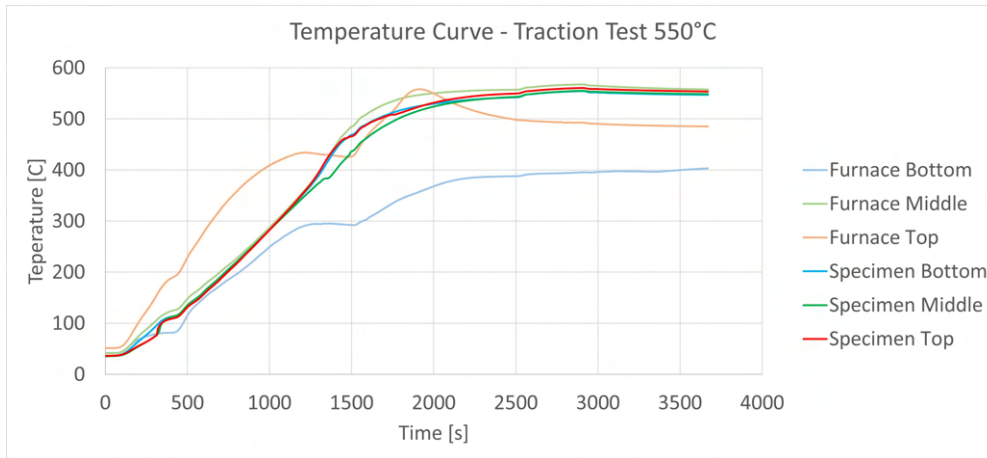
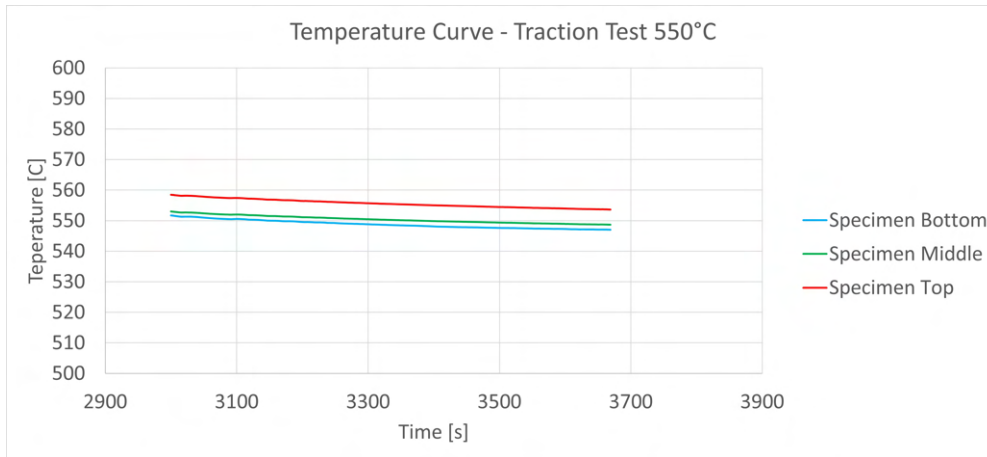


Fig. 6.19 Room and high temperature tensile test specimens geometry

The Zwick Roell Z050 electromechanical 50 kN machine, located at the J-Tech Laboratory of Politecnico di Torino is a high temperature traction tensile machine. It has been employed for the high temperature traction test campaign. The machine has a 3-independent-areas insulated induction furnace controlled by a logarithmic ramping adjustment PID control systems (Figure 6.20a). The PID acquire thermal data from three 1cm equi-spaced thermocouples which make contact with the specimen. This system allows to have a perfect temperature balance along the sample (ISO 6892 requires a maximum difference of ± 5 degree between 2 thermocouples, Figure 6.20b). The machine use a no-contact laser extensometer.



(a) 550°C traction test specimen temperature profile: ramping, waiting and test time



(b) 550°C traction test specimen temperature during the waiting time

Fig. 6.20 550°C traction test specimen temperature profile

The test velocity has been set at 2mm/min and a 20 min waiting time before starting the test is required in order to have a good temperature homogenisation. Note that the 20 min waiting time starts after the time that the machine require in order to achieve the target temperate. During the heating time the machine has been set with a load control: the target was 0 N. This methodology ensures the thermal dilatation compensation. If none of this control typology is applied a buckling compression instability can occur, especially at the 650 high temperature. Finally, just before the tensile test start, a pre-load of 5 MPa have been applied in order to compensate the possibility of a mechanical grip instability during the loading.



(a) Compression grips, DIMEAS Laboratory, Politecnico di Torino



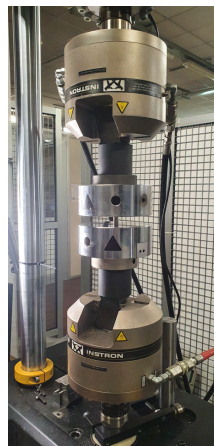
(b) Zwick Roell Z050 machine, J-Tech Laboratory, Politecnico di Torino

Fig. 6.21 High temperature tensile test facilities

6.4.3 Compression

Compression test have been performed according to the ASTM E209. A cylindrical specimen is used: 20 mm height with a 10 mm diameter. The specimens have been removed from the platform CNC machined in order to archive plenary between plane. A hand lateral surface polishing have been done.

Ambient temperature test have been completed with the same INSTRON machine used for room temperature traction tensile test, with different grips. Two parallel massive cylindrical platform have been used.



(a) Compression grips, DIMEAS Laboratory, Politecnico di Torino



(b) INSTRON 8872 machine, CERMEL Laboratory, Université de Tours

Fig. 6.22 Compression test facilities

The high temperature compression test have been performed with a electromechanical INSTRON 8873 at CERMEL laboratory of Université de Tours, France. However, because of the limited 25kN loading cell, only the linear elastic compressive module has been successfully evaluated. The oven is an inductive retroactive controlled furnace.

A manual remote controller is used to provide the target temperature. After the target temperature is reached, as done for all mechanical test already described, a 20 min waiting time with the specimen inside the furnace is applied before starting the test. The test velocity is the same of the tensile test (2mm/min).

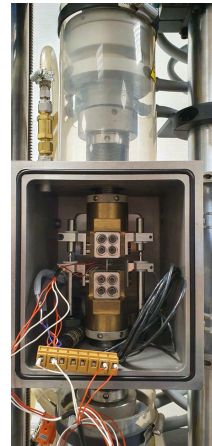
6.4.4 Low Cycle Fatigue

INSTRON Electro-Thermal Mechanical Testing II

The high room and high temperature fatigue tests have been performed via the innovative (and rare, just 3 machie in Europe) INSTRON Electro-Thermal Mechanical Testing II (ETMT II) located in the CEROC Laboratory of Université de Tours, France.



(a)



(b) Zoom inside the void chamber of the ETMT II

Fig. 6.23 INSTRON Electro-Thermal Mechanical Testing II of CEROC Laboratory, Université de Tours, France

The ETMT II is a compact table-top testing system that is developed to perform accelerating high-temperature research. The machine exploits the Joule effect in order to achieve the target temperature. It is a direct resistance heating machine. Rather than common indirectly heating systems (as the oven induction systems used for the traction tensile tests and the compression tests), this particular facility use the miniaturised section of the specimen in order to achieve a high temperature in few seconds. The system is capable of achieving fatigue loading rates up to 1000 N/s with heating and cooling rates of 200°C/s and 100°C/s, respectively. The system is designed for full reverse stress loading to 5000 N. It is capable of delivering specimen temperatures of up to 1500°C.

The machine logic control is divided in two main channels: axe 1 (8800:1) with is the mechanical control (it is responsible for the displacement and the load control) and the axe 2 (8800:2) which is responsible for the current control.

The upper bar is responsible for the motion transmission via a ball screw system and an eclectic motor equipped with an encored in order to monitoring the upper vertical

bar³ displacement. However this control, especially for Low Cycle Fatigue, can not be used because of the multiple different stiffness elements between the control system and the specimen. The lower vertical bar is stationary and it is responsible for the loading control via a 5 kN load cell. The machine can be equipped with one or two LVDT⁴ transducers: one is responsible for the displacement control and the other one, located on the other side of the grips, can be used to evaluate the possible occurrence of bending movement along the specimen during the test or, if set up on reverse-mode, it allows to quantify the lower rob deformation. Both LVDT are linked with a screw system to the specimens grips.

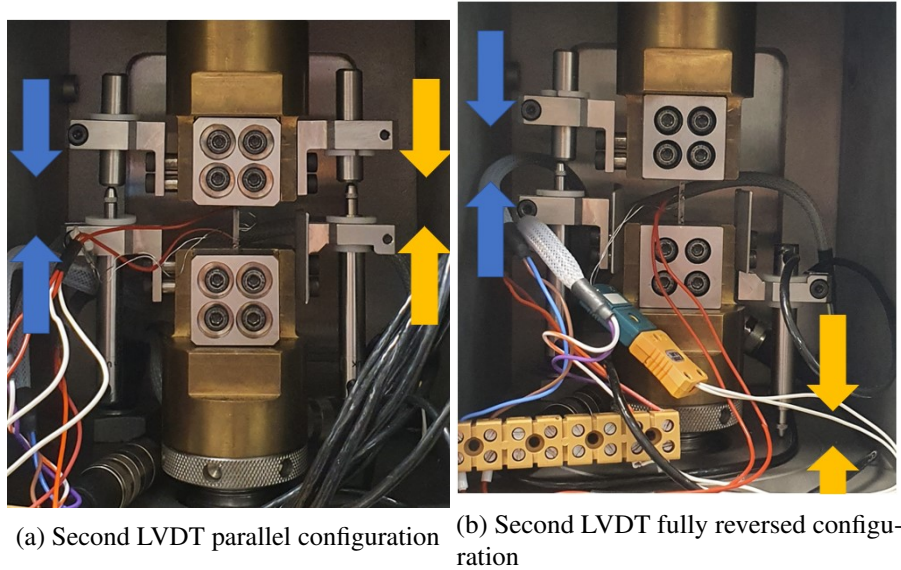


Fig. 6.24 Second LVDT possible configurations

Instron ETMT testing system is supplied with a FastTrack 8800MT digital controller (Figure 6.25 a)), which is capable of running static and high-frequency dynamic tests. The 8800MT controller is integrated into the ETMT system features SCM modules for control of the axial loading axis and the DC direct resistance heating system (Figure 6.25 b)), and provides support to Instron software such as Fast Truck Console, MAX Wave and ETMT II (Figure 6.25 c)). The system offers a high integrity enclosure which allows vacuum evacuation (via a vacuum pump, Figure 6.25 d)) with subsequent gas back-filling (Figure 6.25 e)), opening opportunities to testing under vacuum or back-filled gas purge with facility for inert gas supply built in. The machine can be manually remote controlled (Figure 6.25 f)) or actuated by a custom program that the operator can set up with the specific software.

³the motor moves the ball screw system which is linked to a vertical bar. The vertical bar is that attached to the machine cooled grips which also receive the electricity power. Finally the machine grips are linked to the specimen grips.

⁴Linear Variable Displacement Transducer

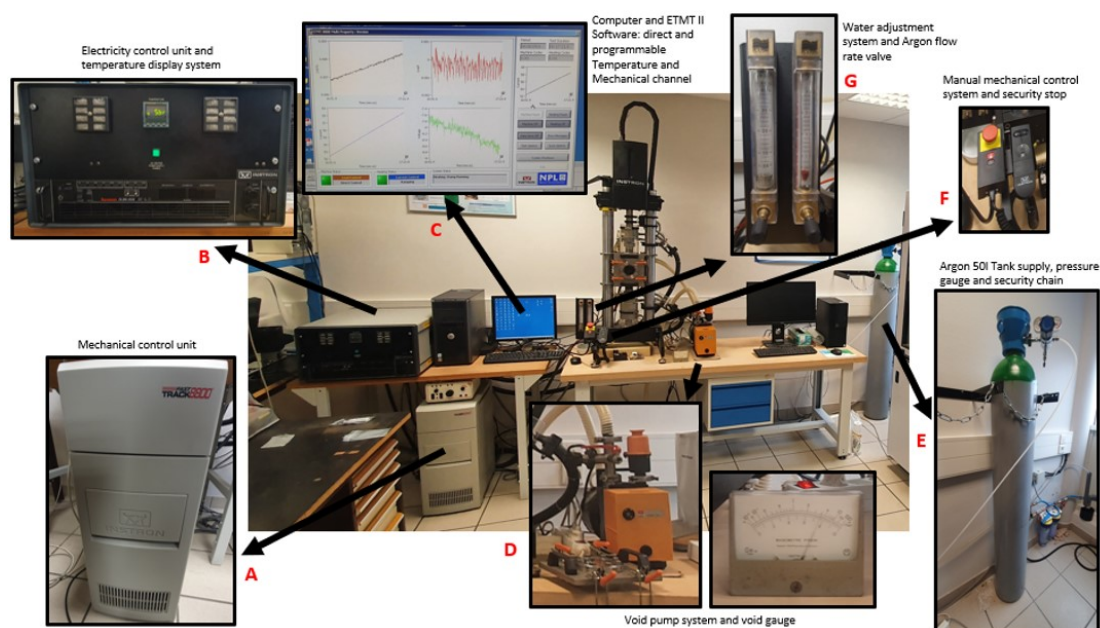


Fig. 6.25 ETMT II system components

The machine is water cooled. The cooling system allows high temperature test without grips dilatation/deformation. The cooling channels are machined inside the machine's grips but do not enter inside the specimen's grips (Figure 6.26). The water and gas flow rate can be adjusted via a manual control system (Figure 6.25 g).

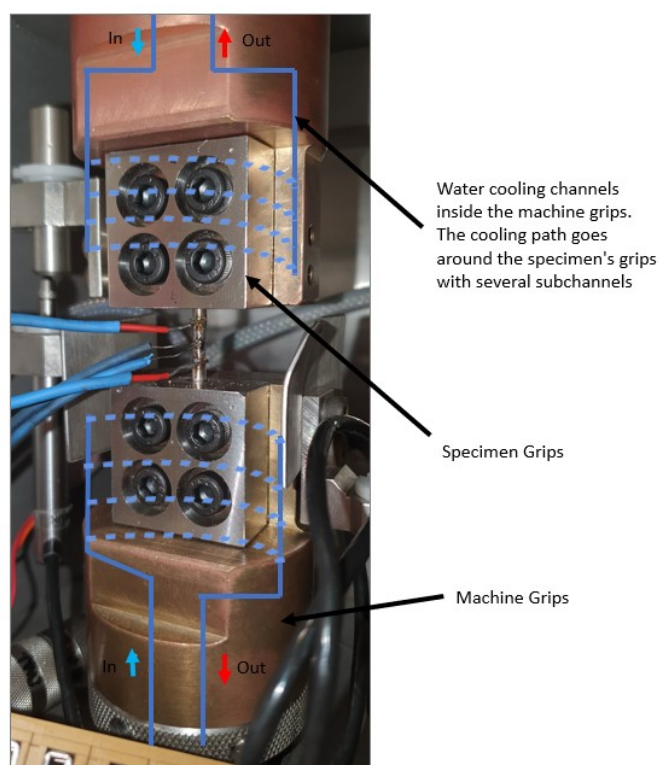


Fig. 6.26 ETMT II water cooling system

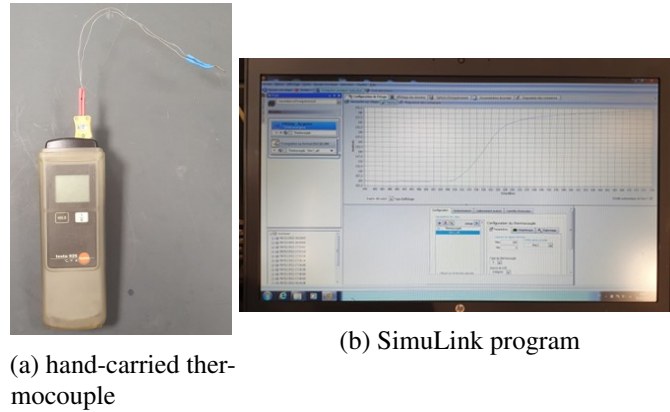


Fig. 6.27 Second thermocouple system facilities

The same machine set up has been employed for the creep realization and the ratcheting tests.

Specimens and Custom Grips

The specimens grips are a critical feature of the experimental set up. A minimum miss alignment between the axe screw thread of the upper and lower grips and the specimen is exposed to bending. In order to avoid this problem a new set of grips have been make from AAMS industry CNC machining manufacturing process with CAM⁵.

Grips are made of the available a Inox Z6CN18-09 steel. This particular selection have been done because of the needs of a high temperature resistant alloy. The two grips have a M6 screw thread and 4 holes each where the mounting screws pass through in order to fix the specimen's grips to the machine grips.

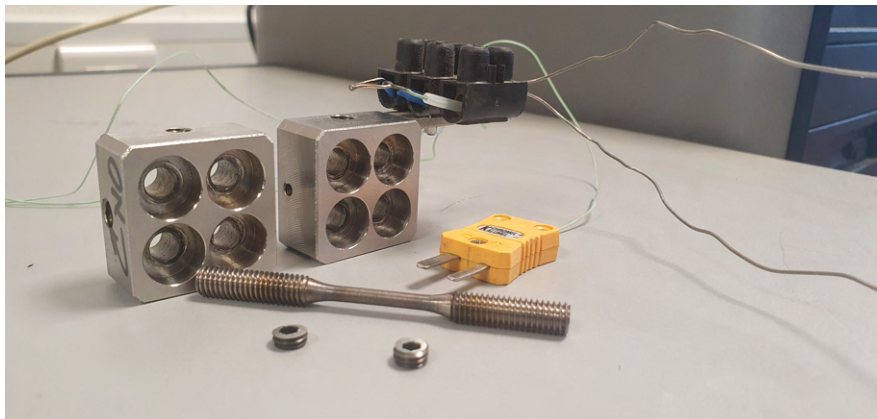


Fig. 6.28 LCF specimen's grips and custom hexagonal screws

Fist test suffer from a vertical very slight backlash therefore an improvement has been done in order to assure a perfect fixed specimen: two small M6 hexagonal screws have been made ad used for the purpose. With those additional elements the threading

⁵Computer-aided manufacturing

has been packed manually by screwing the hexagonal screws to the top and to the bottom of the specimen, after grips screwing (Figure 6.29).

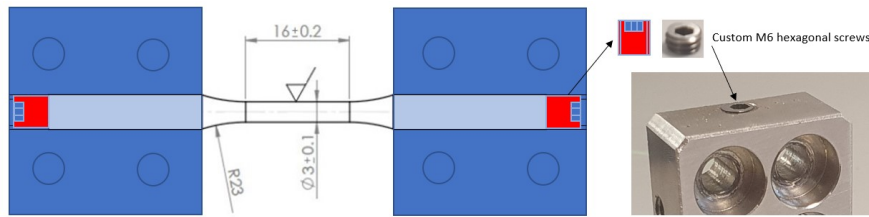


Fig. 6.29 Custom M6 hexagonal screws system

From Job 2 all raw 7 diameter mm x 90 height mm cylinders have been CNC machined by Sophia High tech s.r.l. and the final geometry is achieved (Figure 6.30). The specimen's shape has been selected according to the Low Cycle Fatigue ASTM E 606 and ISO 12106 Normatives, to the machine maximum 5kN loading cell and to the buckling resistant minimum section (Appendix A).

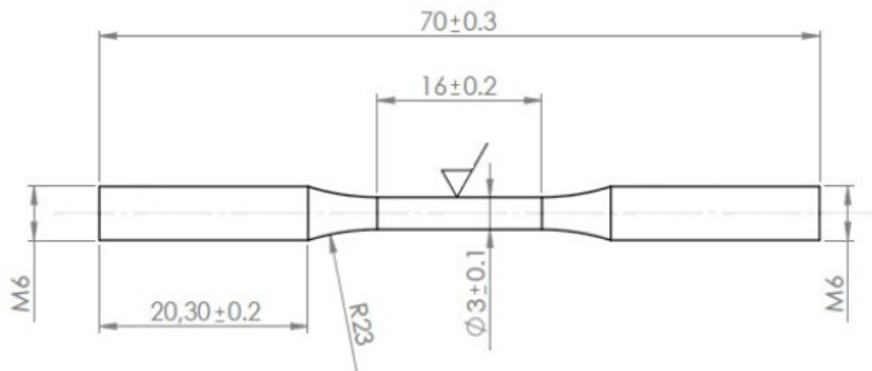


Fig. 6.30 LCF specimen

Because this material is a custom-mix-powder new alloy in this study a first time CNC machining processes has been made. The need for cost and time saving do not have allowed a machining process optimization. Therefore the Low Cycle Fatigue specimens do not have achieved the recommended, but not mandatory, $R_a = 0.2$ roughness surface finishing of the ASTM E 606 and ISO 12106 Normatives. In order to have such a polished surface a hand made process should have been done. Due to the aforementioned situation the specimen's surface roughness was measured with the Veeco Wyko NT1100 Optical Profiling System: the result is a $R_a = 2.45$ roughness. The 3D profile and optic high magnification is presented in Figure 6.31.

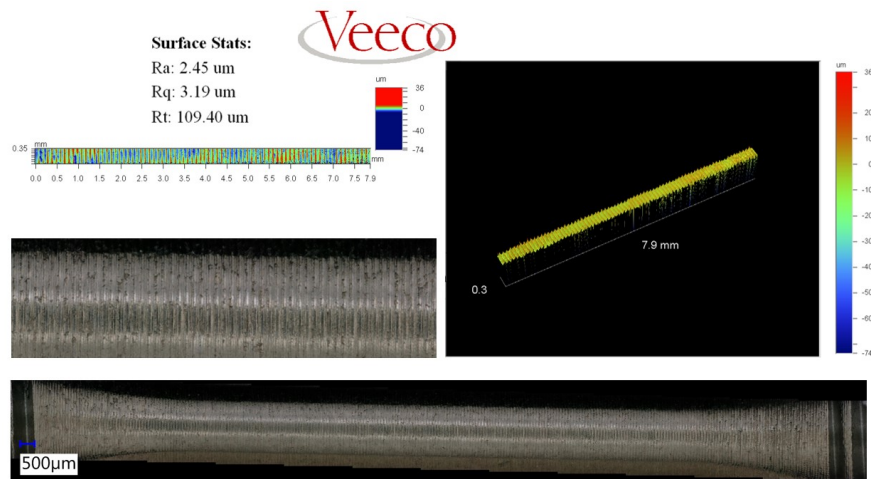


Fig. 6.31 LCF specimen's roughness: 3D profile reconstruction and optical magnification

By analyzing the optical magnification it is possible to see that there are also micro superficial crack. This phenomenon is probably due to the high temperature local gradient induced by the CNC lathe tool. Because the alloy is a AM bi-material matrix composite, probably, the surface porosity, the difference between the two material hardness and the slight difference between the material's thermal dilatation produce the presented micro crack. However, as will be presented in this study, the real LRE cooling channels roughness is higher than the LCF specimens one. Therefore a $R_a = 2.45$ roughness batterer represent the real surface initialization crack phenomenon.

Temperature Control System and Current Calibration

The ETMT II way to control the temperature is a PID controller. The SCM DC direct resistance heating system receives signal from a thermocouple directly welded on the specimen. The temperature is display on the SCM unit box and on the software. Unfortunately, due to technical problems, the PID did not work: only manual temperature control was working. Therefore a manual calibration has been performed: via the software a gradually increment of current is defined and the temperature on the SCM display is manually acquired in an Excel sheet. With this manual procedure it is possible to know the current needed to archive a target temperature.

A spot welding machine is used to fabricate the thermocouple (Figure 6.32). The thermocouple used is a type R with one pure platinum 0.35 mm wire and a platinum-13%rhodium 0.35 mm wire welded together. Then the thermocouple is welded to the specimen with the same machine. The machine was also able to acquire the potential difference across the specimen subjected the imposed DC current: for this reason two more wire are welded to the specimen. The result is presented in Figure 6.33. This method was not able to have good reputability and several specimens have been wasted⁶. Probably this is due to the high sensibility of the thermocouple welding process on

⁶NOTE: because of a microstructure change, especially at high temperature, every new calibration test have to be performed with a new specimen

the specimens or to the electronics of the SCM unit responsible for the electrical post processing of the R thermocouple's signal.



Fig. 6.32 Spot welding machine

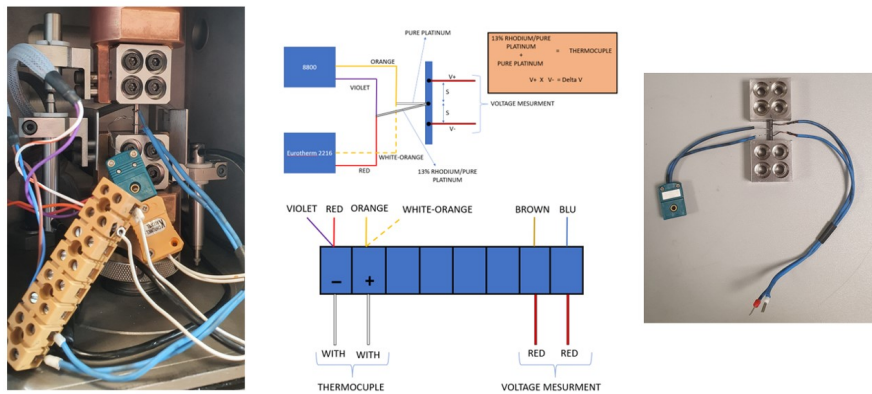


Fig. 6.33 First thermocouple system

In order to achieve the required repeatability of the current need to reach the target temperature a self made facility has been build. In particular, since it was decided that the welding process and the SCM unit were blamed for the lack of repetitiveness, both system have been replaced. The new system uses two different thermocouple in contact (and not welded) to the specimen: a support structure (Figure 6.34) was responsible for keeping in contact the thermocouples to the specimen. One temperature sensor was a K thermocouple wired to a signal post processing unit linked to an external computer with a simple SimuLink program (Fgiure 6.35b) which acquire the live signal from the post processing unit ad display the live temperature of the specimen (Fgiure 6.35c). The second system was a simple external hand-carried thermocouple (Fgiure 6.35a): is has been used just for a double check.

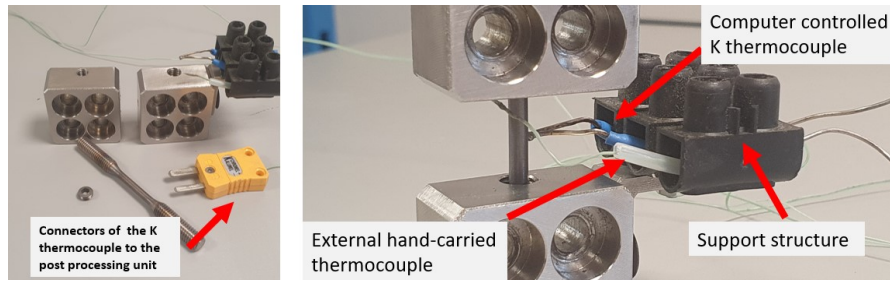


Fig. 6.34 Second thermocouple system (the one from which the result are used)

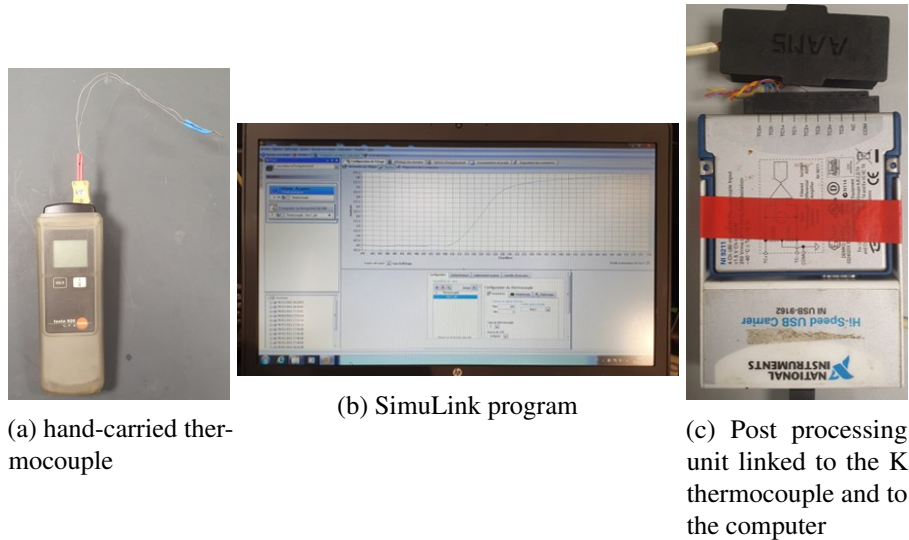
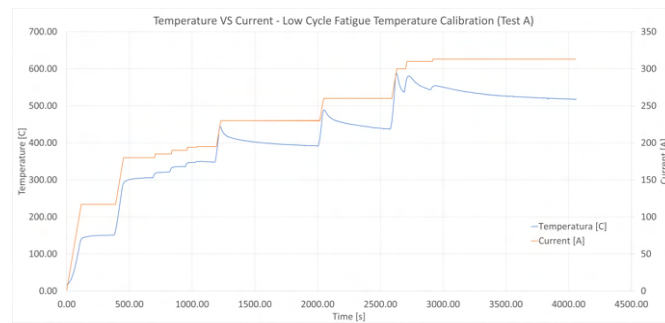
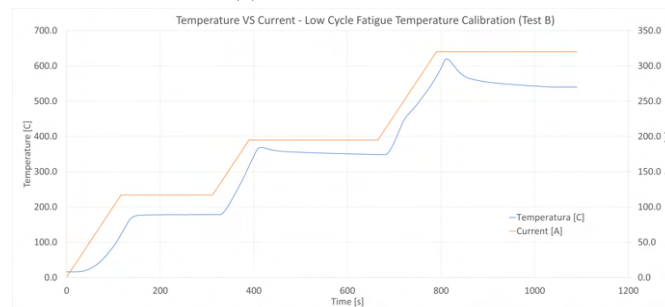


Fig. 6.35 Second thermocouple system facilities

By manually ramping the current and simultaneously acquiring the achieved temperature from the PC programs the current VS temperature calibration have been successfully accomplished. The process was followed five times with a very high repeatability. Two representative Temperature/Current VS Time calibration test are presented in Figure 6.36. In order to avoid thermal inertial effect due to the mass of the spaceman ad to the low temperature water cooled grips, a low step ramp current (1 A/s) is used and a reasonable waiting time is employed.



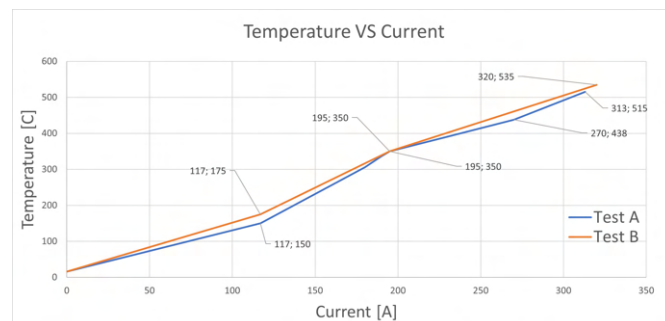
(a) Calibration test A



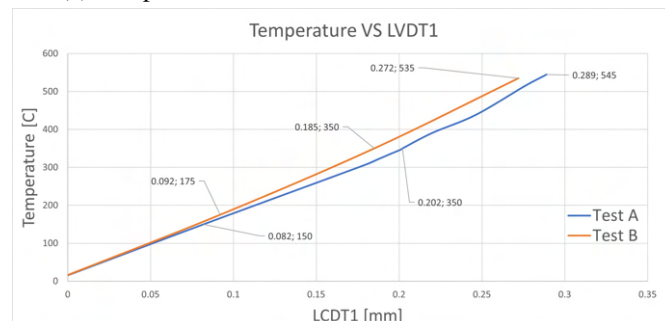
(b) Calibration test B

Fig. 6.36 Temperature VS Current Calibration

The target temperatures were 150°C, 350°C and 550°C: a summary is presented in Figure 6.37a. Figure 6.37b shows the thermal dilatation acquired by the LVDT1 during the calibration procedure.



(a) Temperature VS Current: calibration test A and B



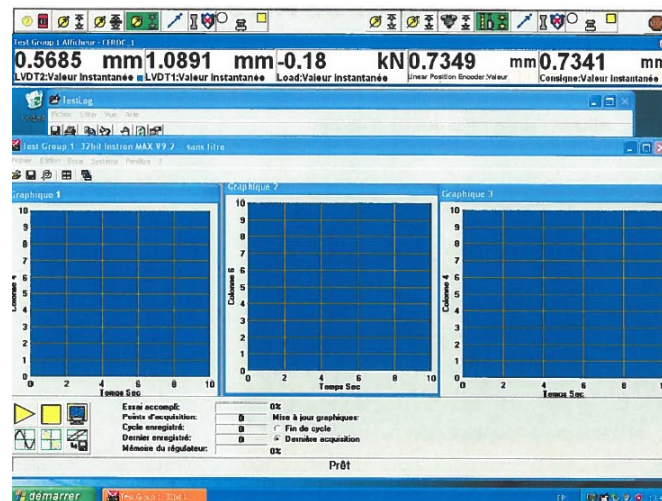
(b) Temperature VS Displacement: calibration test A and B

Fig. 6.37 Temperature VS Current Calibration

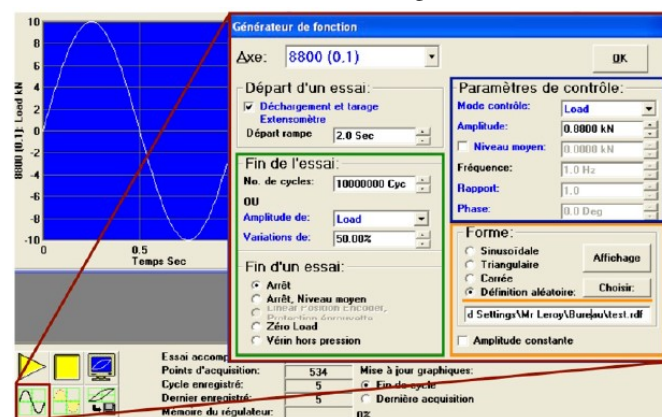
Test procedure

The test procedure can be summarised in the following steps:

1. Specimen grips assembly;
2. Secure the specimen with the hexagonal screws;
3. Mount the specimen respect to the bottom machine grips;
4. Manual displacement of the upper machine bar in order to fix the upper specimen's grips to the upper machine grips;
5. Lock by hand (8 Nm) the 8 screws that fix the specimen's grips to the machine's grips;
6. Activate the 0 N loading control and wait for the thermal equilibrium of the machine+specimen system (the machine grips are water cooled and typically at 16°C respect to the 24°C room temperature of the specimen's one);
7. Close the machine vacuum box door and starting the void process;
8. When the void is archived open the Argon gas supply;
9. When the machine chamber reach the target 1 atmosphere+epsilon the security venting valve process start: It is the time to stop the argon supply, the chamber now full of argon gas;
10. Always with the 0 N loading control on the current is set manually in order to achieve the target temperature (after calibration the current need to have a specific temperature is known);
11. After 20 min waiting time at the target current the LVDT is reset to 0 mm;
12. The test can be now started and the software takes the control of the system. All test parameters can be set up by the dialog box of Fast Track and MAW software (Figure 6.38).



(a) FastTrack dialog box



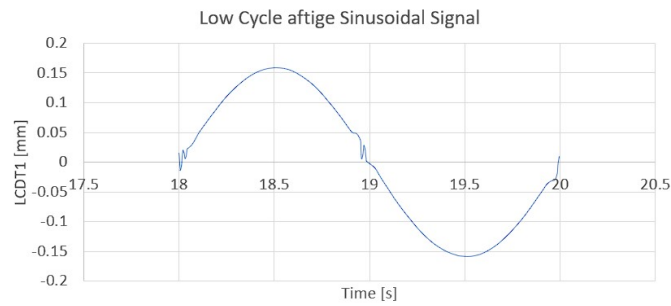
(b) MAX dialog box

Fig. 6.38 Software used for the set up of all LCF tests

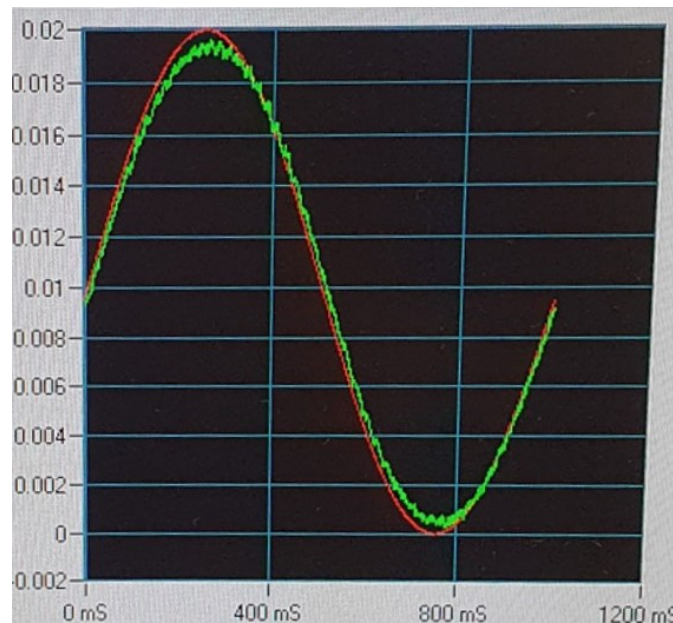
Test Parameters

The Low Cycle Fatigue Test have been performed with a 0.5 Hz frequency. The displacement control⁷ was applied with a sinusoidal curve (Figure 6.39a). The displacement controls work via a PID system control: a target signal is generate by the machine ad the PID is responsible for make a curve that is as overlapping as possible the virtual one (Figure 6.39b).

⁷Remember that the control system is a displacement one, therefore a post processing in required to have the common sigma-epsilon LCF hysterical curves.



(a) 0.5 Hz sinusoidal LCF curve



(b) Red curve: virtual target signal, Green curve: real LVDT acquired signal

Fig. 6.39 Sinusoidal LCF curve

The LVDT PID controller has been calibrated via the INSTRON calibration dialog box. The parameters used for all LCF test are presented in Table 6.2.

	PID
Proportional	22 dB
Integral	1 m/s
Derivative	0 m/s

Table 6.2 PID controller parameters

6.4.5 Machine troubleshooting

Figure 6.39a shows a displacement vs time LVDT1 signal from a on going LCF. It is possible to see that wen the displacement cross the 0 line and It revers its motion an slight instability is recorded. This is due to the fact that the ETMT II INSTRON machine has been fixed from a huge damage that was present and that had never been fixed.

When this activity started the machine had a high number of problems:

- No argon links between the machine and the tank;
- Few gas loss because of different o-ring problems;
- Wrong arrangement of all pins for the LVDT1 and LVDT2 connections: a manual tin soldering process have been done;
- Loading cell not calibrated;
- LVDT1 and LVDT2 not calibrated: manual mV/V calibration process have been done fort both transducers;
- Water cooling system blocked;
- No link for vacuum pump;
- No M6 grips;
- Wrong thermocouple arrangement;

All this problem have been fixed without an official INSTRON technician. The planned stay at CEROC was 3 weeks and because of all these problems, and an additional one that will be shorty presented, it was extended to almost 2 months.

In addition to this starting problems, the LCF test were impossible to start because the LVDT1 signal (Green in Figure 6.40) was not able to follow the virtual target one. At the beginning the problem was blamed to the PID control system but after several days it has been found, by analysing the sinusoidal curve, that the platò of both the displacement signal and the load signal was impossible to be caused by control bug. The only possible way was a mechanical problem.

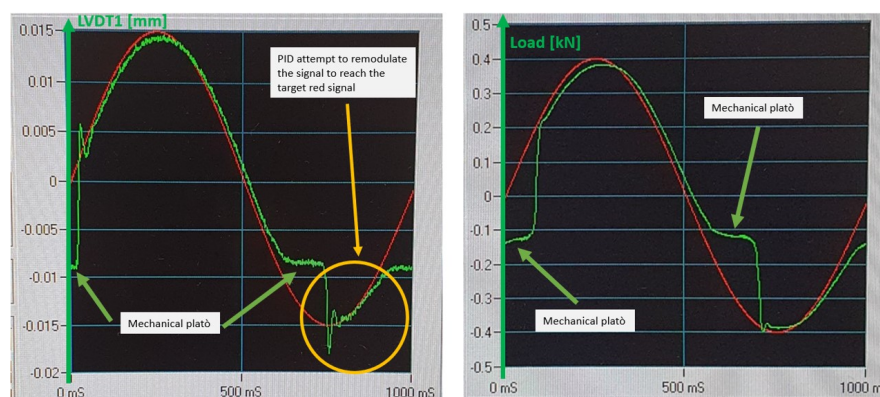


Fig. 6.40 LVDT1 (left) and Load (right) signal problem

Therefore the entire machine has been disassembled (Figure 6.41) and finally the problems has been found: the ball screw damage was damage. The machine was not able to recovering the backlash generated by the damage of the balls path on the ball screw (Figure 6.42).



Fig. 6.41 INSTRON ETMT II disassembly procedure

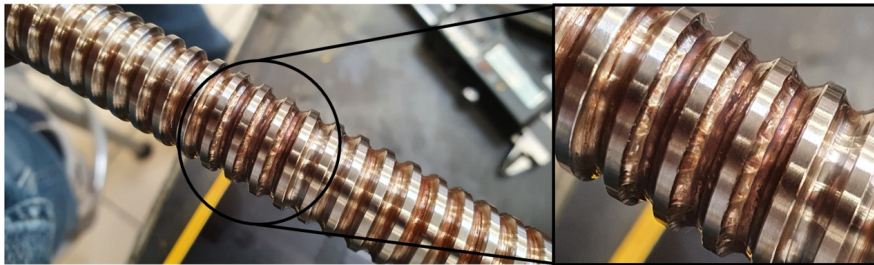


Fig. 6.42 Ball screw damage

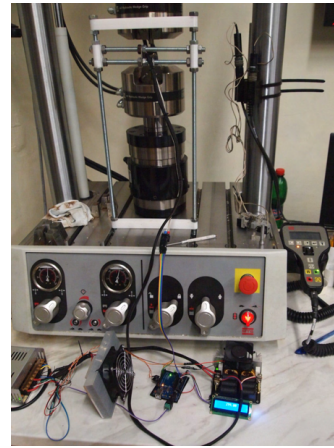
Because INSTRON didn't have the new component in stock and the waiting for the likely delivery was 13 weeks (yes, 13 weeks) there were two opportunities: 1) there will be no LCF test 2) Try to fix the problem some way. The result was excellent: the problem was bypassed by moving down the whole vertical bar linked to the ball screw and move the transverse main top beam up in order to have the distance needed for the specimen between the machine's grips. Therefore the LCF tests have been done, even though a slight not relevant backlash is always present (Figure 6.39a).

6.4.6 Creep

The specimens for the creep test are the same used and presented for the Low Cycle Fatigue tests, according with ASTM E139 Normative. The machine is MTS 370.02 located at Slovak University of Technology, Slovakia. The electrical induction system is a home made one composed by an electrical inductor, a thermocouple and an Arduino control unit (Figure 6.43).



(a) Induction system system

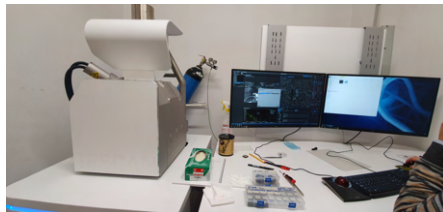


(b) MTS 370.02 machine and the home made control system

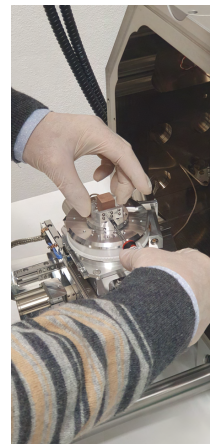
Fig. 6.43 Creep machine, Slovak University of Technology, Slovakia

6.5 Fracture Surface Analysis

A Tescan VEGA SEM microscope (Figure 6.44) located in the DIMEAS laboratory of Politenico is the machine adopted in order to analyse the 3D fracture surface of Low Cycle Fatigue and traction with a high magnification.



(a) Tescan VEGA SEM microscope



(b) Specimen positioning inside the SEM chamber

Fig. 6.44 SEM at DIMEAS Laboratory, Politecnico di Torino

However, also an optical analysis of the fracture surfaces have been done with a particular lighting optional tool for the already presented optical Keyence VHX microscope. This particular optional uses a multi light orientation in order to acquire multiple images of the fracture surface and giving back a 3D rendered image that has been used for profile analysis.

Chapter 7

Experimental Results: Technological Tests

Additive Manufacturing is a very parameter-dependent process. Since the material was never processed before technological specimens have been printed in order to understand the material-process capability to:

- Be able to achieve the typical LRE thrust chamber cooling channels shapes and the common 1 mm - 0.5 mm ribs and hot gas side wall thickness;
- Be able to successfully achieve high Z angle respect to the XY plane: this test has been performed since the thrust chamber is a convergent-divergent object;
- Be able to print a simple lattice structure;

Figure 7.1 clearly shows the island scanning algorithm.

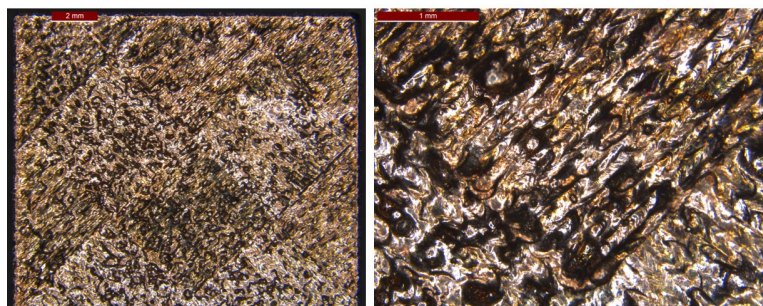


Fig. 7.1 Island scanning algorithm

7.1 Cooling channels

The cooling channel replica specimen is a parallelepiped with a rectangular 10 mm x 60 mm base and a height of 25 mm. Inside this box there are three different technological tests (Figure 7.2): i) two identical rectangular holes test with dimensions from 1.0 mm

to 0.2 mm, 0.1 mm steps; ii) one row of different shape channels with 0.5 mm ribs and hot-gas side wall; iii) one row of same shape channels with a 1 mm ribs and hot-gas side wall. The different shape channels are composed by: n.4 of 1 x 4 mm rectangles, n.4 of 1 x 4 mm slotted shapes with 0.5 radius connections, n.4 of 1 x 4 mm triangles, n.4 of 1 x 4 mm triangles with 0.2 radius connections.

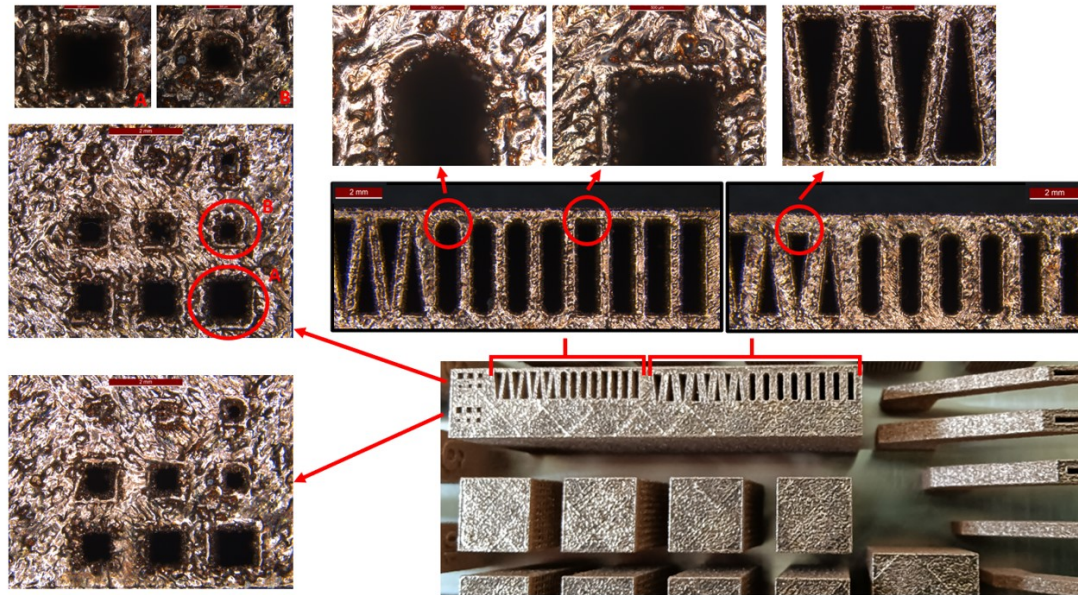


Fig. 7.2 Cooling channel replica specimens

All cooling channels have been successfully printed with both, 1 mm and 0.5 mm ribs and hot-gas side wall. On the other hand, as expected, not all holes have been successfully printed. In particular it is possible to see that the outside melted laser contour has a different behaviour respect to the under layers. It is possible to evaluate this particular behavior by comparing top left images from Figure 7.2 and Figure 7.3. Figure 7.2 shows the unpolished surface and 2 holes seems to be blocked, however after a 2 mm materials removing (from bottom - printing platform - to top) procedure followed by a preliminary polishing process it is possible to see that the starting situation is completely different. This is probably due to the contour particular interaction this the unmelted powder. The irregularity of the surface change with Z direction, therefore for analysing small holes and more particular features it is important to analyse the component not only by a human visual process.

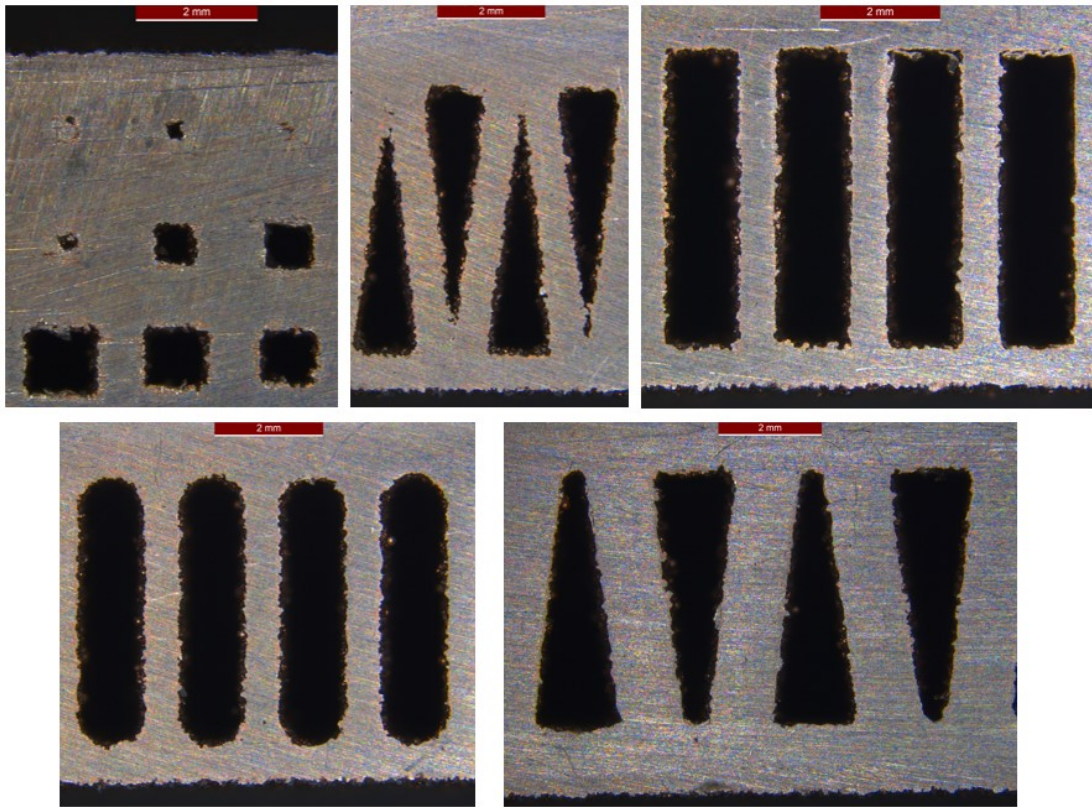


Fig. 7.3 2mm z-direction material removed specimen followed by a coarse surface polishing

This test shows that with this body and contour parameters (Table 5.3) a non-destructive test should be performed in order to compare the CAD geometry to the printed one. Future studies could be performed in order to optimise the contour parameters.

7.2 Channels angle

Different angle building direction have been tested. The specimens have a vertical 10 mm base and that the angular orientation is made for 15 mm. The tested angle, respect to the z-direction (build direction), are: 35°, 45° and 55° (Figure 7.4). All tree shapes are made with a 1mm and a 0.5 mm wall thickness, with the same rectangular replica cooling channel already presented for the replica cooling channels specimen.

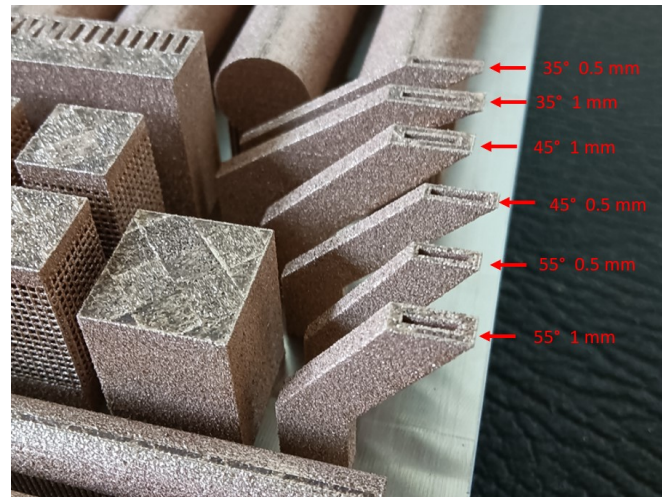


Fig. 7.4 Sloping specimens on the building platform

All specimens have been successfully printed with no particular difference (Figure 7.5). All specimens does not use supports on the sloping segment. The experiment evidence that also the 35° specimens, with no supports, have been properly printed.

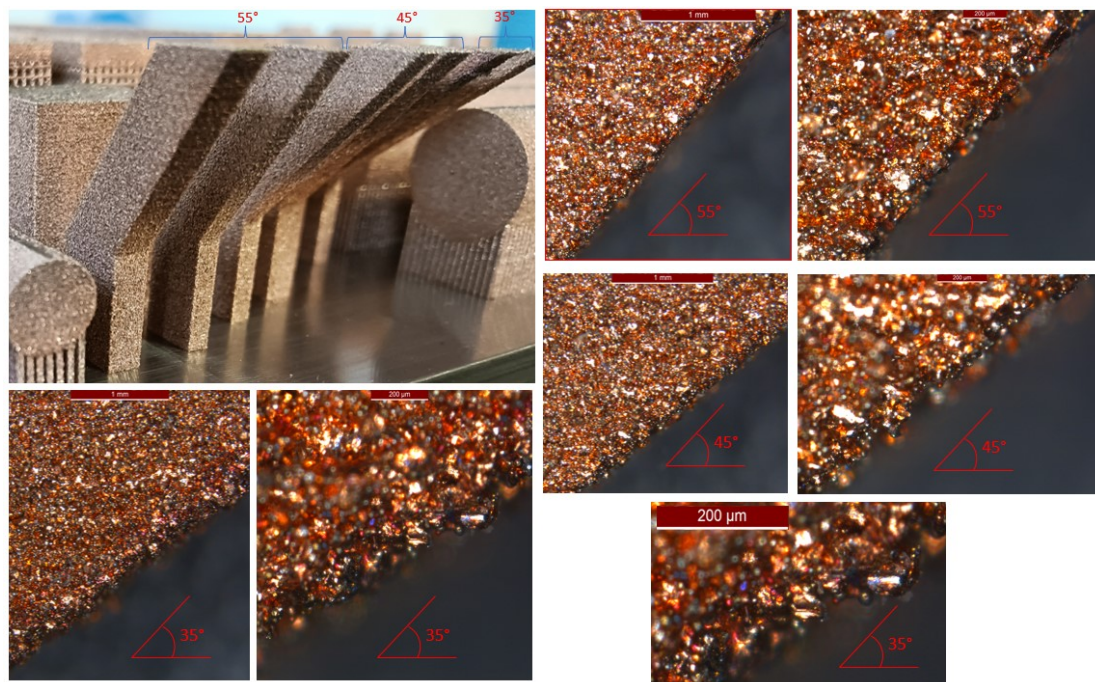


Fig. 7.5 Sloping specimens surface quality

However It is possible to see that the surface quality decreases as the angle decreases. This is due to the fact that the lower the angle is and the more the laser spot is in contact with the bed powder (Green lines in Figure 7.6) instead of the already melted layer (read lines in Figure 7.6). The laser side out of the previous layer is need in order to achieve the CAD contours: the result is that the under powder bad is not well melted and several different spot melted bubbles come out [94],[21].

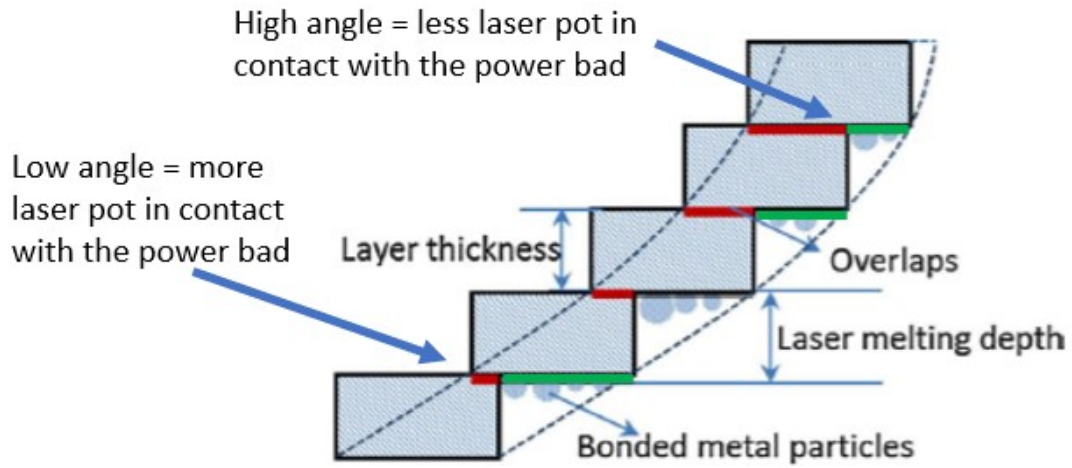


Fig. 7.6 Schematic illustration of the SLM manufacturing process of the angular z-direction build, from [21].

7.3 Lattice Structure

Lattice structure with simple cubic cells have been tested (Figure 7.7). In particular a 0.3 mm and a 0.5 mm links diameter, both with a 1 mm links length. The horizontal 1 mm links do not seams to have structural instability. However, with a more relevant length, such as the 3 mm links from the cubic 17 4PH lattice structure successfully printed by Bertocco et al. with the same Concept Laser M2 machine [94], failure due to the restlessness of the powders bed support could occur.

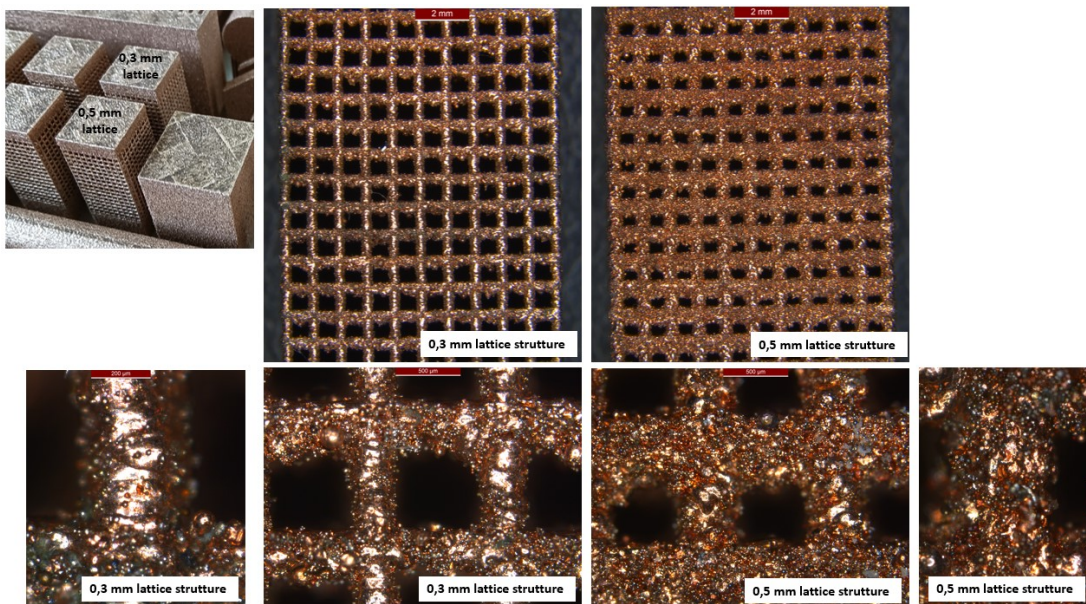


Fig. 7.7 Lattice Structure

Chapter 8

Experimental Results: Physical/Chemical Properties Tests

8.1 Roughness

Figure 8.2 shows the evolution of R_a as a function of the analyzed directions (Figure 8.1) for the side and top surfaces of the replica cooling channels technological specimen. The roughness is performed only for this straight simple (slope technological specimens have not been tested). The experimental outcomes was that all of the samples had a roughness that is typical of L-PBF products ($7 - 25 \mu m R_a$)[95].

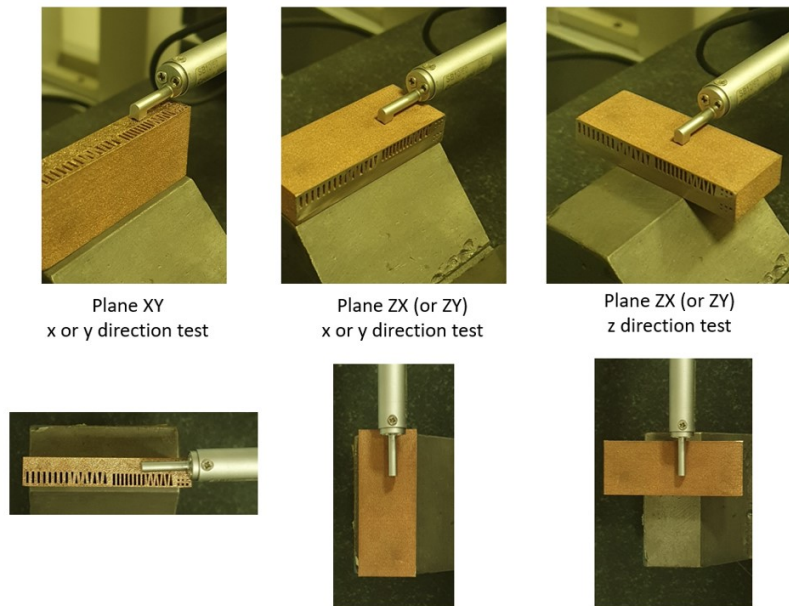


Fig. 8.1 Roughness tests

In particular the XY plane has a average measured R_a of $11.6 \mu m$. Considering the standard deviation of this result it is possible to state that the average measured R_a of the ZX plane respect to the X (or Y) direction, which is $11.8 \mu m$, is very similar. On the other hand the test performed on the ZX plane, but respect to the Z building direction,

is slightly greater, with an average value of R_a of $13.1 \mu m$. This result is according with the typical SLM behavior [80]: since the powder bad layers are overlaid respect to the Z building direction a lower contour quality is achieved. This is due to the fact that the XY plane X or Y direction test analyse the island algorithm, and therefore the body parameters. On the other hand, the ZX/ZY plane Z direction analyse the contours parameters. The fully roughness analysed parameters are presented in the Appendix B.

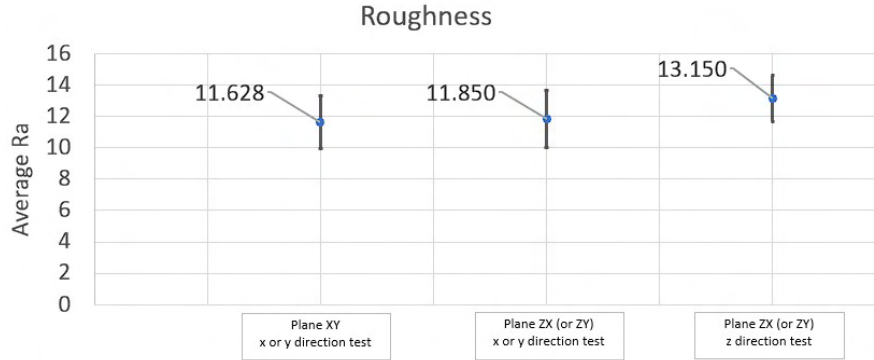


Fig. 8.2 Roughness tests results

A SLM pure copper R_a between $16 - 25 \mu m$ average can be a target reference value [96]. However AM component roughness deepens on a huge number of factors such as the AM SLM machine, the laser spot, contour parameters, powders dimension, layer thickens ecc.

Respect to the LRE application the cooling channels roughness is a very important parameter for both, fluid dynamics and Low Cycle Fatigue field of recherche. While the external surface can be easily machined and therefore a better surface finishing can be achieved, for the internal cooling channel surface it is impossible to machine directly: only high pressure water charged with particular high-hardness particles can improve roughness. However even if no optimization studies have been performed respect to the contour parameter, the achieved roughness is a good start for this new material.

A possible cause of surface high roughness is the flexible re-coating method. As illustrated in Figure 8.3a, the flexible blade was hampered by the small ball and contaminants during the re-coating process. Re-coating with powder causing the ripple to appear on the powder bed, resulting in layer instability, and finally the surface a lower part quality [97]. The flatness of powder distribution, the stability of effective laser power, and the oxygen concentration in the chamber are all important factors to consider while ensuring manufacturing stability [97].

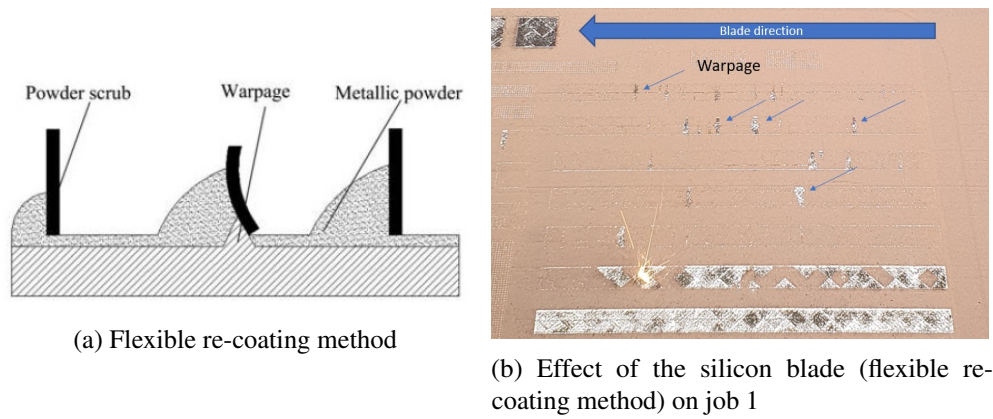


Fig. 8.3 Re-coating method

8.2 Optical Micrography

In order to better understand the following Section results the pure copper miscibility with pure iron is presented (Figure 8.4). By analysing the Fe-Cu phase diagram it is possible to observe that the Copper miscibility into the Fe matrix is much lower than the 65% of the under study composite material: the result is an island structure.

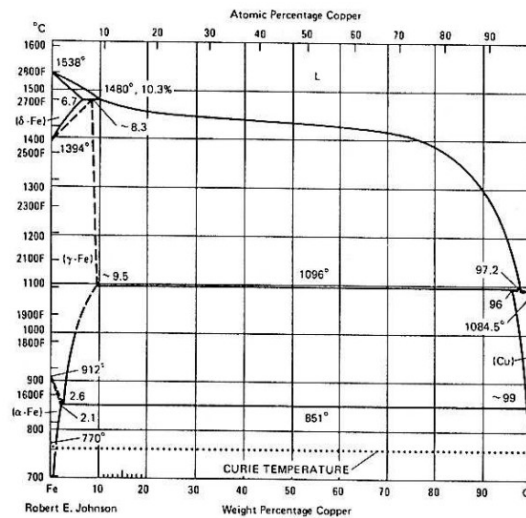


Fig. 8.4 Copper-Iron phase diagram

8.2.1 XY plane

Images from XY plane slices of different specimens are presented and analysed: a 500 μm magnification (Figure 8.5) and a 500 μm magnification with a acid attack (Figure 8.6). The 65% Cu - 35% 174PH custom powder material shows a bi-metal-matrix-composite microstructure. The material has a very high compenetrated bi-material matrix. In particular it is not correct to name this structure as an alloy since the two different materials do not create a real unique material but a more complex composite bi-structure of two different alloys: pure copper and 17 4PH.

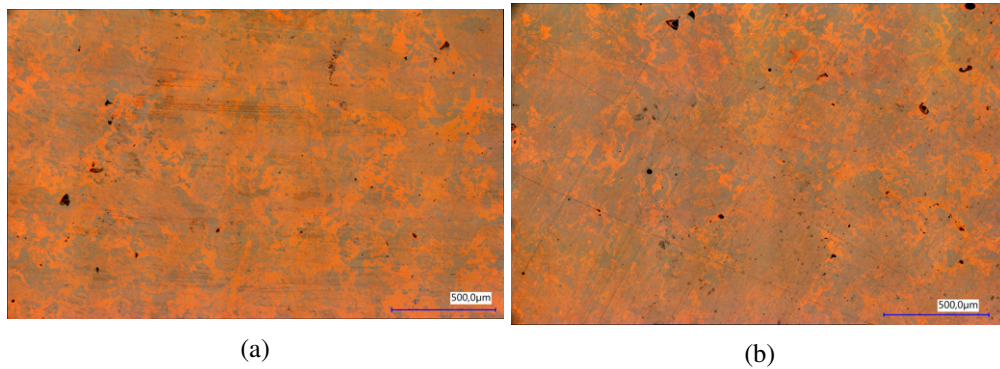


Fig. 8.5 Optical micrography

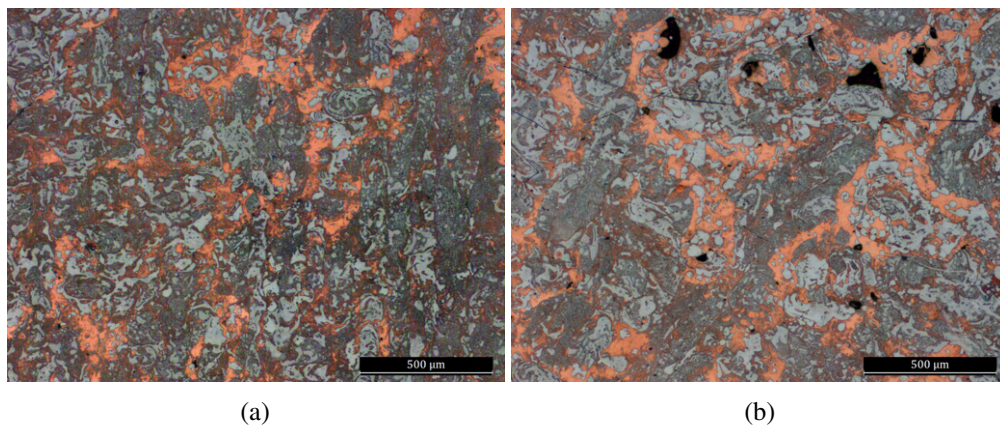


Fig. 8.6 Optical micrography with acid attack

The composite is copper based and therefore it is possible to see that the main matrix is composed by copper. The 17-4PH is presented such a island shape. Since copper has a lower melting point respect to the 17-4PH, it has been successfully well melted. A possible hypothesis is that during the solidification copper process the copper, due to his higher thermal conductivity, it solidifies before the 17-4PH generating the basic matrix. Subsequently the iron, which is 'floating' on the sea of copper, solidifies with a more proper form. This process make this complex composite material. In addition to the aforementioned main hypothesis, another hypothetical phenomenon that make possible such a structure is that copper has a greater capacity to flow in the liquid state because it has no alloying elements and therefore slips into the gaps created by iron which, being highly alloyed, flows more slowly.

The XY microstructure shows that the custom mixed powder is homogeneously spread along both, X and Y direction: the powder mixing process is able to achieve a very good powder distribution. The most interesting and innovative result from this analysis is that the material has two main region that are independently melted and one well mixed region (Figure 8.7):

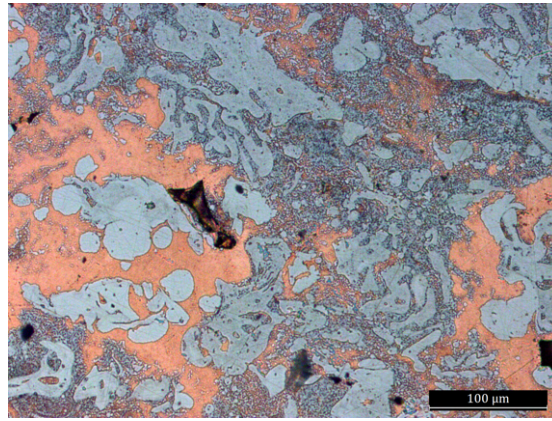


Fig. 8.7 Cu174PH microstructure

- **Copper matrix:** A copper base matrix is clearly visible (orange color) in Figure 8.7. This is the main structure of the composite material;
- **17-4PH islands:** 17-4PH islands are visible (bright blue) in Figure 8.7;
- **Dotted matrix:** This third particular areas are a high densified mixture of copper and 17-4PH. However, also in this particular areas, the copper is the base component, without a standard shape, and the 17-4PH is presented with more spherical shapes inside the copper matrix. In particular there are two different sub-areas: one with a low rate of 17-4PH spherical spots (Figure 8.8) and a second one with a very high rate of spherical spots (Figure 8.9).

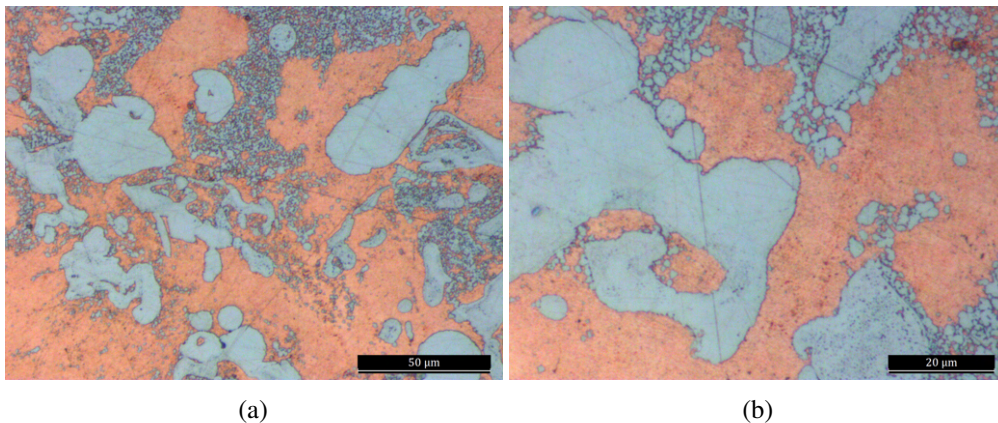


Fig. 8.8 Optical micrography of a common low rate 17-4PH spherical spots area

An interesting feature of the very high rate 17-4PH spherical spots area is that all around the 17-4PH islands there is a very thin circumnavigating layer of copper (Figure 8.9a).

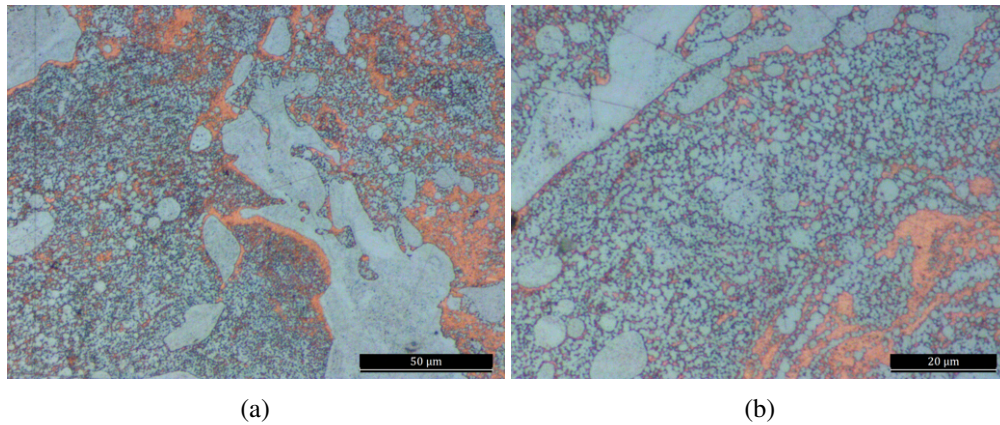


Fig. 8.9 Optical micrograph of a common very high rate 17-4PH spherical spots area

The classic Additive Manufacturing SLM laser track are not visible in this particular material. The adopted island-like scan strategy is almost never visible. The typically encountered laser scanning pattern is never evident. This is probably due to the fact that the non-interaction behavior of the two materials do not generate a proper path while the laser progress in his main straight motion. A previous Sophia High Tech s.r.l. work concerning a Inconel718-Cu material shows a completely different XY microstructure [22]: this is due to the fact that the material has at maximum a 20% of copper and therefore the two different materials had more communication skills.

A better analysis of the surface interface between the copper and the 17-4PH should be performed. C. Tan at al. [98] shows that an important inter-diffusion region at the boundary interface between 316L steel and copper. Another similar work has been performed by L. Liu et al. [68], S. Osipovich et al. [99] propose an interesting study which goal was to analyse the gradient transition zone structure in a steel-copper sample produced by double wire-feed electron beam additive manufacturing: the transition zone is very similar to the microstructure observed in the present study. In particular a multi-island area with different shapes, respect to the Cu concentration, is presented. They state that the composite structure make very good 'continuous interdendrite boundaries'. The new Cu174PH composite material seems to have a qualitative similar structure.

The microstructure of the Cu174PH seems to have a liquid-phase separation. This behavior has been tested by Xiaosi Sun et al. [100]. A specific characterization of the solidification process is presented and the experiment reveals that steel, during the liquid-to-solid solidification, tries to decouple from copper.

Particularity: rare laser track

The majority of the XY plane surface analysed do not shows the common scanning laser tracks that are always present in a AM SLM alloy. The laser track can be also identified in the Inconel718-20%Cu pre-mixed custom powder tested in the aforementioned previous Sophia High tech s.r.l. study (Figure 8.10, [22]).

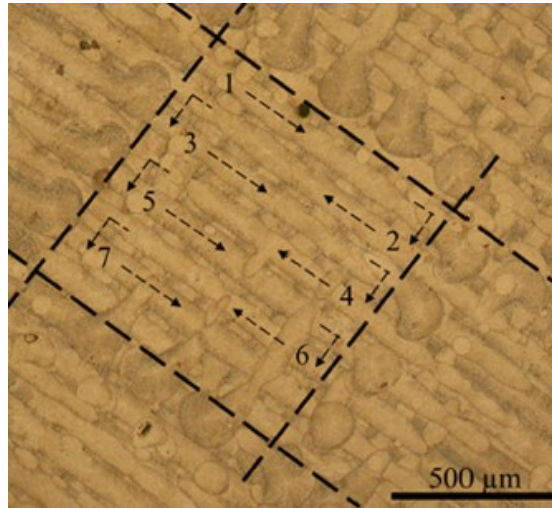


Fig. 8.10 Laser Track of a custom Inocel718-Cu%20, from [22]. Same scanning strategy of the under study Cu-174PH composite material.

However in certain areas there is a statistic higher concentration of 17-4PH. In this particular and very rare areas, because the concentration of copper is very low, a laser track shows up.

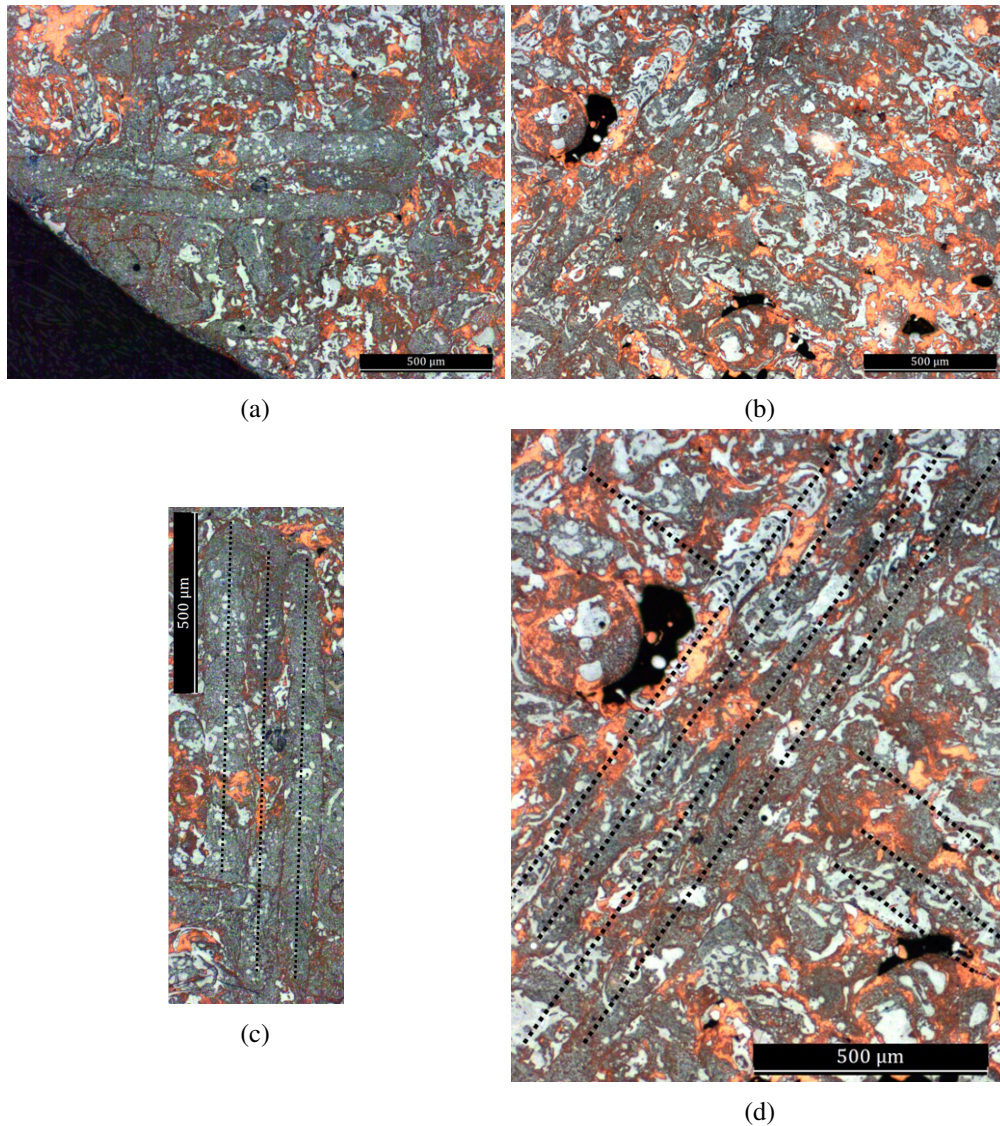


Fig. 8.11 Very rare Laser tracks

8.2.2 ZX/ZY plane

The energy transfer from the laser beam to the powder bed, and the subsequent melting and solidification of the material, is a critical step in SLM AM processes. The process feasibility and the qualities of the printed items are governed by the molten pool creation and heat and mass transfer inside the molten pool. Two separate welding modes can be produced when a laser beam interacts with a metal substrate, either a powder bed or a solid layer: conduction mode and keyhole mode. The establishment of one or the other is mostly determined by the laser beam's power density [101–104] (if you are new to Additive Manufacturing molten pool dynamics please see Appendix C).

In the experiments reported in this work the amount of energy adsorbed by the powder bed under the energy input produced by the 251 [W] laser power was insufficient to activate the keyhole mode (Figure 8.27). Typically this phenomenon is more pronounced when adopting an higher layer thickness because more material is simultaneously

processed. As a consideration for further work, low layer thickness values should be used when powder mixtures are used as starting material [22].

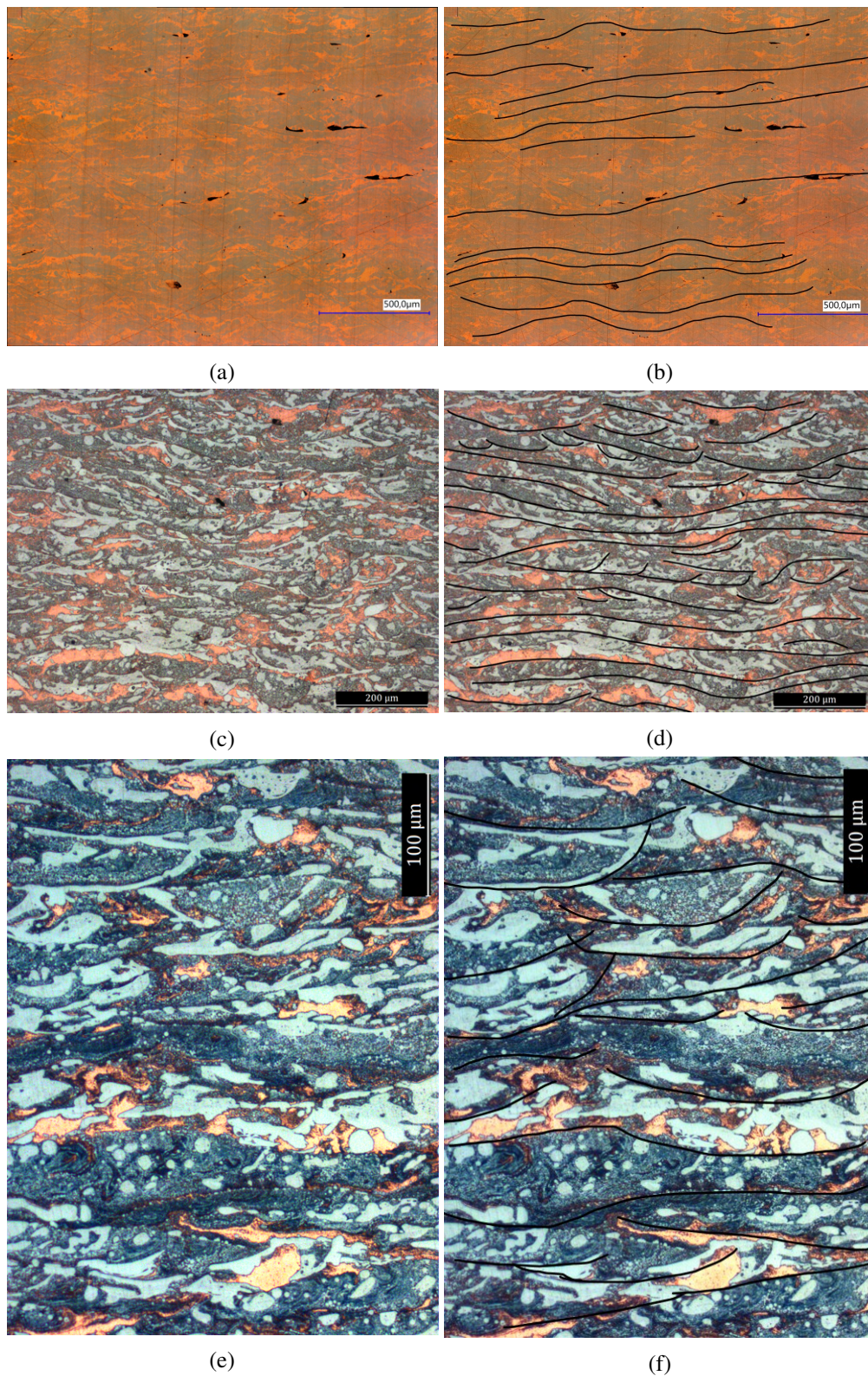


Fig. 8.12 Z plane microstructure

The material does not show evident melting pools. Also the layer by layer stratification is not evident since the material is composite by two different alloys.

A particular behavior of the composite material is the complex melting pool. When is possible to see a melting pool (almost never) the shape is concave respect to the Z building direction (face up curved) as all common AM SLM materials. The particularity is that some times the 'base' of the melting pool is made by copper, some times by the 17-4PH alloy (Figure 8.13). A possible hypothesis for the copper based melting pool is that, since copper powders are smaller than steel one and since copper is slightly heavier than steel, during the melting process copper is encouraged by gravity and fluidity to go down and, therefore, steel floats above copper.

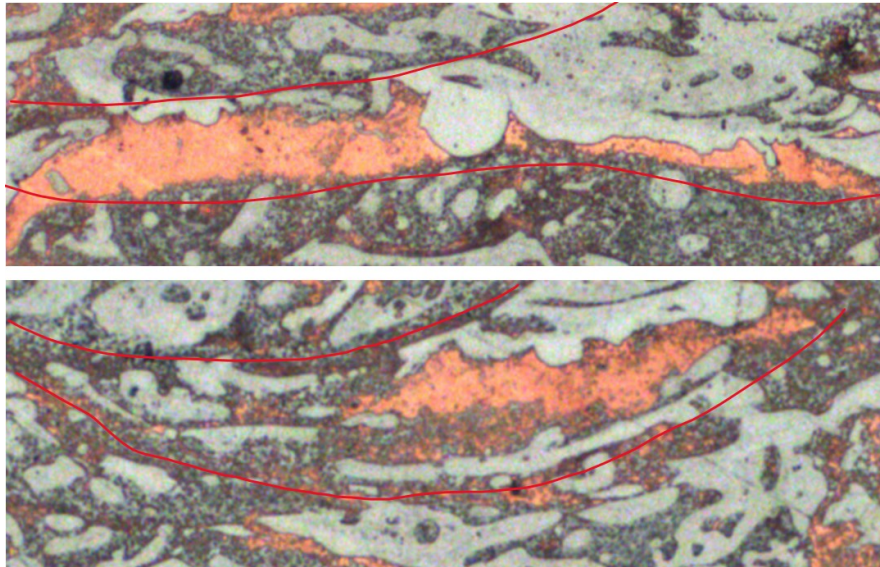


Fig. 8.13 Complex melting pool: top image shows a copper base melting pool, bottom image shows a more 17-4PH base melting pool

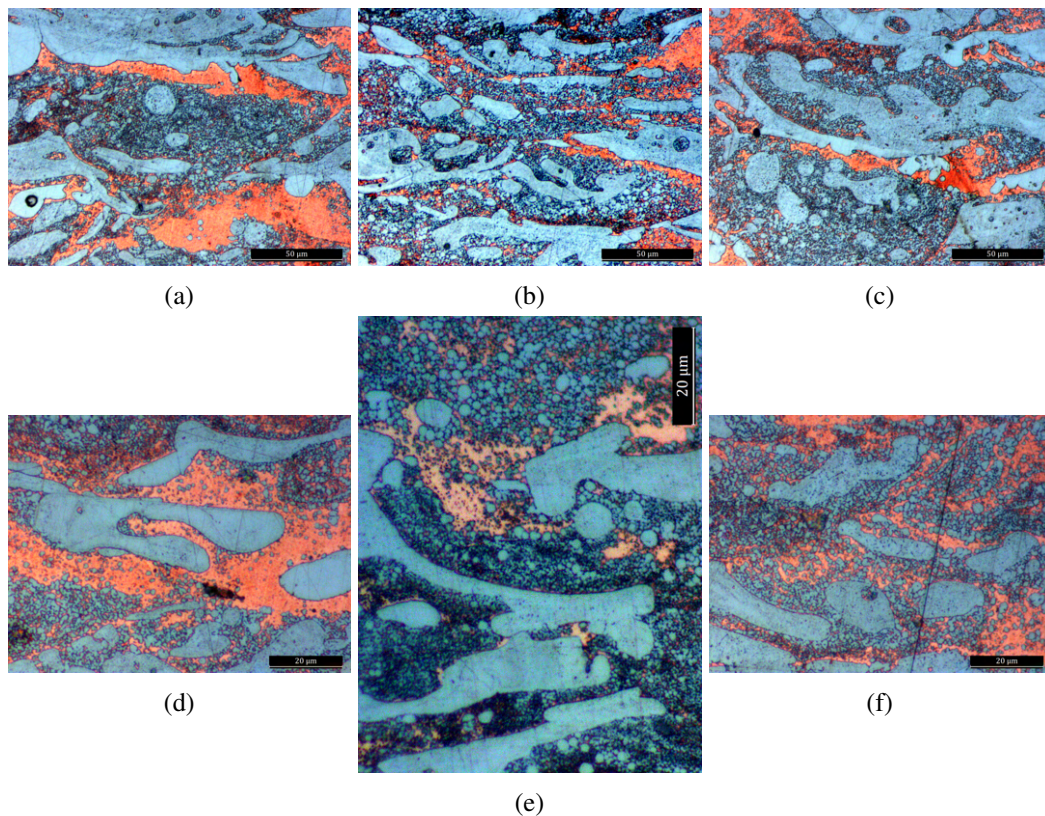


Fig. 8.14 Z plane melting pools

Particularity: rare key-hole melting pool

Even though the main melting mechanism is the conductive one, a very rare key hole mechanism sometime can be identify. In particular Figure 8.15b shows an interesting behavior: tree key holes on the same Z axe but not in consecutive layers. The same mechanism is shows in Figure 8.15a with four key hole. It is possible to identify also the a vortex solidification behaviour at the around a particular rare key hole in Figure 8.15c.

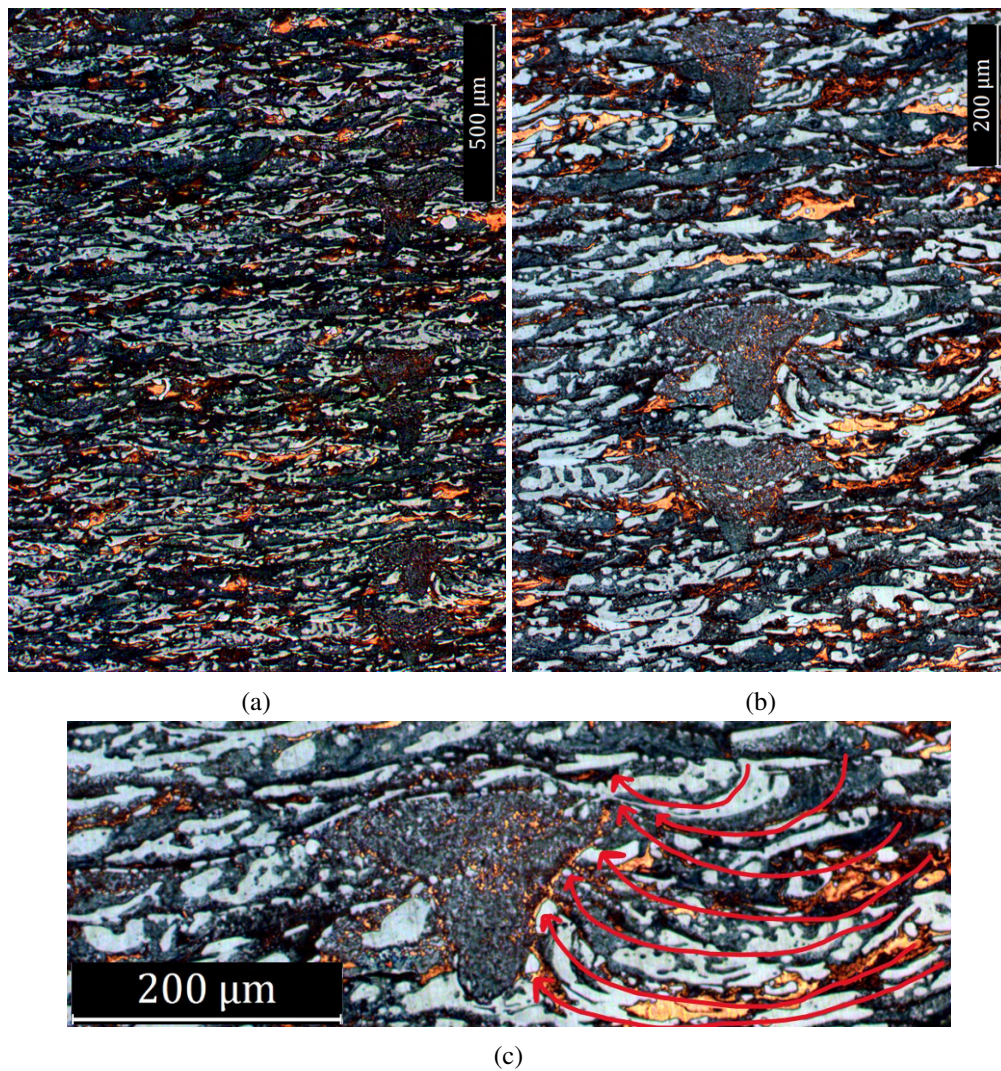


Fig. 8.15 Rare key-hole melting pool

Particularity: Z direction columnar grain

The typical Z building direction micrograph do not shows any columnar grain. However Figure 8.16 shows a very particular and not easy to explain columnar grain close to the boundary contour surface.

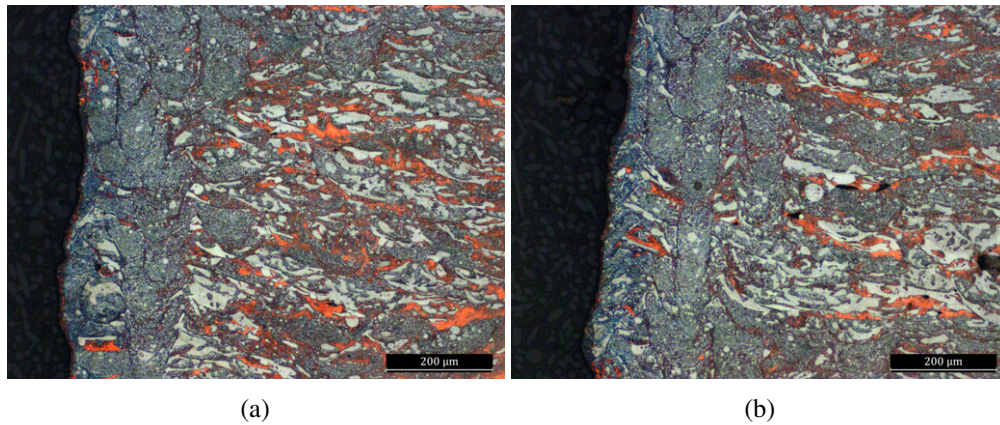


Fig. 8.16 Optical micrography of a rare columnar grain

Particularity: Island inside Island

Some times, in the building Z direction, it is possible to see a strange phenomenon (Figure 8.17: a dotted matrix (identical to the one presented for the XY or Z direction) inside a 17-4PH island.

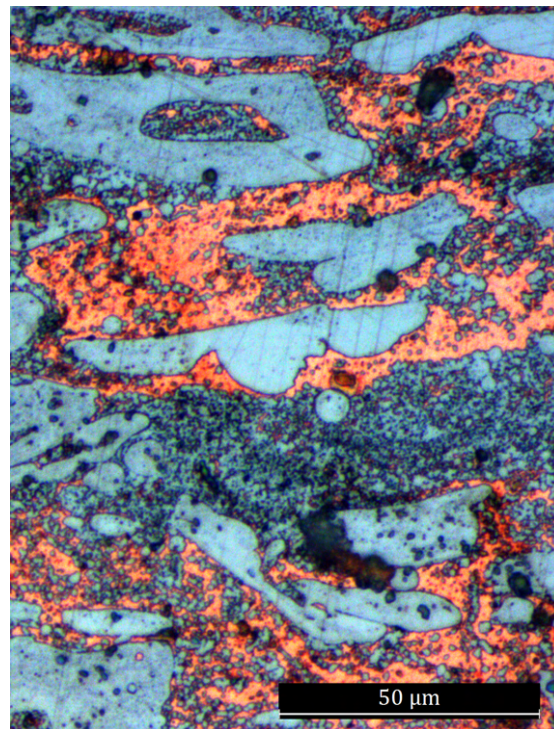


Fig. 8.17 Island inside Island example

8.2.3 Defects

The process parameters employed for this first printed 174PH-Cu composite material shows an exceptional cohesion between the interface of the two alloys. However three common Additive Manufacturing SLM defects can be found:

- **Lack of fusion porosity:** Different number of lack of fusion porosity are spread around the campsite matrix. An interesting method for predicting the presence and location of lack of fusion porosities can be found in the study proposed by Coeck at al.[105].



Fig. 8.18 Lack of fusion porosity example

- **Gas captured porosity:** This porosities are spread around the campsite matrix but not very common as the lakes of fusion. This phenomenon is due to the interaction of the vapor gas produced by the laser in the melting pool and the solidification speed. Since copper is a high conductivity material, come times vapor gas are not able to evaporate way from the melting pools before solidification. This is a very common defect of AM SLM copper alloys [11, 106, 22, 81].

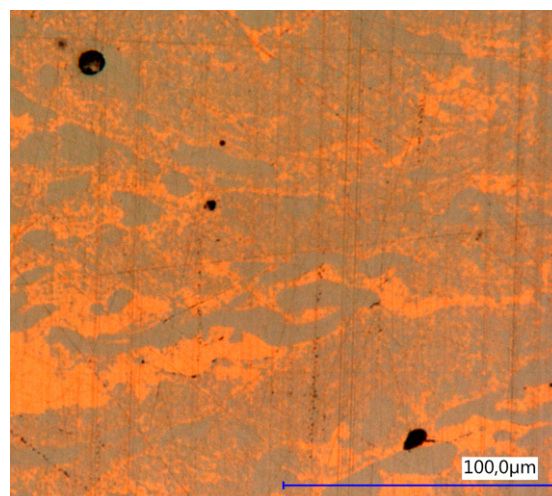


Fig. 8.19 Gas captured porosity example

- **No melted powder:** This defect is very rare inside the material matrix, only few example has been found. By analyse the image it is possible to see that all around the unmelted spherical powder there are several different porosity, and a lake of fusion.

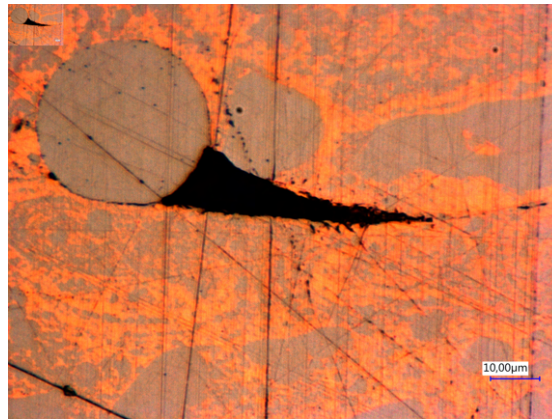


Fig. 8.20 No melted powder example

8.3 SEM Micrography

From the SEM micrography performed respect to the z direction, there are no particular difference/additional information from the optical analysis.

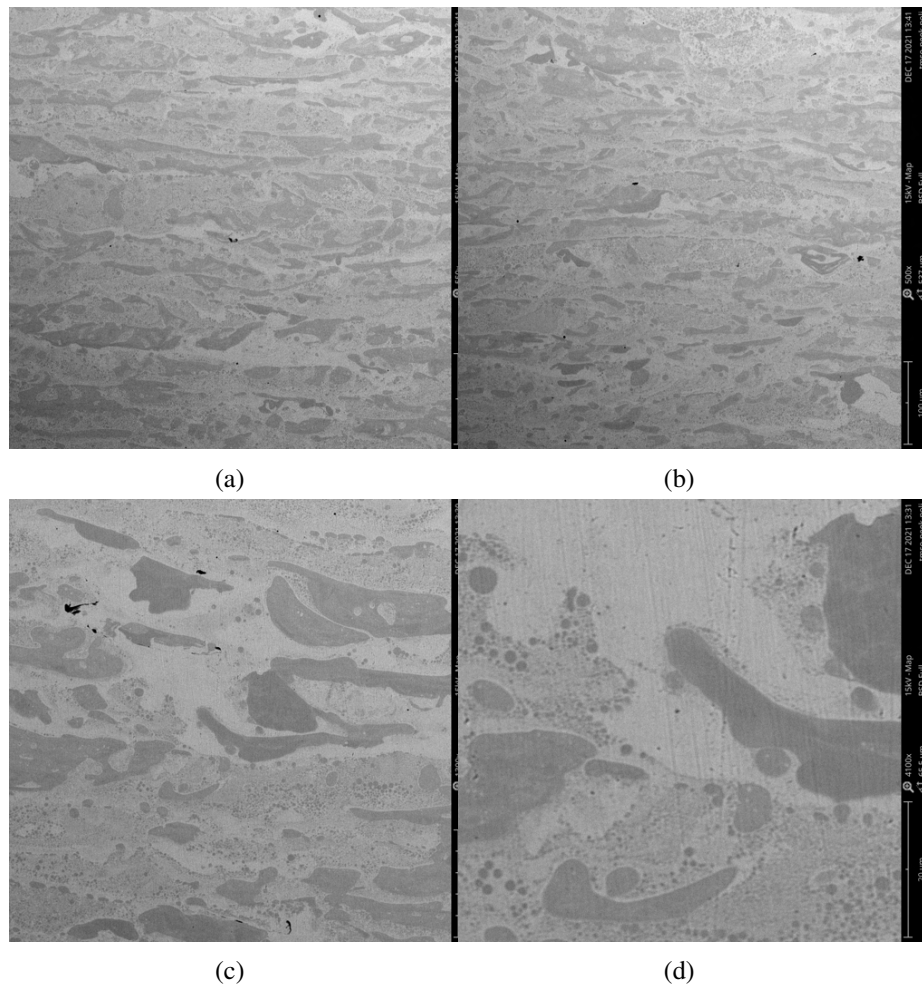


Fig. 8.21 SEM Z building direction micrography.

8.4 Chemical Composition

8.4.1 Overall material chemical composition

The weight chemical composition of the mixed custom powder before the Additive Manufacturing process is: 65% Copper - 35% 17-4PH. On random cubic specimen has been tested in both, middle XY plane and middle Z plane (Figure 8.22). The EDS analysis has been performed with a MAP and a spot analysis: the MAP evaluate the chemical composition inside the target area, the spot analysis is a $1\ \mu\text{m}^3$ more precise analysis. In order to obtain a proper spot analysis the identification of the spot is very important: since the spot is a $1\ \mu\text{m}^3$ area the operator have to perform the analysis in locations where it is possible to be sure that in $1\ \mu\text{m}$ depth the material matrix is the same one of the one visible in the surface.

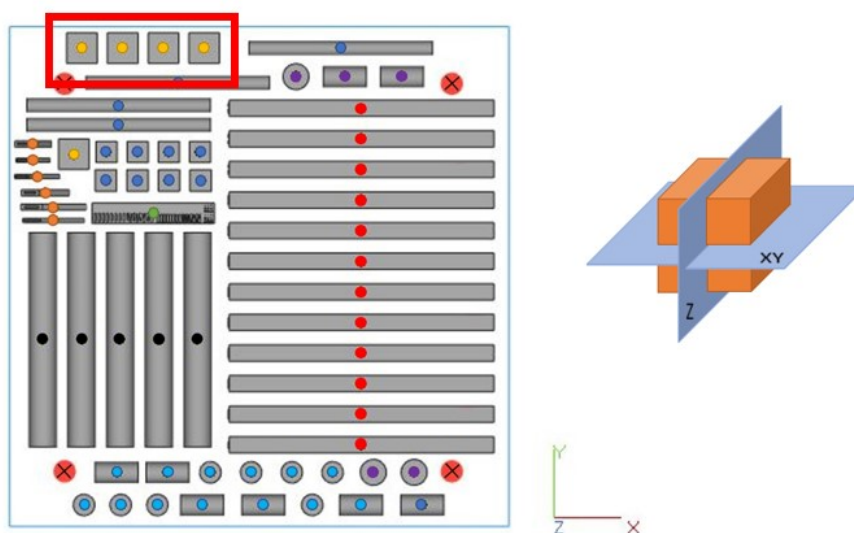


Fig. 8.22 Chemical composition specimen location

The general composite composition have been tested respect to the XY plane with the same $848\ \mu\text{m}$ FoV¹. This is the most accurate plane to obtain the average overall chemical composition. However, also the Z chemical composition have been tested respect to three different FoV areas have been analysed: $548\ \mu\text{m}$, $224\ \mu\text{m}$ and $57\ \mu\text{m}$. Results, respect to the orientation analysed, are presented in Table 8.1. The over all composition is presented in Table 8.2.

¹Field of View: by changing the zoom it is possible to obtain different scale images. In particular the more the FoV is high the less the image is zoomed. Frequently, in order to give a representing FoV value, the scale of the image is associated to the FoV.

Region	FOV	Weight chemical composition							Average					
		Cu	Fe	Cr	Ni	Si	C		Cu	Fe	Cr	Ni	Si	C
XY plane	1	848 μm	54.93	35.25	7.59	1.75	0.48	//						
	2	848 μm	55.61	34.67	7.5	1.7	0.5	0.01	56.9	33.59	7.31	1.69	0.48	0.03
	3	848 μm	60.19	30.84	6.85	1.63	0.46	0.004						
Z palne	1	548 μm	59.21	32.51	6.84	1.44	//	//						
	2	224 μm	59.15	32.12	6.96	1.79	//	//	58.9	32.49	6.97	1.63	//	//
	3	57 μm	58.34	32.84	7.11	1.7	//	//						

Table 8.1 Material XY and Z pale SEM EDS chemical composition

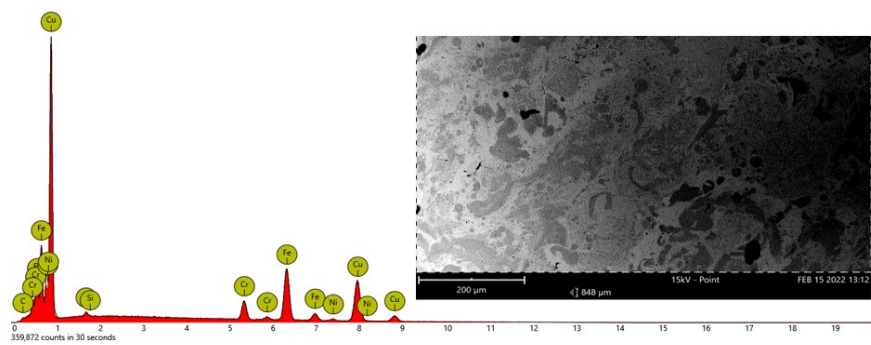


Fig. 8.23 EDS spectrum of XY plane (one example out of three tests)

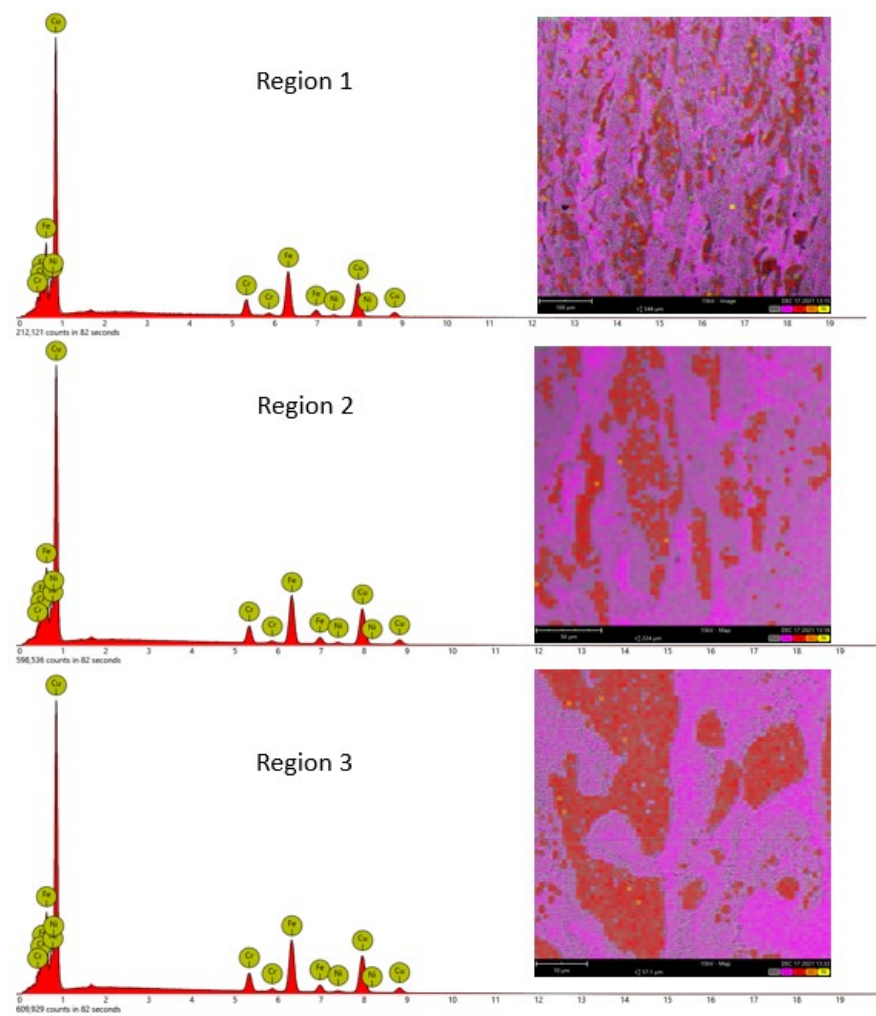


Fig. 8.24 EDS spectrum of Z plane

			Overall			
	Region	FOV	Cu	Fe	Cr	Ni
XY plane	1	848 μm	57.90 DV.ST(2.13)	33.03 DV.ST(1.64)	7.14 DV.ST(0.32)	1.66 DV.ST(0.32)
	2	848 μm				
	3	848 μm				
Z palne	1	548 μm				
	2	224 μm				
	3	57 μm				

Table 8.2 Material overall SEM EDS chemical composition

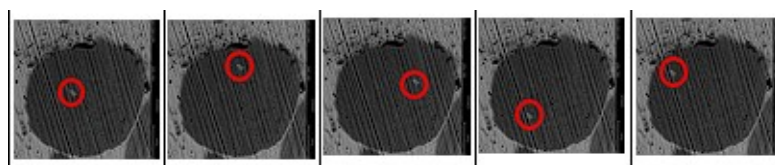
8.4.2 17-4PH phase chemical composition

In addiction the the result presented, also a more accurate spot analysis have been done respect to the 17-4PH phase in both, XY (Table 8.3) and Z (Table 8.4) direction. The

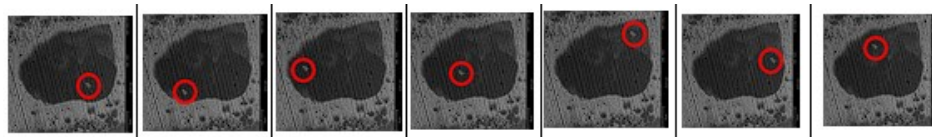
main aim of this analysis is to understand, after the SLM process, the amount of copper inside the 17-4PH.

Region	FOV	Spot	Weight chemical composition					
			Fe	Cr	Cu	Ni	Si	C
1	42.6	1	72.33	14.72	7.94	4.1	0.8	0.1
		2	72.53	15.06	7.42	4.01	0.82	0.16
		3	73.51	14.96	6.68	3.91	0.84	0.1
		4	73.57	14.89	6.96	3.61	0.8	0.17
		5	72.34	15.13	7.65	3.88	0.91	0.09
2	57.1	1	73.44	15.29	6.41	3.89	0.83	0.14
		2	72.58	14.51	8.5	3.55	0.75	0.11
		3	72.64	14.46	8.08	3.86	0.84	0.12
		4	73.22	14.72	7.36	3.73	0.82	0.15
		5	69.01	14.2	12.37	3.42	0.82	0.19
		6	72.97	14.68	7.77	3.53	0.85	0.19
		7	69.67	14.06	11.92	3.39	0.81	0.15
3	50.7	1	75.6	14.56	6.17	2.74	0.77	0.16
		2	74.24	14.51	7.12	3.09	0.81	0.22
		3	75.23	14.89	5.52	3.44	0.75	0.17
		4	73.2	15.17	7.08	3.46	0.93	0.16
		5	74.03	14.79	6.77	3.48	0.8	0.13
		6	74.34	14.53	6.5	3.66	0.84	0.14
		7	73.83	14.22	7.18	3.75	0.86	0.15
		8	75.08	14.52	6.19	3.28	0.78	0.15
Average			73.16	14.69	7.57	3.58	0.82	0.14
DV.ST			1.62	0.33	1.72	0.32	0.04	0.03

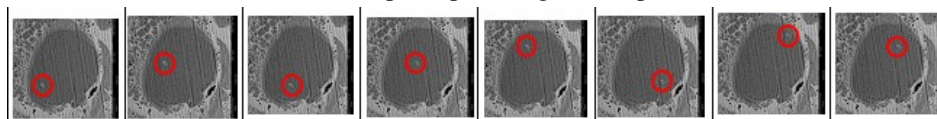
Table 8.3 17-4PH phase chemical composition - XY plane



(a) 17-4PH XY plane phase region 1 - spot 1 to 4



(b) 17-4PH XY plane phase region 2 - spot 1 to 7



(c) 17-4PH XY plane phase region 2 - spot 1 to 8

Fig. 8.25 17-4PH XY plane phase EDS analysis

Region	FOV	Spot	Weight chemical composition					
			Fe	Cr	Cu	Ni	Si	C
1	11.2	1	72.67	15.19	8.5	3.19	0.44	0
		2	73.64	15.32	6.97	3.48	0.45	0.14
		3	73.36	15.34	7.28	3.44	0.47	0.11
		4	73.35	15.21	7.11	3.7	0.5	0.14
2	29.8	1	73.22	15.5	6.8	3.88	0.58	0.02
		2	72.76	15.17	7.04	4.01	0.92	0.1
		3	73.37	15.05	6.85	3.78	0.84	0.12
		4	73.15	15.06	6.91	4.12	0.71	0.06
Average			73.19	15.23	7.18	3.7	0.61	0.08
DV.ST			0.32	0.15	0.55	0.31	0.18	0.05

Table 8.4 17-4PH phase chemical composition - Z plane

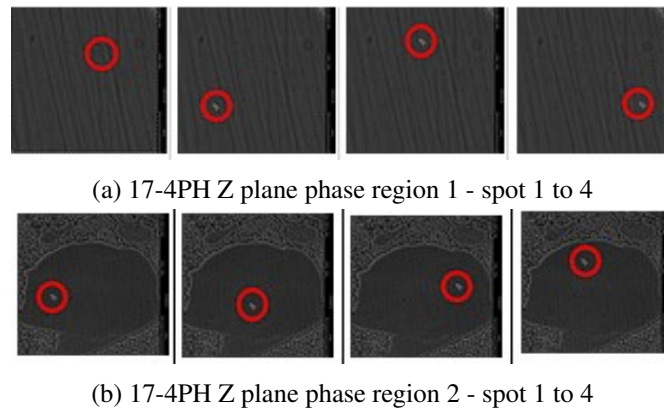


Fig. 8.26 17-4PH Z plane phase EDS analysis

Both XY and Z plane analysis does not shows a difference in the chemical composition within the 17-4PH phase: no experimental evidence have found a chemical composition gradient from the contour to the center body of all 17-4PH islands tested. Every spot has a very similar chemical composition.

From this analysis it is possible to evaluate the 17-4PH chemical composition after the Additive Manufacturing SLM process. Table 8.5 compare the start powder chemical composition declared by the powder supplier to the melted powder which made the layer. In particular the experiments result highlight a lower weight % of Chromium and Nickel, and a higher weight % of Copper inside the 17-4PH phase. Therefore a weight % of Chromium and Nickel, after the melting process, is inside the copper islands and a weight % copper is inside the 17-4PH islands.

17-4PH Weight % chemical composition						
	Fe	Cr	Cu	Ni	Si	C
Average of XY and Z plane measurement	73.47	14.9	7.11	3.64	0.76	0.13
Average Supplier Composition	74.75	16.25	4	4	1	0.07
Supplier Composition	balance	15-17,5	3-5	3-5	1	0,07

Table 8.5 17-4PH islands chemical composition: Start powder VS Melted powder

8.4.3 Copper phase chemical composition

The data presented in Table 8.2 shows the measured real average chemical composition of the composite material respect to the spaceman location and section. If a comparison between experimental data obtained by the average chemical composition of the composite material and the one obtained from the declared 65% Copper - 35% 17-4PH pre custom power mix is performed it is possible to notice that in order to have the

experimental tested chemical composition the pre custom power mix should have been more something like 57,5%Copper - 42,5%17-4PH as presented in Table 8.6.

Premixed Power VS Real Powder measurement							
	Alloy	Powder %	Fe	Cr	Cu	Ni	Si
Pre-Mixed composition	17-4 PH (from supplier analysis)	0.65	74.75	16.25	4	4	1
	Pure Copper	0.35			100		
Expected chemical composition	Cu 17-4 PH composite		26.16	5.69	66.40	1.40	0.35
Analysed chemical composition (From Table 8.2)	Cu 17-4 PH composite		33.04	7.14	57.91	1.66	//
Pre-Mixed composition to obtain the analysed chemical composition	17-4 PH (from supplier analysis)	0.425	74.75	16.25	4	4	1
	Pure Copper	0.575					100

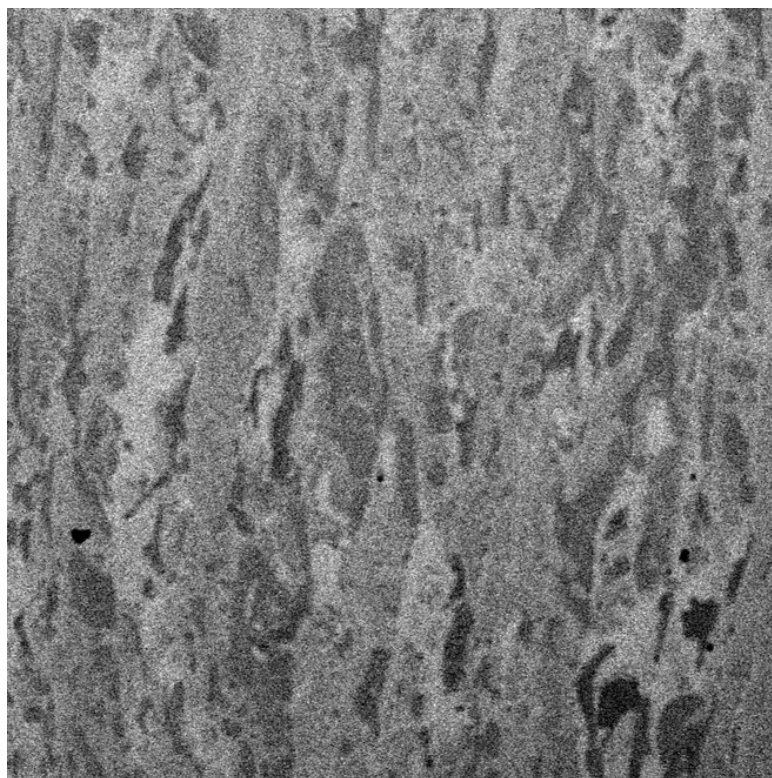
Table 8.6 Pre-custom Cu-174PH powder % composition and the experimental % powder composition

From this result (which is based on the experimental observed chemical composition) it is possible to evaluate the chemical composition of the copper alloy: Table 8.7.

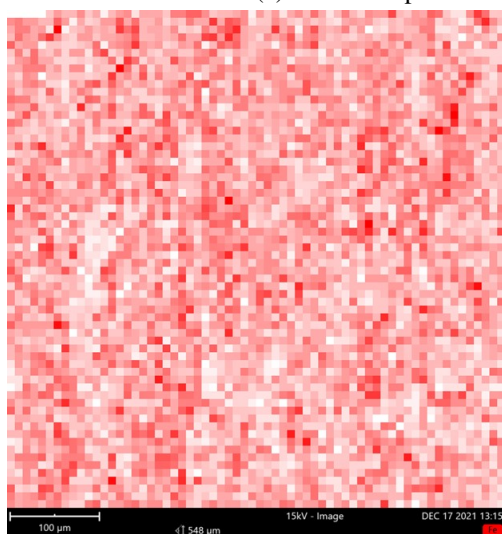
Weight % chemical composition					
	Fe	Cr	Cu	Ni	Si
17-4PH islands measured chemical composition (spot test EDS)	73.47	14.90	7.11	3.64	0.76
17-4PH phase fraction	0.425	0.425	0.425	0.425	0.425
Element quantity in the 17-4PH islands inside the composite	31.22	6.33	3.02	1.55	0.32
Composite measured average chemical composition	33.04	7.14	57.91	1.66	
Element quantity in the Cu islands inside the composite	1.81	0.81	54.88	0.12	
Cu phase fraction	0.575	0.575	0.575	0.575	0.575
Cu islands calculated chemical composition	3.15	1.41	95.45	0.20	

Table 8.7 Copper islands chemical composition

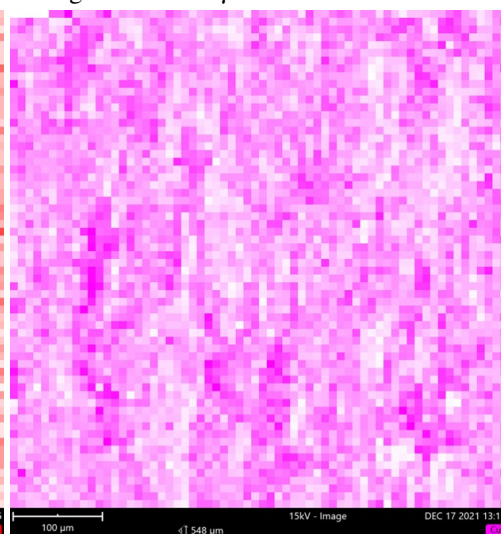
This experimentally result shows that more than one elements has migrated, after the melting process, from the 17-4PH alloy to the pure copper. An additional experimental evidence is provide in order to support the aforementioned thesis. It is possible to see this migration phenomenon by analysis the Z colored EDS maps in figure 8.27. This image shows that the all alloys component of the 17-4PH phase have been spread all around the composite matrix.



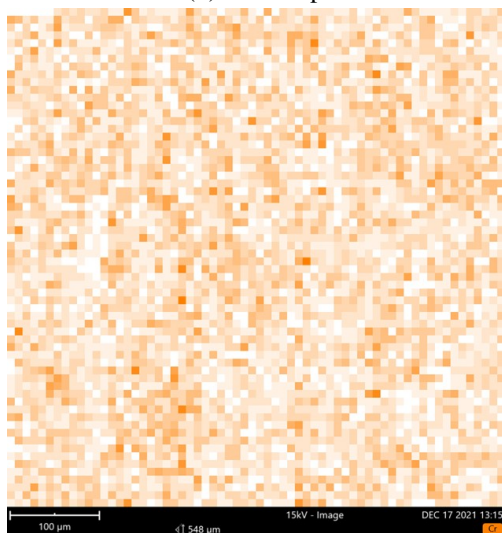
(a) General Z plane SEM image - FOV 535 μm



(b) Iron Map



(c) Copper Map



(d) Chromium Map



(e) Nickel Map

Fig. 8.27 Z plane EDS SEM map chemical composition map analysis

8.4.4 Hypothetical explanation of the mismatch between pre-custom Cu-174PH powder % composition and the experimental % powder composition

A possible explanation of the difference measured chemical composition of the composite (57,5% Cu - 42,5% 17-4PH Table 8.7) respect to the starting 65% Cu - 35% 17-4PH pre-mixed powder could be the vertical movement of the powder supplier tank and the horizontal movement of the blade system which scatters the powder into the printing platform.

During all printing process supplier tank hold the pre-mixed custom powder. In order to create the new powder layer the tank moves up and the printing platform goes down. This movement is actuated by a step mechanical mechanism. This step-by-step movement create a vibration which allows copper powder to go down respect to the Z moving direction of the supplier pre-mixed power tanks. This phenomenon make possible a powders gradient concentration along the Z axe of the powder tank. In addition, this gradient is not constant during the printing process because every new layer there is an additional vibration which store more copper powder to the bottom of the tank highlighting the separation of the two originally mixed powders (Figure 8.28).

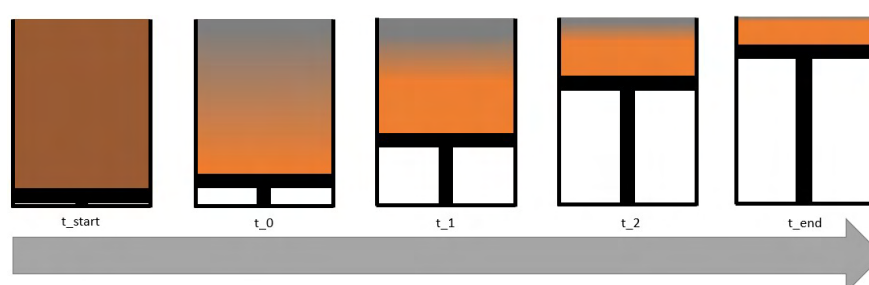


Fig. 8.28 Gradient concentration along the Z axe of the powder supplier tank

This first phenomenon could generate an opposite gradient concentration on the printing platform respect to the Z building direction. The more the building grows the more the building platform goes down and the tank powder supplier goes up, therefore the copper concentration at the end of the job will be slightly greater at the top respect to the bottom (Figure 8.29).

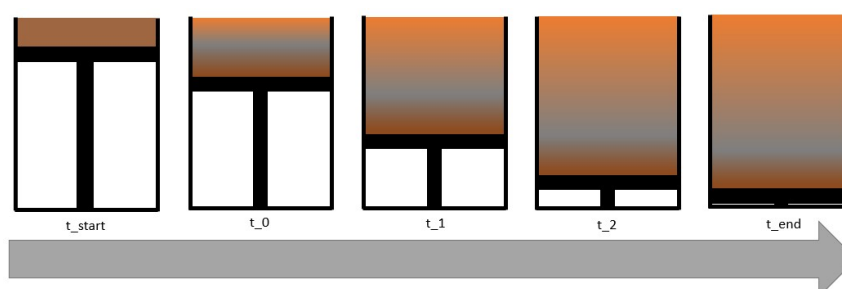


Fig. 8.29 Gradient concentration along the Z axe of the printing platform

This powder behaviour is in addition to the most relevant hypothesis: the horizontal blade movement generate a sliding (flowing) movement between the particles loaded on the blade which promotes the fall of the heaviest and smallest particles (copper) at the beginning of the spreading process. If this hypothesis is correct, and experimental results agrees with this state, the end of the printing platform, respect to the X spread direction of the blade, has a greater 17-4PH concentration of powder and the starting deposition area has an higher concentration of copper powder (Figure 8.30).

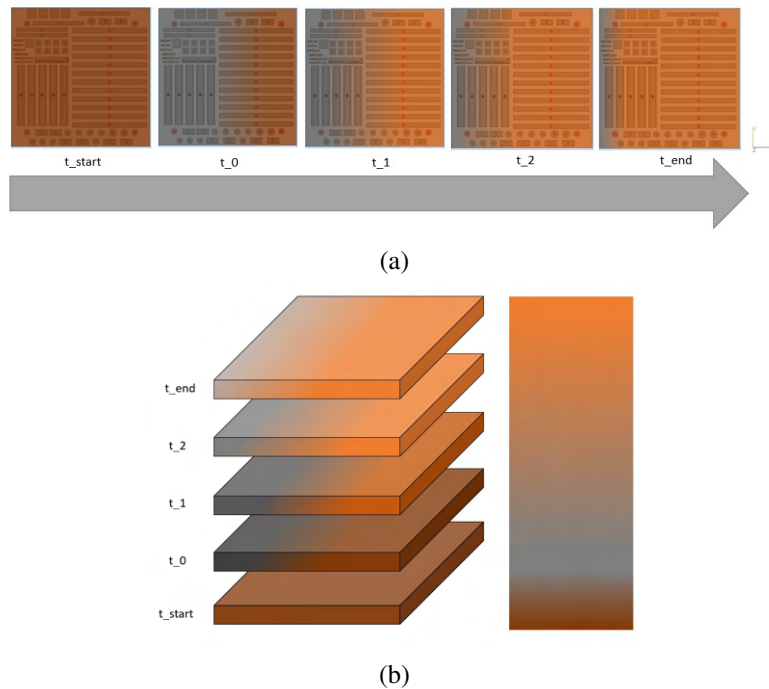


Fig. 8.30 Powders distribution on the platform

The higher 17-4PH chemical concentration evaluated by the EDS chemical analysis could be due to the location of the tested specimen, which is on the bottom of the printings platform respect to the X axe (the blade moves from right to left respect to the X axe in Figure 8.31).

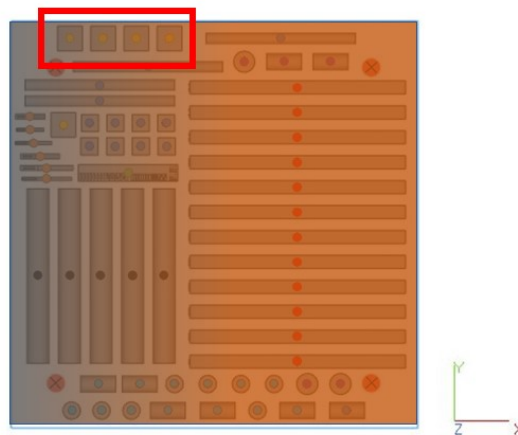


Fig. 8.31 Chemical composition specimen location on the printing platform

A first preliminary analysis has been performed on the top building direction surface of a random traction tensile test specimens (before the test): the z hypothetical chemical concentration gradient has not been analysed. On the other hand the more relevant chemical gradient is the one on the blade spread powders direction. Figure 8.32 shows the analysed sit for the result presented in Table 8.8.



Fig. 8.32 Chemical composition gradient analysis - specimen location on the printing platform

Chemical composition gradient analysis

	Cu %	Fe%	Cr %	Ni %
Start site	63.55	29.00	6.49	0.97
End site	55.51	35	7.90	1.56

Table 8.8 Chemical composition X-direction gradient analysis

This first analysis could be a starting point of a more detailed study. By analysis the results it is possible to observe that the Copper concentration is higher at the beginning of the platform and about 10% lower at the middle of the platform. Results according with the hypothetical theory exposed at the beginning of the present Section.

EDS maps of results exposed in Table 8.8 are presented in Figure 8.34 (attention: unfortunately the program has performed the analysis of same elements with different colors, from one analysis site to the another one).

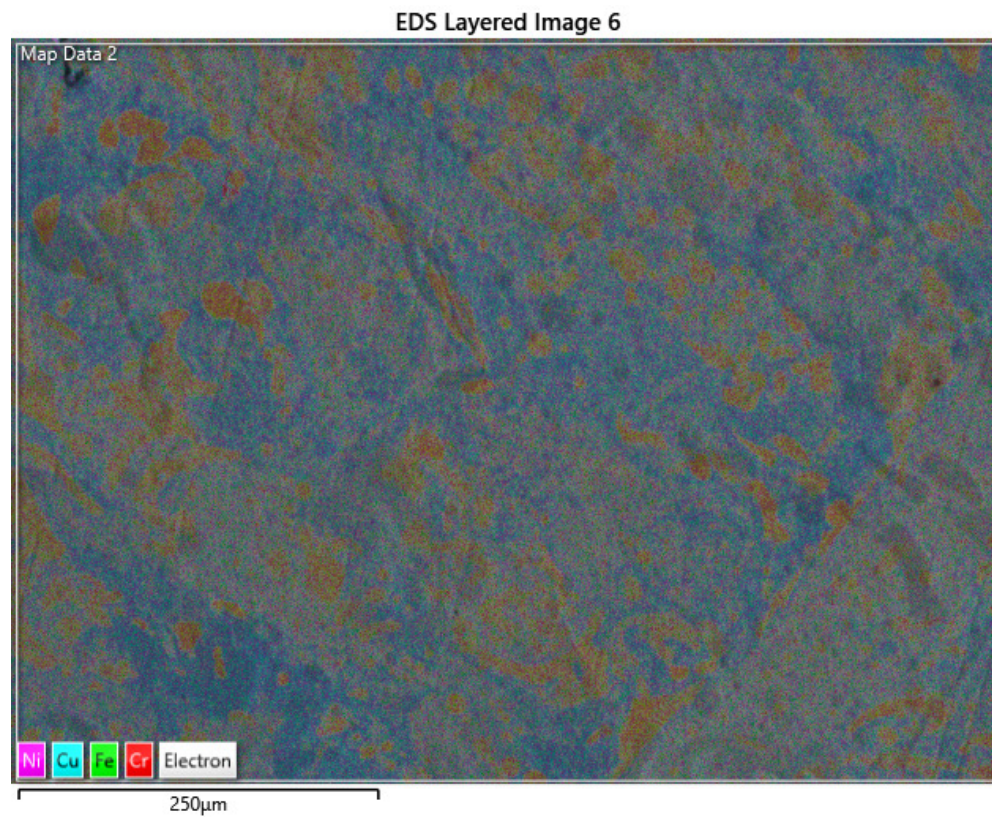


Fig. 8.33 Chemical composition map analysis - Start location on traction specimen - XY direction

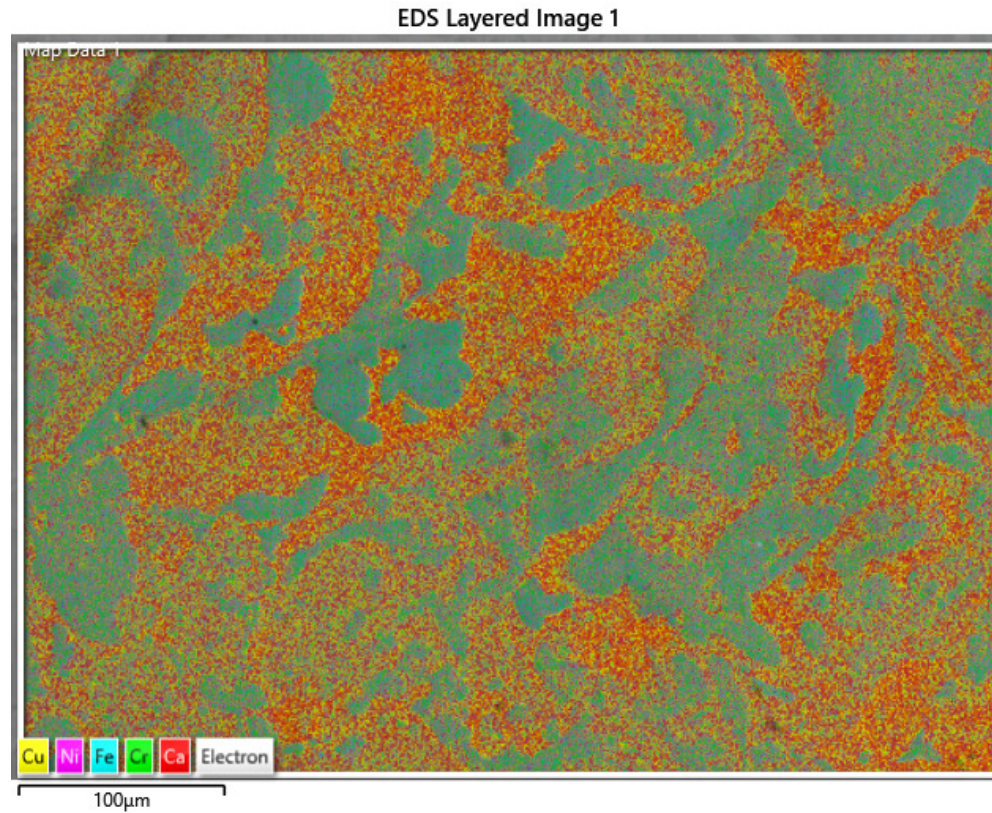


Fig. 8.34 Chemical composition map analysis - End location on traction specimen - XY direction

8.5 Porosity analysis

The present study has been done on 3 random areas for the XY plane and 3 random areas for the Z building direction plane. The analysis has been done respect to two different magnification: $500\ \mu\text{m}$ and $10\ \mu\text{m}$ range. The porosity analysis shows a low porosity level. Figure 8.35 and Figure 8.36 are used to obtain results presented in Table 8.9.

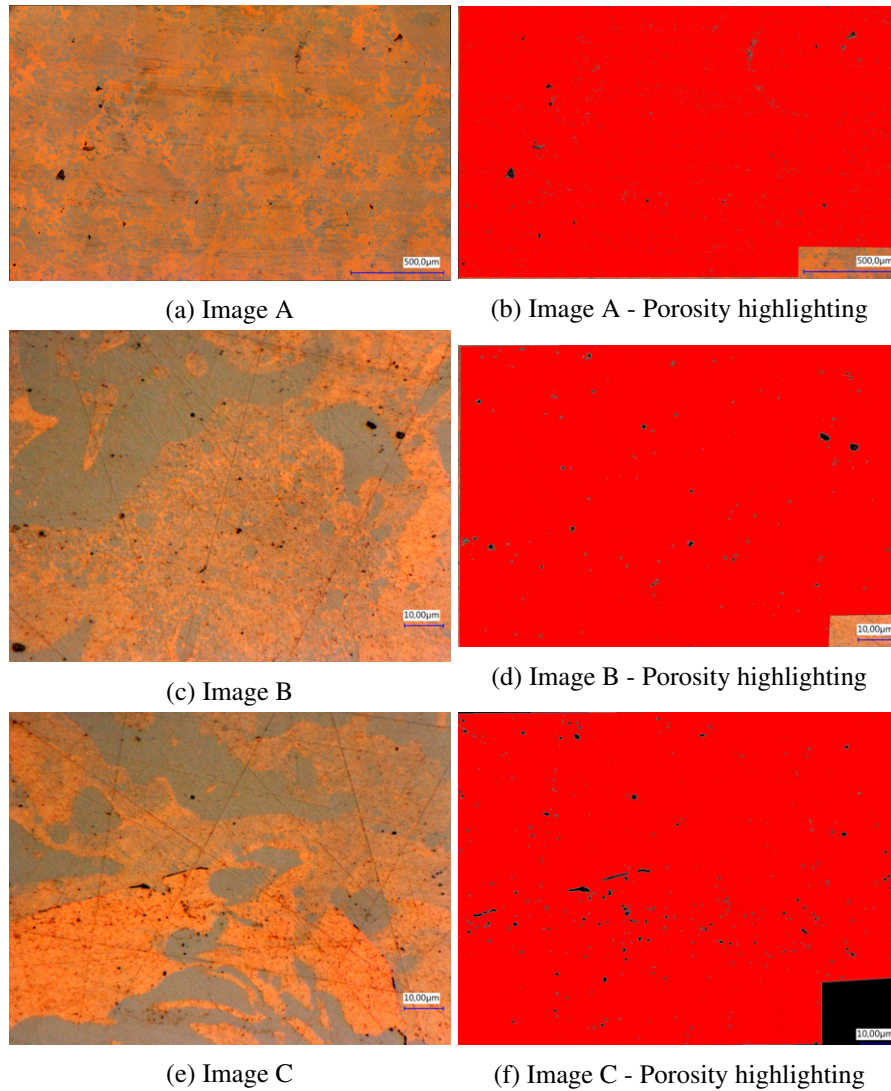


Fig. 8.35 XY plane porosity highlighting

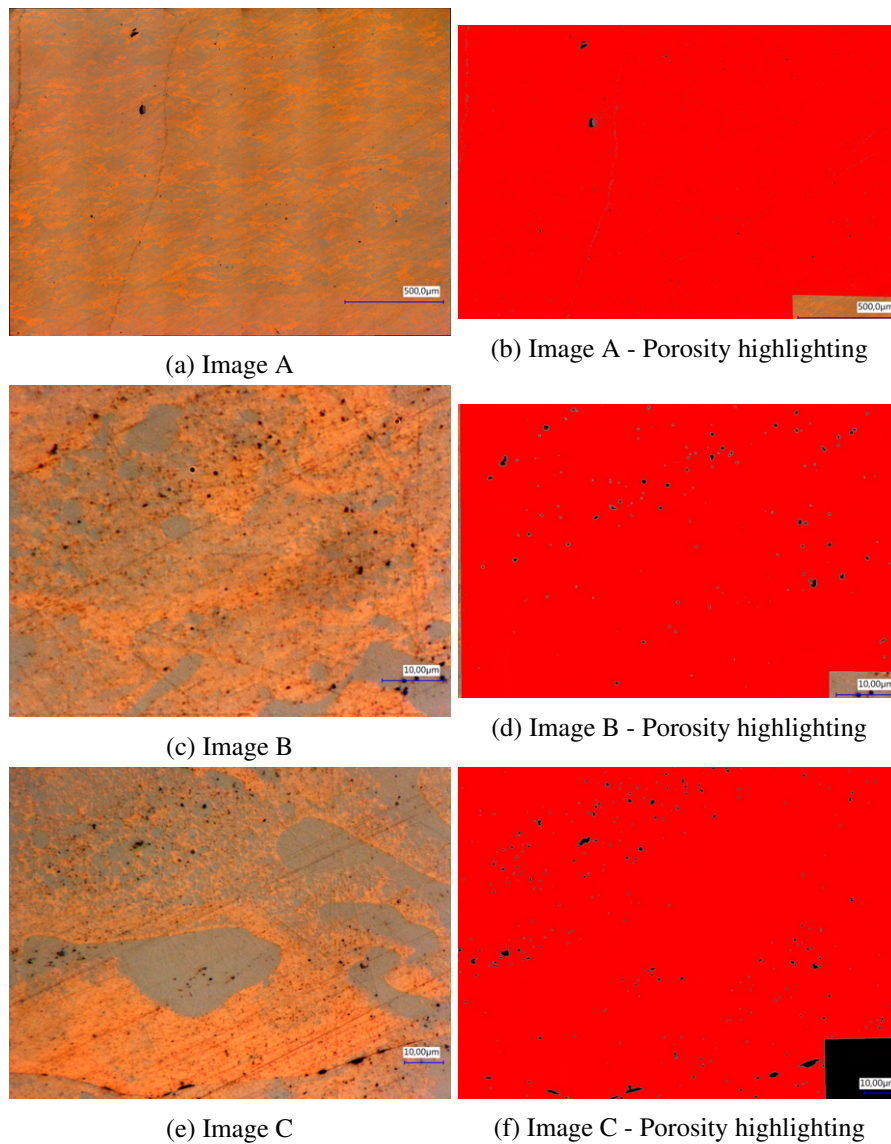


Fig. 8.36 Z plane porosity highlighting

			Value	Diameter	
				Max μm	Min μm
XY Plane	Image A	Average μm		8,2	4,2
		Max		2796,4	1467,0
		%	99,6		
	Image B	Average μm		7,11	4,22
		Max		30,64	18,28
		%	99.63		
	Image C	Average μm		5,41	3,18
		Max		26,85	15,85
		%	99,42		
Z Plane	Image A	Average μm		0,6	0,2
		Max		335,1	33,1
		%	99,8		
	Image B	Average μm		3,85	2,31
		Max		88,46	53,11
		%	99,53		
	Image C	Average μm		11,63	7,01
		Max		139,95	83,92
		%	99,48		

Table 8.9 Porosity analysis

8.6 Void distribution

A qualitative analysis of void (mainly lake of fusion porosity) distribution is presented by the CT scan images in Figure 8.37 and Figure 8.38, for Z direction plane and XY plane respectively. The specimen analysed was a cylindrical compression one (cyan blue dots in Figure 5.15a).

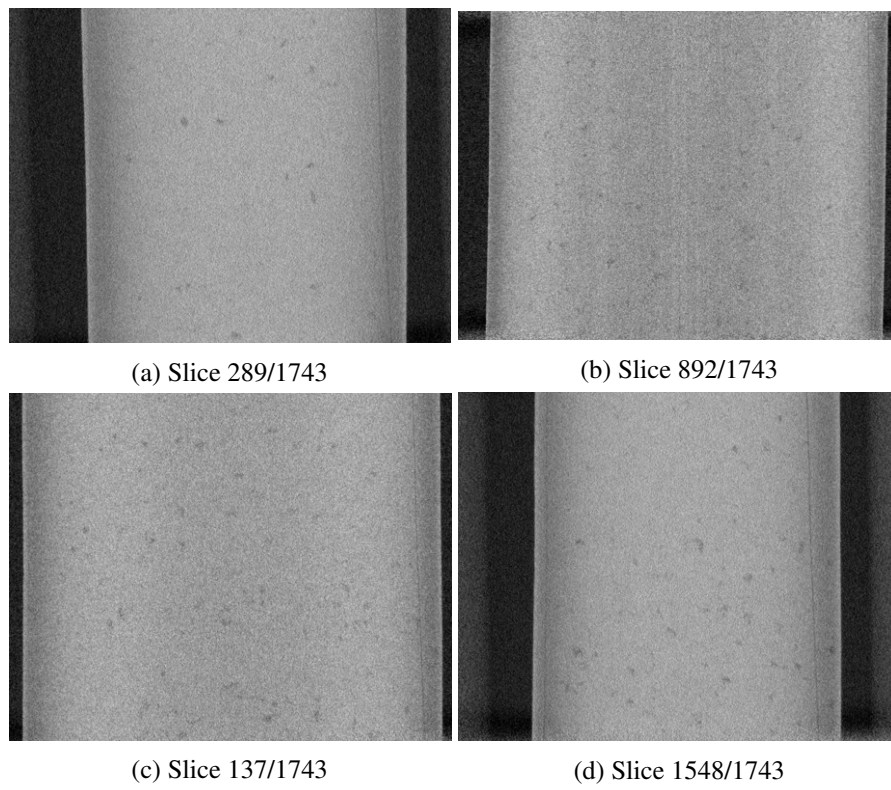


Fig. 8.37 CT scan Z direction images

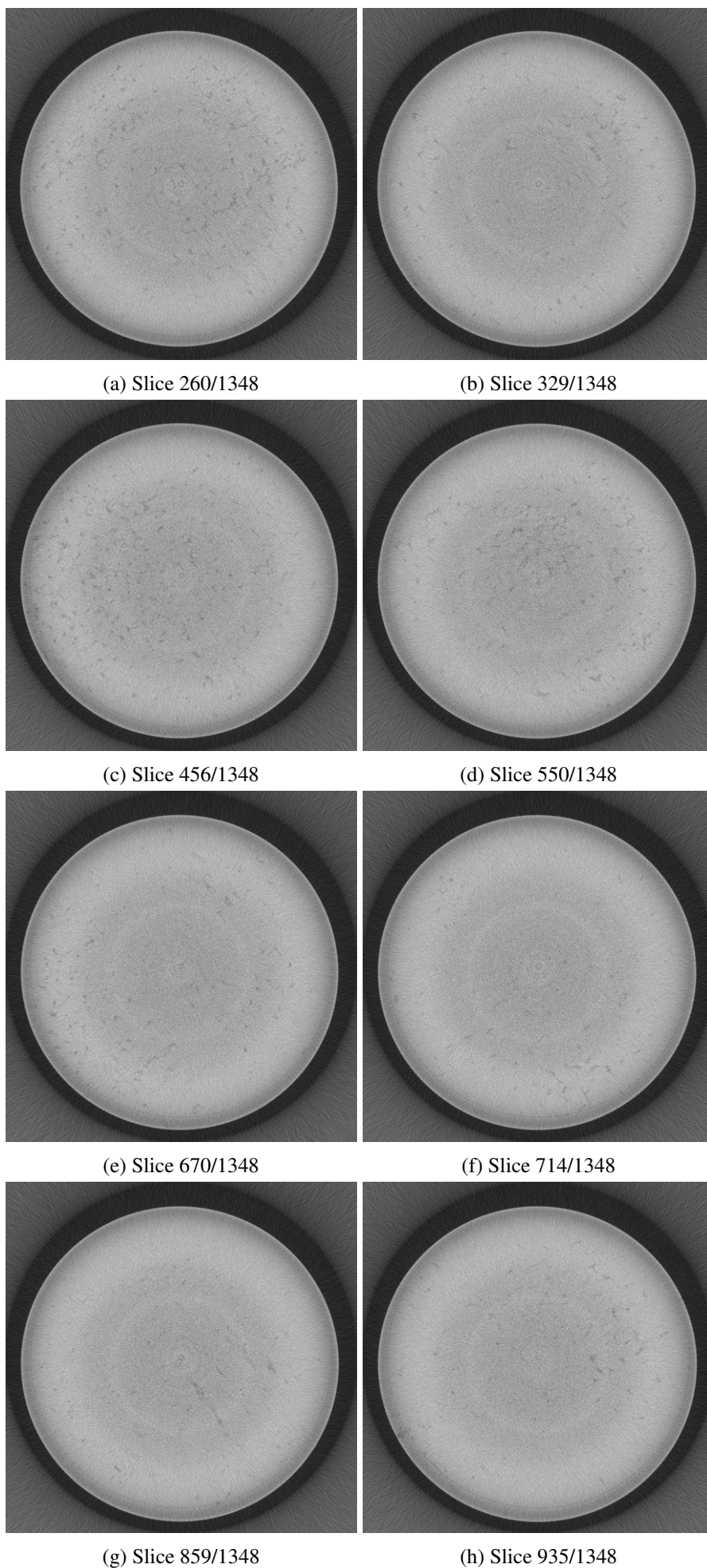


Fig. 8.38 CT scan XY plane images

The result presented shows that the void are randomly spread all around the component respect to both, Z and XY plane. The test do not revealed particular denitrification at the center rather than to the edges of the specimen. It is important to remake that, while the porosity concentration is very low, synonymous of very good local process parameters, the void concentration is very high: this is due to the high number of lake of fusion. A process parameters optimization is recommended.

Chapter 9

Experimental Results: Thermal Properties Tests

9.1 Thermal Conductivity - Hot Disk

The Hot Disk method has been employed in order to indirectly¹ evaluate the Cu-174PH thermal conductivity. Random disk have been cut from the thermal conductivity cylinder specimens and from the cube specimens, both printed in Job 1. Both XY disk and Z direction disk have been successfully tested (Figure 9.1). Note that the thermal conductivity is tested respect to the normal direction of the section plane, therefore the XY section plane gives back the Z direction conductivity and vice versa.

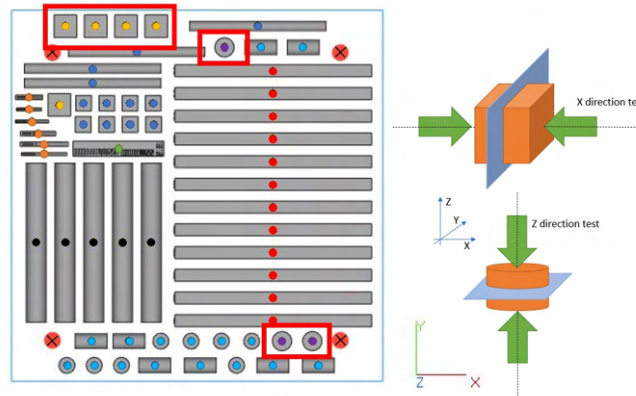


Fig. 9.1 Thermal Conductivity specimens location - Job 1

9.1.1 Z direction thermal conductivity

The first Z direction 10 test set up had a slight high probing depth because of the sine-like residual curve shape (one maximum and one minimum, Figure 9.2d). However the residual sine-like curve could also be generated by a slight (mK) sample temperature

¹This test is not a direct measure of the specific heat capacity of a material: there is a post processing and a calibration procedure

instability during the tests: this behaviour could be explained by the presence of random porosity that could not allow a perfect symmetrical thermal wave propagation. Another possible explanation could be the bi-metal matrix of the tested new material.

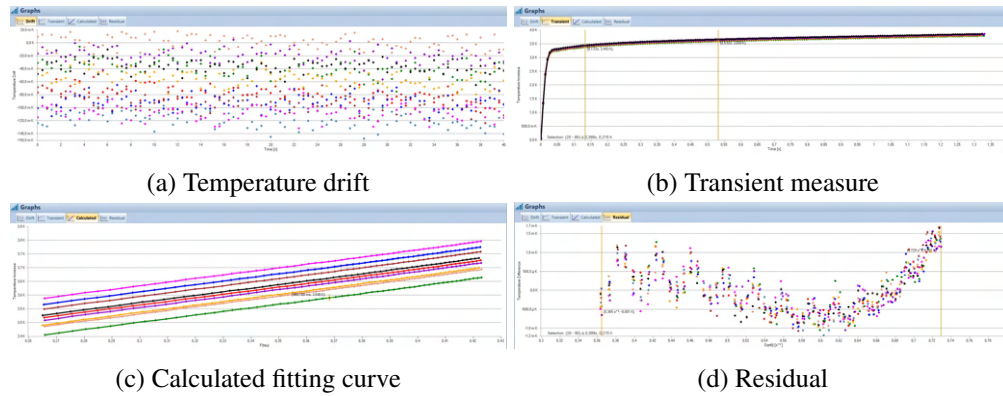


Fig. 9.2 Z direction thermal conductivity test - 4.5 mm Probing Depth - 10 tests

Z Direction Thermal Conductivity - 4.5 mm Probing Depth								
Test Number	Starting Temperature [C]	Total Temperature Increase [K]	Probing Depth [mm]	Heating Power [mW]	Measurement Time [s]	Thermal Conductivity [W/mK]	Average Thermal Conductivity [W/mK]	DV.ST
1	23	3.92	4.56	736,65	1	31.4	31.41	0.09
2	23	3.81	4.57	736,65	1	31.42		
3	23	3.87	4.56	736,65	1	31.49		
4	23	3.84	4.55	736,65	1	31.34		
5	23	3.90	4.56	736,65	1	31.38		
6	23	3.92	4.56	736,65	1	31.32		
7	23	3.94	4.56	736,65	1	31.55		
8	23	3.84	4.57	736,65	1	31.58		
9	23	3.86	4.57	736,65	1	31.36		
10	23	3.88	4.55	736,65	1	31.33		

Table 9.1 Z direction thermal conductivity results - 4.5 mm Probing Depth

In order to have a better residual respect to the one presented in Figure 9.2d, the probing depth has been lowered to 4.0 mm. A different samples has been tested 10 times. The results is a better theoretically fitting curve. However, the reality shows that no remarkable difference between 4.5 and 4.0 mm probing depth.

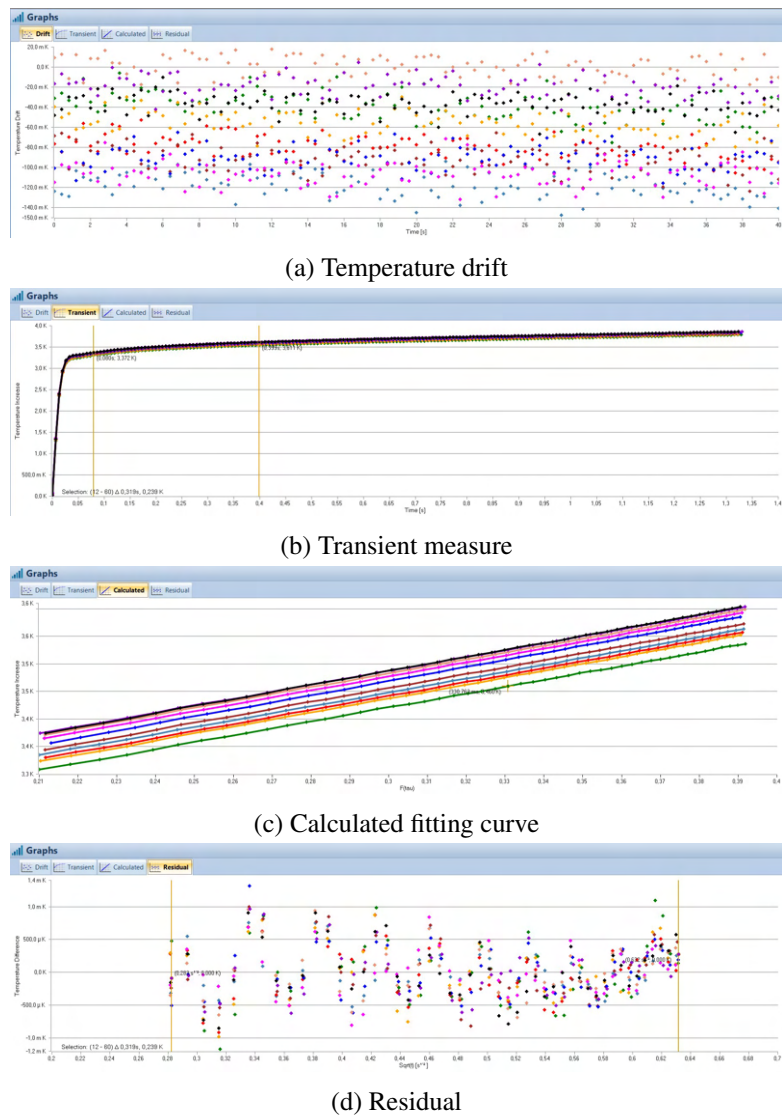


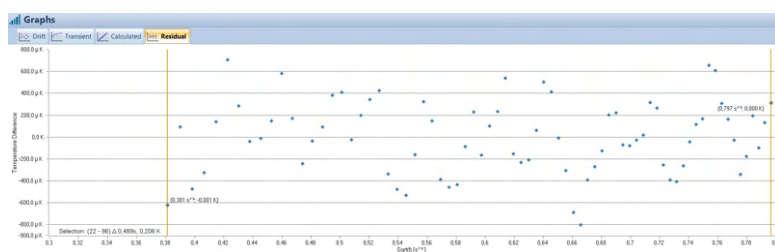
Fig. 9.3 Z direction thermal conductivity test - 4.0 mm Probing Depth - 10 tests

Z Direction Thermal Conductivity								
Test Number	Starting Temperature [C]	Total Temperature Increase [K]	Probing Depth [mm]	Heating Power [mW]	Measurement Time [s]	Thermal Conductivity [W/mK]	Average Thermal Conductivity [W/mK]	DV.ST
1	23	3.81	4.04	736,65	1	32.86	32.66	0.21
2	23	3.78	4.05	736,65	1	32.88		
3	23	3.80	4.02	736,65	1	32.65		
4	23	3.79	4.02	736,65	1	32.62		
5	23	3.81	4.03	736,65	1	32.64		
6	23	3.83	4.00	736,65	1	32.19		
7	23	3.83	4.02	736,65	1	32.67		
8	23	3.84	4.04	736,65	1	32.88		
9	23	3.85	4.05	736,65	1	32.80		
10	23	3.84	4.01	736,65	1	32.43		

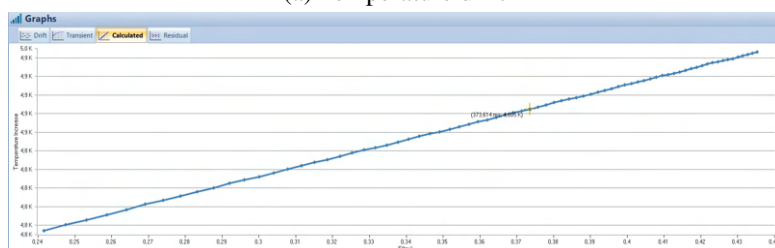
Table 9.2 Z direction thermal conductivity results - 4.0 mm Probing Depth

9.1.2 XY direction thermal conductivity

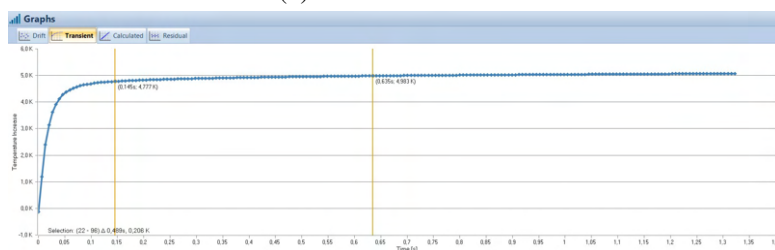
Same procedure has been employed in order to test the XY direction thermal conductivity. Because of the specimen bigger surface and depth a higher probing depth has been used (5 mm). Because of the very high repeatability (low standard deviation) of all Z direction 10 test (for both, 4.0 mm and 4.5 mm probing depth), just 6 tests have been done for the XY direction characterization.



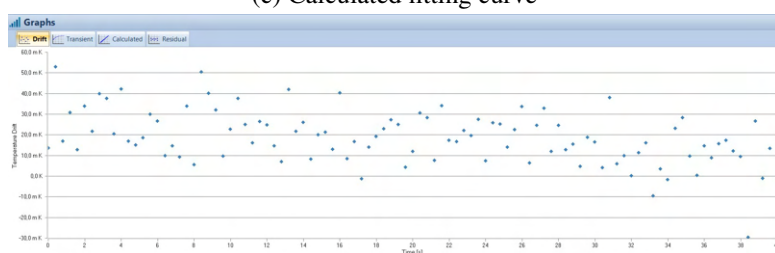
(a) Temperature drift



(b) Transient measure



(c) Calculated fitting curve



(d) Residual

Fig. 9.4 XY direction thermal conductivity test - 5.0 mm Probing Depth - 1 test out of 6

Test Number	Strating Temperature [C]	XY Direction Thermal Conductivity					Average Thermal Conductivity [W/mK]	DV.ST
		Total Temperature Increase [K]	Probing Depth [mm]	Heating Power [mW]	Measurement Time [s]	Thermal Conductivity [W/mK]		
1	23	5.03	4.99	736,65	1	31.35	31.45	0.17
2	23	5.16	5.01	736,65	1	31.66		
3	23	5.09	4.98	736,65	1	31.23		
4	23	5.17	5.00	736,65	1	31.33		
5	23	5.13	5.00	736,65	1	31.57		
6	23	5.16	5.00	736,65	1	31.60		

Table 9.3 XY direction thermal conductivity results - 5 mm Probing Depth

9.1.3 Z direction thermal conductivity: 700° C heat treatment

The chemical composition of the copper matrix, evaluated in Section 8.4.3, has a 3.15 weight % of Iron inside (Table 8.7). A first-tray experimental heat treatment has been performed to a Z direction thermal conductivity specimen in order to evaluate the possibility of a relevant improving of thermal conductivity. Since no remarkable difference of thermal conductivity between Z and XY directions have been found, only Z direction thermal conductivity after the heat treatment has been tested.

The target temperature has been chose in order to have the minimum iron weight % available inside the copper matrix, according with the Fe-Cu phase diagram reported in Figure 8.4. A 16h 700° annealing heat treatment have been done. A slow cooling inside the oven have been used.

The results presented in Table 9.4 shows that the thermal conductivity has an improvements of about 100%: from 32 W/mK to about 60 w/mK proving that the copper has been detoxified by impurities. A better conductivity can be surely achieve after heat treatment optimization via step-by-step EDS chemical analysis.

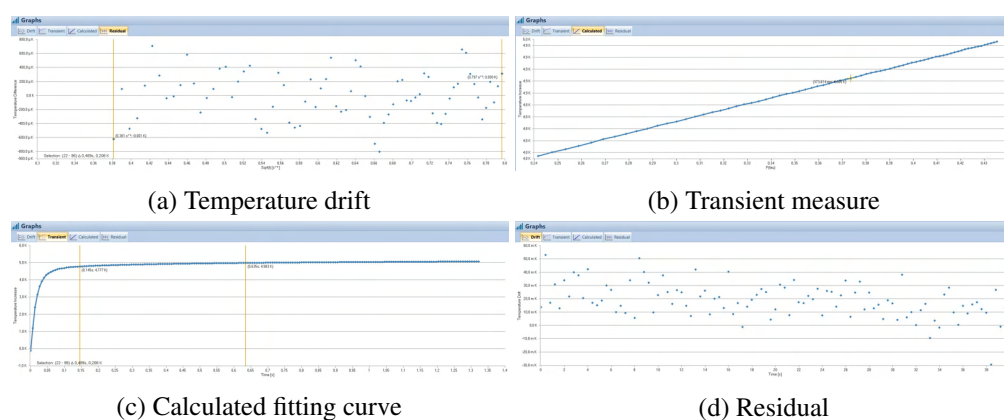


Fig. 9.5 Z direction thermal conductivity Heat Treated test - 4.9 mm Probing Depth - 5 tests

Test Number	Starting Temperature [C]	Total Temperature Increase [K]	XY Direction Thermal Conductivity				Average Thermal Conductivity [W/mK]	DV.ST
			Probing Depth [mm]	Heating Power [mW]	Measurement Time [s]	Thermal Conductivity [W/mK]		
1	23	4.68	4.86	736,65	1	57.24	57.52	0.79
2	23	4.57	4.85	736,65	1	56.78		
3	23	4.68	4.85	736,65	1	56.99		
4	23	4.65	4.87	736,65	1	57.13		
5	23	4.64	4.91	736,65	1	58.19		
6	23	4.69	4.94	736,65	1	58.80		

Table 9.4 Z direction thermal conductivity Heat Treated results - 4.9 mm Probing Depth

9.1.4 Thermal conductivity comparison

A brief resume of thermal conductivity for the new Cu-174PH tested material is presented in Table 9.5. Respect to available common and SM processed materials in rocker engine industry, must of the time the measured Cu-174PH thermal conductivity lower. However the mechanical properties much higher than common alloys.

Cu-174PH Thermal Conductivity			
	Thermal Conductivity [W/mK]	DV.ST	% increment
XY direction	31.45	0.17	reference
Z Direction	32.66	0.21	+ 3.8
Z Direction Heat Treated	57.52	0.79	+ 82.89

Table 9.5 Cu-174PH Thermal Conductivity

Respect to the historical NASA common processed materials (Figure 9.6) the Cu-174PH thermal conductivity is a qualitative average 10%. After the heat treatment is can almost reach the 17%.

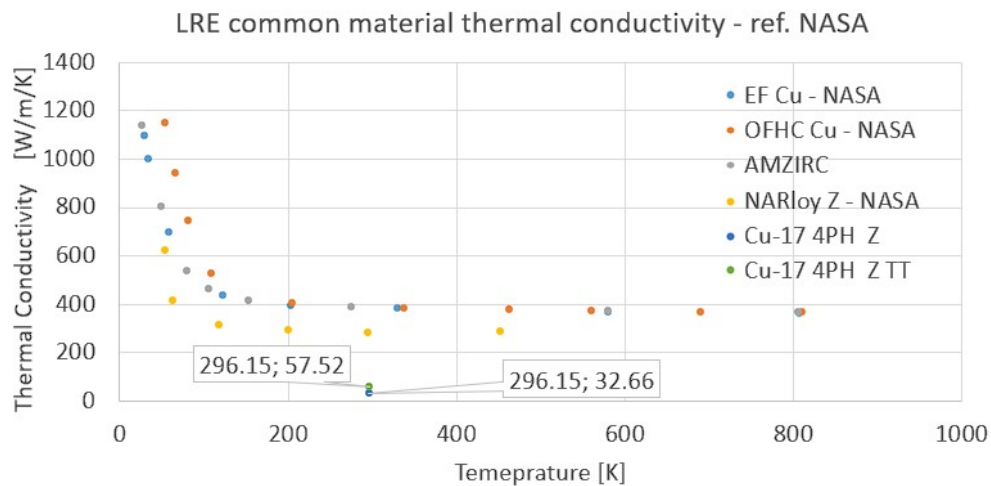


Fig. 9.6 Cu-174PH Thermal Conductivity comparison with LRE historical NASA materials, data from [23]

The average situation slightly improves when Cu-174PH composite is compared with the new NASA's AM SLM alloys: in particular Cu-174PH thermal conductivity is a qualitative 12% of the average new NASA's alloys. It is interesting to highlight that the AM SLM process of the NASA's new copper alloys lower the thermal conductivity respect to the same alloy processed with common manufacturing processes (SLM alloys have a thermal conductivity which is an average 70% of the same alloy processed with standard processes).

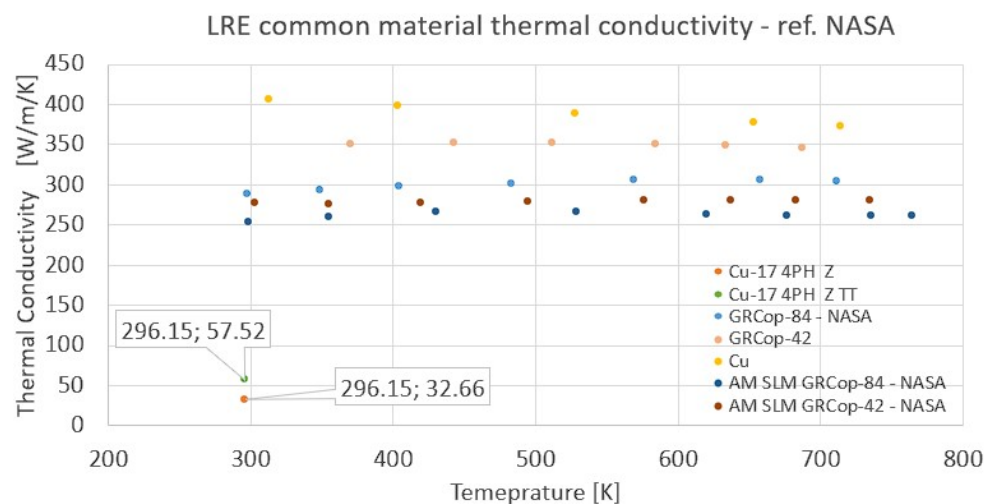


Fig. 9.7 Cu-174PH Thermal Conductivity comparison with modern LRE AM NASA materials, data from [24]

Finally a comparison with a common C18150 copper alloy is presented in Figure 9.8.

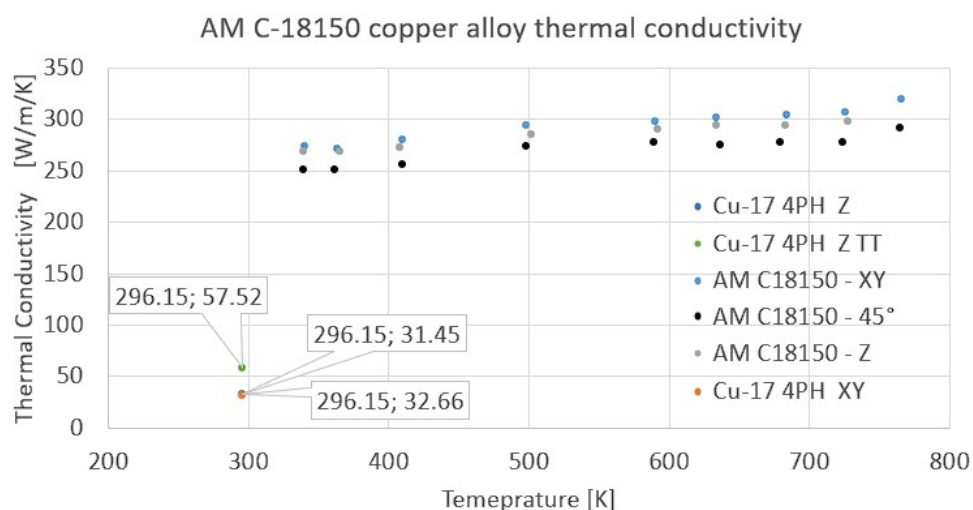


Fig. 9.8 Cu-174PH Thermal Conductivity comparison with AM C18150 copper alloy, data from [25]

9.2 Specific Heat Capacity - DSC

The DSC (Differential Scanning Calorimetry) method has been employed in order to indirectly² evaluate the Cu-174PH specific heat capacity. Simple preparation has been presented in Section 6.3.1. The test shows successfully result for the temperature range from -40°C to 350°C.

By applying the isothermal step temperature ramping (Figure 6.15) the specific heat capacity have been calculated. Result from test post processing of Cu-174PH, pure copper and pure iron materials is presented in Figure 9.9.

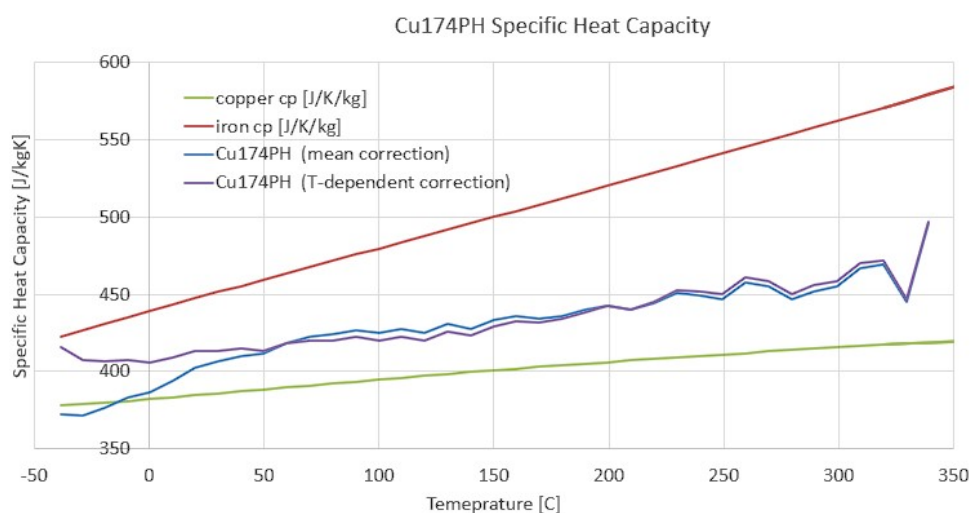


Fig. 9.9 Cu-174PH Specific Heat Capacity vs Temperature

²This test is not a direct measure of the specific heat capacity of a material: there is a post processing and a calibration procedure

Two different correction have been used: the standard ASTM E1269 method and the NIST Temperature-correction method.

The standard method consist on evaluating the variation of the effective heat power (specimen heat power minus the black heat power), ΔQ , during the isothermal 1 min step and dividing it by the heating rate ($10\text{ C/min} = 0.16\text{ K/s}$). In order to obtain the specific heat capacity the result is divided by the specimen's weight. Figure 9.10 shows a schematic representation of the process. By repeating the same process for every isothermal curve is possible to obtain the specific heat capacity vs temperature curve. However this first result have to be corrected by a calibrated constant, as ASTM E1269 propose.

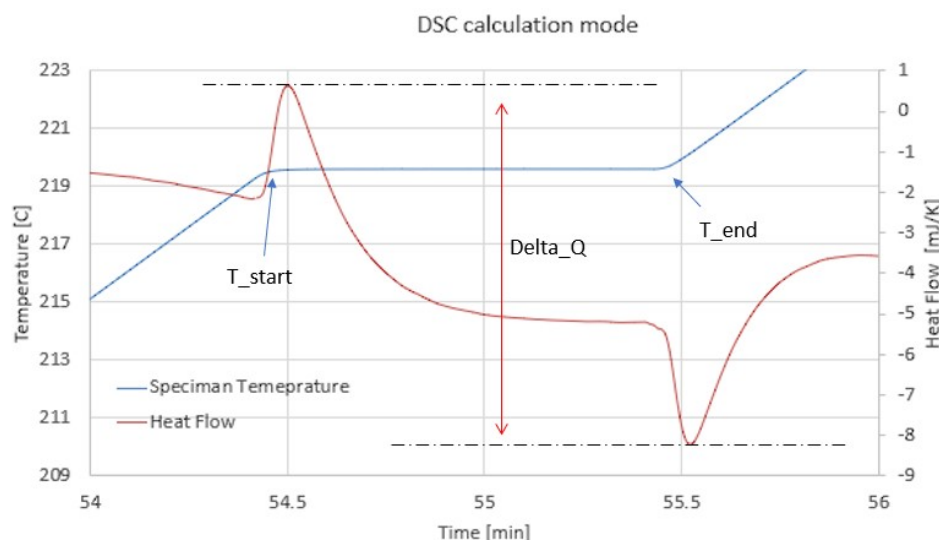


Fig. 9.10 Delta heat power evaluation example

The calibrated correction has been calculated from a calibration procedure from the iron tested sample. The NIST method propose a different calibration related to a more complex polynomial fitting correction.

9.2.1 Specific Heat Capacity comparison

Respect to the historical NASA common processed materials (Figure 9.11) the Cu-174PH specific heat capacity have no particular qualitative difference .

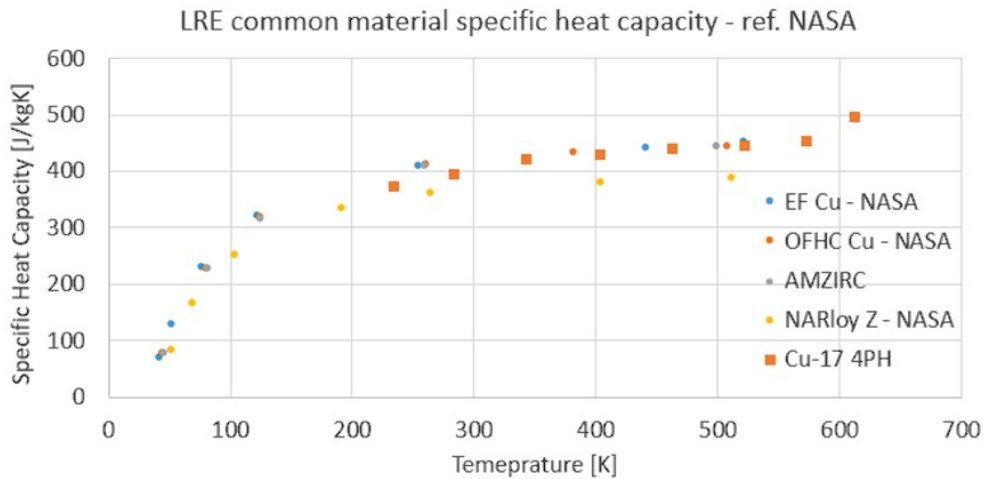


Fig. 9.11 Cu-174PH specific heat capacity comparison with LRE historical NASA materials, data from [23]

The comparison with a common C18150 copper alloy is presented in Figure 9.12. It is possible to see that the trend of the Cu-174PH is the same of the C18150 copper alloy: a temperature raising is followed by a specific heat capacity increase.

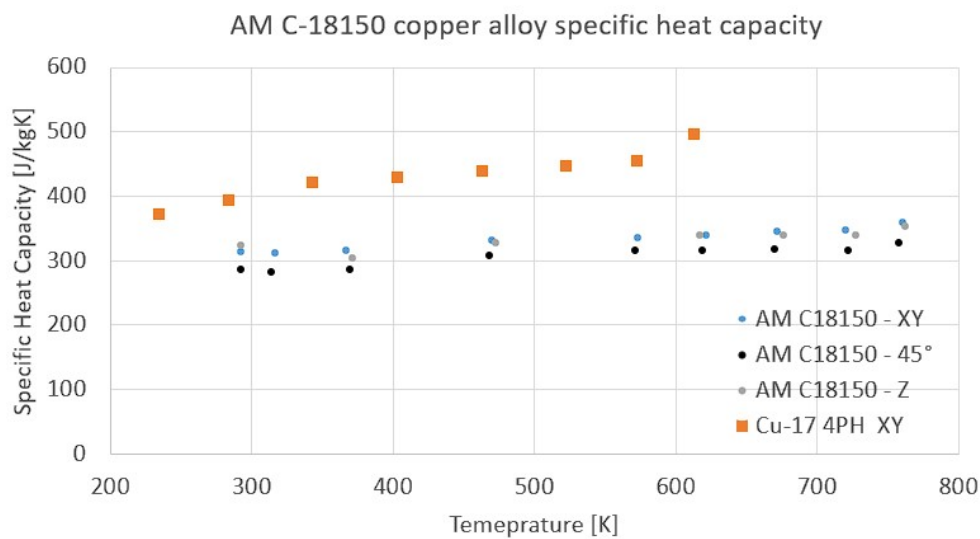


Fig. 9.12 Cu-174PH specific heat capacity comparison with AM C18150 copper alloy, data from [25]

9.3 Coefficient of Linear Thermal Dilatation - TMA

The TMA (Thermomechanical Analysis) method has been employed in order to directly³ evaluate the Cu-174PH coefficient of linear thermal dilatation.

The result of the TMA test is the linear displacement vs temperature presented in Figure 9.13.

³This test is a direct measure of the coefficient of linear thermal dilatation of a material: there are not particular calibration procedures

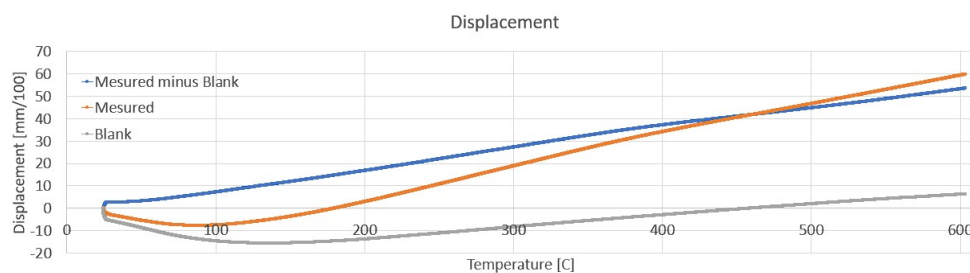


Fig. 9.13 Linear displacement vs temperature test results

Using the simple $\Delta L = \alpha L_0 \Delta T$ relation the α coefficient of linear thermal dilatation is calculated for every temperature increment and reported in Figure 9.14. There is no remarkable time dependent behavior, as expected.

The manual post process gives back a coefficient lower than the one automatic post processed (with a specific machine proprietary correction) by the machine software. This slight difference could be due to the particular matrix of the material, which is bi-metallic, and to the Additive Manufacturing process (porosity, defects, lakes of fusion, ecc).

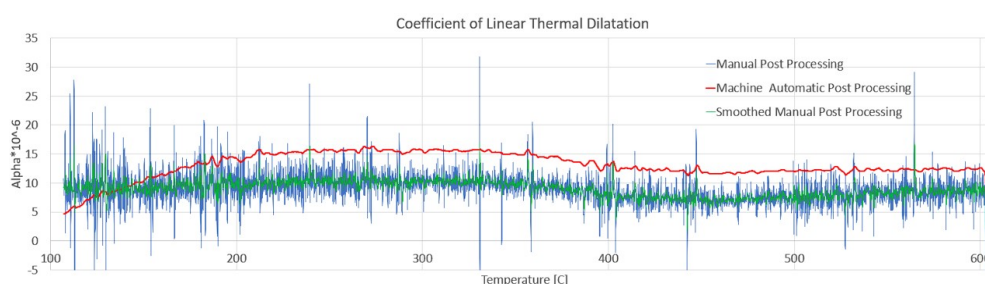


Fig. 9.14 Cu-174PH Coefficient of Linear Thermal Dilatation vs Temperature

The final result and a basic cooperation with some common LRE thrust chamber materials is presented in Table 9.6.

Coefficient of Linear Thermal Dilatation		
Value	Value	DV.ST
Cu-174PH average (Machine post processing)	12.92	2.38
Cu-174PH average (Manual post processing)	8.95	2.66
General Copper	17	
General Iron	12	
AMZIRC Copper alloy - NASA	17.2	
NARloy-Z Copper alloy - NASA	17.2	
OFHC Copper - NASA	17.2	
EF Copper - NASA	17.2	

Table 9.6 Cooperation of different materials coefficient of linear thermal dilatation

Chapter 10

Experimental Results: Mechanical Properties Tests

10.1 Hardness and Micro-hardness

Hardness test has been used in order to characterize two different Cu-174Ph properties, one technological and the other one mechanical: i) with a good repeatability of the test it is possible to state that the powder mixing process (POWMIX) allows a homogeneous Cu and 17-4PH distribution on the printing platform; ii) the test allows to have an extrinsic material property, hardness, which is the resistance presented by a material respect to plastic deformation due to the penetration of an indenter tool; iii) by analysis the result from Z plane and XY plane it is possible to evaluate the anisotropy of the mechanical properties of the composite material; iv) by a proper observation of the indentation shape it is possible to evaluate the compression/tension residual stresses after the AM SLM process.

Two different random cube specimen have been tested for hardness characterization (procedure described in Section 6.4.1). For every specimen's surface analysed 10 test have been performed in a random order all around a centred 15mm X 15 mm square inside the 20 x 20 mm specimen's surface. The average value and the relative standard deviation will be presented.

In order to evaluate the interior¹ mechanical behavior free from surface roughness effect, both XY and Z planes of both, A and B samples, have been polished. Result from polishing employed for the micro-hardness tests is presented in Figure 10.1. For the hardness test a less time-expensive polishing has been performed.

¹Read Section 6.4.1

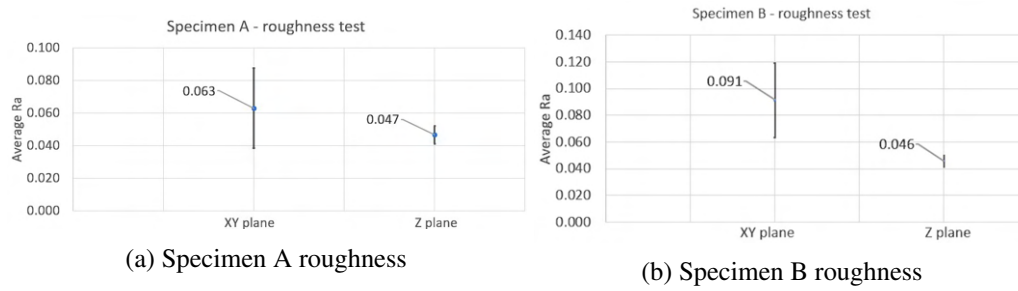


Fig. 10.1 Roughness analysis

10.1.1 Indentation Size Effect Evaluation

A preliminary hardness test results are plotted in Figure 10.2 for different applied loads, run on the A specimen on two different surfaces, parallel and perpendicular to deposition direction. In the same plot the data scattering, i.e. standard deviation, is reported. Every different load has been tested 4 times respect to both, Z and XY planes. The average of 4 tests is reported with the standard deviation. It can be observed that increasing the load no particular decreases of the scattering is performed. HV20 has been identified as the optimal method for hardness properties mainly because of the lowest standard deviation respect to the other tested load.

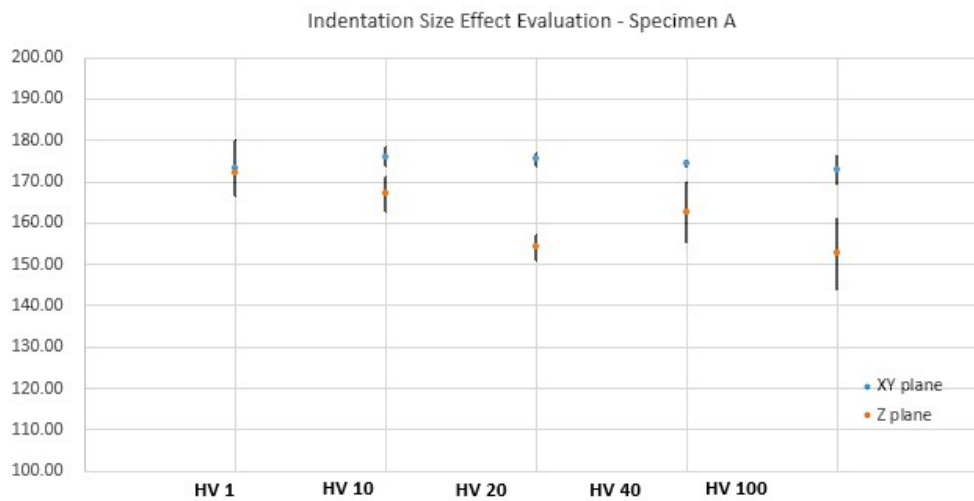


Fig. 10.2 Indentation Size Effect Evaluation - Cu-174PH

The result shows that no relevant Indentation Size Effects are reported. If by raising the load the hardness do not rise then it follows that the elastic behavior is not relevant for the hardness calculation: the Cu-174PH material (as the present work will show) has a low elasticity, close to pure copper. On the other hand, more fragile materials, such as Inconel718 (which has an elasticity 2-3 times the copper one), for lower loads the elastic springback is definitely more relevant and therefore an ISE is presented. This aforementioned theory has been directly proved by a parallel work, performed by the same team of the present study, on AM SLM Inconel718 (Appendix E). A particular ISE of Inconels718 is presented in Figure 10.3.

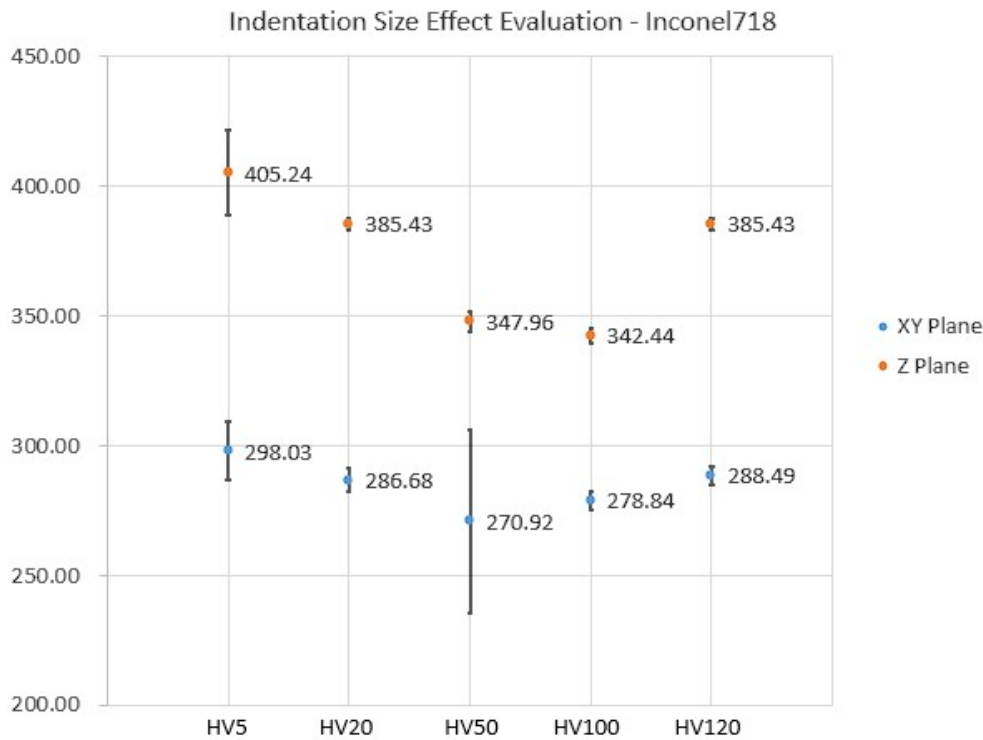
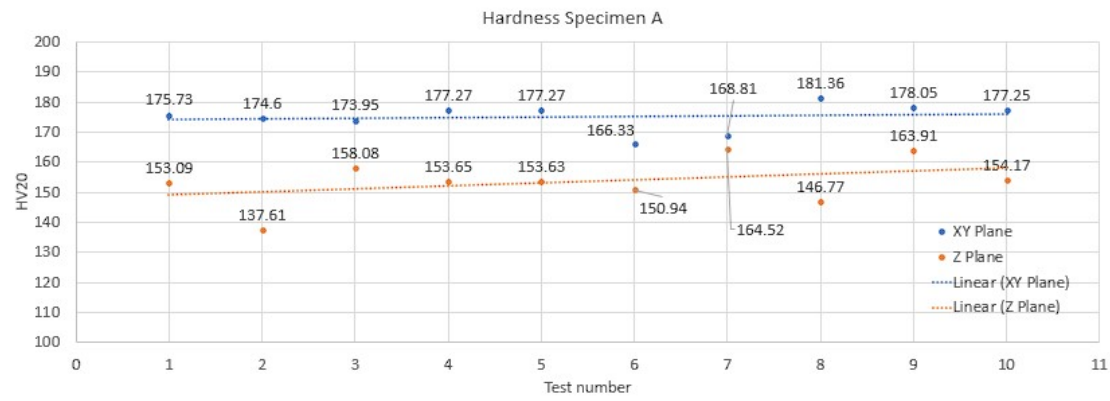


Fig. 10.3 Indentation Size Effect Evaluation - Inconel718

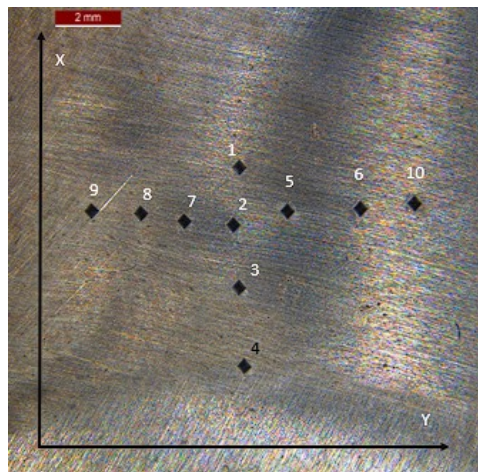
The Inconel718 experimental results presented reveal that specimens exhibit a strong non asymptotic Indentation Size Effect (ISE). For hardness test, this phenomenon was not expected because the elastic deformation is negligible respect to the plastic one. However, the specimens' majority shows an ISE effect. In particular it is possible to identify, for lower loads, an ISE and, for higher loads, a Reverse Indentation Size Effect (RISE). On the other hand, for general micro and nano-hardness testing, the ISE effect is present and often it is a dominant aspect of the study [107–109]. This particular non asymptotic Indentation Size Effect (combination between ISE and RISE) it is probably due to the particular arrangement and movement of dislocation in materials produced by SLM Additive Manufacturing processes.

10.1.2 HV20 hardness results

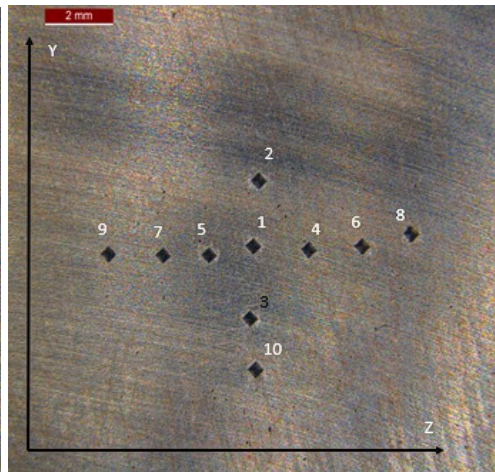
The result of indentation test respect to specimen A is presented in Figure 10.4 (full results in Appendix F). The random sequence of the repeated indentations is attached within the results. The test repeatability, and a low standard deviation, prove that the powder has been homogeneously spread around the platform: no relevant difference from 1 to 10 position of the test have been reported. The most important result is the very low difference between XY and Z plane values. The Cu174PH composite behaves more like a isotopic material, rather than the classic Additive Manufacturing SLM anisotropic material behavior (mechanical properties of AM SLM Inconel178 have a strongly dependence from the printing direction, AppendixE).



(a) Specimen A hardness



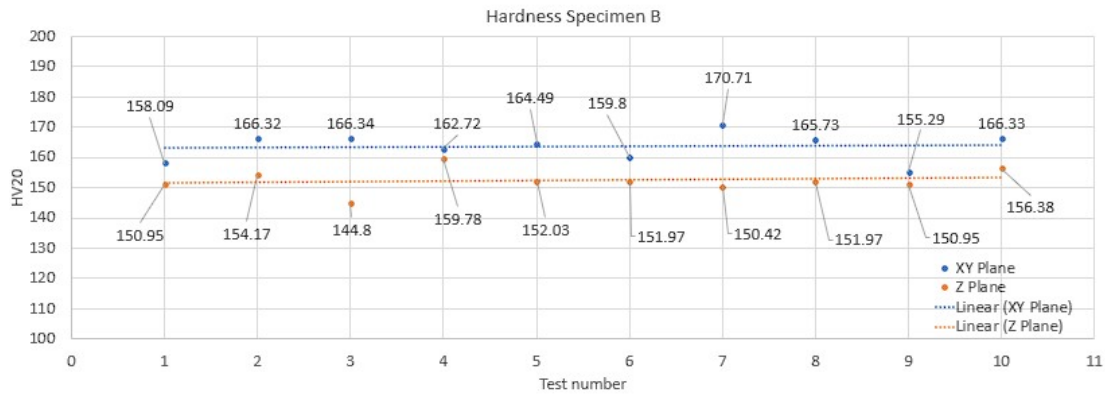
(b) Specimen A hardness XY footprint



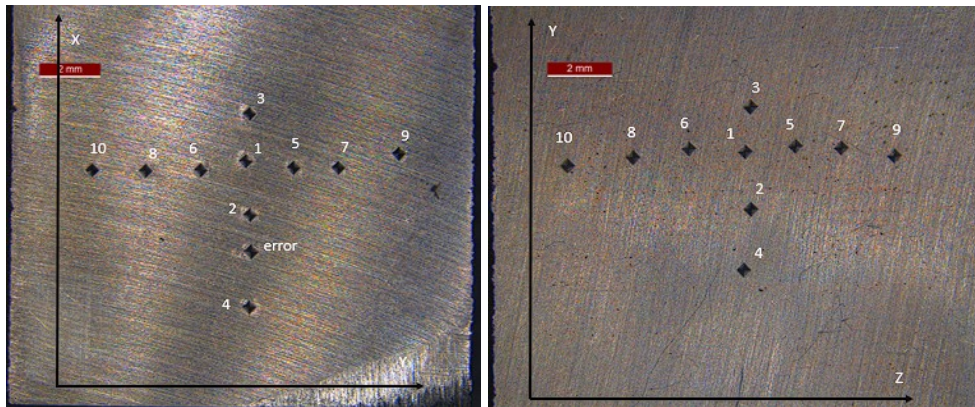
(c) Specimen A hardness Z footprint

Fig. 10.4 HV20 Hardness Tests - Specimen A

No particular difference from specimen B respect to specimen B have been reported (full results in AppendixF).



(a) Specimen B hardness



(b) Specimen B hardness XY footprint

(c) Specimen B hardness Z footprint

Fig. 10.5 HV20 Hardness Tests - Specimen B

The indentation shape of plane XY is very similar to the one respect to the Z plane (Figure 10.6). It is possible to state that, since footprints does not shows diagonal deformations, the compression/tension residual stresses after the AM SLM process are not predominant. A clear analysis of Copper indentation morphology of Vickers indentation has been presented by P. Zhang et al. [57]. By the aforementioned work is possible to understand that the indentation morphology of the Cu174PH is not the classic 'sink-in' one but more close to the 'pile-up' profile. An example of residual stress, and thus hardness test diagonal deformation, is presented in the Inconel718 parallel work in AppendixE.

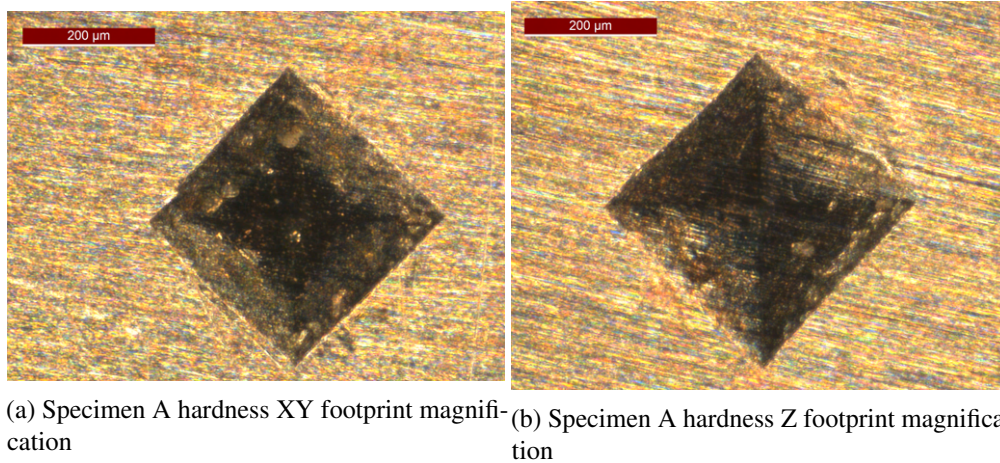


Fig. 10.6 HV20 Hardness Tests - footprint magnifications.

A brief resume is presented in Table 10.1.

HV20 hardness results			
		Value	DV.ST
A specimen	XY plane	175.06	1.52
	Z plane	153.64	7.87
B specimen	XY plane	163.58	3.42
	Z plane	152.34	5.42
Average	XY plane	169.32	//
	Z plane	152.99	//

Table 10.1 HV20 Hardness Tests

10.1.3 HV0.2 micro-hardness results

Micro-hardness have been tested with a HV0.2. The value have been chose in such a way that a 100 scale factor is present respect to the HV20 (full results in Appendix F). No particular differences from HV20 result except for the slight Indentation Size Effect and for a higher standard deviation due to the intrinsic micro-hardness footprint diagonal evaluation.

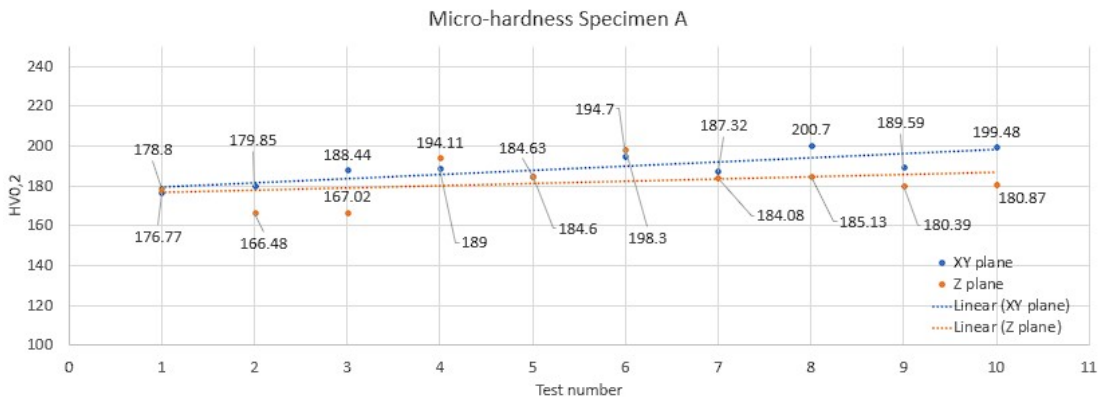


Fig. 10.7 Specimen A micro-hardness

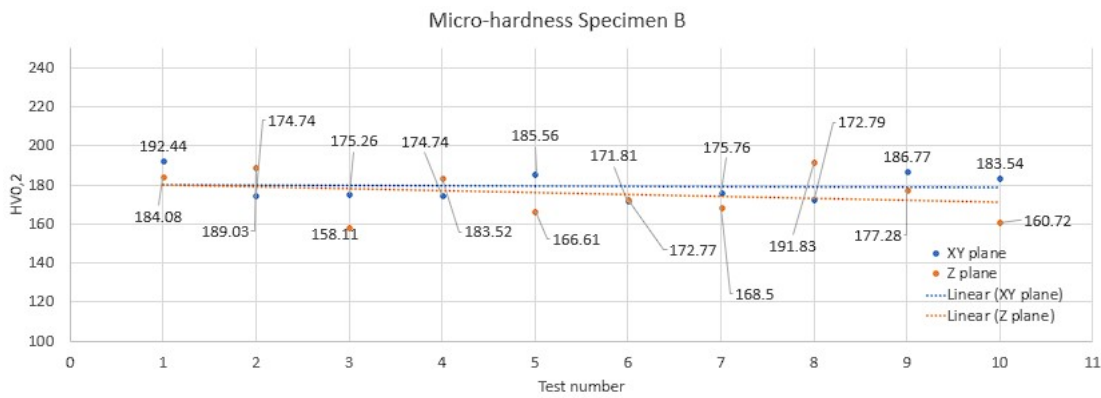


Fig. 10.8 Specimen B micro-hardness

A brief resume is presented in Table10.9.

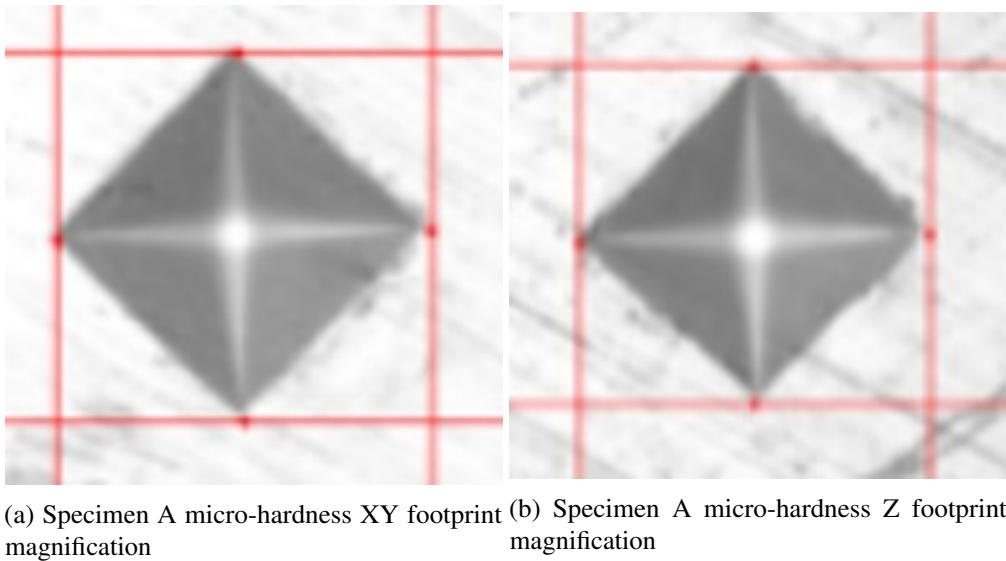


Fig. 10.9 HV0.2 Micro-hardness Tests - footprint magnifications.NOTE: Images are not in proportion to real scale

HV0.2 micro-hardness results			
		Value	DV.ST
A specimen	XY plane	189.03	5.34
	Z plane	181.98	11.8
B specimen	XY plane	179.34	8.09
	Z plane	175.25	13.22
Average	XY plane	184.18	//
	Z plane	178.61	//

Table 10.2 HV0.2 Micro-hardness Tests

10.1.4 Yield strength-Hardness relation

Both the yield strength and tensile strength of classic processed steel material exhibited a linear correlation with the hardness. Empirical relationships are provided that enable the estimation of strength from a bulk hardness measurement [110–112, 93].

There are different available model on the literature for material processed with common methodologies. In particular, E.J. Pavlina et al.[110] propose a model where hardness values as well as yield and tensile strength values were compiled for over 150 nonaustenitic steels.

$$Yeld\ Strength = -90.7 + 2.876 * HV \quad (10.1)$$

S. Chenna Krishna et al.[112] analysed several different copper alloys and developed a very accurate model for tree different hardness steps: High, Medium and Low.

$$Yeld\ Strength = 2.594 * HV \quad (10.2)$$

M. Tiryakioğlu at al. [111] propose successfully tested relation for Al 7010 alloys.

$$Yeld\ Strength = 0.383 * HV - 182.3 \quad (10.3)$$

On the other side, for Additive Manufacturing processes, not relevant and consistent study have been done on this subject. One of the available complete works is the one proposed by Jayme S. Keist et al.[93] on Titanium alloys.

$$Yeld\ Strength = \frac{HV(MPa)}{3.34} - 56 \quad (10.4)$$

All the aforementioned models has been used in order to evaluate the most accurate Yield strength of the Cu174PH composite (Table 10.3). In future sections, after mechanical tensile tests, a more accurate estimation of the results will be possible.

Hardness/Micro-hardness VS Sigma estimation										
		Cu174PH HV	Conventional processes Models						AM Models	
			Pavlina		Krishna		Tiryakioglu		Keist	
			Sigma_S [MPa]	Sigma_R [MPa]	Sigma_S [MPa]	Sigma_R [MPa]	Sigma_S [MPa]	Sigma_R [MPa]	Sigma_S [MPa]	Sigma_R [MPa]
Hardness	XY plane	169.32	379.01	510.04	439.21	573.82	nonsense	nonsense	371.38	441.30
	Z plane	152.99	349.3	471.46	396.85	518.48	nonsense	nonsense	326.66	393.10
Micro-hardness	XY plane	184.18	439.00	587.93	477.76	624.18	nonsense	nonsense	411.66	484.71
	Z plane	178.6	422.98	567.13	463.28	605.27	nonsense	nonsense	396.66	468.55

Table 10.3 Hardness/Micro-hardness VS Sigma estimation

10.2 Tensile Traction

Because of very high cost of both, copper and 17-4PH, powders and because of the uncertainty about the success of the new material (the present work is a preliminary study which mean goal is to understand if this new alloy is suitable for LRE thrust chamber applications), the choice of processing only XY tensile test specimens has been taken into account. The traction specimens are the longest one and therefore would have been the most expensive to print. Therefore all tensile specimen have been printed only respect to the XY direction (Figure 5.4).

However it is important to remake that, as already shown in Figures 6.1 and 6.2, the most important mechanical load of a LRE thrust chamber generates tensile and compressive stresses in the direction of the test, i.e. the XY direction (more precisely, the most important tensions are the circumferential tensions, normal to the direction of printing, thus the one on the XY plane).

Since the specimens is printed in the XY plane of the reference printing platform system (Figure 10.25a) the traction test has been performed respect to the 'fiber main orientation direction'. The micrograph in Figure 10.25a represent the microstructure orientation of the tensile test specimen.

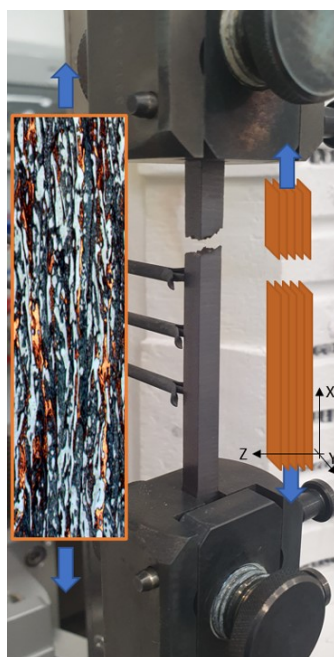


Fig. 10.10 Traction tensile test direction

Room temperature and high temperature tests have been repeated two times each.

10.2.1 Poisson Ration

Room temperature tensile tests have been tested with a bi-axial extensometer, therefore the Poisson's ration is available. The result are presented in Figure 10.11.

The first test shows a correct stabilization of the Poisson's ratio before the inelastic behavior. The second test, instead, shows a very small stabilised gap just before the yield strength. In addition, respect to pure copper (0.34-0.38, from [113]) and common steel (0.3-0.32, from [113]), the Poisson's ratio of Cu174PH is higher than the expected one.

This two particular behaviors are strictly related to the Additive Manufacturing process. Since the Poisson's ration can be defined as the measure of the Poisson effect, the deformation (expansion or contraction) of a material in directions perpendicular to the specific direction of loading, the presence of a high number of porosities and lake of fusion drastically modify the behavior of the the material. Porosity generates random vacuum areas inside the material matrix, thus: i) the material is able to reduce his traversal section more than a classic processed material, therefore is shows a higher Poisson's ratio; ii) the random coalescence and union of porosity do not allows the material to exhibit a constant reduction of area, thus the Poisson's ratio, respect to the linear stretch, is not constant. Concerning the Poisson's ratio of AM material, there is little experimental evidence in the literature. However a established trend demonstrate that the Poisson's ration in higher the bulk material [114].

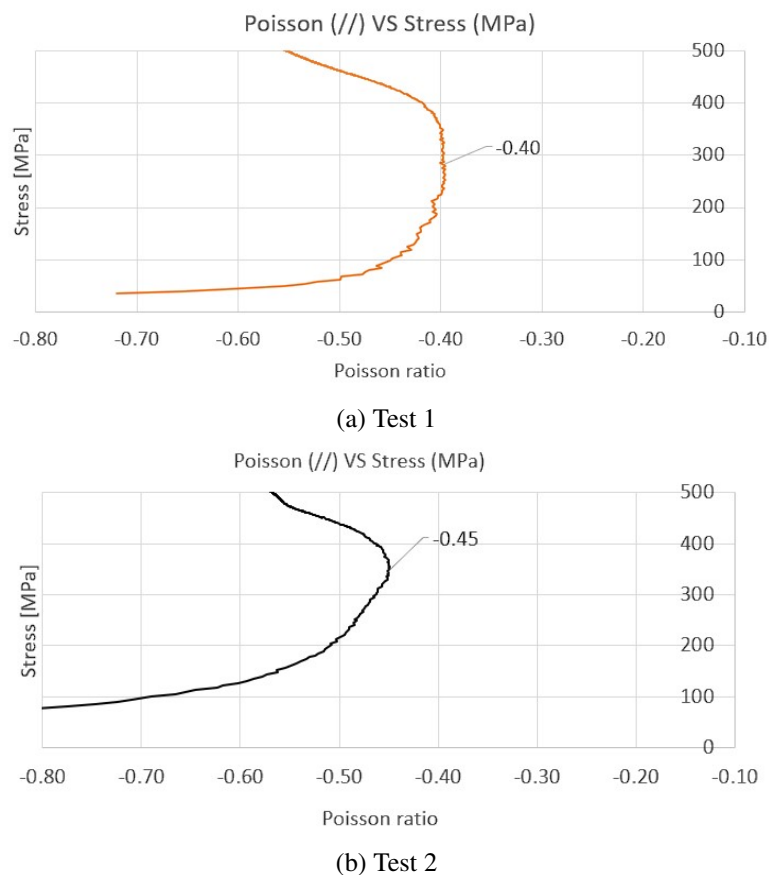


Fig. 10.11 Poisson Ration - Room Temperature

A higher reduction of the traversal section, respect to bulk materials, could be thinking about a more necking effect. However the experimental evidences of the traction tests do not shows necking (Section 10.2.2). This mean that the union of a

high Poisson's ratio and a very low elongation do not show an evident reduction of the section.

Table 10.4 shows the experimental results of Poisson's ratio evaluation during traction test 1 and 2 at room temperature.

poisson's Ration Cu174PH (Room T.)		
	Value	Average
Test 1	0.4	0.425
Test 2	0.45	

Table 10.4 Poisson's Ration Cu174PH (Room T.)

Another relevant consideration is that the Poisson's ratio, in Additive Manufacturing processes, is highly linked to the printing direction of the specimens [114]. Therefore a future investigation of traction tensile properties respect to the Z building direction should be performed.

10.2.2 Young Module

Porosity leads to a non-perfect linear behaviour in the rigid section. Because of this the Young Modules at different temperatures have been calculated in different range of stress (Table 10.5). The general trend shows that the more the temperature rise the lower the Young Modules are. A previous work of copper alloys, from Wnlong et al. [115], shows a similar non-perfect-linear rigid behavior.

Young Module - Cu174PH									
Stress Range [MPa]		E [GPa]				E [GPa]		E overall [GPa]	
		20	50	100	200	50	100	50	100
		40	100	200	300	200	300	200	300
Room	1			137	119		128		131.5
	2			143	126		135		
150°C	1			116	78		97		107.5
	2			129	104		118		
350°C	1		109	84		95		93	
	2		115	81		91			
550°C	1		84					83	
	2		82						
650°C	1	33							

Table 10.5 Young Modules VS Temperature - Cu174PH

Figure 10.12 is an example of the non-perfect linearity of the rigid section. Full Young Module results and calculation methodology is provided in Appendix G.

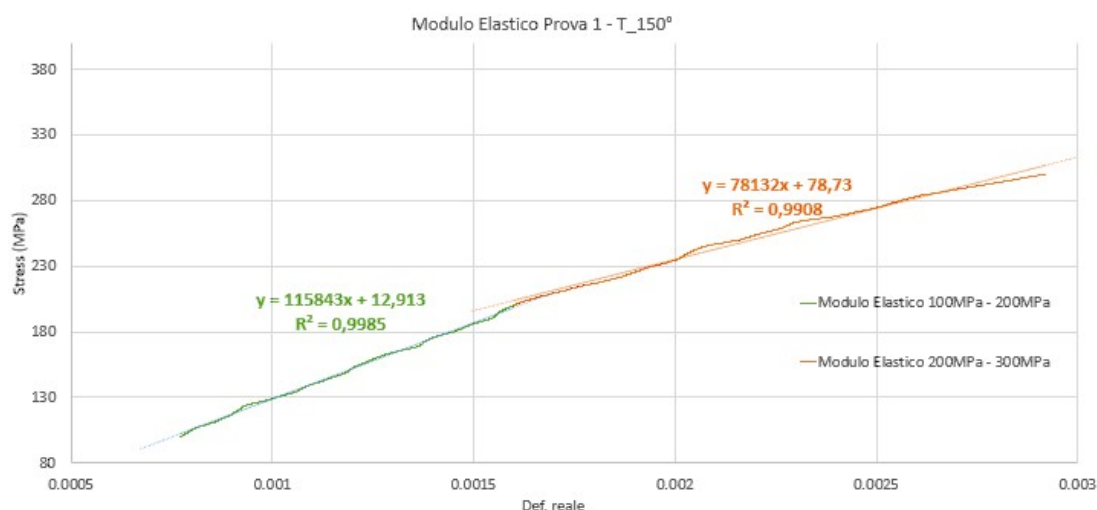


Fig. 10.12 Young Module non-linearity - Traction test 150°C n.1

10.2.3 Tensile Traction test

Traction tensile engineering tests at different temperatures are presented in Figure 10.13 and the relative properties resume in Table 10.6. No strain rate affect have been investigated, all traction tensile tests have been performed with a 2mm/min velocity.

The tests logic was to apply a raising 200°C temperature step, but after the results of the 550°C a 100°C increment has been applied. By analysing the result at 650°C the material behavior seems to be inelastic and therefore the limit for rigid behavior of the Cu174PH composite has been target an achievable temperature of maximum 550°C.

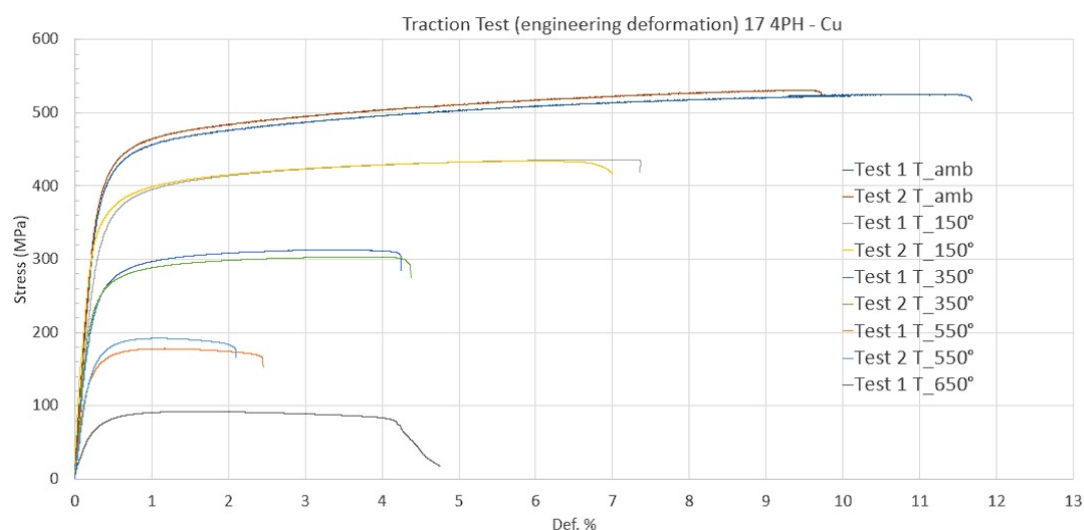


Fig. 10.13 Traction tensile test - engineering % deformation

Tensile Properties

		σ_s [MPa]				σ_r [MPa]	σ_{max} [MPa]	Elongation %
		min	max	average	overall			
Room	1	415	426	420	428	517	524	11.6
	2	430	442	436		524	529	9.7
150°C	1	356	381	368.5	369.7	421	436	7.35
	2	366	376	371		416	433	7
350°C	1	267	278	272.5	269.5	300	312	4.24
	2	263	270	266.5		293	303	4.35
550°C	1	163		163	169	157	177	2.44
	2	175		175		176	191	2.09
650°C	1	79		79	79	17	91	4.75

Table 10.6 Tensile Properties VS Temperature - Cu174PH

The overall repeatability of tensile tests at different temperatures is very good. No necking effects have been observed. Indeed the traction slope is almost positive for the entire test. This is probably mainly due to the in-homogeneity of the material. In the literature there is a common results form additive manufacturing Copper alloys necking behavior and no evident necking is present [116, 115, 24, 28, 117]. However is in important to remark that Copper alloys, especially the most recent SLM AM GRCo-42 and GRCo-84 from NASA [24, 117], after heat treatment shows an evident necking behavior. On the other side, pure copper alloys, processed via AM, shows a quite common evident necking [118].

The Cu174PH composite shows a high reliance from temperature. Respect to a common copper alloy, because of the low elongation to feature of the tensile tests, is possible to state that the Cu174PH is a fragile composite, however a more detailed surface fracture analysis shows a 45° fracture. Therefore the fracture mechanism is an hybrid between a ductile behavior and a fragile one (in-depth study of the fracture surface will be presented in Section 13.1).

An overall tensile properties VS temperature chart is proposed in Figure 10.14.

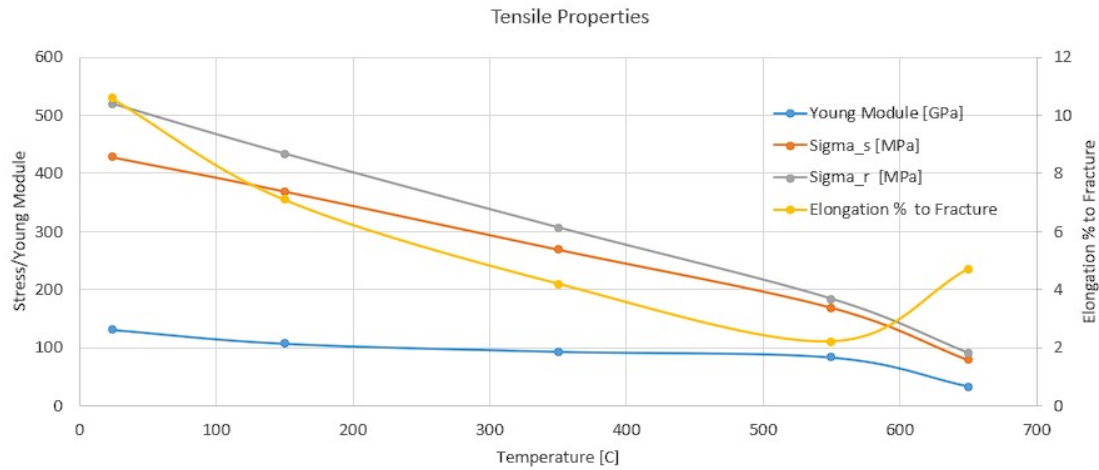


Fig. 10.14 Engineering Traction properties VS Temperature

10.2.4 Ramberg Osgood Model

The real stress - real strength post processed traction test is presented in Figure 10.15.

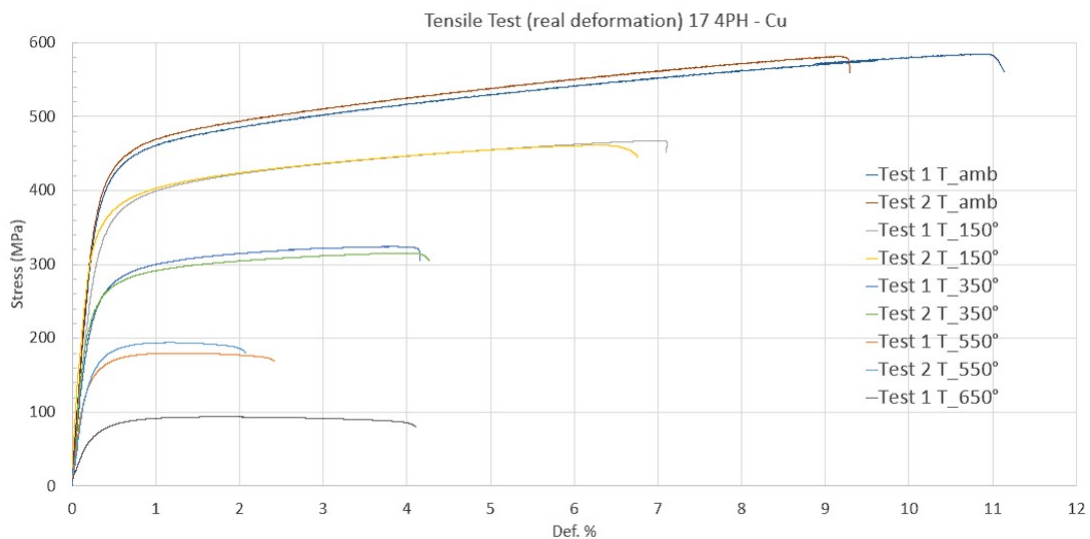


Fig. 10.15 Traction tensile test - real % deformation

Ramberg and Osgood proposed one of the most common model in order to model a correct plasticity behavior. The model has been successfully applied to the Cu174PH composite with excellent results (Figure 10.16, real strain-real deformation curve VS R.O. model, 350°C, test n.1). The entire R.O. results are collected in Appendix H.

The relevant aspect of the aforementioned outcomes is that the R.O. models can be applied also for this particular metal composite material. However the model has some difficulty representing the curve at very high temperatures (650°C), when the material becomes visco-plastic. In particular there is a slight underestimation of the plastic behavior after the yield strength (Appendix H).

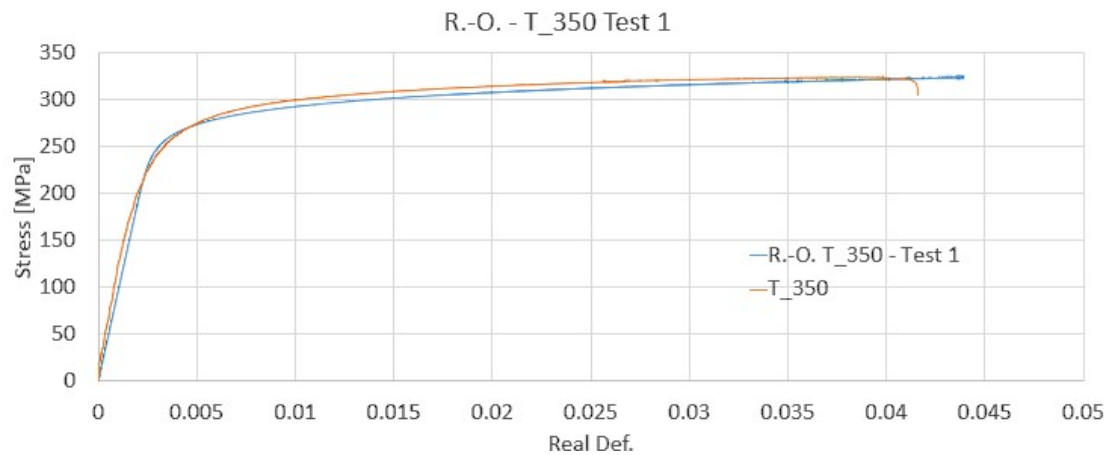


Fig. 10.16 Ramberg - Osgood model - Test 1 T350

The R.O. model parameter for the Cu174PH composite are reported in table 10.7.

Ramberg - Osgood relationship - Cu174PH

		K		n	
		Value	Average	Value	Average
Room	1	707.95	715.35	0.102	0.099
	2	722.76		0.097	
150°C	1	575.44	568.89	0.082	0.078
	2	562.34		0.074	
350°C	1	389.05	384.615	0.057	0.057
	2	380.18		0.057	
550°C	1	199.53	206.66	0.031	0.028
	2	213.79		0.025	
650°C	1	120.23	120.23	0.073	0.073

Table 10.7 Ramberg Osgood Parameters - Cu174PH

10.2.5 Comparison with competitors

A comparison with historical NASA common processed LRE thrust chambers copper-based materials is presented in this section and, when available, also more recent copper alloys, such GRCop NASA family, are presented.

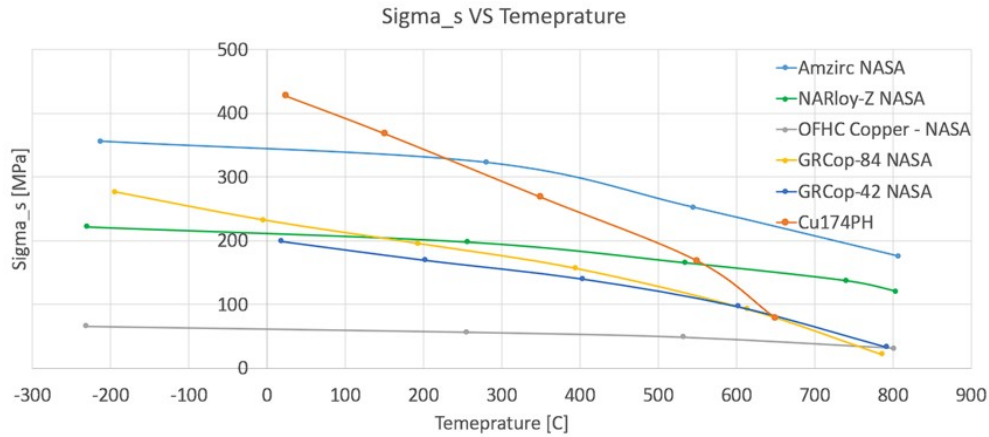


Fig. 10.17 NASA historical [23] and modern [24] Copper alloy VS Cu174PH - yield strength (respect to temperature)

By analysing Figure 10.17 the new composite material under study has a better yield strength almost for all the temperature range related to the LRE application, except for the Amzirc alloy which after the physical limit of 200°C behaves better than the Cu174PH.

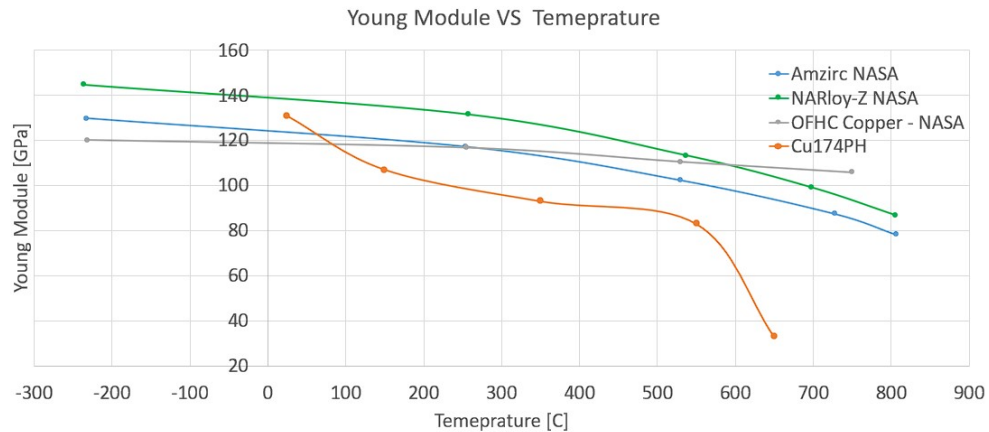


Fig. 10.18 NASA historical Copper alloy [23] VS Cu174PH - Young Module (respect to temperature)

On the other side, the Young Module seems to be lower than the competitive NASA materials (Figure 10.18). In addition to this common copper alloys shows a better overall rigidity in terms of temperature stability. In particular the slope of the rigidity VS temperature curve is significantly less aggressive respect to the one of the Cu174PH.

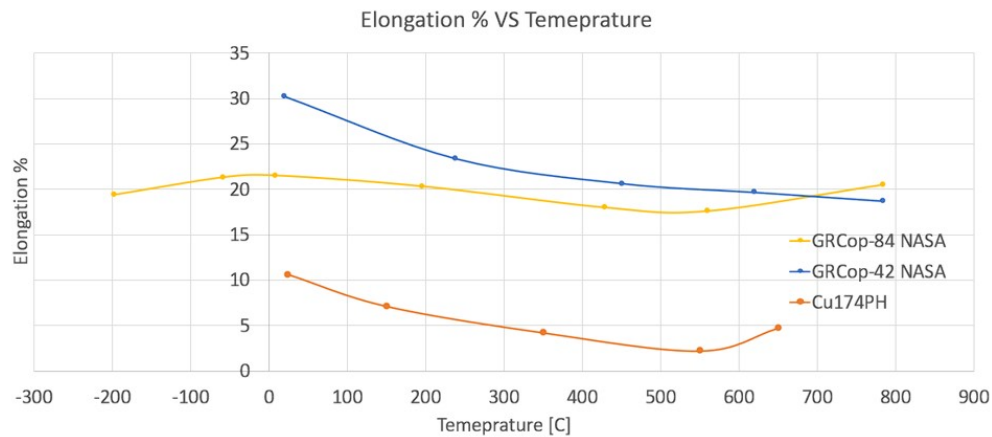


Fig. 10.19 NASA modern Copper alloy [24] VS Cu174PH - Elongation to fracture (respect to temperature)

The low elongation to fracture of the Cu174PH composite is a clear demonstration the fragile behavior of the material. This is in contrast with the Young Module results. The fragile behavior could be target to the complex compenetrated bi-metallic matrix of the material: dislocations could have great difficulty in navigating between islands of the two different materials (Figure 10.20). The edges of islands and the dotted-matrix areas (Section 8.2.1) behave exactly like a stop-movement firewall (in addition to porosity, lake of fusion and layers stratification).

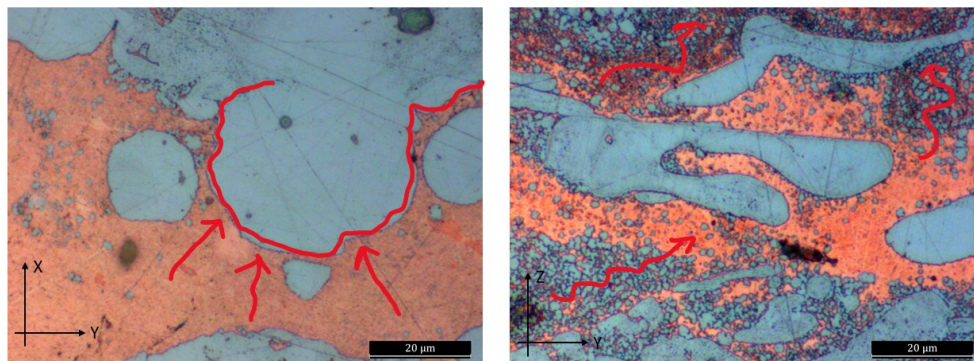


Fig. 10.20 Hypothetical dislocation block mechanism

An interesting comparison with room temperature elongation to fracture of AM NASA copper alloys is presented in Table 10.8. NASA AM SLM alloys are in accordance with the elongation presented of the Cu174PH. However after HIP heat treatment properties of SLM NASA alloys are completely different to the as-built one, with particular reference to the elongation to fracture [24, 28].

NASA AM Copper alloy VS Cu174PH (Room T.)

	Sigma_s [MPa]	Elongation %
AM GRCop-84 Vertical	391	15.4
AM GRCop-84 horizontal	471	16.6
AM GRCop-42 general	290	14
Cu174PH	428	10

Table 10.8 NASA AM Copper alloy VS Cu174PH (Room T.), from [28] and [24]

Unfortunately the Cu174PH behaviour at cryogenics temperature is not steel available. In general also AM materials shows a more fragile behavior when tensile test are performed at very low temperature [47].

In general Cu174PH composite shows a drastically decrease of tensile properties when temperature rise: important mechanisms are activated inside the material matrix as the temperatures increase.

10.2.6 Z direction estimated tensile properties

Additive Manufacturing processes are characterised by a strong and remarkable anisotropy [25], [35]. To fully exploit the design potential of metal AM, particularly for load-bearing structural components, a complete understanding of the anisotropic and heterogeneous microstructure (successfully provided in Section 8.2) and mechanical characteristics that frequently exist within metal AM parts is required. Unfortunately the Z tensile test are not available for the Cu174PH.

In general it is possible to link hardness properties to the tensile one, as proved in Section 10.1.4. Before choosing the more accurate model for estimate the tensile properties respect to the Z building direction from hardness Z plane tests of Cu174PH, a particular consideration is presented. Since NASA's AM GRCop-84 does not shows difference in hardness between horizontal and vertical specimens [28] and since the alloy has a similar hardness behavior of the Cu174PH under study, is is possible to state that because of low hardness difference between Z and XY plane on the Cu174PH (approximately 15 Vickers points of difference which is about the 10%, Table 10.1) the tensile Z and XY direction properties of this composite should not behave differently. On the other hand As-build AM SLM GRCop-84 has a vertical yield Strength of 391 [MPa] and a 471 [MPa] transversal one [28]: this proves that a AM copper alloy, also if does not shows difference in horizontal and vertical hardness, has a remarkable difference in the yield strength. In addition to this, the aforementioned NASA's materials are copper alloys and not composite, therefore Cu174PH could present a strong anisotropy.

After this brief hypothetical warning presented foreword, the models that best feet for our composite material is the on presented by Pavlina et al. [110] using micro hardness (and not hardness) value. The choice has been done because of the high reliability of the

hardness-yield strength relation for the tensile tested XY direction. Table 10.9 shows the estimated Z tensile properties of the Cu174PH composite material at room temperature.

Estimated Cu174PH Z direction tensile properties (Room T.)

	σ_s [MPa]	σ_s offset	σ_r [MPa]	σ_r offset
Cu174PH XY direction	428	//	540	//
Estimated Cu174PH XY direction	423	1.4%	567	5%
Estimated Cu174PH Z direction	439	not available	587	not available

Table 10.9 Estimated Cu174PH Z direction tensile properties

Is very important to remark that the XY hardness tests are related to the Z direction traction tensile properties, and the ZX or ZY hardness tests are related to the X or Y tensile properties. Thus the estimated Z direction traction properties have been evaluated via the XY hardness test. Figure 10.21 shows a schematic representation of the indentation plane and the indentation axe: it is the axe hardness penetration direction which is linked to the tensile properties, and not the indentation plane.

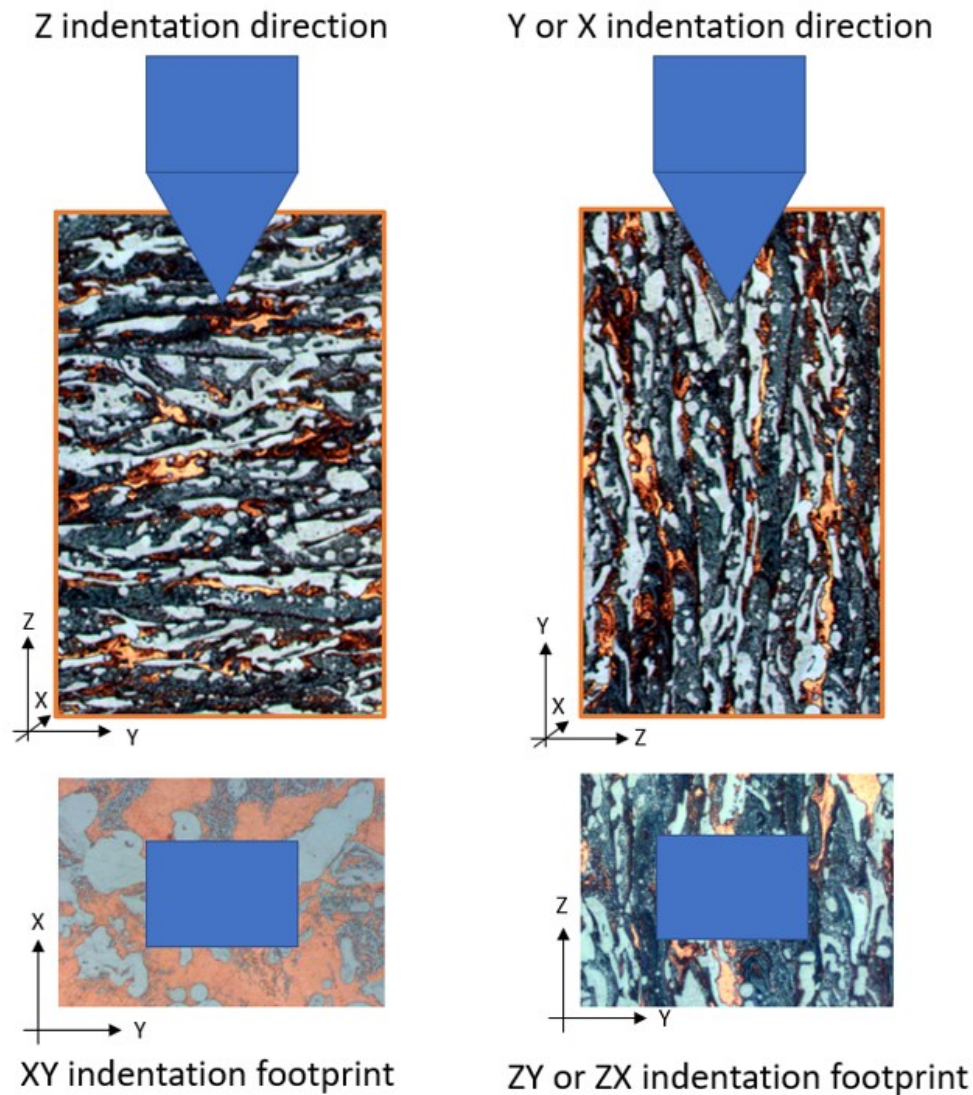


Fig. 10.21 Hardness-Tensile direction relation

Results presented in Table 10.9, according to the hardness results, shows a higher Z overall estimated traction properties respect to the XY direction tested one. This is due to the fact that since the XY hardness tests (thus with a Z penetration axe) has higher hardness value the Z traction tensile properties are better than the XY direction one.

This result is in contrast with common Additive Manufacturing materials. This is probably due to the fact that for common non-composite Additive Manufacturing materials the keyhole melting pool is correctly achieved and therefore the indentation process respect to the ZX or ZY plane, and thus respect to the Y or X axe, have more difficulties to footprint the material. In the Cu1174PH, on the other side, the melting pool seems not to be achieved and therefore the indentation process has less problems to be performed respect to the X or Y direction (ZY or ZY planes).

The Inconel718 parallel work, presented in Appendix E, proves that in common AM alloys the XY plane present a lower hardness value and it is related to the Z direction tensile properties. Figure 10.22 shows the XY and the ZX/ZY hardness of the Inconel 718 Design of Experiment work: it is possible to proof, by compare the hardness results

with the traction tensile results (Figure 10.23), the aforementioned common Additive Manufacturing behavior.

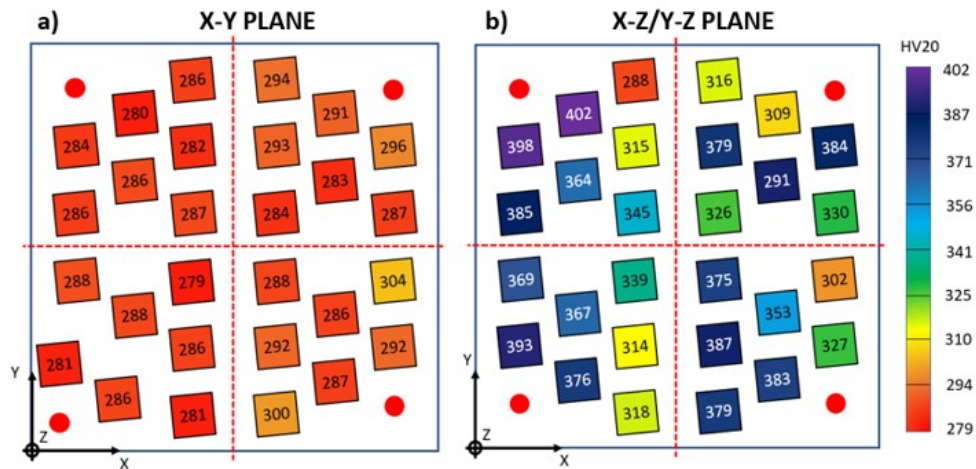


Fig. 10.22 Color scale-based hardness representation for as-build Inconels 718 specimens: a) x-y plane; b) x-z or y-z plane

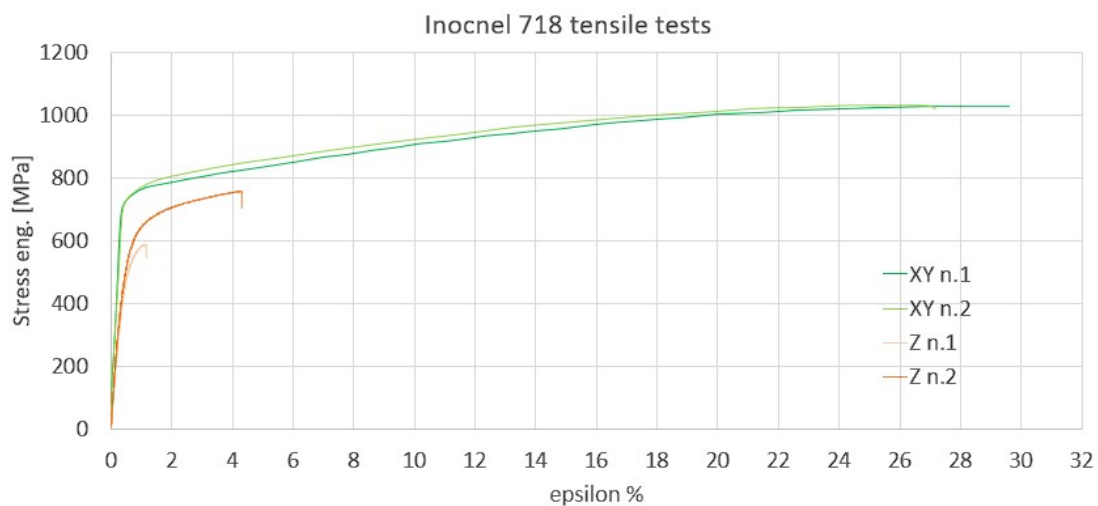


Fig. 10.23 As-build traction tensile tests - Inconel 718

10.3 Compression

Compression tests, because of the maximum specimens high of 20mm, have been performed for both, Z and XY direction. In addition the Z direction compression module of elasticity has been characterized also at 150°C and 240°C (No XY results are available).

10.3.1 Compression Young Module

The elastic section of the engendering stress - engendering deformation compression curve do not shows a perfect linearity (Figure 10.24). A similar behavior was already

presented for the tensile Young Module, but with a lower relevance respect to the compression one.

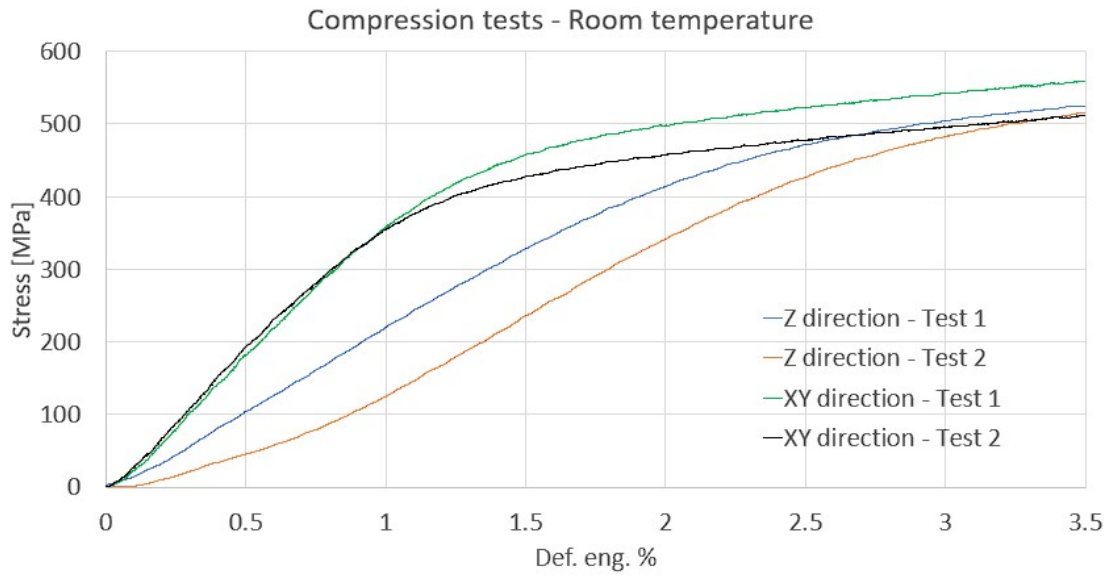


Fig. 10.24 Pre-yield elastic region

Due to this slight non-linearity the Young Module has been calculated as an average of the different linear slopes (same method employed for the traction tests). Different Additive Manufactured alloys shows a similar behavior. In particular Ponnusamy et al. tested a SLM 17-4 PH stainless steel under compressive loading and a qualitative similar non-linear slope was found [119]. Fashanu et al. evaluated the effect of SLM build parameters on the compressive properties of a 304L stainless steel and the pre-yield region of the stress-strain curve was not linear [120]. Also CuCrZr copper alloys, as tested by Yuchao et al. [40], shows the same particular behavior during compression tests.

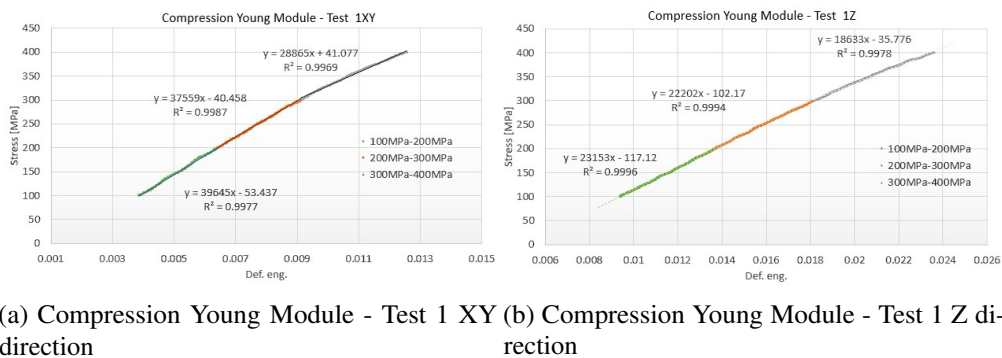


Fig. 10.25 Compression Young Module

The stress-strain curve's pre-yield region of a bulk material is frequently linear. Additive Manufacturing materials, on the other hand, are heterogeneous, complicated, and anisotropic materials that does not act like completely elastic materials. As a result, it has been demonstrated to exhibit non-linear behavior, notably in the lower portion of

the pre-yield elastic area of the stress-strain curve, which is likely owing to abnormalities in the specimen. In particular this first portion is the region where 'less material' is able to sustain the load because of porosity. The non linear behavior of this first section is probably due to the non-identical size of void and to the random arrangement inside the material matrix.

The compressive Young Module is much lower then the traction one. This is, one more time, due to the non homogeneity of the matrix: porosity are one more time governing the physical material's behavior.

Compression test at 150°C and 250°C provide an interesting quasi non-dependence of the compression Young Module from temperature (Figure 10.26). This is another relevant difference respect to the traction tests, where the material elasticity from room temperature to 150°C was decreased of qualitative 30%.

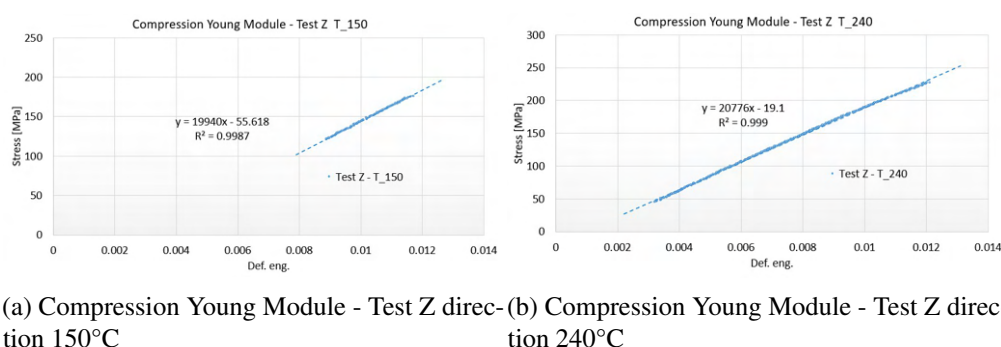


Fig. 10.26 Compression Young Module at high temperature

Young Module result are presented in table 10.10. All calculation procedure can be found in Appendix I.

Compression Young Module							
		E [GPa]			E [GPa]		E overall [GPa]
		100	200	300	100	100	100
Stress Range [MPa]							
		200	300	400	400	300	400
Room XY direction	1	39	37	28	35		36.5
	2	42	35			38	
Room Z direction	1	23	22	18	21		21
	2	21	22	18	21		
150°C Z direction							19
240°C Z direction							20

Table 10.10 Compression Young Module

XY and Z direction Young Module are different. From hardness test this behavior was not expected. However a difference between Young Module for Z and XY direction

has been found also in other recent works [120]: it seems to be a common results in Additive Manufacturing.

10.3.2 Compression test

The compression tests have been repeated two times for both, Z and XY direction at room temperature. Figure 10.27 present the full engineering stress - engendering deformation % curve. A good repeatability of results is achieved.

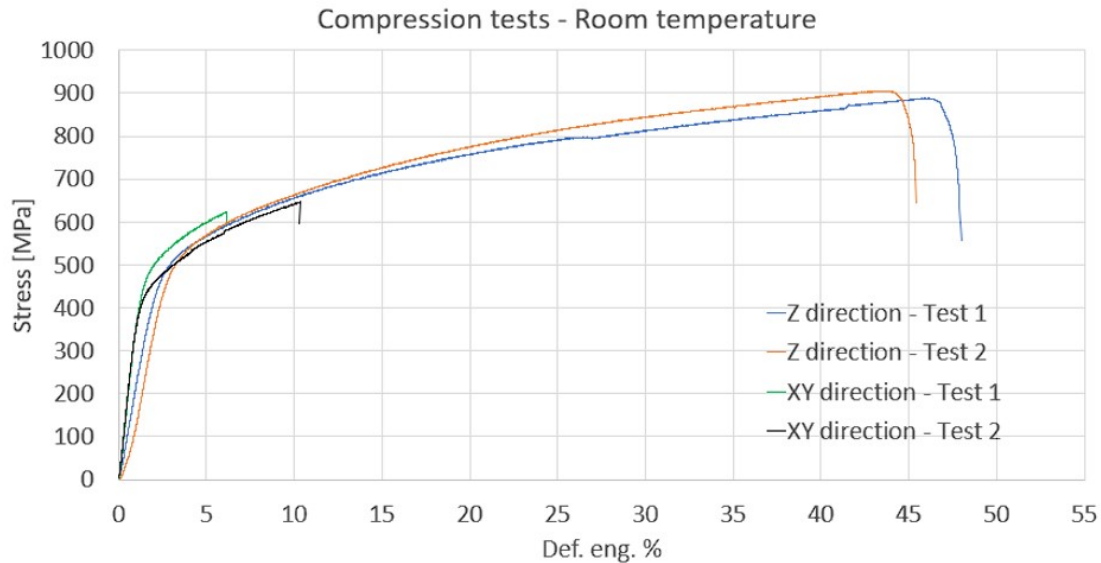


Fig. 10.27 Compression Tests

After yielding, non-uniform plastic deformation was observed in test 1 Z direction sample at high strains. This non-uniform local plastic deformation starts at $\varepsilon = 25\%$ and is seems to be fully recovered at $\varepsilon = 40\%$.

The most relevant result concern the elongation to fracture. Z and XY direction provide a very high anisotropy. Common AM Z direction specimens have lower traction tensile properties and elongation to fracture. Results from compression test prove an opposite behavior for this material in compression mode respect to the traction one: Z direction specimens show very high elongation to fracture respect to the XY direction one. In addition XY direction specimens have a higher compressive Young Module, thus this result agrees with the compression elongation to fracture: the more the material is fragile (high compressive Young Module) the less the elongation to fracture is.

A hypothetical first explication of the high anisotropy behavior of the Cu174PH composite is the layer arrangement. Unlike the traction test, during compression the XY specimens suffers from layer detachment. The phenomenon is presented in Figure 10.28a: during compression the material is prone to barrel-shaped deformation and therefore the layers connections are not strong enough to sustain the same load that the material is able to do in the XY direction (Figure 10.28).

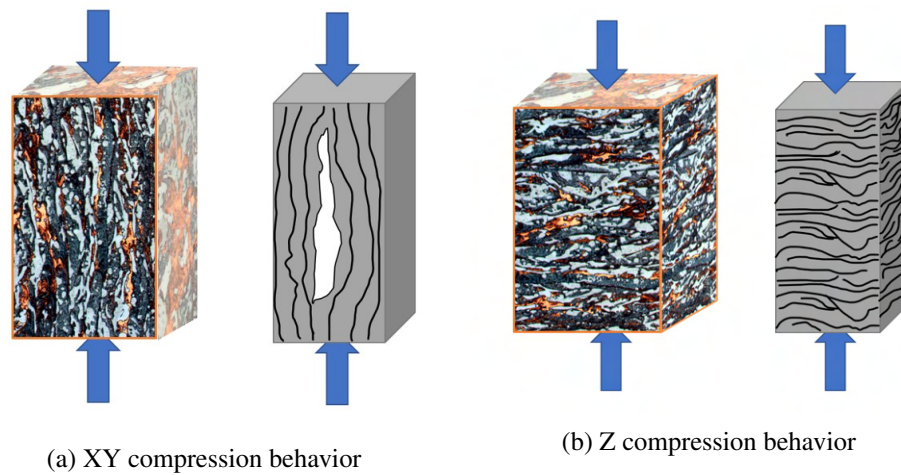


Fig. 10.28 Schematic compression behavior

Table 10.11 present a brief resume of the compression properties at room temperature. The best orientation, because of the higher elongation to fracture and therefore the best plastic behavior, is the Z building direction.

Compression Properties - Room Temperature

		σ_s [MPa]				σ_r [MPa]	Elongation %
		min	max	average	overall		
XY direction	1	420	460	440	447.5	616	6.2
	2	440	470	455		646	10.4
Z direction	1	420	470	445	445	868	46.8
	2	420	470	445		860	44

Table 10.11 Compression Properties - Room Temperature

10.3.3 Lattice structure Compression test

The Z direction printed 0.3 mm and 0.5 mm lattice structure have been successfully tested at room temperature. The 0.3 mm lattice shows a clear instability under load (Figure 10.29a), the 0.5 mm one a more misaligned one (Figure 10.29b).

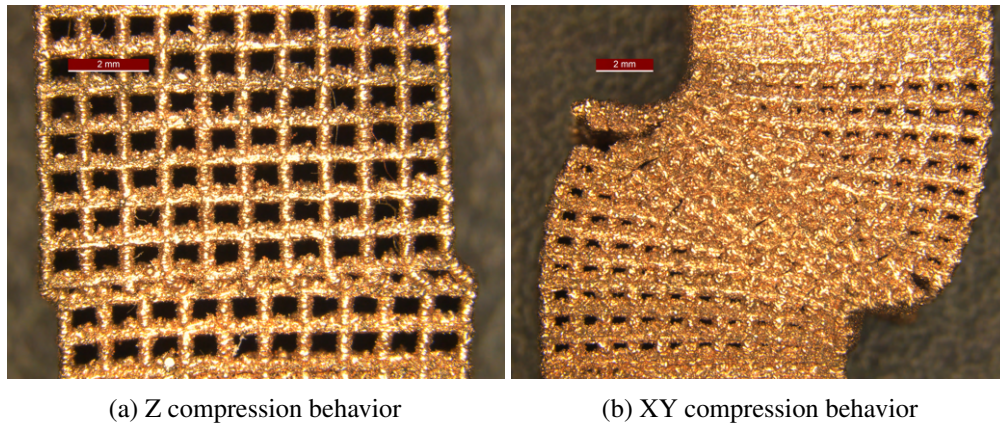


Fig. 10.29 Lattice Compression Test fractures

The overall behavior during the compression tests is presented in Figure 10.30.

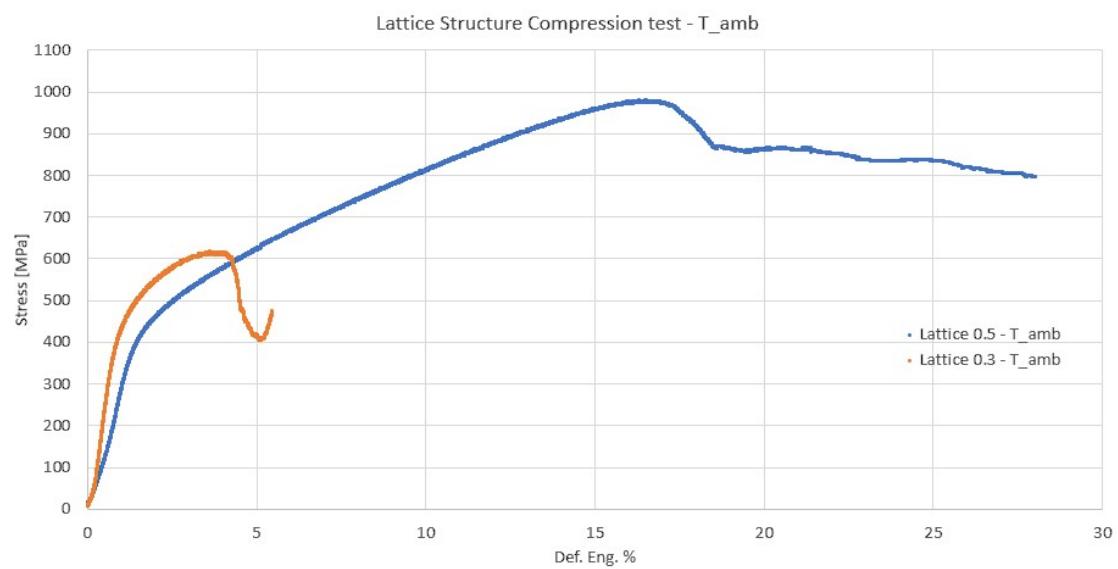


Fig. 10.30 Lattice Compression Tests - Room temperature

Chapter 11

Experimental Results: Low Cycle Fatigue Tests

During the low cycle fatigue tests, at least 100 points were collected for each cycle in order to describe its shape on the stress-strain plane correctly. All tests were carried out until the specimen fractured (except for two room temperature low deformation tests). The same temperature levels of the tensile tests have been preformed for each strain amplitude used. All strain amplitude are centred cycles: the same amount of tensile deformation has been applied for the compression deformation. Unfortunately only few 550°C tests have been repeated. Table 11.1 present a summary of all Low Cycle Fatigue results.

LCF high temperature and room temperatures Tests											
			$\epsilon_{eng.}\%$		Stress eng. [MPa]		Stress [MPa] 50% cycles			Re-testing	
$\Delta\epsilon_{eng.}\%$			Cycles to Fracture		Max	Min	Max	Min	Delta	Cycles to Fracture	Difference
T_amb	0.5	>6000	0.25	-0.25	200	-131	184	-94	278		
	1.4	>6000	0.71	-0.70	346	-279	318	-269	588		
	2.0	4180	1.01	-1.00	422	-393	382	-384	767		
	2.8	635	1.41	-1.40	487	-470	460	-469	930		
	3.6	136	1.81	-1.80	530	-529	517	-520	1037		
T_150	2.0	1447	1.01	-1.00	369	-335	338	-334	672		
	2.8	271	1.41	-1.40	418	-403	394	-392	787		
	3.6	63	1.80	-1.80	446	-440	429	-413	842		
T_350	2.0	795	1.00	-1.00	287	-350	280	-283	564		
	2.8	33	1.41	-1.40	352	-342	339	-338	677		
	3.6	14	1.80	-1.79	362	-364	354	-350	704		
T_550	1.0	1539	0.50	-0.50	162	-164	160	-156	316		
	1.4	546	0.70	-0.70	183	-187	178	-184	362	430	21.24%
	2.0	144	1.00	-1.00	203	-210	200	-207	407		
	2.8	39	1.40	-1.40	250	-255	247	-252	499	30	23.07%
	3.6	12	1.81	-1.80	232	-229	231	-228	459		

Table 11.1 LCF high temperature and room temperatures Tests

The effect of a main amplitude does not have been investigated. In addition, also the effect of the strain rate does not have been studied. This last one is not trivial and

negligible as demonstrated by NASA's studies for bulk copper alloys [27]. The effect of strain rate on the low-cycle fatigue behavior of the Narloy-z alloy at 538°C was studied using strain rates of 4×10^{-4} , 1×10^{-2} and 5.2×10^{-2} Hz. A comparison of these data indicates a definite increase in the fatigue life as the strain rate is increased.

11.1 LCF Results: Room temperature

Cu174PH composite hysteresis loops at room temperature are presented in this section together with the plots of the highest and minimum peak stress for each cycle acquired until stabilization to better understand the material's cyclic hardening or softening behavior during the transient phase. The room temperature tests have been performed also for lower $\Delta\epsilon$ range respect to the high temperature experiments. This is due to the fact that the strain range has been increased step by step because of the unknown material properties.

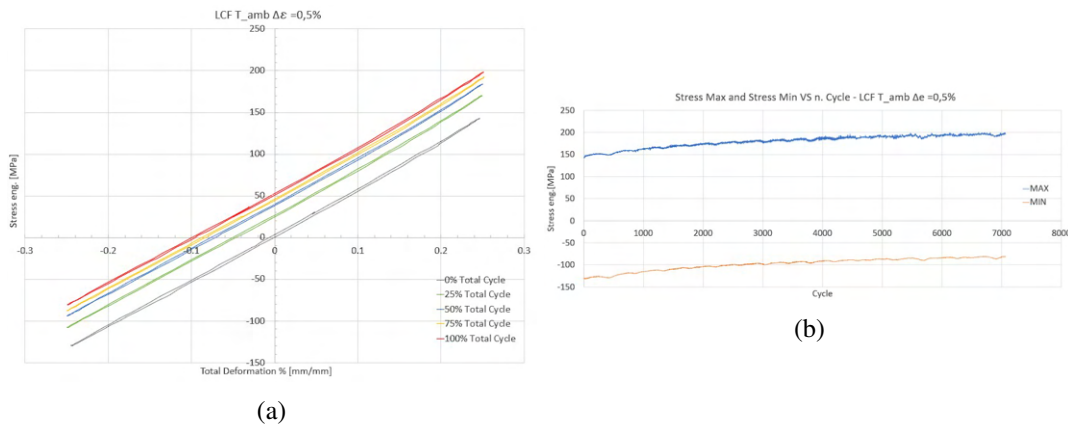


Fig. 11.1 LCF room temperature $\Delta\epsilon = 0.5\%$

The first room temperature LCF test at $\Delta\epsilon = 0.5$ shows a strong general hardening behavior. The max-min stress chart in Figure 11.1b shows a rising maximum stress and minimum respect to time (cycle number) increasing. The non perfect linear shape of the curve, for both maximum and minimum plots, is probably due to the non homogeneity of the interior material structure.

The presence of voids create a clear up and down curve shape. In particular when the local slop is positive the material is hardening (the stress in increasing) and therefore the rigidity of material is higher than the starting one (the more the material is stiff the more the behavior is hardening): this is probably due to the local voids coalescence and union. The more the voids collapse or combine the less available resistant area there is and therefore the materials try to reply with an hardening behavior.

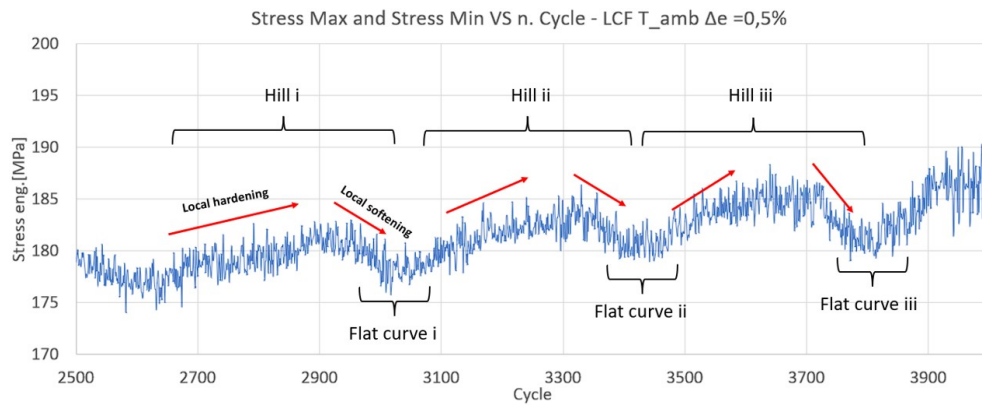
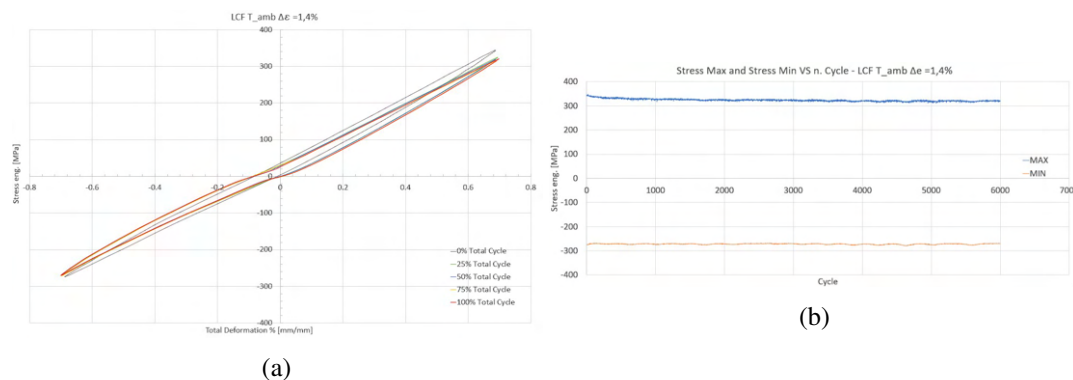


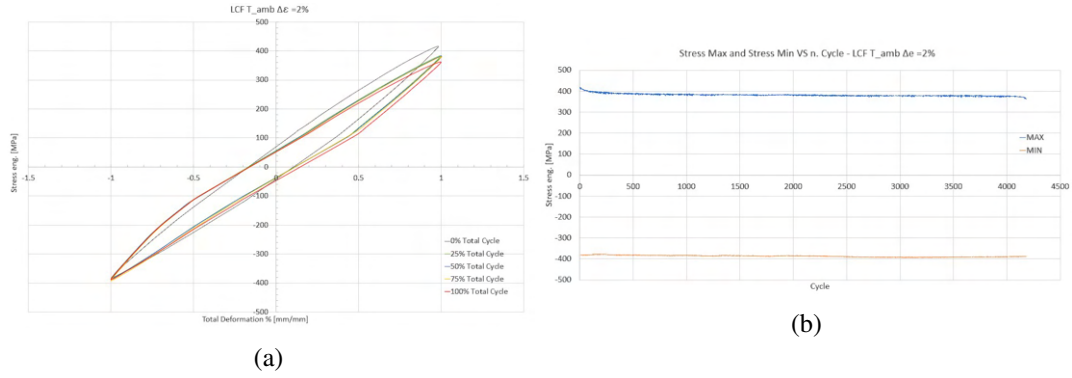
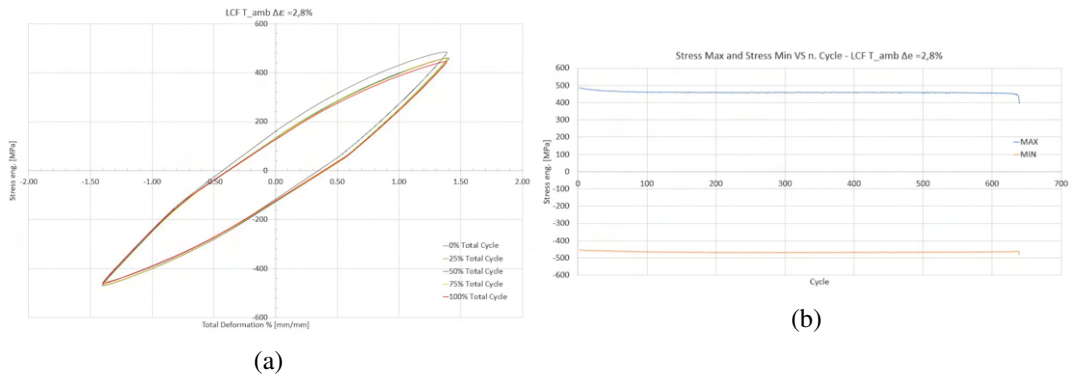
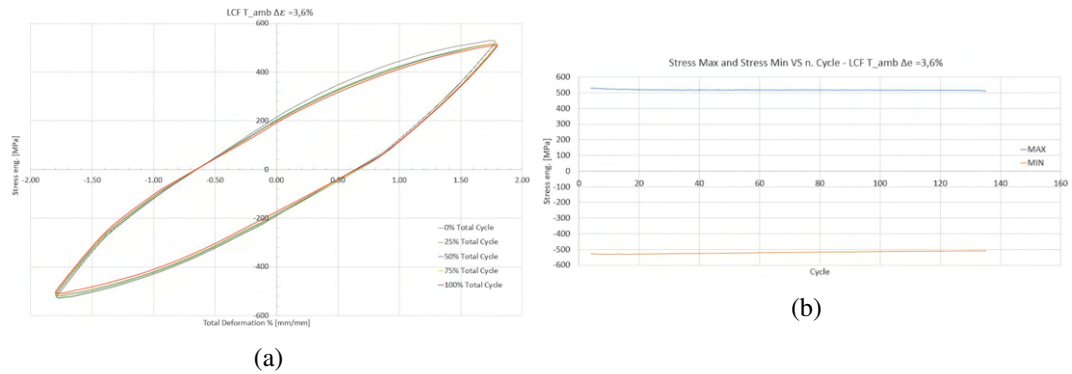
Fig. 11.2 Local hill phenomenon

On the other hand when the local slop is negative the material is softening (the stress in decreasing) and therefore the rigidity of material is getting lower than the previous maximum of the hills. This is the a growing voids phase. Porosity are stretching on the axial traction direction without combine each other: the local resistant area do not change and therefore for the same required deformation the material is able to better strain with less stress. After the local softening phase is is possible to observe a little flat curve.

However, after few cycle, voids (different shape, dimension and location) start a new coalescence: this phenomenon is repetitive and the experimental evidence of cycling local softening and hardening can be observed.

This particular hypothetical phenomenon can be observed only for low deformation. This could be due to the fact that, probably, there is a characteristicly time for activate the phenomenon. By observing the following higher strain and higher temperature LCF tests this phenomenon does not show up, therefore there is a threshold limit for the combination of strain and the temperature over which it is not possible to observe this phenomenon.

Fig. 11.3 LCF room temperature $\Delta\epsilon = 1.4\%$

Fig. 11.4 LCF room temperature $\Delta\epsilon = 2.0\%$ Fig. 11.5 LCF room temperature $\Delta\epsilon = 2.8\%$ Fig. 11.6 LCF room temperature $\Delta\epsilon = 3.6\%$

All other tests at room temperature, above the $\Delta\epsilon = 0.5$ strain one, shows a general softening behavior without a specific local hill phenomenon. An starting predominant softening can be notice for every room temperature test. However after an average of 1000 cycles the more the strain is high the less the softening is dominant, after the aforementioned starting phase. It can be observed that in the middle of the tests the maximum/minimum stress shows a flat behavior. Finally close to the fracture ultimate a second relevant softening behavior shows up. The more the strain is high the more this three steps softening-flat-softening phenomenon is remarkable.

11.2 LCF Results: 150°C

Cu174PH composite hysteresis loops at a temperature of 150°C are presented in this section together with the plots of the highest and minimum peak stress for each cycle acquired until stabilization to better understand the material's cyclic hardening or softening behavior during the transient phase.

The more relevant difference respect to the room temperature test, except for the bigger area inside the hysteresis loop due to the higher energy of deformation acquired from the material, is the non-symmetrical softening behaviour: the traction phase seems to softening more that the compression one. This behavior was slightly showed up also in the room temperature tests, but it was not so relevant. Also for this set of LCF tests it can be observed that in the middle of the tests the maximum/minimum stress shows a flat behavior.

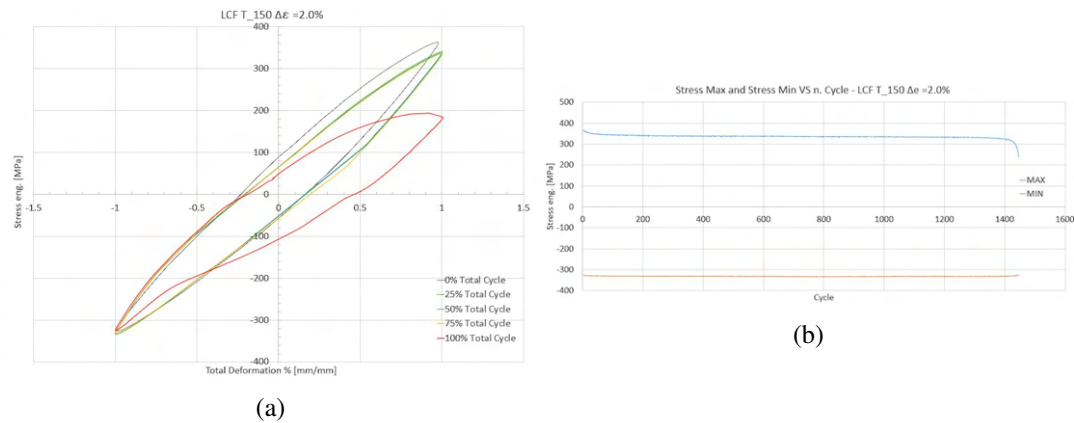


Fig. 11.7 LCF 150°C $\Delta\epsilon = 2.0\%$

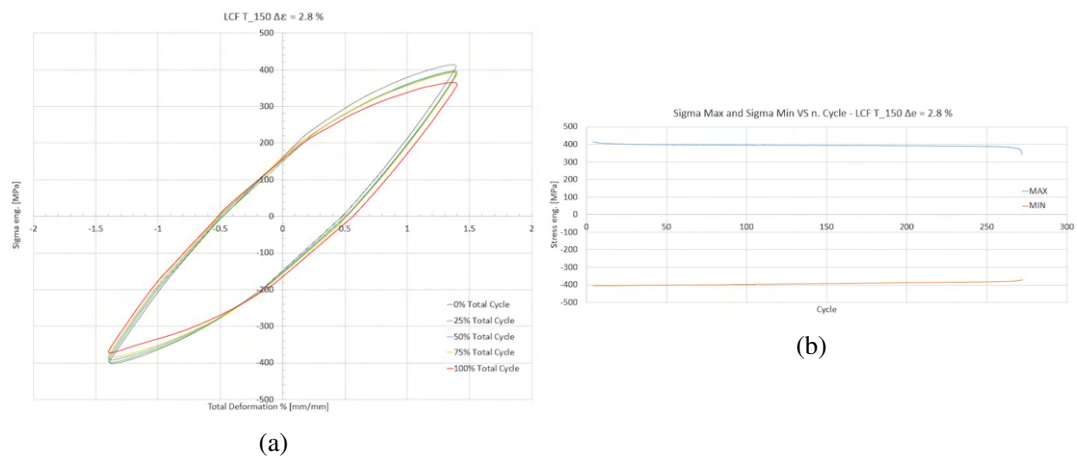
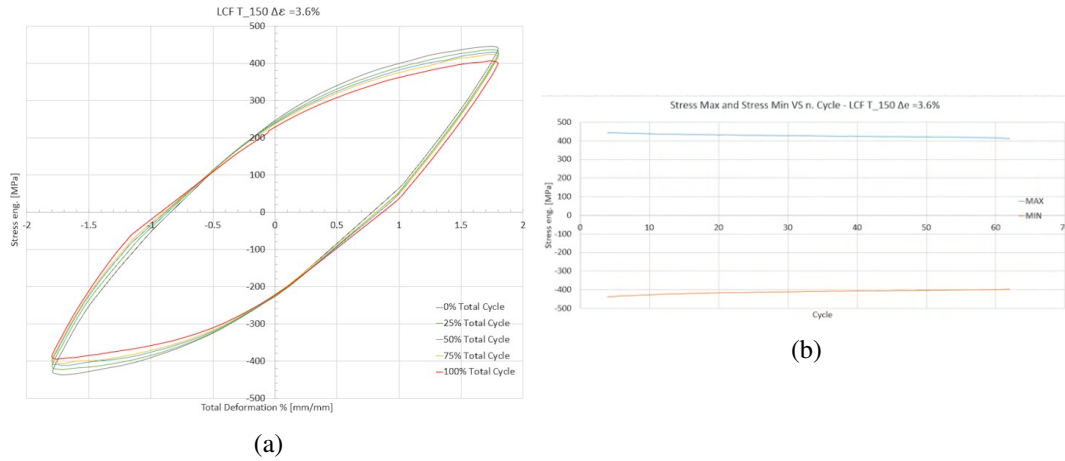
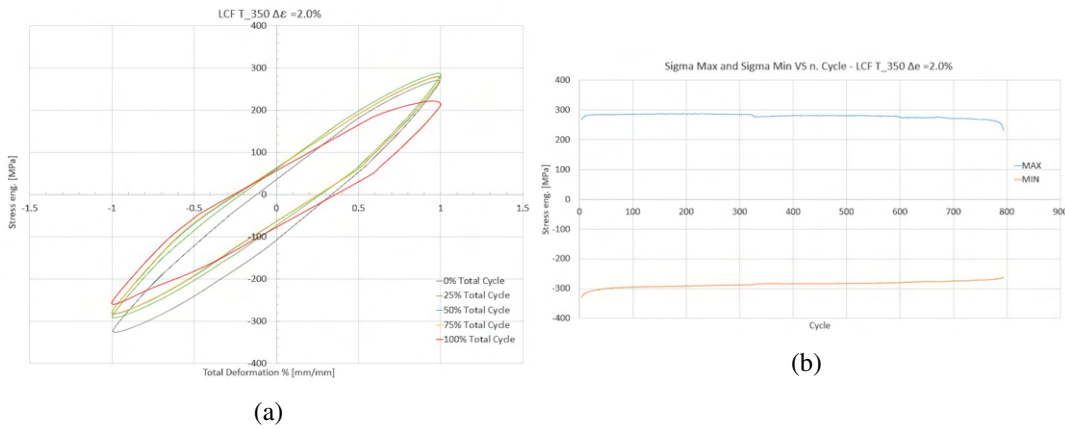


Fig. 11.8 LCF 150°C $\Delta\epsilon = 2.8\%$

Fig. 11.9 LCF 150°C $\Delta\epsilon = 3.6\%$

11.3 LCF Results: 350°C

Cu174PH composite hysteresis loops at a temperature of 350°C are presented in this section together with the plots of the highest and minimum peak stress for each cycle acquired until stabilization to better understand the material's cyclic hardening or softening behavior during the transient phase.

Fig. 11.10 LCF 350°C $\Delta\epsilon = 2.0\%$

The maximum/minimum of the LCF 550°C test at $\Delta\epsilon = 2.0$ (Figure 11.10b) shows two particularity: i) a starting hardening behavior is present for several cycles (about 20 cycles); this attitude has already been observed in LCF Narloy-z NASA's bulk copper alloy [27]; ii) a double evident breakdown can be observed; The first stress failure is came up slightly after the 300th cycle and the second one around the 600th cycle (Figure 11.11).

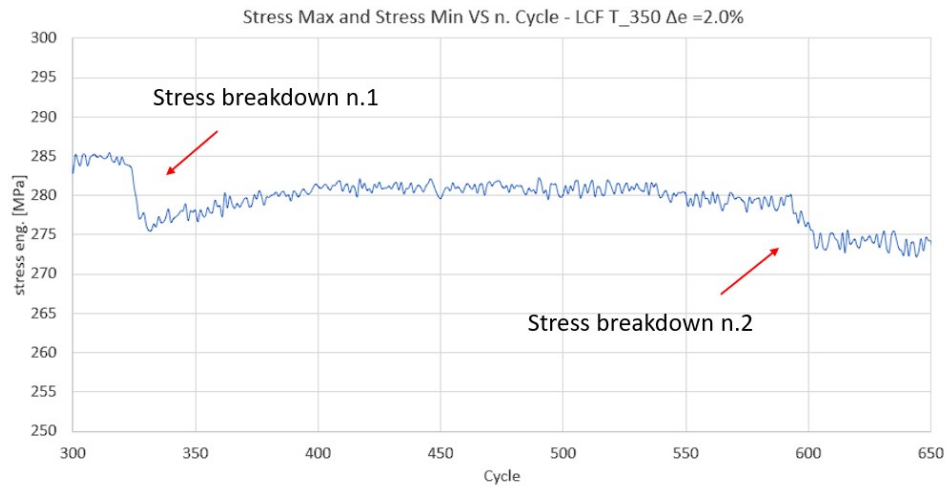
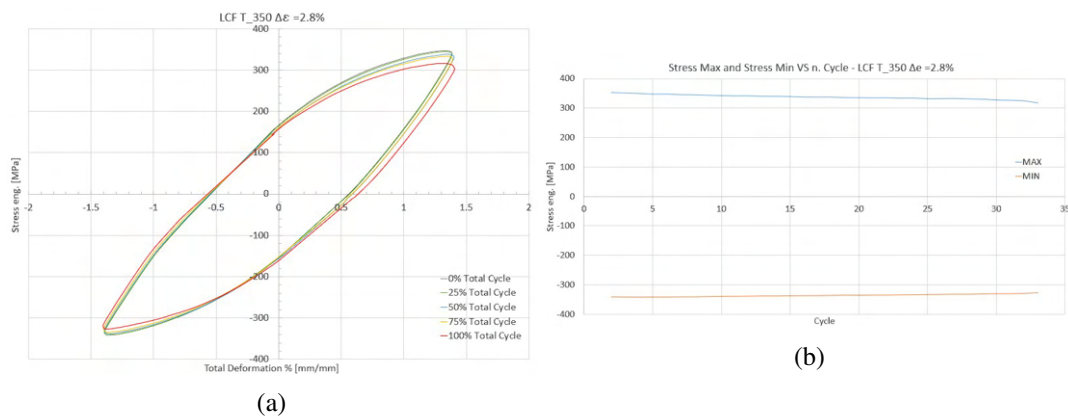
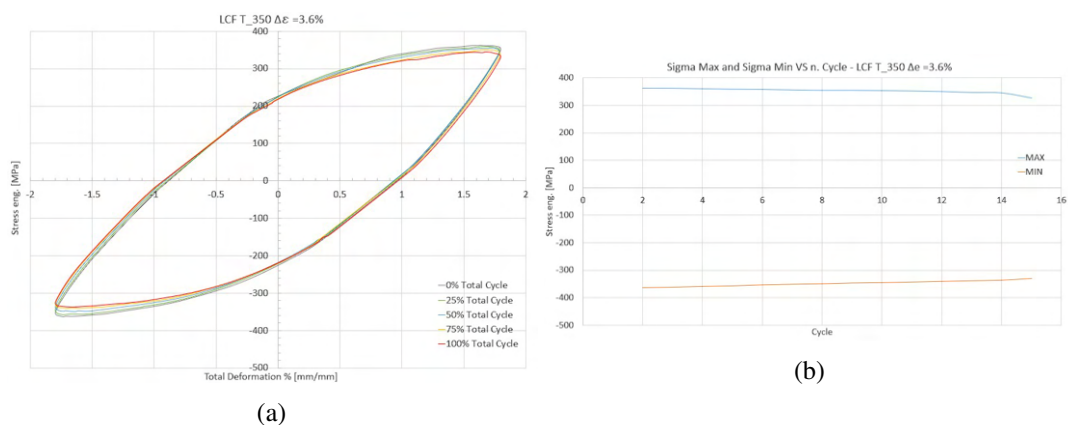


Fig. 11.11 Double stress breakdown

Fig. 11.12 LCF 350°C $\Delta\epsilon = 2.8\%$ Fig. 11.13 LCF 350°C $\Delta\epsilon = 3.6\%$

Also the overall LCF test at 350° are governed by a general softening behavior but, in contrast with the experimental evidences of room temperature and 150°C LCF tests, in the middle of the the maximum/minimum stress chart no flat behavior is observed.

The temperature raising is starting to governing the matrix behavior and to have more influence with respect to the phenomenon of elongation and coalescence of voids.

11.4 LCF Results: 550°C

Cu174PH composite hysteresis loops at a temperature of 550°C are presented in this section together with the plots of the highest and minimum peak stress for each cycle acquired until stabilization to better understand the material's cyclic hardening or softening behavior during the transient phase. LRE thrust chamber can easily achieve temperature between 750-850 K, therefore this set is the most relevant one.

By analysing all 550°C tests is clearly visible that the behavior is completely different respect to the lower temperature tests: the material shows an hardening attitude after a starting very little softening activity. Only the $\Delta\epsilon = 2.0$ LCF test a flat maximum/minimum stress behavior can be observed. The cyclic deformation behaviour and the fatigue life of metallic materials depend critically on the stability of the microstructure during cyclic loading and on the cyclic slip mode both of which in turn, and depending on temperature and testing mode, govern the cyclic hardening/softening and the mode of fatigue crack initiation and propagation [121]: in this case the new Cu174PH composite material manifests an evident temperature change on the microstructure which leads to an hardening behavior instead of the softening one observed at lower temperatures. A more detailed investigation should be performed in future.

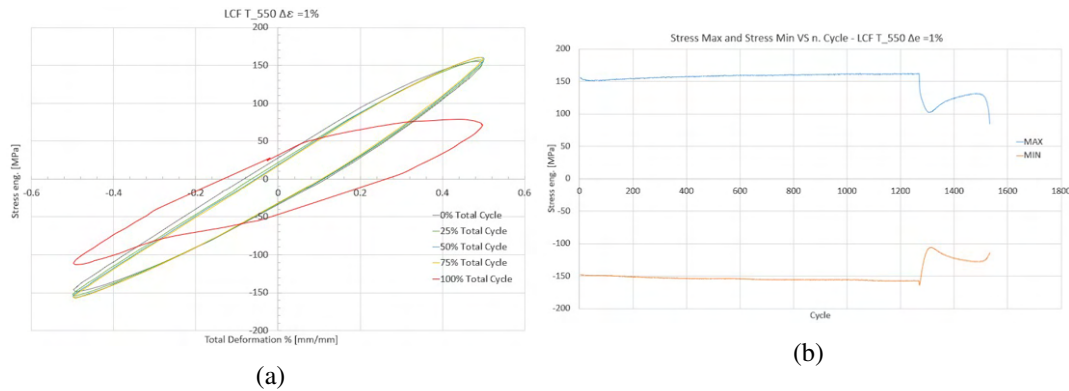


Fig. 11.14 LCF 550°C $\Delta\epsilon = 1.0\%$

Figure 11.15 shows a particular random¹ tensile and compression stress breakdown. In particular there is a local failure of the composite matrix which is probably caused by an instantaneous crack propagation which increases cycle after cycle. When the growing voids phase end the material starts hardening until the final fracture starts.

¹The phenomenon could show up for a different range of $\Delta\epsilon$

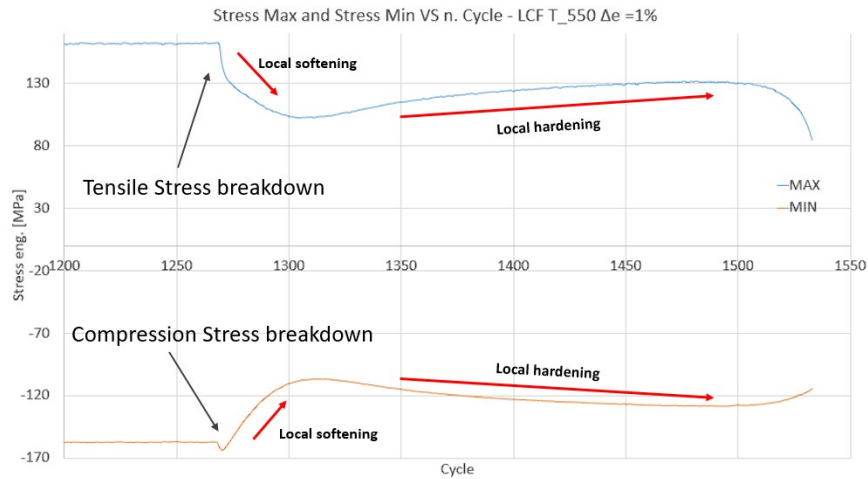
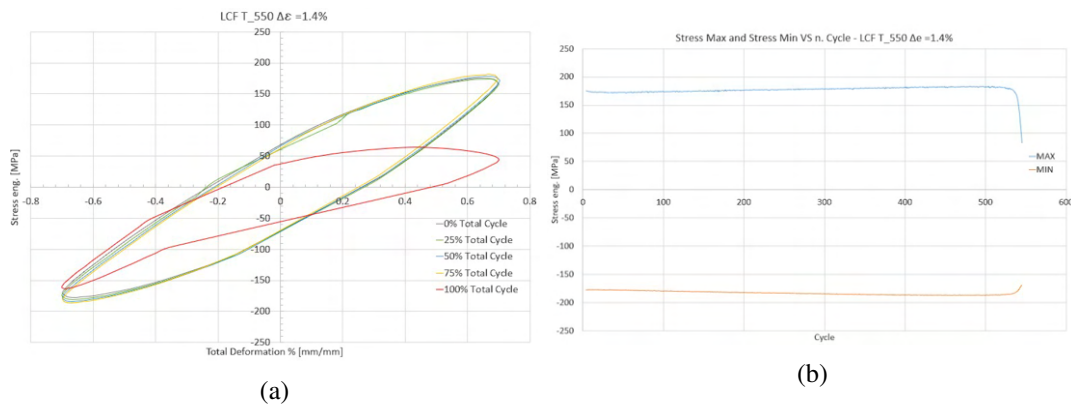


Fig. 11.15 Stress breakdown phenomenon

Fig. 11.16 LCF 550°C $\Delta\epsilon = 1.4\%$

The $\Delta\epsilon = 1.4\%$ and the $\Delta\epsilon = 2.0\%$ LCF Cu174PH 550°C tests shows a common result from LCF test of historical NASA's copper alloys: a cusp at the compression minimum stress NASA studies from Esposito et al. [23], according with conwaynarloy et al. [27], on LCF 538°C $\Delta\epsilon = 3.5\%$ Narloy-z copper alloy tests show that the formation of cusp indicate the presence of a crack (Figure 11.17). The same behavior can be observed at a similar temperature (550°C) and a different strain amplitude ($\Delta\epsilon = 1.4\%$) also for the Cu174PH meaning that the fracture mechanism of this complex metal-matrix-composite does not seems to be so different from common copper alloys (Figure 11.18). This observation must be viewed as only tentative, however, until this phenomenon can be studied in more detail.

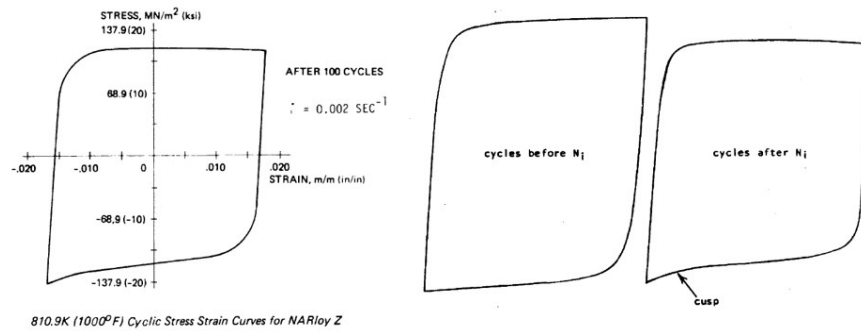


Fig. 11.17 NASA Narloy-z copper alloy LCF R-24-17 test at 538°C - Cusp behavior after N_f cycle

For this type of cycling the presence of a crack leads to the formation of a cusp near the compression tip of the hysteresis loop. While the cusp is well-developed in this illustration, the very first indication of a point of inflection in the compression portion of the hysteresis loop can be assumed to represent the crack initiation point at the first cusp-behave cycle, which is the 539th out of 546. Therefore the point occurs just slightly before end-life over the entire strain range regime employed in this test.

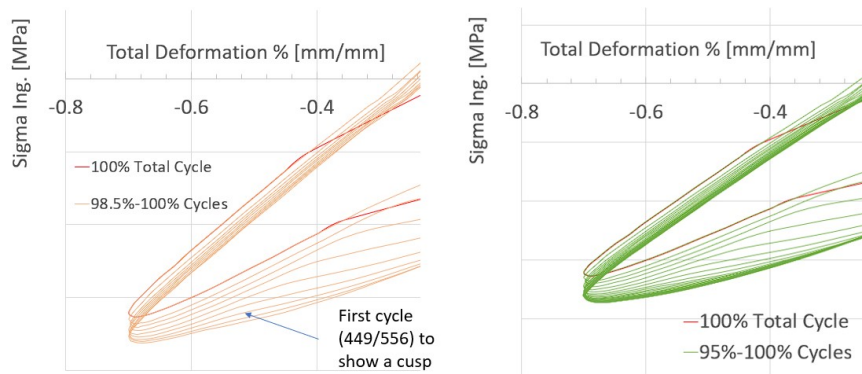
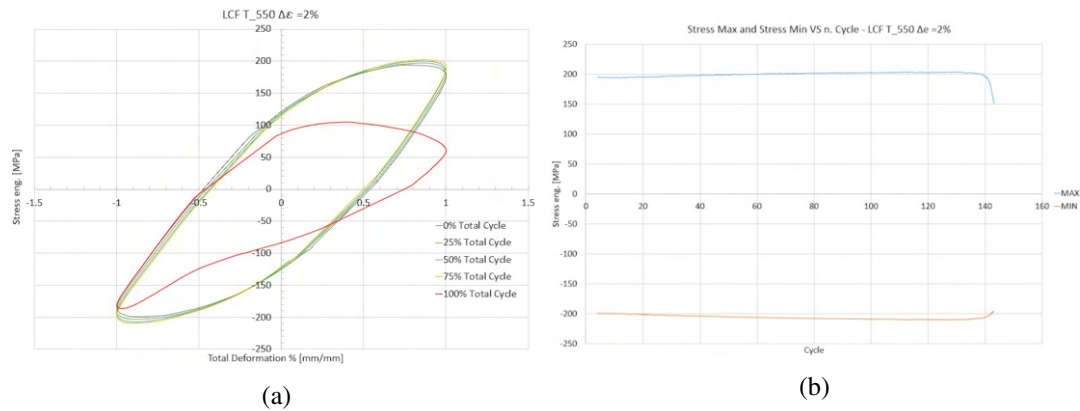
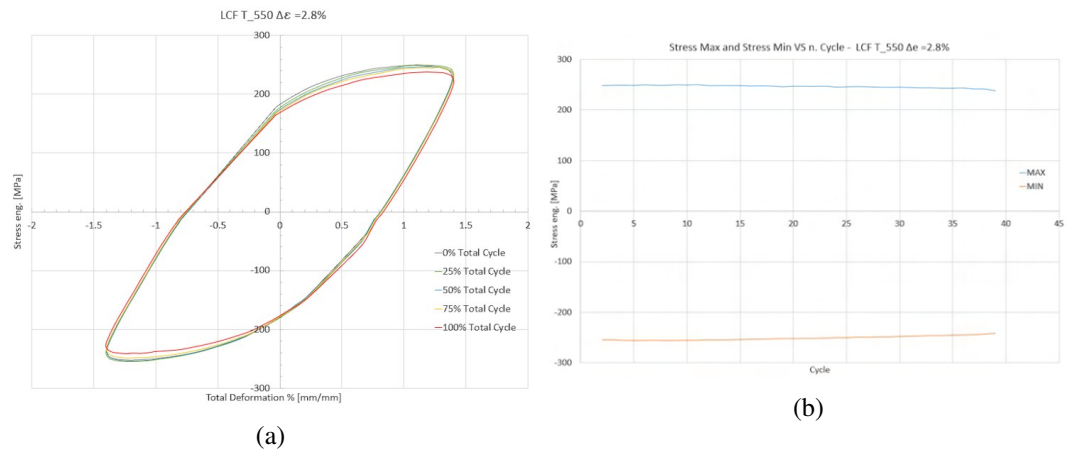
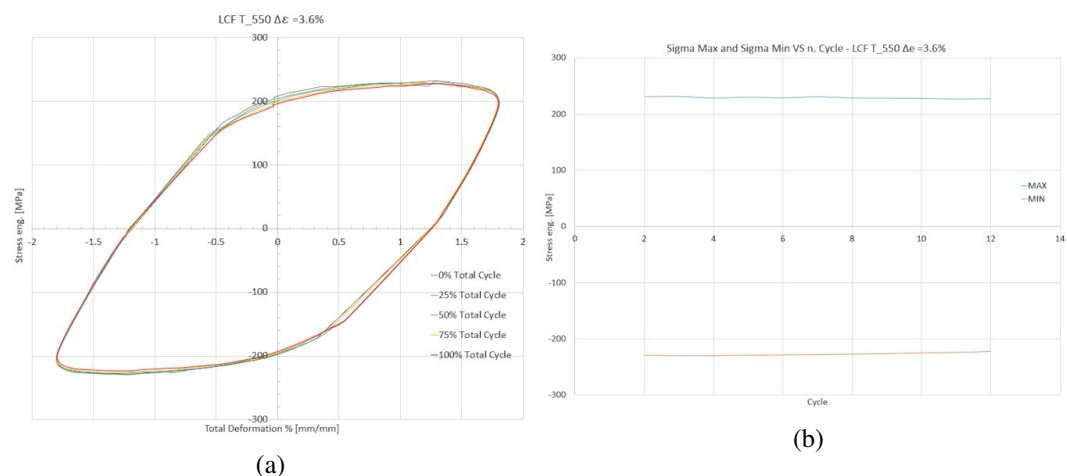


Fig. 11.18 Cu174PH $\Delta\epsilon = 1.4\%$ LCF test at 538°C - Cusp behavior after the 539th cycle out of 546 total cycle to failure

On the other hand NASA [27, 23] noted the cusp formation was in the hysteresis loops in the region close to half-life for all the testing except those in which the strain rates were greater than 0.2 Hz. In these higher strain rate tests the cusp formation appeared much later than half-life. Since the LCF Cu174PH LCF tests have been performed at 0.5 Hz, and since the cusp shows up slightly before end-life, this results is according to the NASA tests at a strain rate higher than 0.2 Hz [27], even though the strain total amplitude at which the cusp shows up is different for Cu174PH respect to the NASA's Narloy-Z copper alloy.

Fig. 11.19 LCF 550°C $\Delta\epsilon = 2.0\%$

The $\Delta\epsilon = 1.4\%$ and the $\Delta\epsilon = 2.0\%$ shows a remarkable final traction stress non-symmetric breakdown behavior. The way the voids affect the traction stresses seems predominant on the same effect respect to the compression stresses.

Fig. 11.20 LCF 550°C $\Delta\epsilon = 2.8\%$ Fig. 11.21 LCF 550°C $\Delta\epsilon = 3.6\%$

11.5 LCF Results: Deformation VS Temperature Analysis

A comparison of multiple stabilised (50% cycles to fracture) cycles for 3 different strain amplitudes is provide in Figure 11.22, 11.23, 11.24, for $\Delta\epsilon = 2.0\%$, $\Delta\epsilon = 2.8\%$ and $\Delta\epsilon = 3.6\%$, respectively.

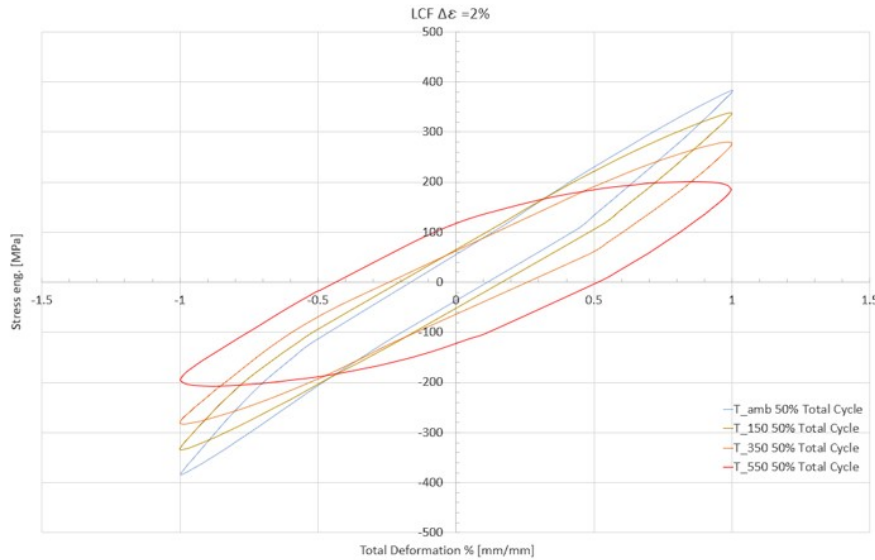


Fig. 11.22 LCF $\Delta\epsilon = 2.0\%$ vs temperatures

The $\Delta\epsilon = 2.0\%$ tests shows a remarkable difference between curves below the 550°C temperature and the one at 550°C . Therefore it is possible to state that the capability of the material to dissipate energy do not change drastically until the 550°C for a $\Delta\epsilon = 2.0\%$ amplitude.

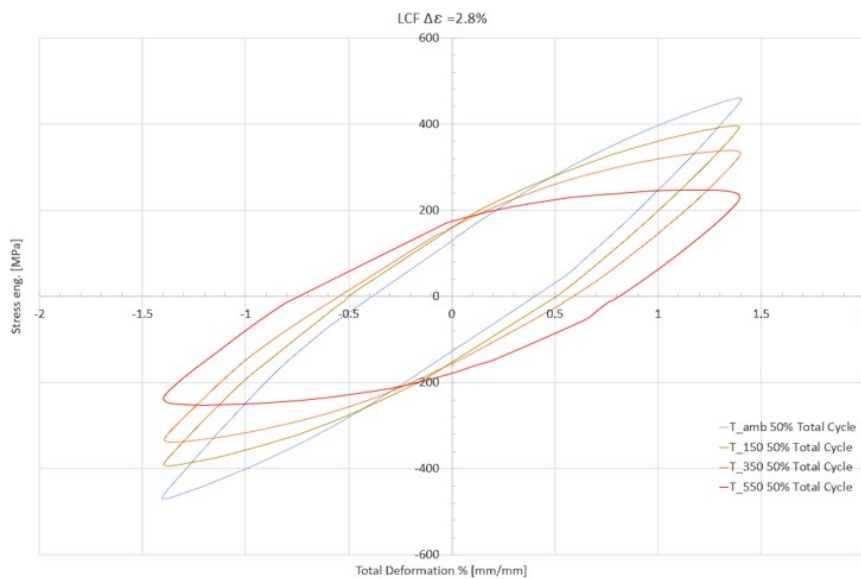


Fig. 11.23 LCF $\Delta\epsilon = 2.8\%$ vs temperatures

On the other hand, when a $\Delta\epsilon = 2.8\%$ is applied, the temperature seems to less affect the hysteresis curve shape. However at 550°C there still is a slightly breakdown and a overall bigger hysteresis curve.

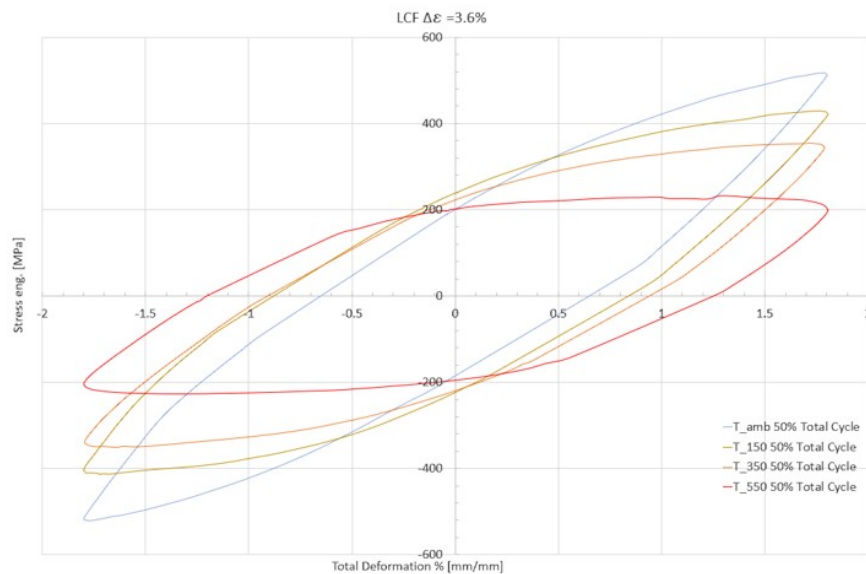


Fig. 11.24 LCF $\Delta\epsilon = 3.6\%$ vs temperatures

The higher $\Delta\epsilon = 3.6\%$ strain amplitude demonstrates, instead, that for very high strains the temperature does not affect the mechanical behavior of the Cu174PH as was appearing for lower amplitudes. In this particular case it is possible to state that the mechanical load is predominant respect to the temperature effects on the material's matrix.

11.6 LCF Results: Cyclic Curve

The cyclic behaviour of the material subjected to increasing strain cycles can be represented by a cyclic curve which relates the amplitude of the total real strain cycle to the real stress variation for stabilised hysteresis cycles. The construction of the curve is based on the envelope of the vertices of the stabilised hysteresis cycles at various strain levels.

The cyclic curve can be expressed in the same way as the monotonic tensile curve was expressed using the Ramberg-Osgod model (Appendix H). The only difference respect to the monotonic model is the exponent and coefficient of hardening are computed in order to fit the experimental cycling curve. Figure 11.25 shows the different cycling curves for temperature from room to 550°C .

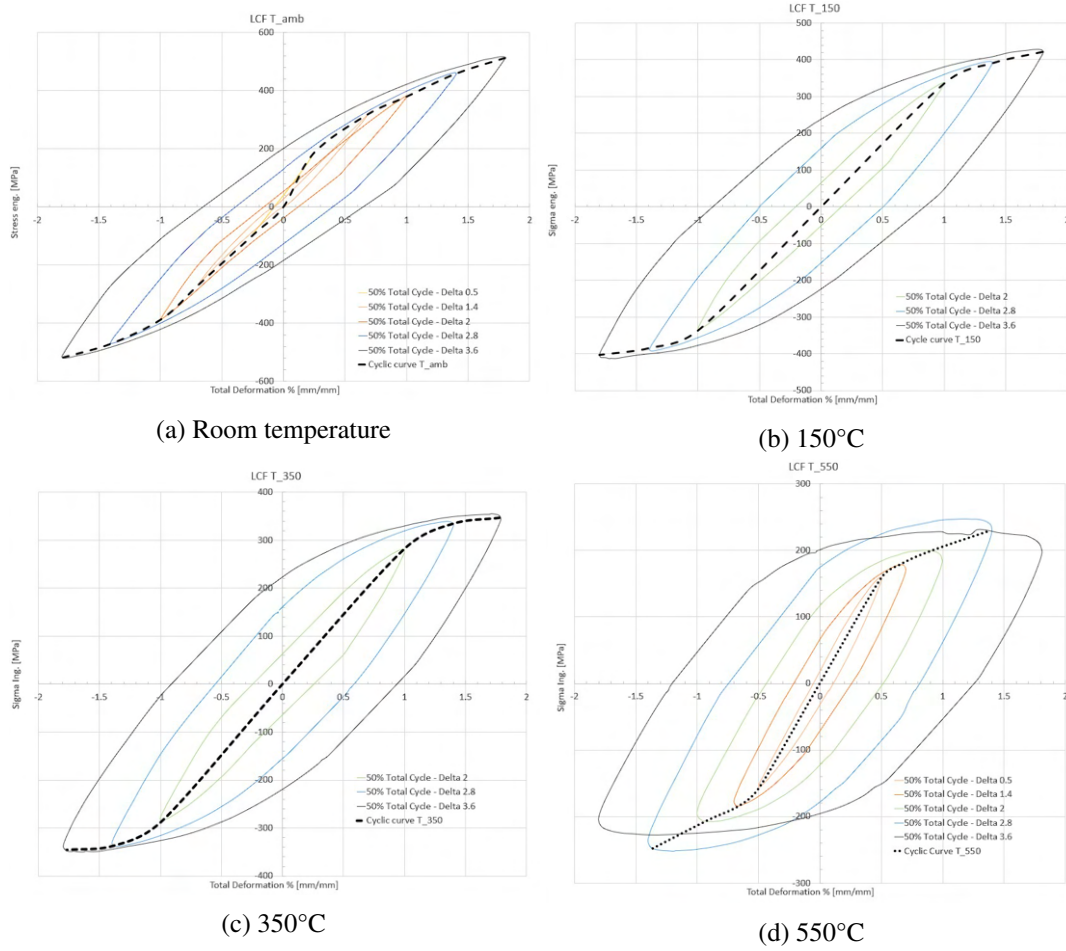


Fig. 11.25 LCF Cyclic Curve

The R.-O. has been employed for the cycling curve models and the results are presented in Figure 11.26. It is possible to observe that the model has a very high accuracy and it seems to be able to well replicate the experimental real results. Therefore it is possible to state that the model can replicate the behaviour of an AM SLM bi-metallic composite material with excellent results.

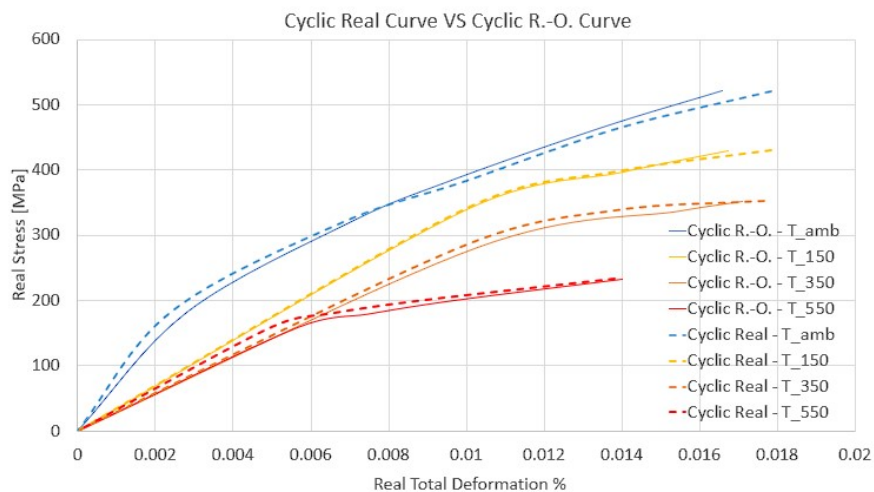


Fig. 11.26 R.-O. Cyclic Curve

Table 11.2 present the exponent and the coefficient of cycling hardening at different temperatures (Appendix J).

Ramberg - Osgood Cycling curve relationship

	K'	n'
Room	4265.79	0.48
150°C	2187.76	0.37
350°C	1737.8	0.37
550°C	1122.01	0.35

Table 11.2 Ramberg - Osgood Cycling curve relationship

The monotone curve is always located above the cyclic curve (Figure 11.27). This is a common result for softening materials. Therefore an evidence of the softening attitude of the Cu174PH is successfully presented, according with the NASA's softening copper alloys for LRE applications [23]. However the 550°C test shows slight hardening behavior, probably due to a microstructure modification.

The different attitude observed between quasi-static traction tensile R.-O. model and the Low Cycle Fatigue Cyclic curve R.-O- models is due to the fact that the traction test is an elastic-plastic behavior and the cycling curve is an elastic-visco-plastic model because of the time dependent mechanism.

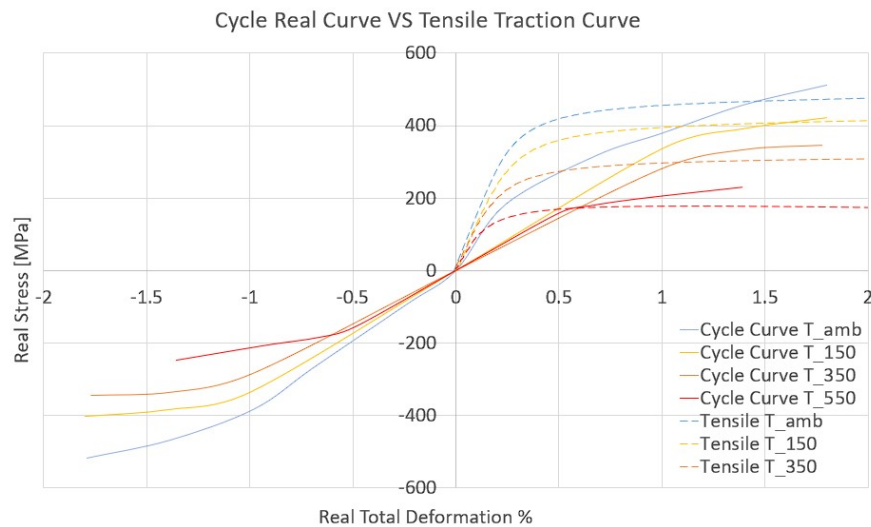


Fig. 11.27 Cyclic Curves and Tensile Traction Curves

11.7 LCF Results: Coffin Manson Model

The following chart shows the amplitude range vs cycle to fracture of the Cu174PH composite at different temperatures. It is possible to observe (Figure 11.28b) that at low temperatures such as room and 150°C no remarkable differences respect to the slope of

the curves are qualitatively visible. There is a qualitative linear proportion between room temperature and 150°C tests: for a given strain amplitude life increases or decreases by a quasi-constant amount (Table 11.1 for numerical tabular results).

On the other side, at higher temperature, such as 350°C and 550°C the material's behavior change: for 350°C Cu174PH shows a lower life at high strain amplitudes and a higher life at lower amplitudes, respect to the 550°C.

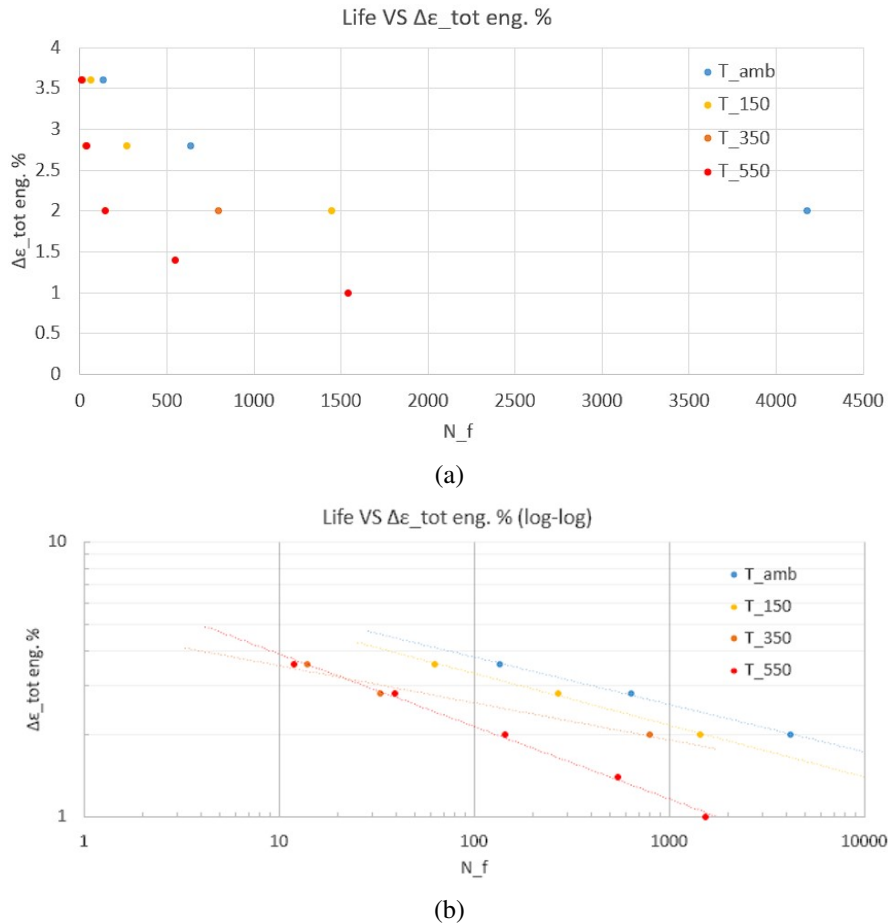


Fig. 11.28 LCF life

A brief comparison with common historical and modern bulk NASA's copper alloys at different temperatures is presented in Figure 11.29.

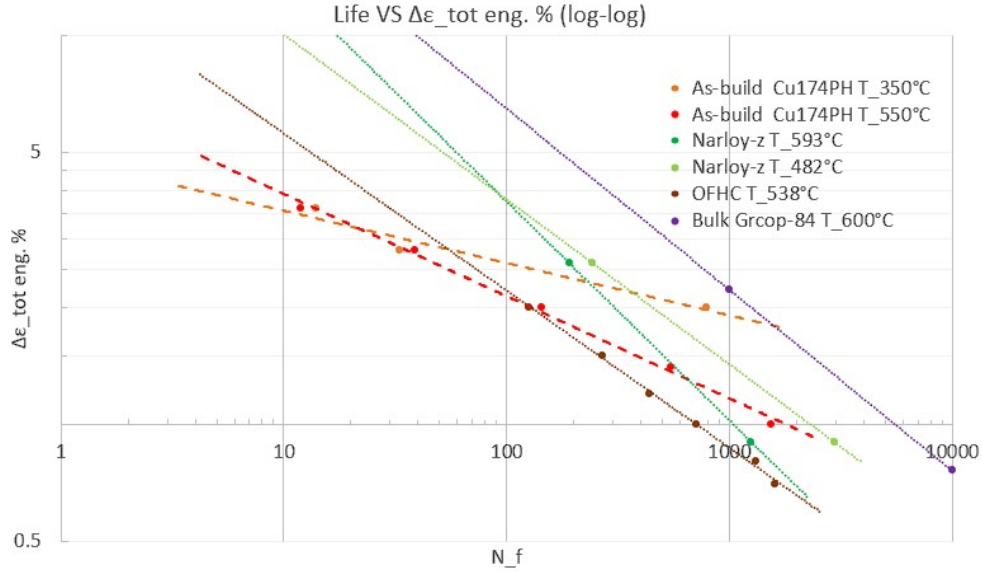


Fig. 11.29 Cu174PH and historical NASA's copper alloys life comparison, NASA's data from [26], [24] and [27].

Uniaxial damage models purposefully designed to process experimental data from test campaigns on standard specimens can be used to estimate the low cycle fatigue life of materials. The goal is to discover a number of fatigue parameters for the material. Furthermore, the calibration of uniaxial damage models is the foundation for applying multiaxial damage criteria, which allows complicated component fatigue life to be predicted [122]. The plastic strain component has been thoroughly explored by two independent pioneering research on low cycle fatigue of ductile metals [122] carried out by Manson and Coffin in 1954. As a result, the Coffin-Manson model, which is an empirical model based on the strain-partitioning technique, has been successfully employed for the Cu174PH LCF uniaxial life.

The model shows that the fatigue life, in terms of number of cycles to fracture N_f , can be connected to the plastic strain range $\Delta\epsilon_p\%$ by a simple exponential relationship, similar to the one already proposed by Basquin for High Cycle Fatigue, presented as follows:

$$\frac{\Delta\epsilon}{2} = \epsilon'_f N_f^c \quad (11.1)$$

where, the fatigue ductility coefficient ϵ'_f and the exponent c are material parameters.

Table 11.3 shows the parameter of the model (full calculations in Appendix K). A log-log chart representation of the model vs reality is presented in Figure 11.30.

Coffin-Manson equation Parameters

	ϵ_f'	c
Room	8.31	-0.173
150°C	7.76	-0.188
350°C	4.78	-0.130
550°C	6.76	-0.240

Table 11.3 Coffin-Manson equation Parameters

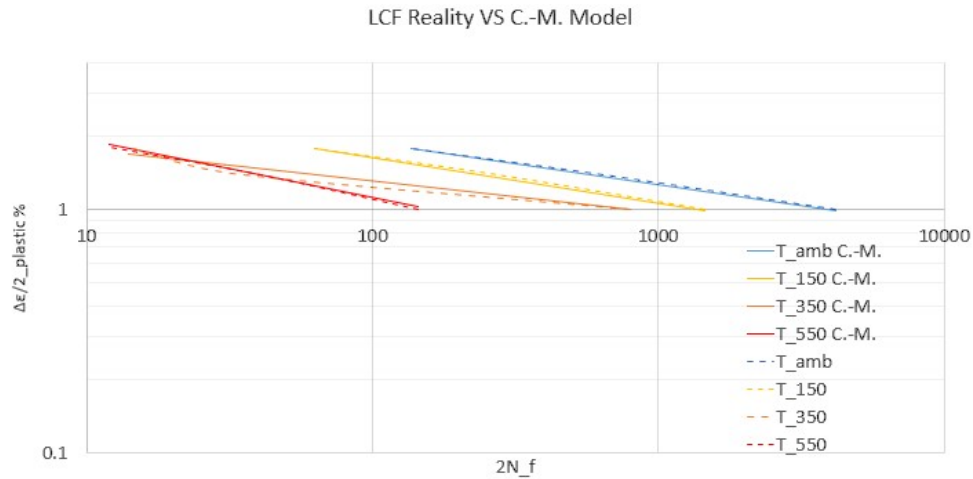


Fig. 11.30 Cu174PH Coffin Manson Model vs Experiments results

11.8 Ratcheting tests result

The damage phenomena of ratcheting and fatigue due to cyclic loading may occur simultaneously in the low cycle fatigue regime. There is a strong interaction and a separation of the damage processes is impossible. Furthermore, each phenomenon alone is characterised by different aspects. The accumulation of plastic strains is one phenomenon of cyclic plasticity failure of LRE thrust chambers. The gas hot wall side of LRE thrust chamber shows ratcheting strain cycle after cycle and the interaction with fatigue phenomenon is still today under study, especially at high temperature. Experimental evidence [5] has shown that, as the cycles accumulate, the inner wall exhibits progressive incremental thinning and bulging during the heating and cooling cycles associated with each firing: up to failure [5]. Consequently, channel wall thinning is the dominating factor in defining the reusable life of regeneratively cooled thrust chambers and a first characterization of the Cu174PH behavior is provided.

The following result are just a simple ratcheting characterization in order to understand if the ratcheting strain is linear, as for common bulk materials, or not. Table 11.4 shows a brief result presentation. Note that the $\Delta\sigma 260MPa$ test and the $\Delta\sigma 330MPa$ test have been stopped at 1500 cycle and at 350 cycle, respectively because of ratcheting strain stabilization.

Ratcheting test - 550°C					
		$\Delta\sigma_{eng.}$	260	330	400
		Cycles to Fracture	test stopped at 1500	test stopped at 350	120
0% Cycle	$\epsilon_{eng.}\%$	Max	0.42	0.63	0.90
		Min	-0.44	-0.54	-0.76
25% Cycle	$\epsilon_{eng.}\%$	Max	0.35	0.89	1.28
		Min	-0.44	-0.29	-0.53
50% Cycle	$\epsilon_{eng.}\%$	Max	0.29	0.93	1.80
		Min	-0.46	-0.20	-0.115
75% Cycle	$\epsilon_{eng.}\%$	Max	0.24	0.90	2.31
		Min	-0.49	-0.18	0.32
100% Cycle	$\epsilon_{eng.}\%$	Max	0.22	0.85	3.37
		Min	-0.50	-0.21	0.99

Table 11.4 Ratcheting test - 550°C

The ratcheting test performed at the lowest stress amplitude of 230 MPa do not shows ratcheting.

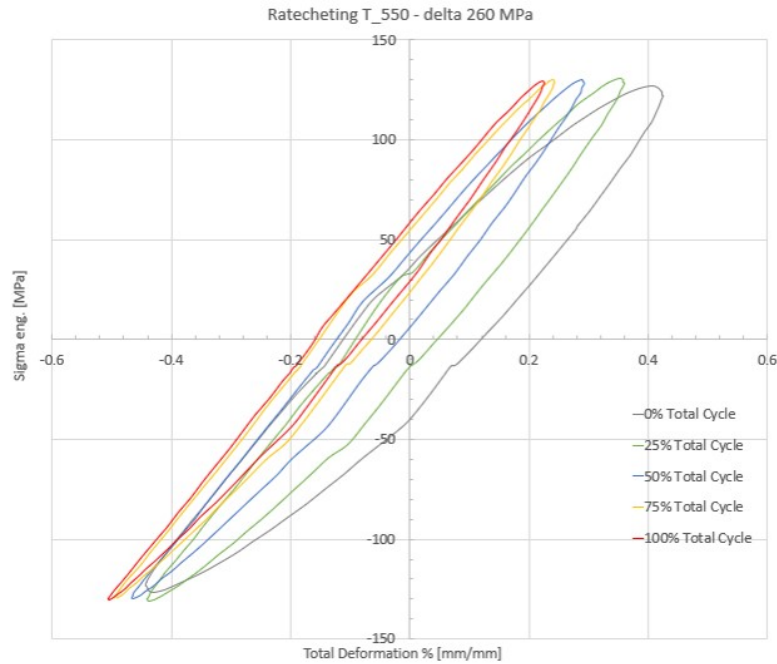


Fig. 11.31 Ratcheting tests - 550°C 130 MPa

The ratcheting test performed at the stress amplitude of 330 MPa shows a first ratcheting behavior. However after about 170 cycle an hardening attitude seem to govern one more time the phenomenon.

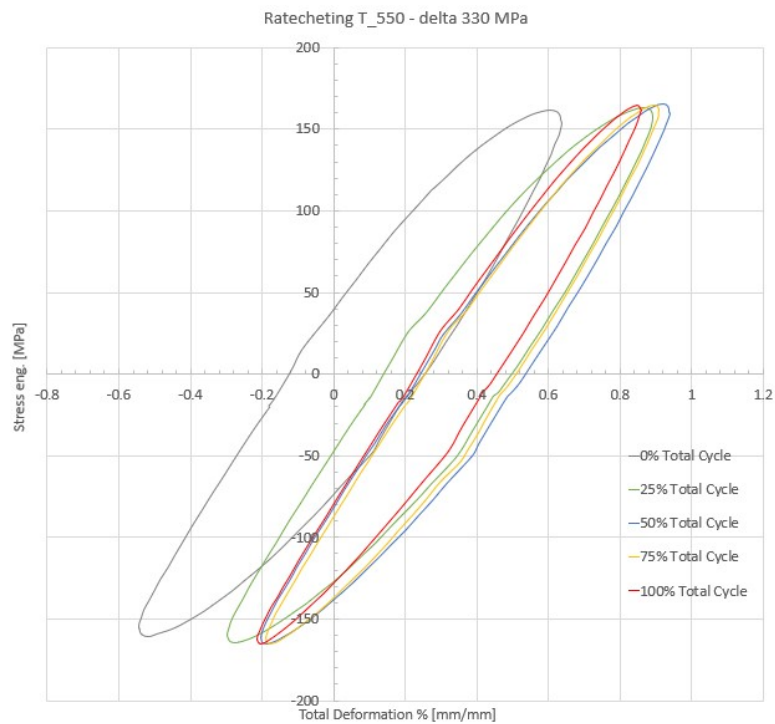


Fig. 11.32 Ratcheting tests - 550°C 160 MPa

The ratcheting test preformed at the stress amplitude of 400 Mpa shows a fully developed ratcheting behavior. A remarkable experimental evidence is the non-linearity of the ratcheting strain (Figure 11.34).

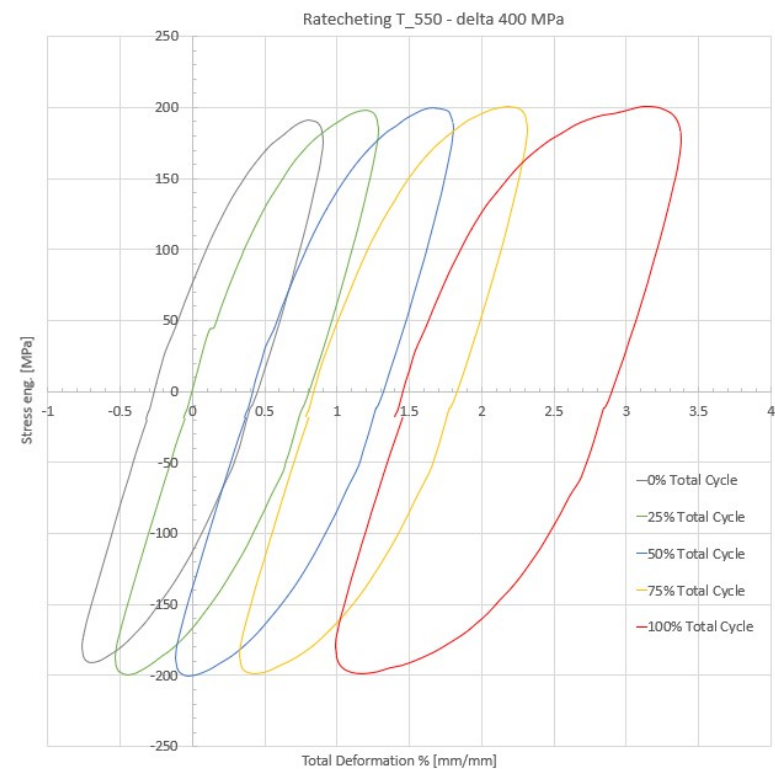


Fig. 11.33 Ratcheting tests - 550°C 200 MPa

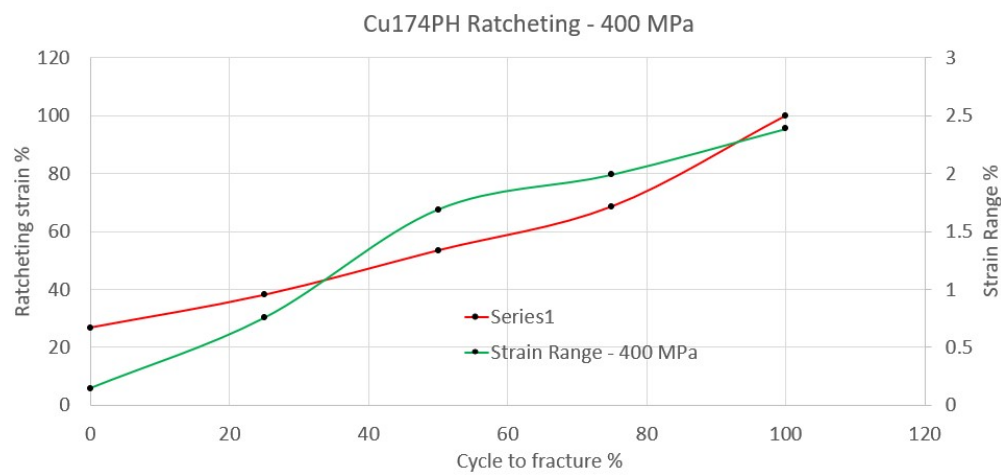


Fig. 11.34 Cu174PH ratcheting analysis

Chapter 12

Experimental Results: Creep Tests

Creep tests have been performed respect to two different temperatures, 300°C and 500°C. Unfortunately, because of the high processing costs only 3 specimens have been creep tested. In addition all tests have been stopped after 100 h because of the need to use the machine for other research projects (and therefore the tertiary creep phenomenon can not be observed).

Cu174PH is a new innovative material and therefore the creep behavior was completely unknown: the main objective of the 300°C test was to have a first trial test in order to better understand the mechanical visco-plastic attitude of the under study composite. The 300°C test have been performed with a stress load which allowed the material to exhibit at least a plastic deformation. Therefore, by analysing the traction tensile test, a stress of 270 MPa, at 300°C, have been chosen in order to target a 0.5 % total strain and therefore to be sure that the plastic domain was achieved.

On the other hand, the 500°C, have been performed because of the more close temperature condition of a common LRE thrust chamber. The same logic was applied in order to achieve a 0.5 % total strain, thus a 170 MPa stress has been applied. The second 500°C test have been performed with the purpose of providing a strain rate for a different stress load at the same temperature, and therefore obtaining a strain rate vs stress trend profile.

12.1 Creep tests

Result from creep test shows a remarkable primary creep and a low rate secondary creep, as expected for a low elongation to fracture material, such as the under study Cu174PH.

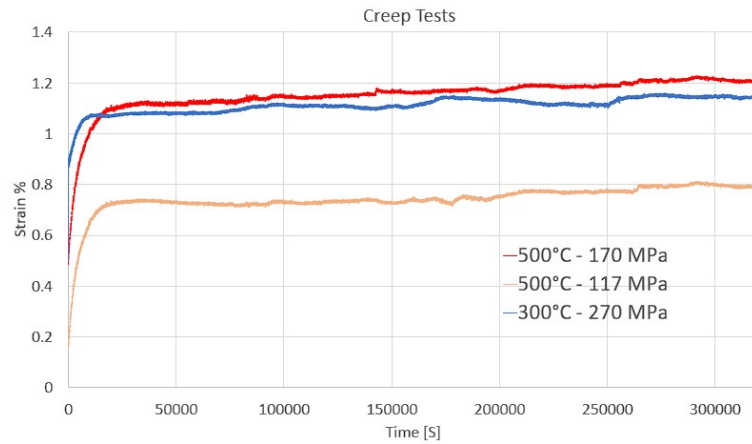


Fig. 12.1 Cu174PH Creep tests results

A logarithmic representation is provided in Figure 12.2. The secondary creep is clearly distinguishable from the primary phenomenon. The logarithmic time representation allows to observe the general behavior of the Cu174PH respect to an instantaneous load: by monitoring the creep typology transition point it is possible to observe that there is a no direct starting point for the secondary creep. After evident primary non-linear creep a hump is present and then a slight creep relaxation phenomenon comes up, thus the strain decreases with time. After this first decline phase and the local flat stabilization, the secondary creep phenomenon starts.

This particular hump-behavior is evident at 500°C independently from the load range and it seems to be negligible for the lower 300°C temperature.

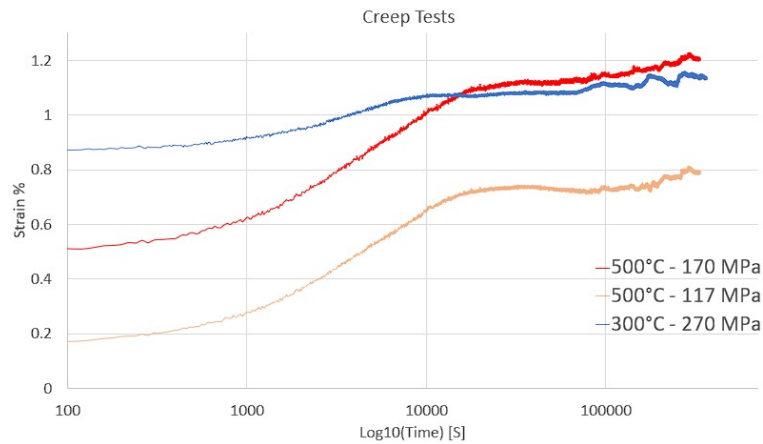


Fig. 12.2 Cu174PH Creep tests results in a Log-Log representation

The strain rate $\dot{\epsilon}$ has been evaluated with a linear regression respect to the more linear as possible largest time range. In particular all tree creep tests strain rates have been calculated in the range between 50000 [s] and 300000 [s], corresponding to a total 70 [h] range.

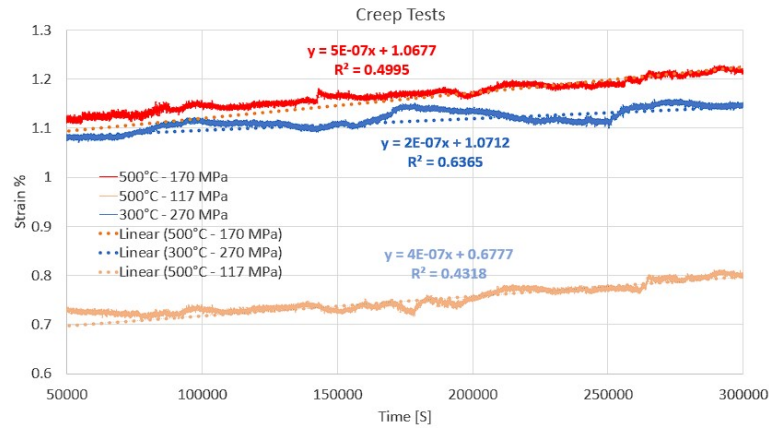


Fig. 12.3 Cu174PH Creep Strain rate

The chart presented in Figure 12.4 shows the time-stress vs strain rate behavior of the Cu174PH composite, the modern bulk GRCo-84 and GRCo-42 NASA's copper alloys [24]. It is possible to observe that the Cu174PH has a very low creep strain rate dependence respect to stress. This is due to the mail fragile behavior of the composite.

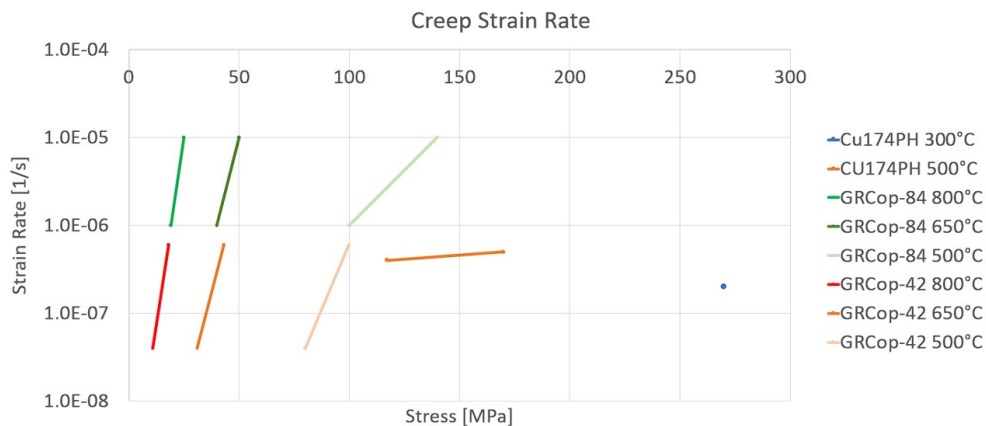


Fig. 12.4 Cu174PH and modern bulk NASA's copper alloys Creep strain rates VS stress and temperature dependence

12.1.1 Breakdown Limit Effect

The Low cycle Fatigue tests have proved that after a precise amount of time the Cu174PH composite shows a local hill phenomenon (Section 11.1 and Section 11.3). During creep tests is possible to observe a very similar behavior, thus there is an other addition experimental evidence of the aforementioned hypothesis about the relation between the material matrix and porosities.

In particular, in Figure 12.5 it is possible to observe two main material breakdowns in both, 500°C@117MPa and 300°C@270MPa tests, thus the phenomenon do not seems to be highly dependent on stress and temperature loads. This phenomenon occurs approximately at the same time for all tree tests. The same behavior can be observed also in the 500°C@170MPa creep test.

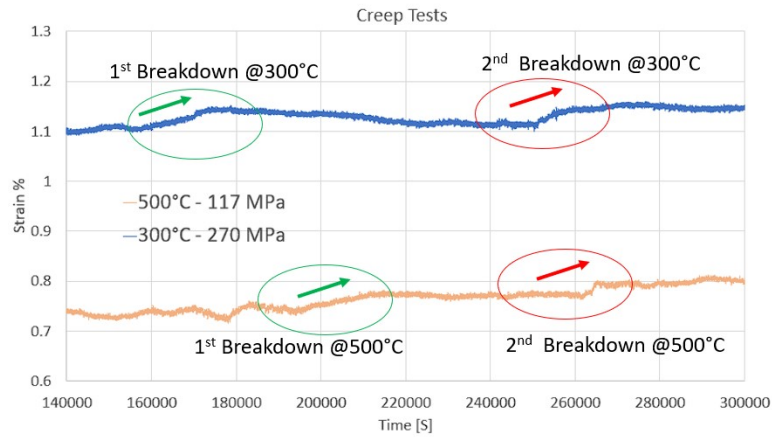


Fig. 12.5 Cu174PH Breakdown phenomenon

A proof that the phenomenon is not due to an experimental control problem is provided by the load vs time development in Figure 12.6. The load is constant and there were no particular problems during all the test time. By analysing a more detailed magnification (Figure 12.7) of a generic creep test load (300°C@270MPa) it is possible to see a local micro instability: this is normal and is due to the PID controller. However the local micro variation of respect to the load are not able to produce a strain breakdown magnitude as the one observed during creep tests.

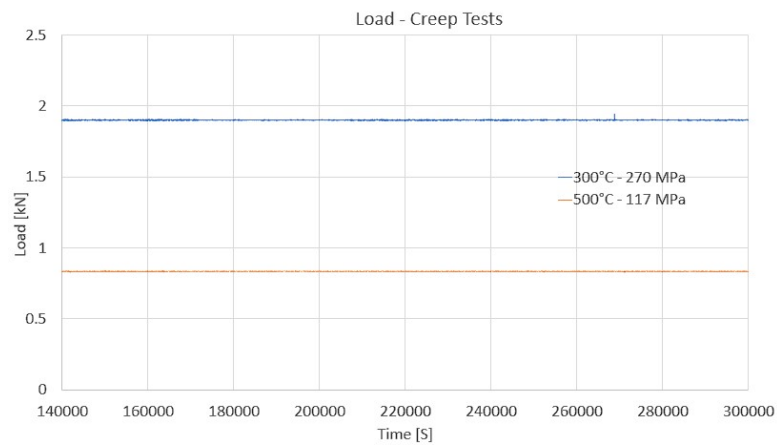


Fig. 12.6 Cu174PH Creep 300°C@270MPa and 500°C@117MPa tests loads

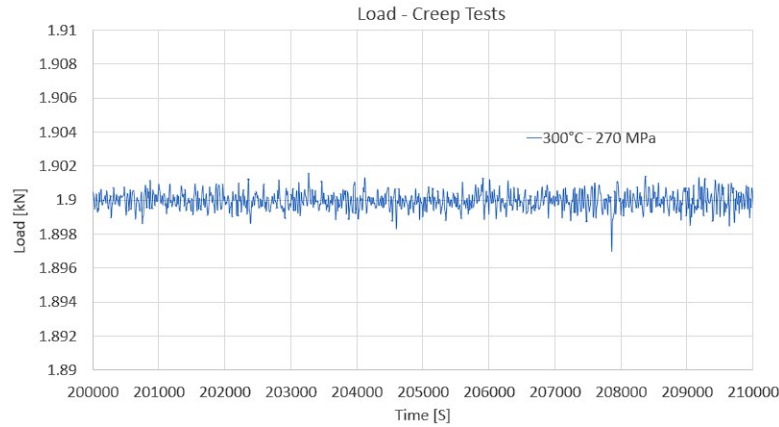


Fig. 12.7 Cu174PH Creep tests loads magnification

Another remarkable fact that has been revealed by the observation of all creep test is that the multiple strain breakdown phenomenon requires a precise activation time (Figure 12.8). Therefore before a qualitative amount of 2 hours there are no noticeable strain breakdowns. This 'breakdown limit' do not seems to be load of temperature highly dependent. The exactly same 'limit' behavior was found during the LCF tests, where before a certain number of LCF cycles no 'hill local phenomenon' was observed.

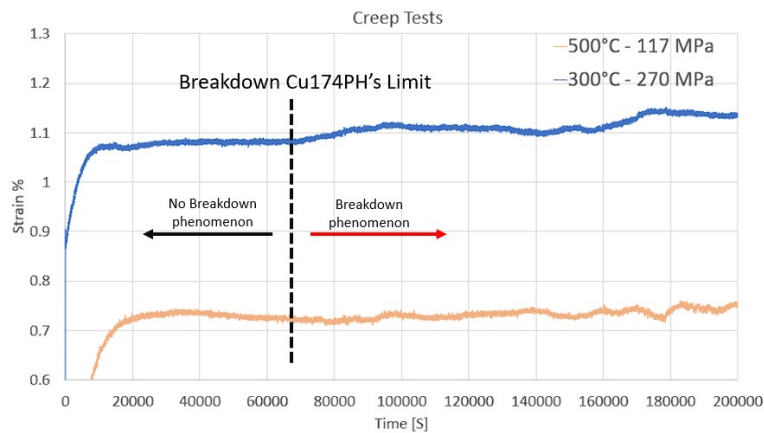


Fig. 12.8 Cu174PH Breakdown Limit

This particular creep experimental evidence, observed for a second time (first time during LCF test), can be an additional proof of the remarkable problems caused by porosity in Additive Manufacturing processes.

12.2 Creep Model

The common creep power law [123] represents a preliminary model for represent the temperature and stress dependence of secondary creep rate which are described by, respectively, Arrhenius's and Norton's laws. In the present work the power low is used as a first try model for the composite matrix Cu174PH material:

- **Arrhenius's Law:** As the strain rate, $\dot{\epsilon}$, increases with increasing the temperature, T , a straight line relationship can be obtained when plotting $\ln(\dot{\epsilon})$ against $1/T$, thus:

$$\dot{\epsilon} \propto \exp\left(\frac{-Q_c}{RT}\right) \quad (12.1)$$

where Q_c is the activation energy for creep and R is the gas constant;

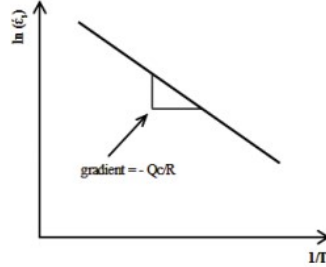


Fig. 12.9 Arrhenius's creep activation energy determination

- **Norton's Law:** As the strain rate, $\dot{\epsilon}$, increases with increasing the stress, σ , another straight linear relationship can be obtained when plotting $\ln(\dot{\epsilon})$ against $\ln(\sigma)$:

$$\dot{\epsilon} \propto \sigma^n \quad (12.2)$$

where n is the stress exponent;

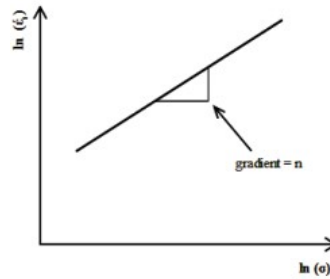


Fig. 12.10 Norton's creep exponent determination

Unfortunately there are not sufficient data available for the Arrhenius's Law. On the other hand, the Norton's Law has been successfully implemented for the 500°C secondary creep behavior by the determination of the Norton's exponent in Figure 12.11. A more in-depth study should be performed also if LRE thrust chambers, because of the low firing time (aprox. 200-300 s), do not show a relevant creep behavior. However, since strain during firing phase is relevant a visco-plastic creep model should be implemented. The creep or not creep models implementation on a structural LRE thrust chamber analysis is still today, for common alloys, under investigation.

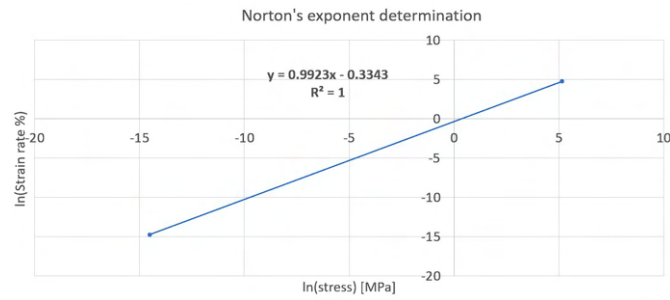


Fig. 12.11 Norton's creep exponent

12.3 Creep (traction) Relaxation tests

A first creep relaxation test have been performed at 550°C with a 1.4 % strain. This test will be important to better characterise the material visco-plastic behavior during numerical calibration procedure. The test consist in applying a certain constant deformation (end not a stress, as for the 'classic' creep tests) and acquire the stress response of the material during time.

Is is possible to observe that after amount 100 s from the starting allayed load, no more strain can be observed.

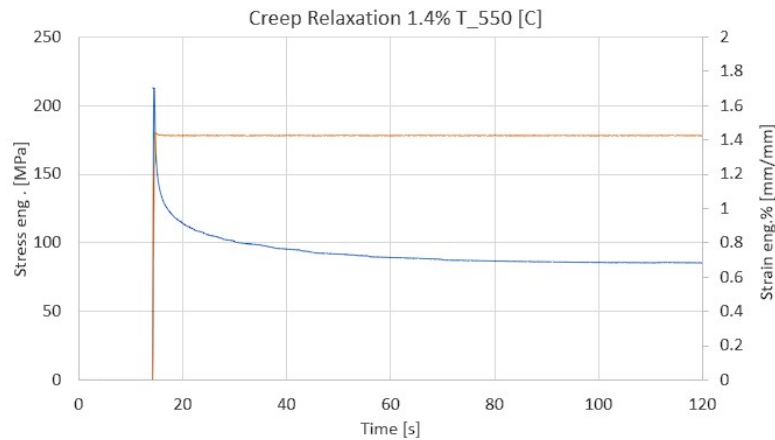


Fig. 12.12 Cu174PH Creep Relaxation tests

After the first strain test other increasing strains have been applied in order to evaluate the material response.

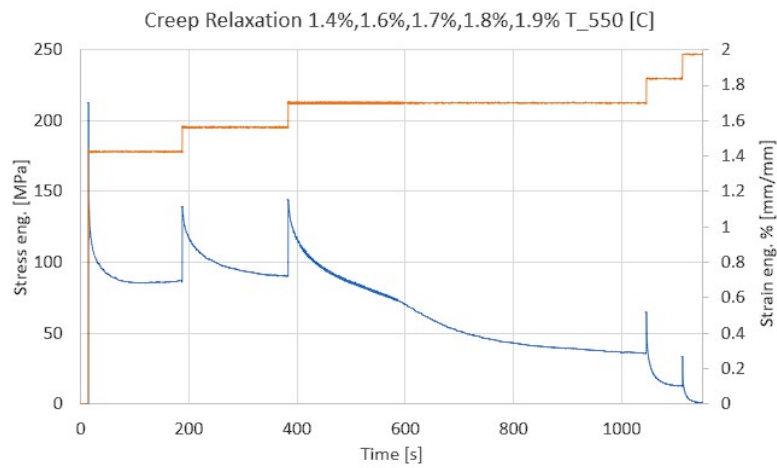


Fig. 12.13 Cu174PH Creep Relaxation tests history

Chapter 13

Experimental Results: Fracture surface analysis

13.1 Tensile traction tests

The traction tensile tests shows a fragile overall behavior due to the low elongation to fracture, but on the other hand the surface fracture angle (respect to the axial loading direction) seems to be close to a 45°C, thus a ductile fracture mechanism. This particular and unexpected behaviour could be the result of the bi-metal matrix of this particular composite. The angle of the fracture could by linked to the pure copper behavior and the fragile elongation to fracture to the 174PH.

By analysis fractures at room temperature, 150°C and 350°C it is possible to observe that a slight reduction of the central section (necking is visible). In addition, this three test temperature shows a 45° fracture. On the other hand the 550°C fracture appears more horizontal and thus fragile.

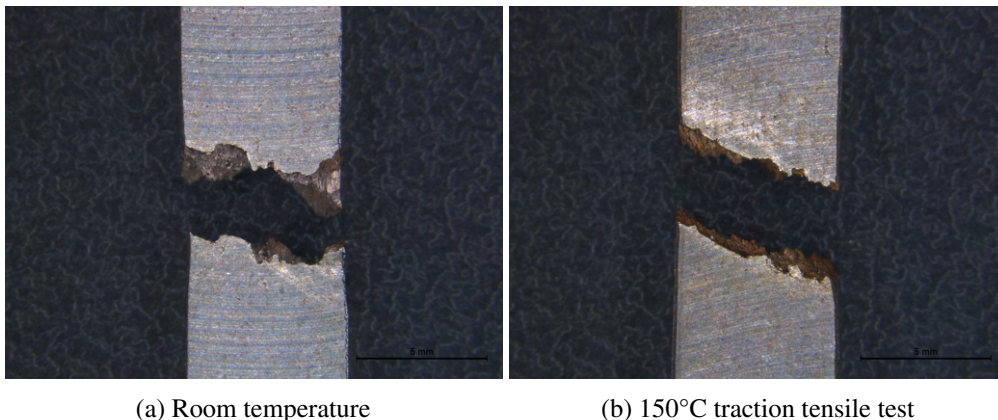


Fig. 13.1 Optic images of the tensile traction fracture surfaces - part A

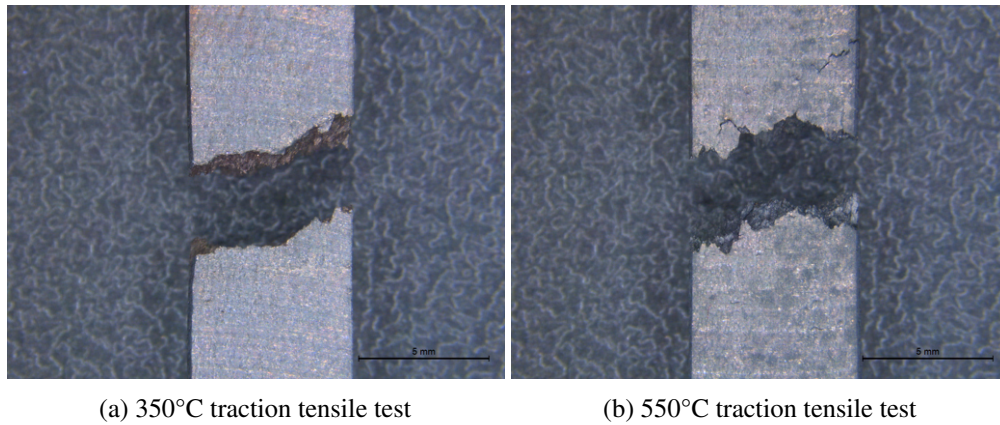


Fig. 13.2 Optic images of the tensile traction fracture surfaces - part B

The 550°C has a particular brittle behavior: a multi cracks - multi directions mechanism can be clearly observed. In particular the traction specimen, after fracture, presents several cracks all around the fracture area. This different multi cracks distribution, site nucleation and propagation proof the fragile behavior of the material: a more ductile material nucleates the crack in a specific site and then the instantaneous failure of cracks allows the fracture of the material. In this case, even though the fracture is a 45° one, there are multi crack and therefore the nucleation of the fracture is not focused in one point. A multi nucleation mechanism can be clearly observed.

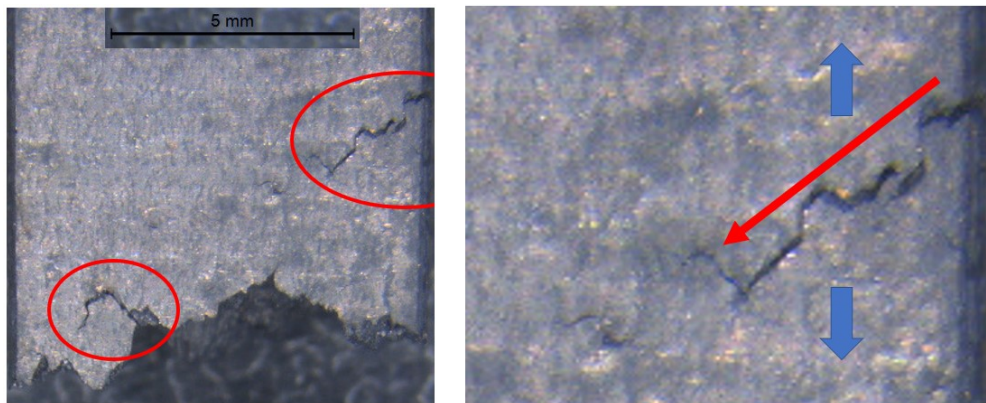


Fig. 13.3 Optic images of the tensile traction fracture surfaces - Top side of the 550°C traction specimen

On the top side of the 550°C traction specimen there is a clear surface nucleation and an in-body propagation of a 45° crack (Figure 13.3, red arrows = propagation direction, blue arrows = traction test direction). On the other hand, by analysis the bottom site of the same specimen, the proof of others multiple surface cracks is presented. The propagation cracks, in this case, seems to be horizontal (Figure 13.4, red arrows = propagation direction, blue arrows = traction test direction).

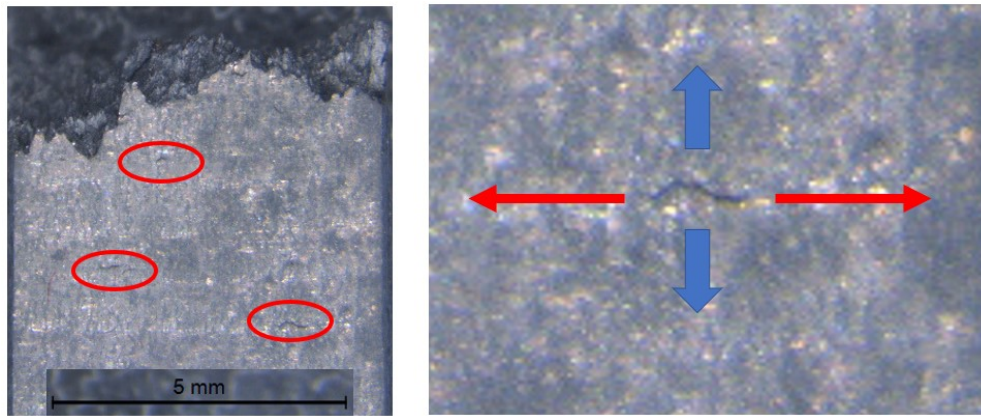


Fig. 13.4 Optic images of the tensile traction fracture surfaces - Bottom side of the 550°C traction specimen

13.1.1 Tensile test - Room temperature (SEM)

A more detailed SEM image allows to better understand the external surface nucleation of the fracture and the in-body propagation. The central body of the fracture (blue lines, Figure 13.5b) has a jagged surface which could be linked to a quicker fracture propagation respect to the external body surface (red lines, Figure 13.5b). The bounding surface, indeed, is smoother than the central one.

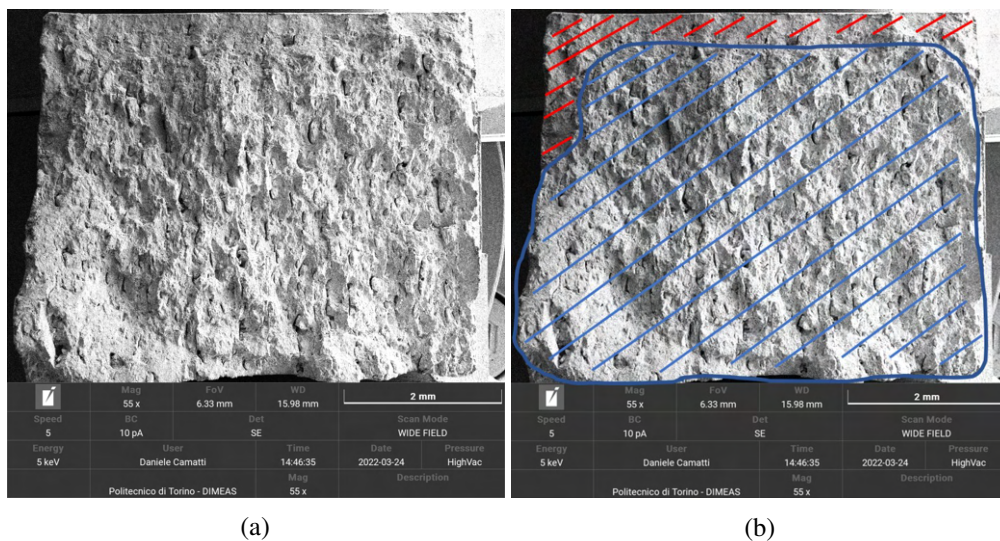


Fig. 13.5 SEM image of the tensile traction crack propagation - Room temperature test

The room temperature fracture surface seems to have a porosity/lack of fusion growth and a no coalescence of porosities (Figure 13.6a). This not-union behavior can be due to stop action performed by the 174PH islands. When a porosity/lack of fusion tries to open a crack path the less ductile and more resistant 174PH islands do not allow movements.

In addition, sometimes it is possible to observe entire spherical 174PH island almost completely detached from the copper matrix (Figure 13.6b). This is an example of

behavior already presented in the micrography analyse Section. The laser density is able to correctly melt Copper, which create the base matrix of the composite. On the other hand not all the 174PH achieve a correct melting dynamic and therefore it is able to float inside the copper 'see'. This phenomenon create a copper matrix with melted/unmelted 174PH islands.

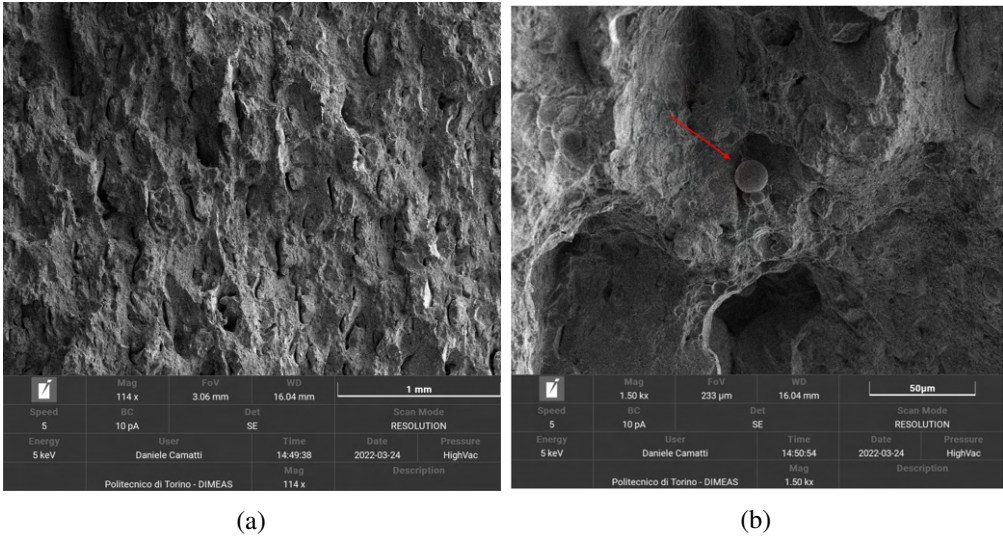


Fig. 13.6 SEM image of the tensile traction fracture surface - Room temperature test

It is possible to observe that there are two different fracture typologies: one is ductile and is linked to the Copper matrix, the other one is fragile and is due to the detachment of the interface between Copper and 174PH.

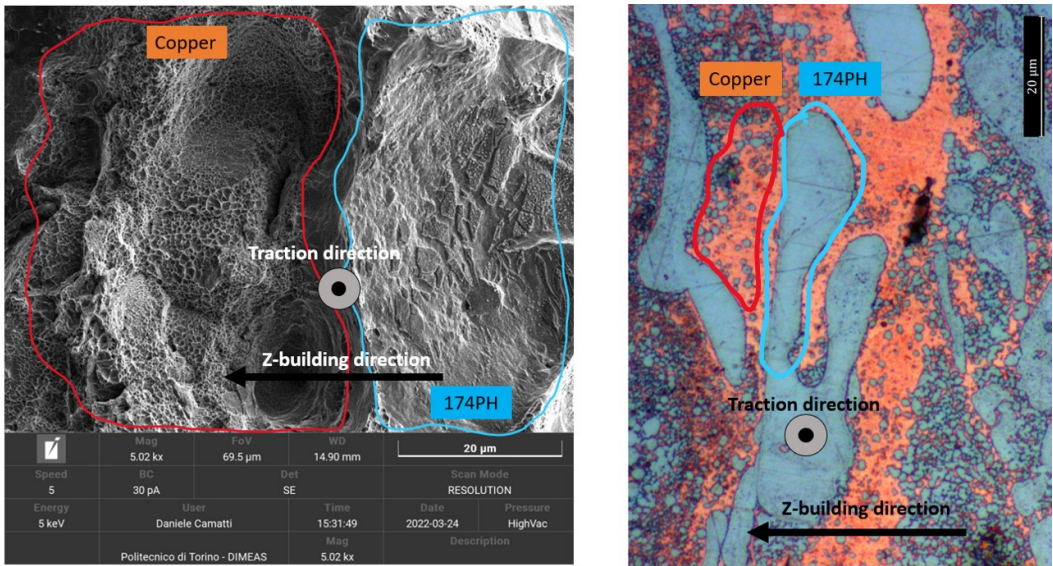


Fig. 13.7 SEM magnification of the tensile different material’s traction fracture - Room temperature test

13.1.2 Tensile test - 150°C (SEM)

The SEM magnification of the tensile traction 150°C test fracture surface (Figure 13.27) shows that a relevant amount of porosity expanded but do not join together until fracture. The surface nucleation and smooth propagation of the cracks is not clear as for the room temperature specimens (the elongation to fracture is starting to getting lower).

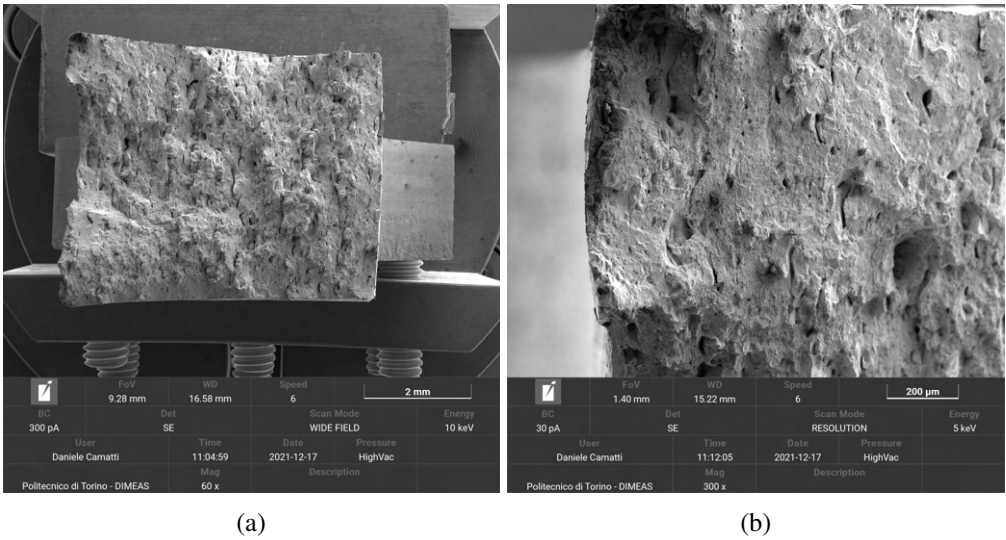


Fig. 13.8 SEM image of the tensile traction fracture surface - 150°C test

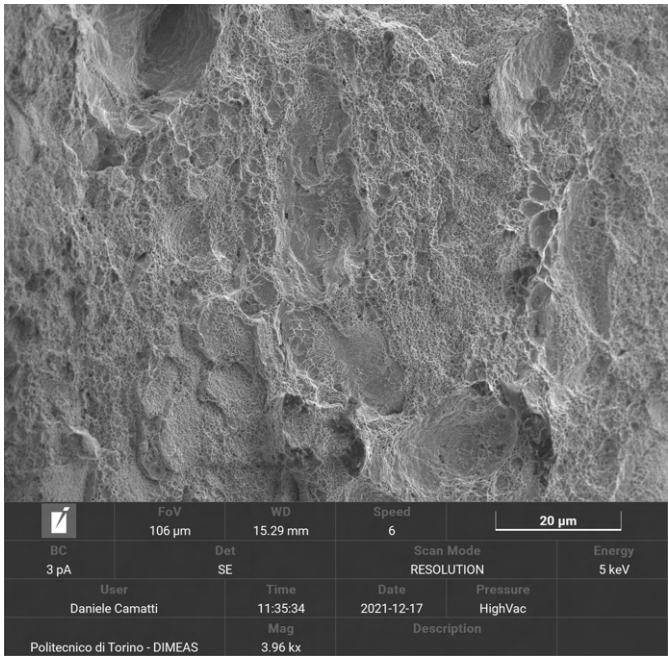


Fig. 13.9 SEM magnification of the tensile traction fracture surface - 150°C test

Via a more detailed image, presented in Figure 13.9 the surface can be better observed and the presence of four different mechanism can be better detected:

- **Dimples fracture:** A dimple fracture morphology corresponding to the areas in where the pure copper amount is dominant (same mechanism observed at room temperature);

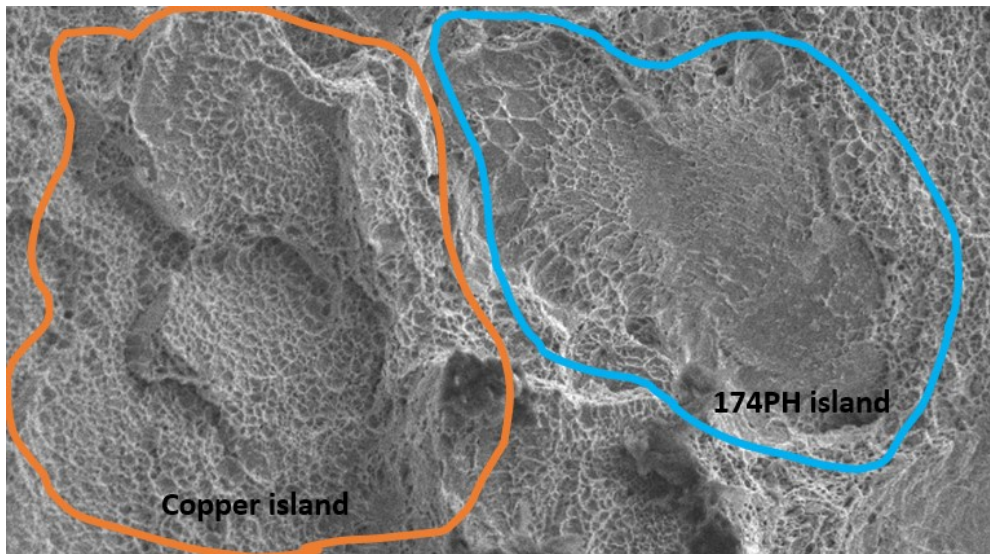


Fig. 13.10 Copper vs 174PH fracture mechanism at 150°C

- **Flat fracture:** A more flat area where probably the 174PH detachment of the interface surface is dominant (same mechanism observed at room temperature). This area, however, is not an evident fragile fracture, as expected for the 174PH. This particular behavior is due to the fact that the copper island are all around the 174PH one and therefore when the fracture starts proceed on its way around the 174PH island a small amount of copper remains attached to the 174PH island. A more clear explanation will be presented in the following section;
- **Porosity fracture:** Around porosities is is possible to observe a cusp shape. This is a clear proof that porosities do not seem to grow during the fracture propagation.

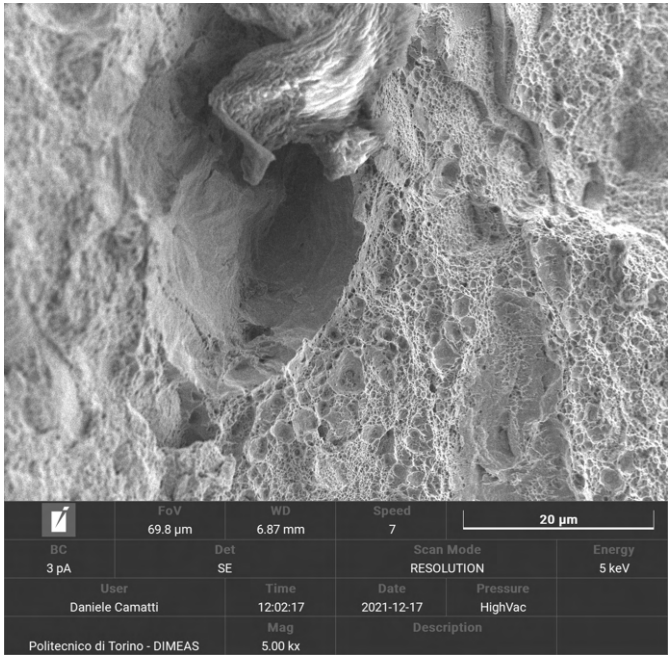


Fig. 13.11 Porosity fracture

- **Circumnavigation fracture:** A clear net line shape of fracture can be sometimes observed. This is probably due to the fact that cracks can easier pass around islands rather than through;

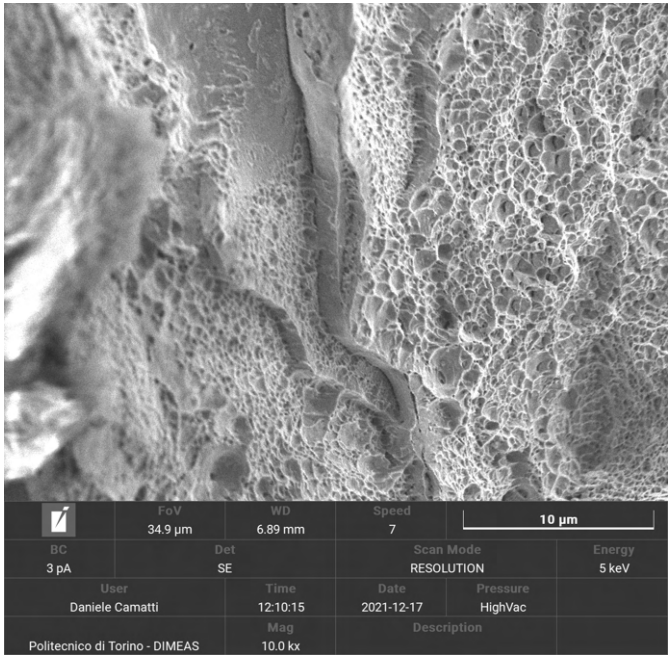


Fig. 13.12 Circumnavigation fracture

13.1.3 Tensile test - 550°C (SEM)

Since the 350°C tensile test fracture does not has particular observation, the 550°C is directly presented. The overall fracture surface do not seems to have any smooth propagation of the cracks (Figure 13.13).

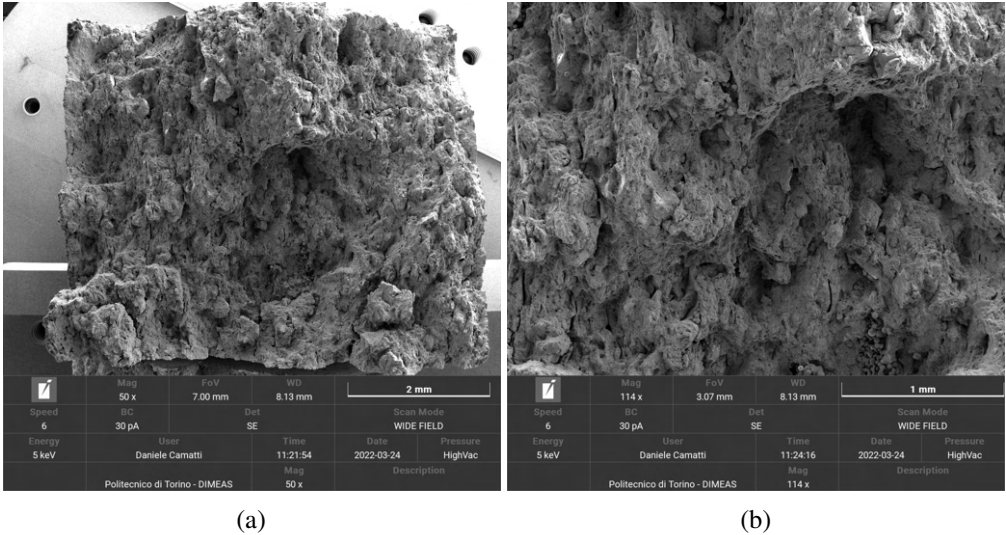


Fig. 13.13 SEM image of the tensile traction fracture surface - 550°C test

The 550°C fracture surface proof that, also at very high temperature, the X (or Y) traction direction is not able to expand porosities and lacks of fusion. Figure 13.14a do not shows a growing behavior of the lack of fusion. This experimental evidence can be observed for all lack of fusions. A tensile test performed respect to the Z building direction will probably open lacks of fusion: however, since parasites are spherical, and since proprieties does not seem to grow in the X or Y tensile traction test, there are no reason why in the Z direction tensile test they should grow as should happen for lakes of fusion. Another interesting aspect is the presence of very rare 174PH fractures. These mechanisms have been observed only on the 550°C tensile fractures surfaces (Figure 13.14b).

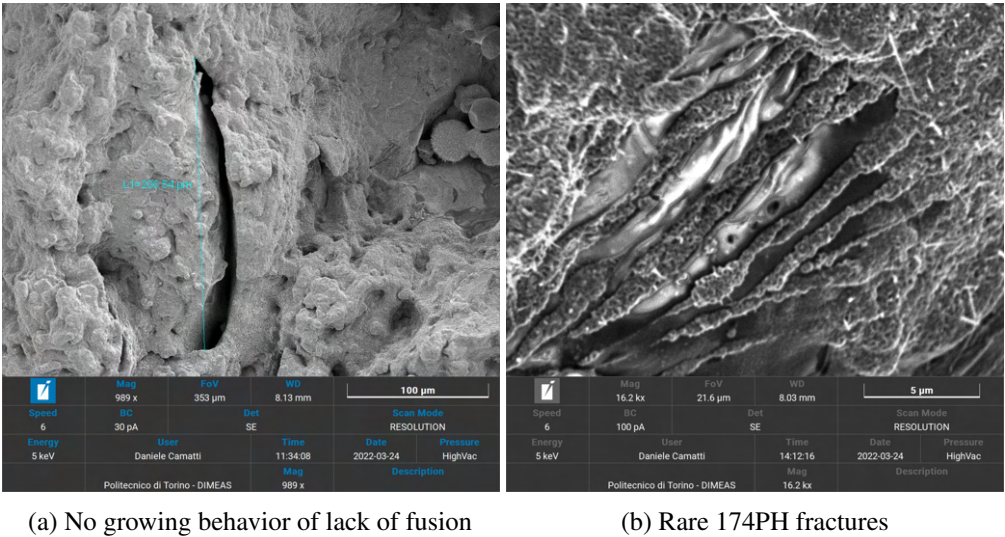


Fig. 13.14 SEM image of the tensile traction fracture surface - 550°C test

A clear Copper-174PH interface link has been successfully identified. By analysing Figure 13.15 is is possible to understand that the copper matrix achieve a inter granular fracture, while the 174PH do not seems to fracture.

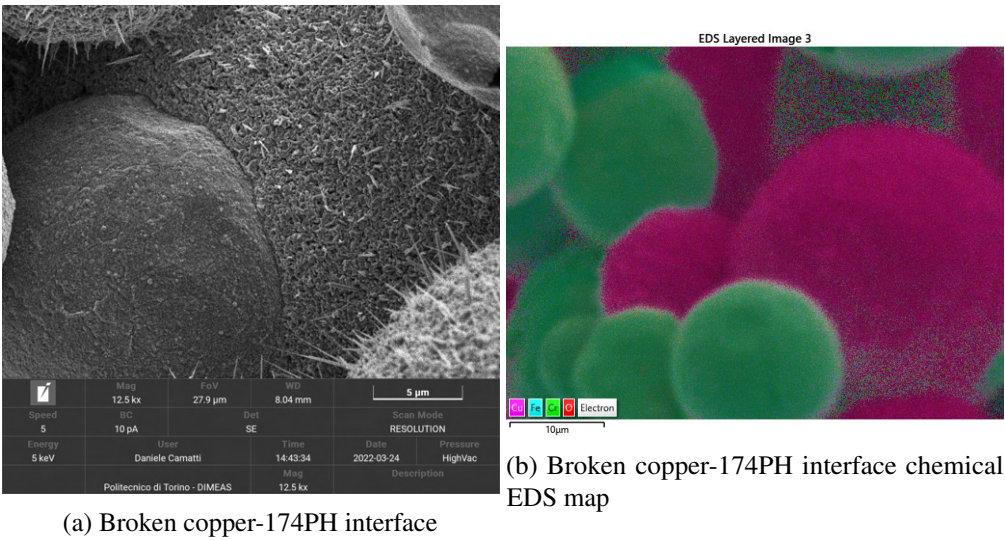


Fig. 13.15 SEM image of the broken copper-174PH interface - 550°C test

Also at 550°C is is possible to observe particular areas, all around the fracture surface, where spherical 174PH are completely detached from the copper matrix (Figure 13.16).

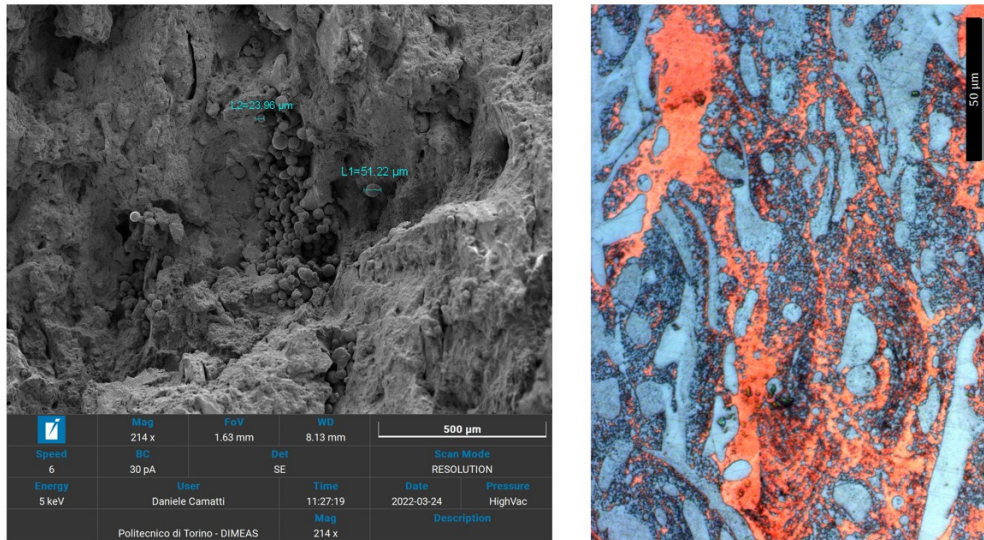


Fig. 13.16 SEM image of the broken copper-174PH spherical interface - 550°C test

13.2 Low Cycle Fatigue tests

The general LCF fracture mechanism can be observed by a transverse section of a LCF specimen presented in Figure 13.17. The fracture path circumnavigates the 174PH islands and pass through the copper matrix. However the crack propagation seems to prefer to taring to pass around the islands, rather than through the copper.

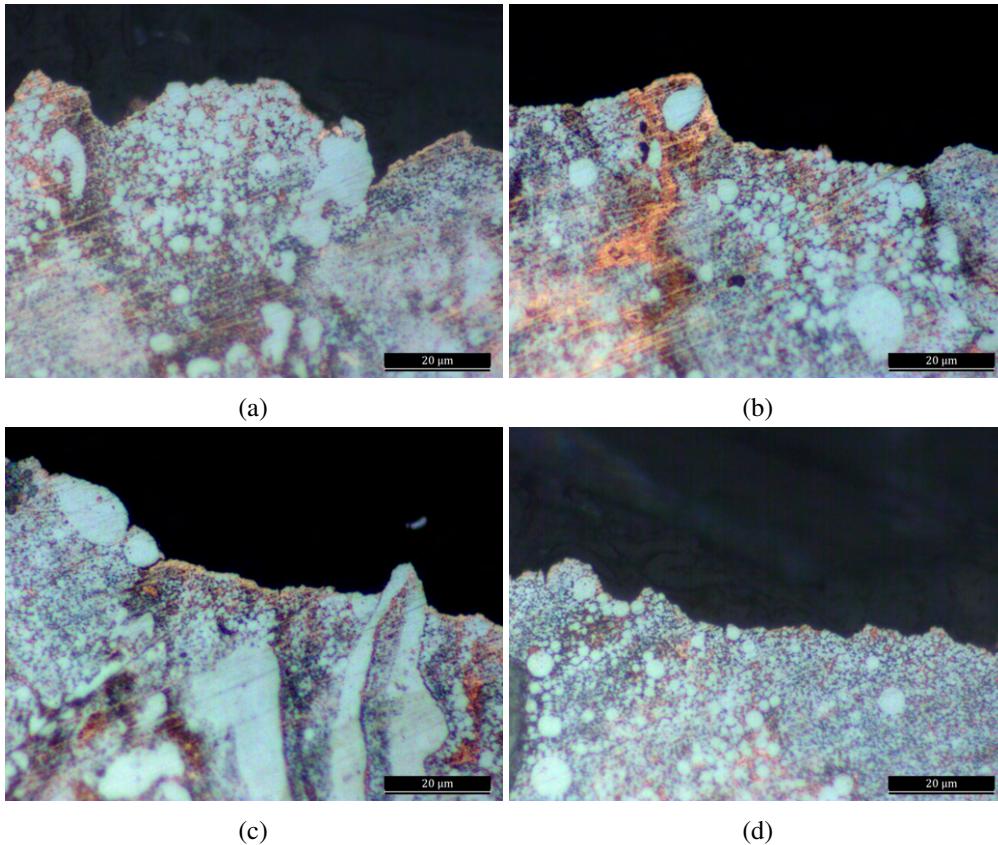


Fig. 13.17 LCF transverse magnification of the fracture surface - general room temperature test

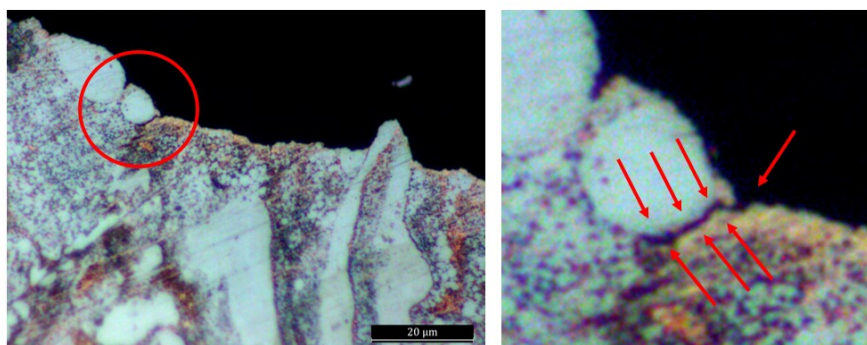


Fig. 13.18 LCF circumnavigation fracture

A magnification of the trans-copper can be related to the dimples fracture already presented for the tensile test (Figure 13.19). On the other hand, also the more planar fracture, related to the circumnavigation the entire 174PH islands, has been successfully identified on the Low Cycle Fatigue fracture (Figure 13.20). This experimental evidence shows that no relevant differences between the tensile traction fracture and the Low Cycle Fatigue one.

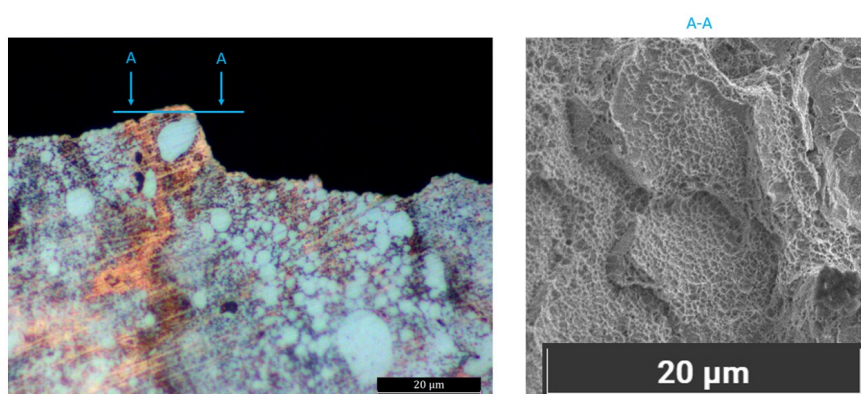


Fig. 13.19 Trans-copper general Low Cycle Fatigue fracture

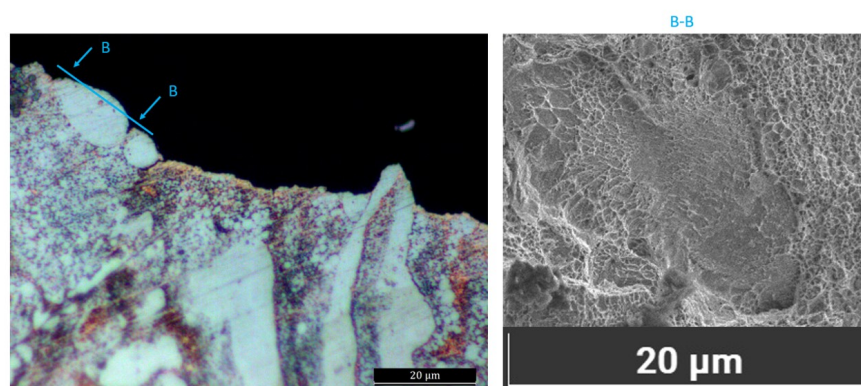


Fig. 13.20 174PH circumnavigation general Low Cycle Fatigue fracture

13.2.1 Room temperature fracture surfaces

The LCF surface shows two different areas of fracture. The first one is the tilted area of the fracture surface which is the place where the fracture progress from the external surface to the inside of the material. The other areas is the central one which is the place where the resistant material is no more able to sustain the deformation and therefore an instantaneous fracture mechanism, similar to the tensile test one, shows up.

As already observed for the tensile test fracture, also the fatigue fracture shows an angle close to the 45°C, thus the fracture seems to be ductile.

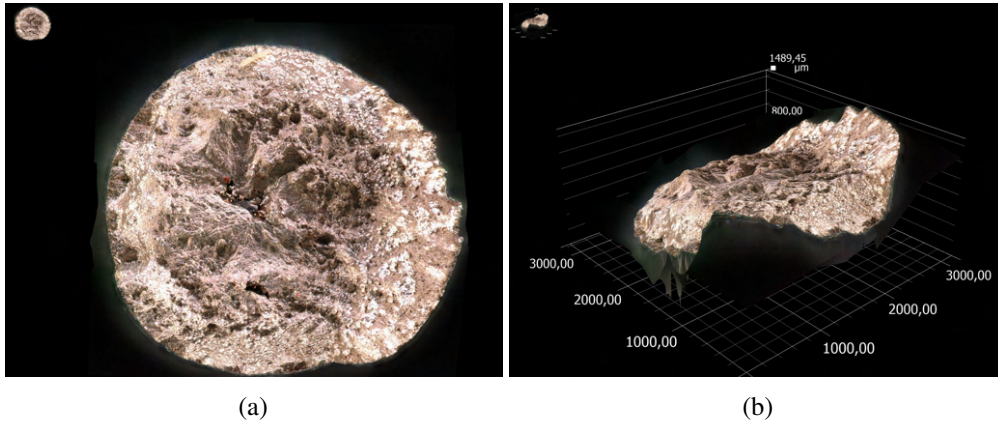


Fig. 13.21 LCF $\Delta\epsilon = 1.0\%$ room temperature test fracture surface

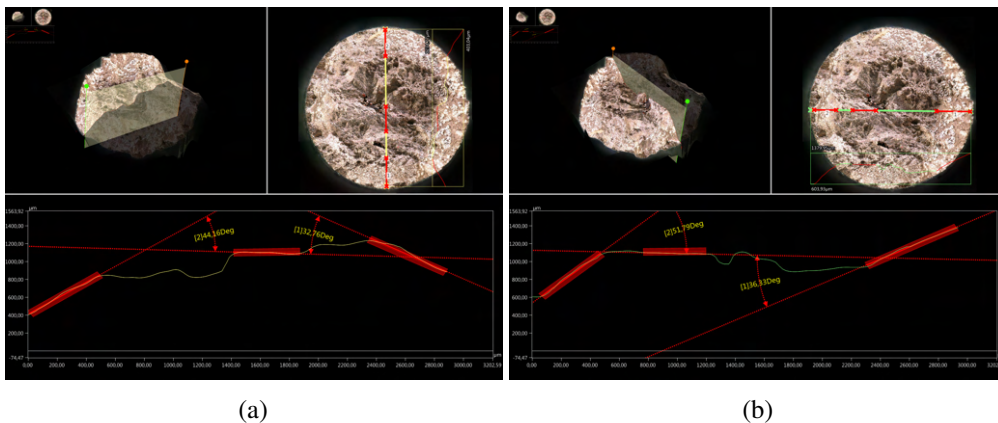
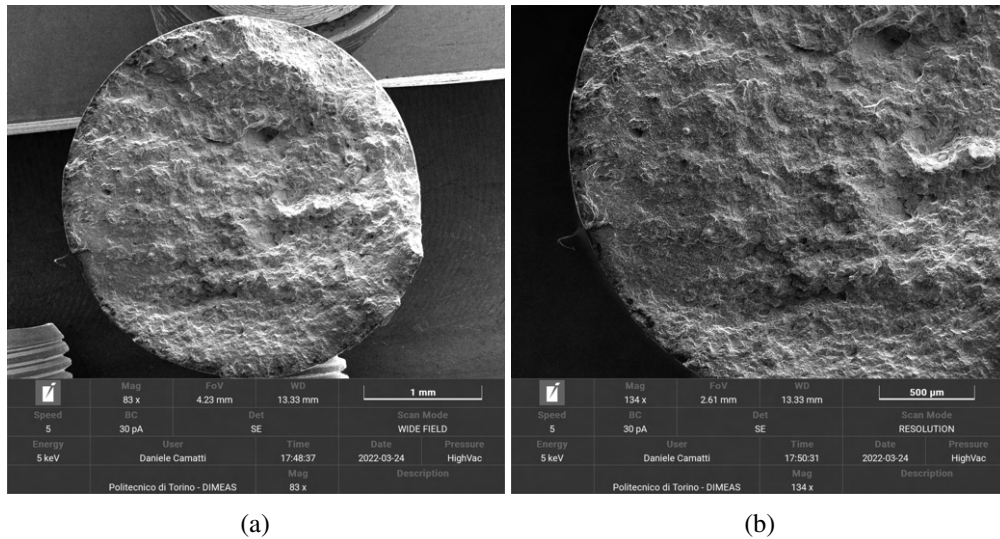
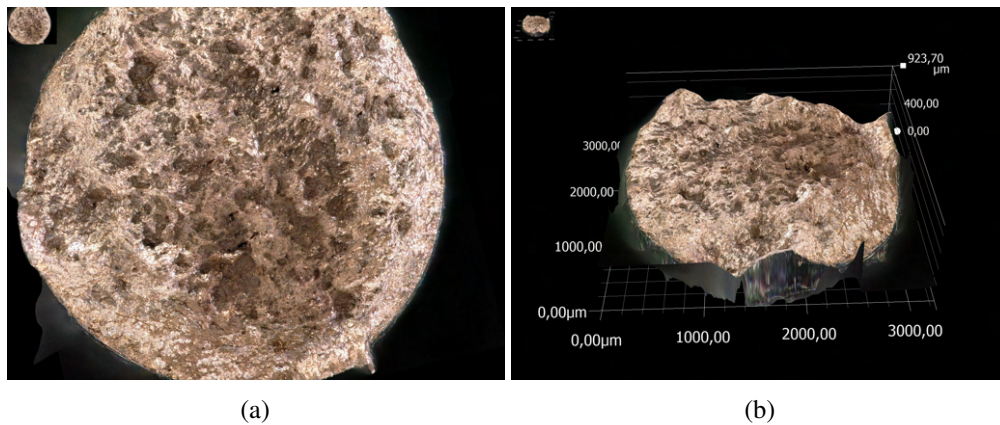
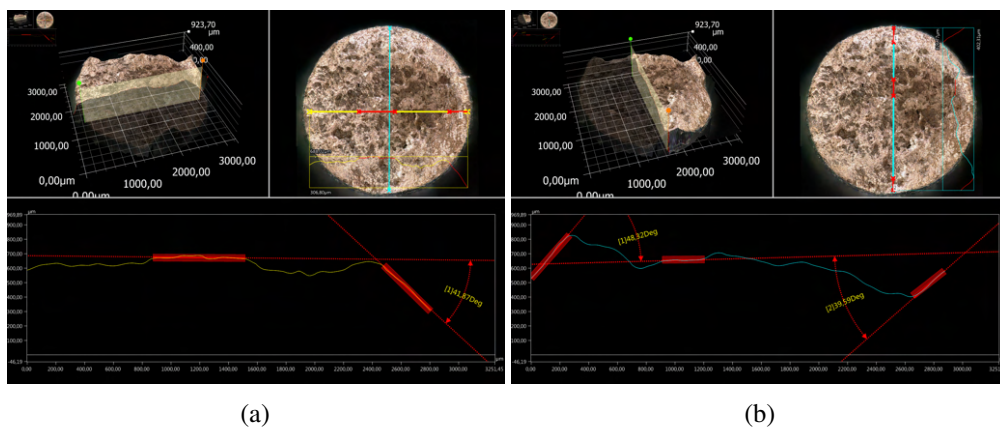


Fig. 13.22 LCF $\Delta\epsilon = 1.0\%$ room temperature test fracture surface

The SEM analysis (Figure 13.23) do not shows a classic evident crack nucleation side and propagation direction.

Fig. 13.23 SEM LCF $\Delta\epsilon = 1.0\%$ room temperature test fracture surface

No remarkable difference have been observed with a larger $\Delta\epsilon\%$.

Fig. 13.24 LCF $\Delta\epsilon = 1.8\%$ room temperature test fracture surfaceFig. 13.25 LCF $\Delta\epsilon = 1.8\%$ room temperature test fracture surface

The SEM analysis (Figure 13.26) shows a more clear crack nucleation site (external surface) but steel no propagation direction have been observed.

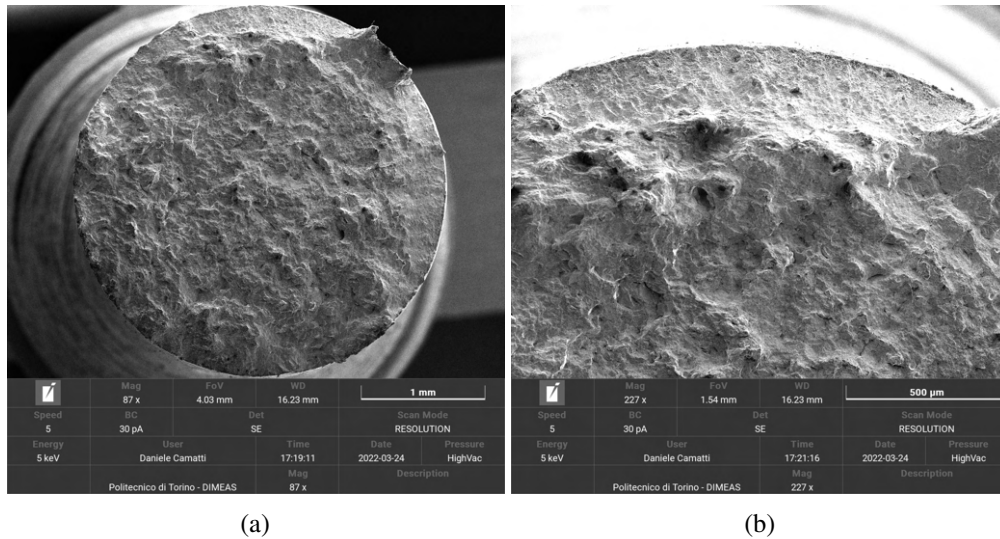


Fig. 13.26 SEM LCF $\Delta\epsilon = 1.8\%$ room temperature test fracture surface

13.2.2 150°C fracture surfaces

The high temperature analysis have not been performed because of the local arc spot welding phenomenon which happen during the fracture: the INSTRON ETMT II machine achieves high temperature thanks to the Joule effect. Since the current control did not work well the current was not stopped when the fracture occurred and therefore the fracture surfer of every LCF tests at high temperature has been locally welded.

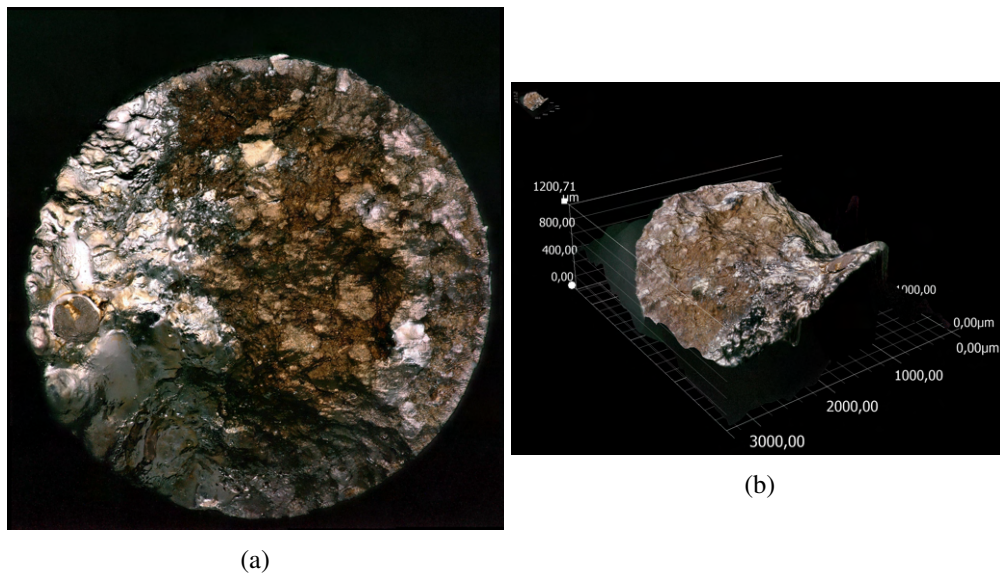


Fig. 13.27 LCF $\Delta\epsilon = 1.4\%$ 150°C test fracture surface

However a qualitative shape analysis of the $\Delta\epsilon = 1.4\%$ has been performed. The angle of the fracture and the mechanism does not seems to be different from the one at room temperate presented above. The surface has a central flat area and a lateral sloping area of about 30° (Figure 13.28).

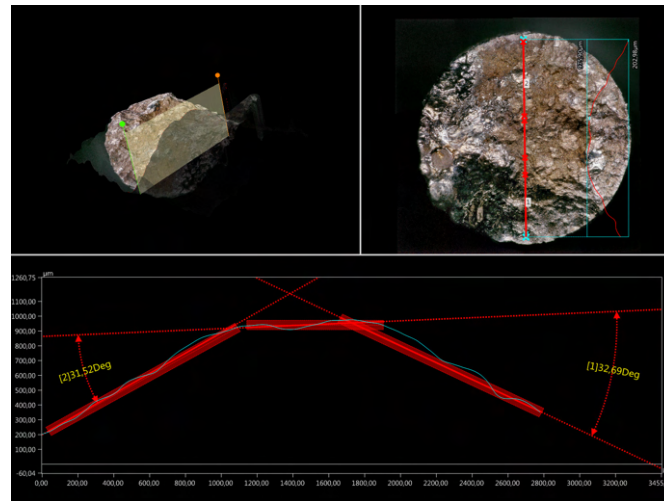


Fig. 13.28 LCF $\Delta\epsilon = 1.4\%$ 150°C test angle of fracture surface

Chapter 14

Conclusion

The present work has been developed in order to understand the a new innovative, never tested, Additive Manufacturing composite material was able to be used for future Liquid Rocket Engine application. In addition, the pre-mixing patented manufacturing process by Sophia High Tech s.r.l. has been employed and tested for the second time (first time was previous work on a composite made by Cu and Inconel718 powders).

The present work involved several public entities: Poltecnico di Torino (Italy), Italian Space Agency (ASI), Université de Tours (France), Slovak University of Technology (Slovakia) and Sophia High tech srl industry (Italy). Thanks to the effort of all different teams the results achieved have been evaluated as scientifically relevant. Therefore three papers are under writing.

The experimental campaign do not only achieve the room temperature mechanical characterization, but also several high temperature static and dynamics tests. Furthermore, because the remarkable importance of the thermal behavior of the material respect to the thrust chamber application, a thermal characterization (within a first-try heat treatment) has been performed. The chemical composition have been analysed and interesting microstructures have been discovered.

This project has required two different printing jobs in order to obtain the correct shape and amount of specimens for the test activity. The starting Cu and 174PH stainless steel have been mixed with the patented new Sophia High tech srl technology, the POWMIX. In particular 54 specimens have been processed and a massive post machining activity has been made: the Standard shape according to ISO/ASTM regulation has been achieved for every mechanical/chemical or thermal test.

Results from all Technological tests shows a good capability to reproduce Liquid Rocket Engine cooling channels with different geometries. No particular problems have been identified. Both straight and curved junction have been successfully printed. All tested angles respect to the z-direction (build direction) were able to be printed without particular supports structures.

The contour parameters, responsible for the surface roughness, function of the analyzed directions, have made an overall results typical of L-PBF products.

The 65% Cu - 35% 174PH custom powder material shows a bi-metal-matrix-composite microstructure. In particular the composite is copper based and therefore it is possible to see that the main matrix is composed by copper. The 17-4PH is presented such a island shape. The XY microstructure shows that the custom mixed powder is homogeneously spread along both, X and Y direction: the powder mixing process is able to achieve a very good powder distribution. The Z-direction microstructure shows a non-key-hole melting pool phenomenon, therefore an more detailed optimization of the energy density should be performed. No relevant gas parasites have been found, evidence of an overall good melting temperature. On the other hand, several lake of fusion have been identified.

The chemical composition analysis, via SEM EDS, highlight a lower weight % of Chromium and Nickel, and a higher weight % of Copper inside the 17-4PH phase. Therefore, after the melting process, more than one elements has migrated from 17-4PH alloy to the pure copper.

Thanks to a more detailed analysis respect to the specimens location on the platform a slight powder distribution problem has been identified. Because of the micro vibration of the powder supplier electromechanical system, and because of the high powder dimension difference between Copper and 174PH, an average 8% chemical composition difference between the starting and the ending platform points have been found.

The overall thermal behavior of the composite have to be improved via a heat treatment. Thermal conductivity does not show a relevant difference between XY and Z direction. After a first-try heat treatment the thermal conductivity is able to double the stating value. Specific heat capacity according whit general metal materials. On the same side, the coefficient of linear thermal dilatation exhibits a slight fluctuation which could be due to the particular matrix of the material, which is bi-metallic, and to the Additive Manufacturing process (porosity, defects, lakes of fusion).

Experimental result from hardness demonstrate the quasi-isotropic behavior of the composite. NO particular Indentation Size Effect have been found. Furthermore, since footprints does not shows diagonal deformations, the compression/tension residual stresses after the AM SLM process are not predominant. The high prove of the indentation test proves that the copper and 174PH powder have been correctly spread respect to the platform. Mico-hardness tests presents similar results. An interesting hardness-tensile properties has been employed in order to evaluate the Z-direction mechanical properties (because of costs and time no Z-direction tensile test have been done).

The tensile properties present a very high tensile and compressive yield strength but a very low elongation to fracture, especially at high temperatures. This is probably due to the different materials indie the composite. An hypothetical dislocation block mechanism has been presented. Ramberg and Osgood proposed one of the most common model in order to model a correct plasticity behavior. The model has been successfully applied to the Cu174PH composite with excellent results.

Low Cycle Fatigue (LCF) test at room and high temperatures have been successfully performed. Results hows a general slight softening behavior, except for the 550°C

tests, where a more hardening effect can be clearly observed. Furthermore, also a cusp behavior has been found, similar to the one presented for the NASA's copper alloys. The material behavior respect to cycling fatigue seems to be governed by the amplitude for room, 150°C and 350°C environments, and from temperature at 550°C: at high temperature the influence of high strain amplitude is less important than the rising of temperature it self. A particular and never-analysed stress breakdown time-activation phenomenon has been identified and named as 'local hill phenomenon'. The cycling curve model has been correctly employed in order to have an analytical model for cycling at different temperature. Finally, Coffin-Manson damage models has been correctly adopted for life prediction analysis. The overall LCF attitude of the under study material can be classified as interesting respect to the new NASA's alloys because of the better life at middle strain amplitude at high temperatures. This results shows that the Cu17PH composite can have an interesting and remarkable role in future Liquid Rocket Engine applications, since the main failure mechanism is the Low Cycle Fatigue one.

Finally, creep tests have been performed at different temperatures and stress levels. Also during the visco-plastic analysis the breakdown limit effect has been identified. The experimental results prove a very low creep-rate of the Cu174PH, as expected because of the complex material matrix. This is an additional positive behavior because of the low capability to strain respe to time.

No particular differences between the Low Cycle Fatigue ans the traction tensile fracture surface can be observed. Both fracture mechanisms seems to be rare mixed ductile-fragile failure. Copper is responsible for the ductile fracture, 174PH for the more fragile one. Porosities and lakes of fusion do not seem to grow during fracture. Eave if a clear 45°C fracture might suggest that the fracture is ductile the immediately separation of Copper from 174PH generates also micro horizontals fragile cracks. The most relevant results is that the higher the temperature the more brittle the fractures are. Therefore the fracture surfaces analyses prove the aforementioned general temperature hardening behavior.

In conclusion, the present study is a firs thermo-mechanical characterization of the new Cu174PH material, developed with Sophia High Tech s.r.l.. A process parameters optimization should be performed ion order to achieve a better density and a specific heat treatment have to be developed to increase the elongation to fracture and the thermal conductivity. Unfortunately, due to Covid-19 emergency, several delays in supplies and machine technical problems (example: the France Low Cycle Fatigue experimental campaign was expected to be performed in 3 weeks, but since the machine does not worked, the overall experience in CEROC laboratory have taken more than 1 month an a half), the numerical implementation of the constitutive models and the subsequent geometrical optimization do not have been performed. This last point can be a starting point for a Ph.D. program.

References

- [1] M.E. Orme. Additive manufacturing of lightweight, optimized, metallic components suitable for space flight. 2017.
- [2] F. Kerstens. End to end process evaluation for additively manufactured liquid rocket engine thrust chambers. 2021.
- [3] Paul R. Gradl. Advanced and additive manufacturing technologies for liquid rocket engine components. 2021.
- [4] S. Soller. Development of liquid rocket engine injectors using additive manufacturing. 2015.
- [5] R. J. Quentmeyer. Rocket combustion chamber life-enhancing design concepts. 1990.
- [6] Marco Pizzarelli. Regenerative cooling of liquid rocket engine thrust chambers. 2019.
- [7] P. Gradl. Additive manufacturing of liquid rocket engine combustion devices: a summary of process developments and hot-fire testing results. 2018.
- [8] B. Blakey-Milner. Metal additive manufacturing in aerospace: A review. 2021.
- [9] Y. Gao. Aerospace additive manufacturing implementation for manned spaceflight production.
- [10] A. Hissam. Additive manufacturing design considerations for liquid engine components. 2014.
- [11] Qi Jiang. A review on additive manufacturing of pure copper. 2021.
- [12] Oskar J. Haidn. Advanced rocket engines.
- [13] Marco Pizzarelli. An algebraic model for structural and life analysis of regeneratively-cooled thrust chambers. 2020.
- [14] A. P. Baiju. A technology for improving regenerative cooling in advanced cryogenic rocket engines for space transportation. 2021.
- [15] R. T. Cook. Some main combustion chamber life prediction - nasa. 1983.
- [16] M. Deguchi. Damage propagation mechanism in low-cycle creep fatigue of cu–cr–zr alloy. 2016.
- [17] P. HANNUM. Experimental and theoretical investigation of fatigue life in reusable rocket thrust chambers. 1976.

- [18] R. T. Cook. Space shuttle orbiter engine main combustion chamber cooling and life. 1973.
- [19] official *Carpenter Additive 17-4* ph data sheet.
- [20] C. Kusuma. The effect of laser power and scan speed on melt pool characteristics of pure titanium and ti-6al-4v alloy for selective laser melting. 2016.
- [21] C. Yan. Advanced lightweight 316l stainless steel cellular lattice structures fabricated via selective laser melting. 2014.
- [22] A. El Hassanin. Selective laser melting of cu-inconel 718 powder mixtures. 2020.
- [23] John J. Esposito. Thrust chamber life prediction volume i. 1975.
- [24] Paul R. Gradl. Grcop-42 development and hot-fire testing using additive manufacturing powder bed fusion for channel-cooled combustion chambers-nasa. 2019.
- [25] Congyuan Zeng. Effect of temperature history on thermal properties of additively manufactured c-18150 alloy samples congyuan zeng. 2020.
- [26] J.B.Conway. High temperature, low-cycle fatigue of copper-base alloys in argon; part i. 1973.
- [27] J.B.Conway. High temperature, low-cycle fatigue of copper-base alloys in argon; part i. 1973.
- [28] C. Hayes. Characterization of selective laser melted grcop-84.
- [29] A. Di Veroli. New space economy: (space 4.0). l'analisi dell'impatto socio-economico delle attività spaziali nella promozione dello sviluppo dell'economia europea. 2021.
- [30] ASTM International. Astm international, astm f2792: Standard terminology for additive manufacturing technologies. 2012.
- [31] N. Tepylo. Laser-based additive manufacturing technologies for aerospace applications, advanced engineering materials. 2019.
- [32] S. Soller. Selective laser melting (slm) of inconel 718 and stainless steel injectors for liquid rocket engines. 2016.
- [33] S. Soller. Design and testing of liquid propellant injectors for additive manufacturing. 2017.
- [34] Haolin Jia. Scanning strategy in selective laser melting (slm), a review. 2021.
- [35] Y. Kok. Anisotropy and heterogeneity of microstructure and mechanical properties in metal additive manufacturing a critical review. 2018.
- [36] F. Sausto. Anisotropic mechanical and fatigue behaviour of inconel718 produced by slm in lcf and high temperature conditions. 2020.
- [37] K. Kassym. Atomization processes of metal powders for 3d printing. 2019.
- [38] P.R. Gradl. Geometric feature reproducibility for laser powder bed fusion (l pbf) additive manufacturing with inconel 718. 2021.

- [39] Pouya Moghimian. Metal powders in additive manufacturing a review on reusability and recyclability of common titanium, nickel and aluminum alloys. 2021.
- [40] Mostafa Yakout. Density and mechanical properties in selective laser melting of invar 36 and stainless steel 316l. 2019.
- [41] C.P. Jones. Additive manufacturing a liquid hydrogen rocket engine. 2016.
- [42] E. Sacco. Additive manufacturing for space: status and promises, international journal of advanced manufacturing technology. 2019.
- [43] A. Terracciano. Additive layer manufacturing technology in avio injector head design. 2017.
- [44] I. Waugh. Additive manufacture of rocket engine combustion chambers using the abd-900am nickel superalloy. 2021.
- [45] C. Katsarelis. Additive manufacturing of nasa hr-1 material for liquid rocket engine component applications.
- [46] E.M. Betts. Using innovative technologies for manufacturing rocket engine hardware. 2011.
- [47] R. Carter. Materials characterization of additively manufactured components for rocket propulsion. 2015.
- [48] D. Liuzzi. Development of an alm thrust chamber for vega-e m10 rocket engine. 2021.
- [49] D. Guichard. Additive manufacturing opportunities in combustion devices for liquid rocket engines. 2018.
- [50] D. K. Huzel and D. H. Huang. Modern engineering for design of liquid-propellant rocket engines. 1992.
- [51] G. P. Sutton. Rocket propulsion elements. 2001.
- [52] Marco Pizzarelli. Modeling of cooling channel flow in liquid-propellant rocket engines. 2007.
- [53] O. E. Lancaster. Jet propulsion engines. 1959.
- [54] S.R. Shine. Review on film cooling of liquid rocket engines. 2015.
- [55] A. Woschnak. Thermo and fluidmechanical analysis of high aspect ratio cooling channels. 2001.
- [56] J. Quentmeyer. An experimental investigation of highaspect-ratio cooling passages. 1992.
- [57] X. Zhang. An additively manufactured metallic manifold-microchannel heat exchanger for high temperature applications. 2018.
- [58] Tristan Briard. G-dfam a methodological proposal of generative design for additive manufacturing in the automotive industry. 2020.
- [59] A. Niknam. Additively manufactured heat exchangers, a review on opportunities and challenges. 2020.

- [60] R. AVENALL. Use of metallic foams for heat transfer enhancement in the cooling jacket of a rocket propulsion element. 2004.
- [61] AVIO s.p.a. United states patent application publication (10) pub. no.: Us 2017/0122258 a1. 2017.
- [62] C. E. Dexter. Scaling techniques for design, development, and test, liquid rocket thrust chambers: Aspects of modeling, analysis, and design. 2004.
- [63] M. Shiwa. Evaluation of deterioration damage for liquid oxygen/hydrogen combustion chamber of copper alloy by replica method for oxide film. 2019.
- [64] J. M. Kazaroff. Hot fire test results of subscale tubular combustion chambers. 1992.
- [65] A. J. Pavli. Hot fire fatigue testing results for the compliant combustion chamber. 1992.
- [66] F. Hotte. Experimental lifetime study of regeneratively cooled rocket chamber walls. 2020.
- [67] R.J. Quentmeyer. Experimental fatigue life investigation of cylindrical thrust chambers.
- [68] D. Liu. Thermo-structural analysis of regenerative cooling thrust chamber cylinder segment based on experimental data. 2019.
- [69] E. Anderson. Rocket combustor experiments and analyses.
- [70] W. Miller. Low-cycle-fatigue analysis of a cooled copper combustion chamber. 1974.
- [71] R. G. Thiede. Life prediction of rocket combustion-chamber-type thermomechanical fatigue panels. 2017.
- [72] J. S. Parowski. Development of a simplified procedure for thrust chamber life prediction.
- [73] Xiaowen D. Life prediction of the thrust chamber wall of a reusable rocket engine.
- [74] V. Arya. Viscoplastic analysis of an experimental cylindrical thrust chamber liner. 1992.
- [75] D. Kuhl. Thermomechanical analysis and optimization of cryogenic liquid rocket engines. 2002.
- [76] W. Schwarz. Life prediction of thermally highly loaded components: modelling the damage process of a rocket combustion chamber hot wall. 2011.
- [77] J. Song. Thermal-structural analysis of regeneratively-cooled thrust chamber wall in reusable lox/methane rocket engines. 2017.
- [78] *Legor Powmet* pure copper data sheet.
- [79] A. Bandyopadhyay. Additive manufacturing of multimaterial structures. 2018.
- [80] D. Borrelli. On the effect of the layer thickness in laser-powder bed fusion of pre-mixed inconel718-cu powders. 2021.

- [81] D. Borrelli. Laser-powder bed fusion of pre-mixed inconel718-cu powders: An experimental study. 2021.
- [82] B. Onuike. Additive manufacturing of inconel 718—copper alloy bimetallic structure using laser engineered net shaping (lens. 2018.
- [83] Y. Lu. Study on the microstructure, mechanical property and residual stress of slm inconel718 alloy manufactured by differing island scanning strategy. 2015.
- [84] A. Salmi. An integrated design methodology for components produced by laser powder bed fusion (l-pbf) process. 2018.
- [85] N. J. Harrison. Reduction of micro-cracking in nickel superalloys processed by selective laser melting: A fundamental alloy design approach. 2015.
- [86]
- [87] J. Jiang. Path planning strategies to optimize accuracy, quality, build time and material use in additive manufacturing a review.
- [88] J. Jiang. Support structures for additive manufacturing: A review. 2018.
- [89] A. Plessis. Effects of defects on mechanical properties in metal additive manufacturing: a review focusing on x-ray tomography insights. 2019.
- [90] Shigley-McGraw-Hill. Mechanical engineering design. 2004.
- [91] McGraw-Hill. Materials science and technology. 2016.
- [92] J. Slotwinski. Applicability of existing materials testing standards for additive manufacturing materials.
- [93] S. Keist. Development of strength-hardness relationships in additively manufactured titanium alloys.
- [94] A. Bertocco. Influence of slm parameters on the compressive behaviour of lattice structures in 17-4ph stainless steel. 2020.
- [95] N. Sanaei. Analysis of the effect of surface roughness on fatigue performance of powder bed fusion additive manufactured metals. 2020.
- [96] Y. Tang. Direct laser sintering of a copper-based alloy for creating three-dimensional metal parts. 2003.
- [97] Di Wang. Theoretical and experimental study on surface roughness of 316l stainless steel metal parts obtained through selective laser melting. 2016.
- [98] C. Tan. Additive manufacturing of steel–copper functionally graded material with ultrahigh bonding strength. 2020.
- [99] S. Osipovich. Gradient transition zone structure in “steel–copper” sample produced by double wire-feed electron beam additive manufacturing. 2020.
- [100] Xiaosi Sun. Solidification microstructure evolution of undercooled cu-15 wt.% fe alloy melt. 2018.
- [101] L. Jy. Mechanism of keyhole formation and stability in stationary laser welding. 2002.
- [102] S.Katayama. Fundamentals of laser welding - introduction. 2012.

- [103] A. Paul. Free surface flow and heat transfer in conduction mode laser welding. 1988.
- [104] King WE. Observation of keyhole-mode laser melting in laser powder-bed fusion additive manufacturing. 2014.
- [105] S. Coeck. Prediction of lack of fusion porosity in selective laser melting based on melt pool monitoring data. 2019.
- [106] S. Jadhav. Surface modified copper alloy powder for reliable laser-based additive manufacturing. 2020.
- [107] Hao Wang. Nanoindentation based properties of inconel™ 718 at elevated temperatures: A comparison of conventional versus additively manufactured samples.
- [108] K. Kampouris. On the interpretation of the indentation size effect (ise) through gradient theory for vickers and berkovich indenters.
- [109] V.S. Kathavate. Analysis of indentation size effect (ise) in nanoindentation hardness in polycrystalline pmn-pt piezoceramics with different domain configurations.
- [110] E.J. Pavlina. Correlation of yield strength and tensile strength with hardness for steels. 2008.
- [111] M. Tiryakioglu. Hardness–strength relationships in the aluminum alloy 7010. 2015.
- [112] S. Chenna Krishna. On the prediction of strength from hardness for copper alloys. 2013.
- [113] Matweb material online properties database.
- [114] E. Sert. Tensile strength performance with determination of the poisson's ratio of additively manufactured als10mg samples. 2019.
- [115] L. Wenlong. Additive manufacturing of isotropic-grained, highstrength and high-ductility copper alloys. 2020.
- [116] Congyuan Zeng. Tensile properties of additively manufactured c-18150 copper alloys. 2021.
- [117] A.H. Seltzman. Fracture characteristics and heat treatment of laser powder bed fusion additively manufactured grcop-84 copper. 2021.
- [118] P. Tarafder. Quasi-static tensile properties of unalloyed copper produced by electron beam powder bed fusion additive manufacturing. 2021.
- [119] P. Ponnusamy. Mechanical performance of selective laser melted 17-4 ph stainless steel under compressive loading.
- [120] O. Fashanu. Effect of slm build parameters on the compressive properties of 304l stainless steel. 2019.
- [121] H. Mughrab. Cyclic plasticity and fatigue of metals. 1993.
- [122] S. S. Manson. Thermal stress and low cycle fatigue. 1996.
- [123] B. Wilshire. Introduction to creep. 1993.

- [124] C. Panwisawas. Keyhole formation and thermal fluid flow-induced porosity during laser fusion welding in titanium alloys: experimental and modelling. 2017.
- [125] T.Log and S.E.Gustafsson. Fire and materials, vol. 19, 43 - 49. 1995.
- [126] F. Calignano. Overview on additive manufacturing technologies. 2017.
- [127] E. Hosseini. A review of mechanical properties of additively manufactured inconel718. 2017.
- [128] Shigley – 2004 McGraw-Hill. Mechanical engineering design.
- [129] Materials science and technology – 2016 - mcgraw-hill.
- [130] J. Datsko. On the tensile strength and hardness relation for metals.
- [131] E. Meyer. Untersuchungen über härteprüfung und härte brinell methoden. 1903.
- [132] Mechanical metallurgy - dieter george ellwood.
- [133] Rockwell test - bs en iso 6508.
- [134] Brinell test - bs en iso 6506.
- [135] C. Zopp. Processing of a metastable titanium alloy (ti-5553) by selective laser melting. 2017.
- [136] F. C. Pinto. Defects in parts manufactured by selective laser melting caused by delta-ferrite in reused 316l steel powder feedstock. 2020.
- [137] L. Dai. Characterizing the intrinsic properties of powder – a combined discrete element analysis and hall flowmeter testing study. 2021.
- [138] W. Zhai. Characterization of nanoparticle mixed 316l powder for additive manufacturing. 2020.
- [139] J. P. Kruth. Selective laser melting of iron-based powder. 2004.
- [140] C. Hauser. Direct selective laser sintering of tool steel powders to high density. part a: Effects of lasr beam width and scan strategy. 2003.
- [141] Tonelli. Cocr alloy processed by selective laser melting (slm): effect of laser energy density on microstructure, surface morphology, and hardness. 2020.
- [142] DebRoy. Debroy, t., wei, h. l. l., zuback, j. s. s., mukherjee, t., elmer, j. w. w., milewski, j. o. o., beese, a. m. m. (2018). 286 a. wilson-heid, a. de, w. zhang. prog. mater. sci, 92, 112-224. 2018.
- [143] Herzog. Additive manufacturing of metals. 2016.
- [144] Ams 2773 e.
- [145] A. Strondl. Microstructure and mechanical properties of nickel based superalloy in718 produced by rapid prototyping with electron beam melting (ebm).
- [146] Y. Tian. Rationalization of microstructure heterogeneity in inconel 718 builds made by the direct laser additive manufacturing process.
- [147] E. L. Stevens. Variation of hardness, microstructure, and laves phase distribution in direct laser deposited alloy 718 cuboids.

- [148] E. Hosseinia. A review of mechanical properties of additively manufactured inconel 718.
- [149] S. Anfossi. Fabbricazione additiva laser a letto di polvere di inconel™ 718 analisi di rugosità, porosità residua e microdurezza.
- [150] Formability microstructure and properties of inconel.
- [151] D. Deng. Microstructure and mechanical properties of inconel™ 718 produced by selective laser melting sample orientation dependence and effects of post heat treatments.
- [152] K.N. Amato. Microstructures and mechanical behavior of inconel™ 718 fabricated by selective laser melting.
- [153] S. Gribbin. Low cycle fatigue behavior of direct metal laser sintered inconel alloy 718.
- [154] W. E. Luecke. Mechanical properties of austenitic stainless steel made by additive manufacturing.
- [155] R. Konecna. Long fatigue crack growth in inconel 718 produced by selective laser melting.
- [156] D. Denga. Microstructure and mechanical properties of inconel 718 produced by selective laser melting: Sample orientation dependence and effects of post heat treatments.

Appendix A

LCF specimen buckling instability analysis

The minimum available section for the LCF specimens have been evaluated in order to perform the LCF test also in compression mode. The Euler's low have been successfully applied. The maximum calculated compression stress available for the LCF specimens is 962 MPa. Since the material maximum compression yield strength at room temperature is above 962 MPa (it is about 700 MPa), no problems for buckling instability have been found.

The LCF test is a constrained-constrained rod problem: the Euler constant is therefore $K=0.5$.

$$\sigma_{cr} = \frac{F_{cr}}{A} = 962 MPa \quad (A.1)$$

$$F_{cr} = \frac{\pi^2 EI}{kL_0} \quad (A.2)$$

$$I = \frac{\pi}{64} D_0^4 \quad (A.3)$$

Appendix B

Roughness test

A detailed overview of all roughness test result is presented in Figure B.1 and Figure B.2.

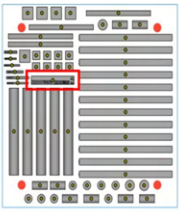
	Plane XY x or y direction test	Operator	Test	Machine	Number	Year	Month	Day	Method	Ra	Rq	rt	Rc	Rp	Rv	Rsk	Rsm
		Matteo Craci	Roughness	@ Rugosimetro RTP 80	1	2021	novembre	17	UNI EN ISO 4287	12.203	14.963	86.987	58.059	25.876	32.183	-0.198	143.34
		Matteo Craci	Roughness	@ Rugosimetro RTP 80	2	2021	novembre	17	UNI EN ISO 4287	9.397	12.369	77.721	53.225	23.25	37.813	-0.168	163.90
		Matteo Craci	Roughness	@ Rugosimetro RTP 80	3	2021	novembre	17	UNI EN ISO 4287	9.465	11.512	62.821	44.554	25.087	19.467	-0.028	151.96
		Matteo Craci	Roughness	@ Rugosimetro RTP 80	4	2021	novembre	17	UNI EN ISO 4287	11.934	14.967	68.139	50.428	26.862	23.566	-0.091	114.92
		Matteo Craci	Roughness	@ Rugosimetro RTP 80	5	2021	novembre	17	UNI EN ISO 4287	11.488	16.148	88.004	54.965	22.345	32.82	-0.105	160.90
		Matteo Craci	Roughness	@ Rugosimetro RTP 80	6	2021	novembre	17	UNI EN ISO 4287	14.005	16.235	77.302	57.438	26.935	30.503	-0.022	130.90
		Matteo Craci	Roughness	@ Rugosimetro RTP 80	7	2021	novembre	17	UNI EN ISO 4287	12.905	15.895	76.057	64.655	29.95	34.705	-0.141	140.90
	Plane ZX (or ZY) x or y direction test	Operator	Test	Machine	Number	Year	Month	Day	Method	Ra	Rq	rt	Rc	Rp	Rv	Rsk	Rsm
		Matteo Craci	Roughness	@ Rugosimetro RTP 80	1	2021	novembre	17	UNI EN ISO 4287	14.037	17.066	88.02	66.302	34.473	31.829	0.084	121.90
		Matteo Craci	Roughness	@ Rugosimetro RTP 80	2	2021	novembre	17	UNI EN ISO 4287	11.389	13.79	73.821	61.008	32.836	28.172	0.113	104.90
		Matteo Craci	Roughness	@ Rugosimetro RTP 80	3	2021	novembre	17	UNI EN ISO 4287	11.008	13.306	70.763	51.058	26.876	26.332	0.161	106.90
		Matteo Craci	Roughness	@ Rugosimetro RTP 80	4	2021	novembre	17	UNI EN ISO 4287	13.039	15.496	90.465	63.252	33.283	29.669	0.11	131.90
		Matteo Craci	Roughness	@ Rugosimetro RTP 80	5	2021	novembre	17	UNI EN ISO 4287	9.34	12.023	66.311	53.003	29.963	23.035	0.145	113.90
		Matteo Craci	Roughness	@ Rugosimetro RTP 80	6	2021	novembre	17	UNI EN ISO 4287	13.903	16.86	91.832	68.499	36.852	31.607	0.027	123.90
		Matteo Craci	Roughness	@ Rugosimetro RTP 80	7	2021	novembre	17	UNI EN ISO 4287	10.456	12.71	76.637	53.003	26.452	26.551	-0.186	148.90
	Plane ZX (or ZY) z direction test	Operator	Test	Machine	Number	Year	Month	Day	Method	Ra	Rq	rt	Rc	Rp	Rv	Rsk	Rsm
		Matteo Craci	Roughness	@ Rugosimetro RTP 80	1	2021	novembre	17	UNI EN ISO 4287	14.933	18.279	94.695	74.291	38.601	35.69	0.195	103.90
		Matteo Craci	Roughness	@ Rugosimetro RTP 80	2	2021	novembre	17	UNI EN ISO 4287	14.719	17.365	88.243	68.561	34.393	34.168	-0.027	142.90
		Matteo Craci	Roughness	@ Rugosimetro RTP 80	3	2021	novembre	17	UNI EN ISO 4287	10.542	13.464	77.158	54.397	30.966	23.431	-0.063	130.90
		Matteo Craci	Roughness	@ Rugosimetro RTP 80	4	2021	novembre	17	UNI EN ISO 4287	12.294	14.951	74.54	63.145	36.176	34.21	0.167	103.90
		Matteo Craci	Roughness	@ Rugosimetro RTP 80	5	2021	novembre	17	UNI EN ISO 4287	12.614	15.369	81.677	62.471	32.748	29.723	0.156	127.90
		Matteo Craci	Roughness	@ Rugosimetro RTP 80	6	2021	novembre	17	UNI EN ISO 4287	13.372	16.366	87.412	65.985	35.335	30.65	0.21	118.90
		Matteo Craci	Roughness	@ Rugosimetro RTP 80	7	2021	novembre	17	UNI EN ISO 4287	13.576	16.539	81.887	65.399	31.171	34.228	0.211	110.90

Fig. B.1 Roughness tests results - part A

Ra (MEDIA)	Ra (DEV ST)	Rq (MEDIA)	Rq (DEV ST)	Rt (MEDIA)	Rt (DEV ST)	Rz (MEDIA)	Rz (DEV ST)	Rv (MEDIA)	Rv (DEV ST)	Rp (MEDIA)	Rp (DEV ST)	Rsk (MEDIA)	Rsk (DEV ST)	Rsm (MEDIA)	Rsm (DEV ST)
11.628	1.702	14.141	1.777	76.719	9.141	54.761	6.342	25.758	2.536	30.122	6.420	-0.107	0.067	390.857	50.188
Ra (MEDIA)	Ra (DEV ST)	Rq (MEDIA)	Rq (DEV ST)	Rt (MEDIA)	Rt (DEV ST)	Rz (MEDIA)	Rz (DEV ST)	Rv (MEDIA)	Rv (DEV ST)	Rp (MEDIA)	Rp (DEV ST)	Rsk (MEDIA)	Rsk (DEV ST)	Rsm (MEDIA)	Rsm (DEV ST)
11.850	1.819	14.757	2.017	79.591	10.204	59.726	6.689	31.526	3.919	28.199	3.193	0.065	0.118	177.571	49.027
Ra (MEDIA)	Ra (DEV ST)	Rq (MEDIA)	Rq (DEV ST)	Rt (MEDIA)	Rt (DEV ST)	Rz (MEDIA)	Rz (DEV ST)	Rv (MEDIA)	Rv (DEV ST)	Rp (MEDIA)	Rp (DEV ST)	Rsk (MEDIA)	Rsk (DEV ST)	Rsm (MEDIA)	Rsm (DEV ST)
13.150	1.511	16.045	1.604	83.659	6.945	64.893	6.087	34.199	2.779	31.729	4.244	0.121	0.116	201.000	30.578

Fig. B.2 Roughness tests results - part b

Appendix C

Molten pool dynamics: AM SLM Conduction and Keyhole mode

In conduction mode, the beam sends energy to the substrate's top surface, then conduction from the surface provides heat to build a molten pool in the material, generating a superficial and regular-shaped molten pool [104]. On the other side a deep and narrow vaporized metal channel is created in keyhole mode. Following that, the laser's energy is absorbed by the keyhole's wall and transferred to the metal[124].

A scheme of the molten pool dynamics for both the welding mechanisms is reported in Figure C.1.

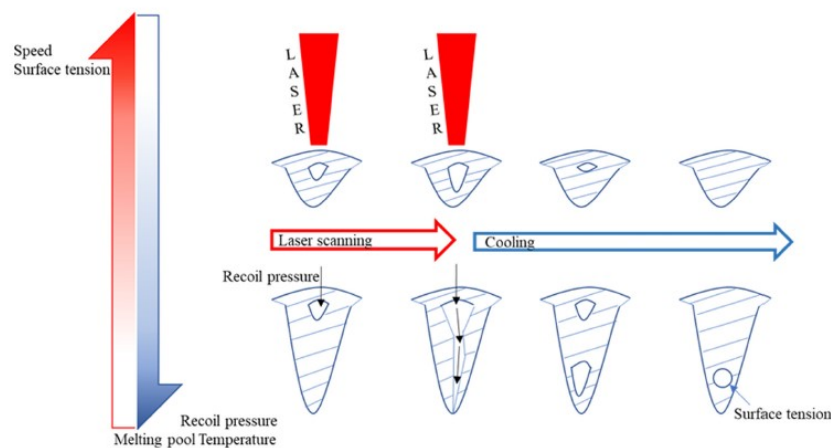


Fig. C.1 Different molten pool dynamics, from [22]

Conduction welding occurs when the laser power density is low, allowing the metal to be heated with little or no evaporation. The upper surface of the metal absorbs the majority of the laser energy in this case. Increasing the laser density up to critical values that mainly depend on the processed material, the metal directly exposed to the center of the laser beam can be vaporized, leading to the formation of a keyhole that will penetrate deeply through the molten pool [124]. During L-PBF, gravity also plays a key role in this mechanism. Due to the gaps between the unmelted powders, the melted powders will flow down to fill the gap, and the molten pool's upper surface will be lower than the

top surface of the loose powders. Following that, under the influence of gravity, the new molten particles will flow towards the initial molten zone. In general, The keyhole mode can process a thicker powder layer than the conduction mode.

When the real powder layer thickness is greater than the printed one, the powders at the bottom of the consolidated layer cannot be entirely melted, causing entrained porosities. Due to the extra energy input, if the actual powder layer thickness is less than the printable one, part of the substrate or the previously printed layer is re-melted. In the conduction mode, the temperature distribution during multiple-track printing is more uniform than in the keyhole mode, resulting in a more uniform microstructure. This shows that adjusting laser parameters like as power, scanning speed, and hatch spacing can aid in adjusting the temperature distribution in the molten pool and, as a result, the production of a homogeneous and defect-free microstructure in AM products.

The vapour cavity is surrounded by molten material when the keyhole is formed, and it is maintained through an equilibrium between opening forces arising from material ablation and plasma formation, i.e. recoil pressure, and closing forces arising from the surface tension and hydrostatic pressure of the molten pool. New material is gradually melted at the leading edge of the molten pool as the beam scans the loose particles layer, and it flows around the deep penetration cavity to the pool's rear, where it solidifies. The scan speed must be carefully managed to preserve this equilibrium; otherwise, high speed causes the keyhole to collapse, while excessive low speed causes the weld bead to droop.

Appendix D

Transient Plane Source technique (ISO 22007-2)

Based on the theory of the Transient Plane Source technique (recognized in ISO 22007-2), the Hot Disk Thermal Constants Analyser utilises a sensor element in the shape of a double spiral. This Hot Disk sensor acts both as a heat source for increasing the temperature of the sample and as a "resistance thermometer" for recording the time-dependent temperature increase. In most cases the sensor element is made of a $10\ \mu\text{m}$ thick Nickel-metal double spiral, with precisely designed dimensions (regarding width, number of windings and their radii). This spiral is supported by a material to protect its particular shape, to give it mechanical strength and keep it electrically insulated. The polyimide "Kapton" is such a material, which can be used throughout the temperature range from 10 K to 500 K.

The encapsulated Ni-spiral sensor is then sandwiched between two halves of the sample (solids), or embedded in the sample (powders, liquids). During a pre-set time, 200 resistance recordings are taken, and from these the relation between temperature and time is established. A few parameters, like the Heating power to increase the temperature of the spiral, the Measurement time for recording 200 point and the size of the sensor are used to optimise the settings for the experiment, so that thermal conductivities from 0.005 W/mK to 1800W/mK can be measured.

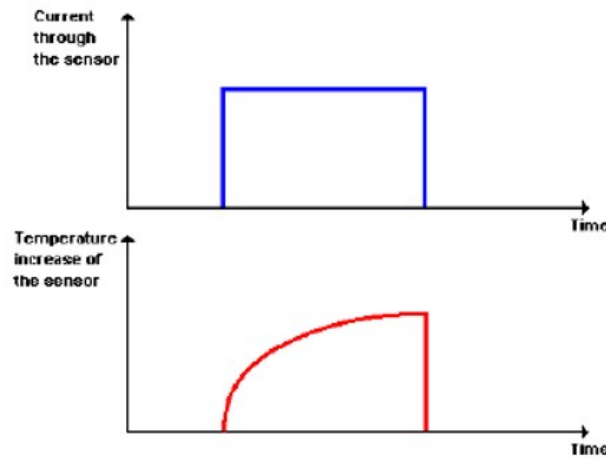


Fig. D.1 Transient recording of the thermal transport properties of the material surrounding the sensor.

Measurements on standard materials ranging from Polystyrene to Aluminium metal show that the accuracy over the whole range of Thermal Conductivities is within $\pm 5\%$ and the reproducibility is within $\pm 2\%$ [125]. There are many types of instruments available today, based on different principles (listed below). To mention a few, the Guarded Hot Plate, a steady state method, is very often used for highly insulating materials. It is an ASTM-standard and gives quite accurate values. However, it takes a long time to prepare and in most cases requires large samples. Another principle is evinced in the Laser Flash methods, where a disc-shaped sample is irradiated on one side for a short period with a laser pulse, creating a temperature increase in the sample. The variable temperature is then measured on the other side by either a thermocouple that is soldered to the sample surface, or recorded by an IR-sensor placed at a certain distance from the sample. In both cases a temperature versus time relation is obtained, and the thermal diffusivity is calculated. In order also to obtain the thermal conductivity, however, it is necessary that one know the heat capacity of the sample from separate measurements with other experimental techniques. For this method, although fast enough during the measurement proper (a flash and response comes within seconds), the painstaking sample preparation required (precise dimensions, soldering, black surfaces etc.) makes the total time, effort and cost involved rather considerable. While generally working well at high temperatures in different atmospheres, it can only be applied to rather dense materials.

To theoretically describe how the Hot Disk behaves, the thermal conductivity equation has been solved assuming that the Hot Disk consists of a certain number of concentric ring heat sources located in an infinitely large sample. If the Hot Disk is electrically heated, the resistance increase as a function of time can be given as:

$$R(t) = R_0 (1 + \alpha [\Delta T_i + \Delta T_{ave}(\tau)]) \quad (D.1)$$

R_0 is the resistance of the disk just before it is heated or at time $t = 0$, α is the Temperature Coefficient of the Resistivity (TCR), ΔT_i is the constant temperature difference

that develops almost momentarily over the thin insulating layers which are covering the two sides of the Hot Disk sensor material (Nickel) and which make the Hot Disk a convenient sensor. $\Delta T_{ave}(\tau)$ is the temperature increase of the sample surface on the other side of the insulating layer and facing the Hot Disk sensor (double spiral).

From Equation D.1 we get the temperature increase recorded by the sensor:

$$\Delta T_{ave}(\tau) + \Delta T_i = \frac{1}{\alpha} \left(\frac{R_t}{R_0} - 1 \right) \quad (D.2)$$

Here ΔT_i is a measure of the "thermal contact" between the sensor and the sample surface with $\Delta T_i = 0$ representing perfect "thermal contact" closely realised by a deposited (PVD or CVD) thin film or an electrically insulating sample.

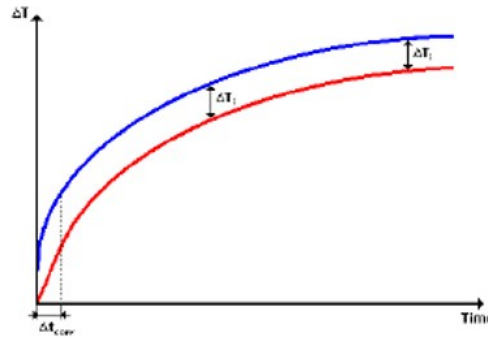


Fig. D.2 Sensor and sample temperature increase curves

In Figure D.2 the blue curve indicates the temperature increase of the sensor itself and the red one shows how the temperature of the sample surface is increasing.

ΔT_i becomes constant after a very short time ΔT_i which can be estimated as:

$$\Delta T_i = \frac{\delta^2}{k_i} \quad (D.3)$$

where δ is the thickness of the insulating layer and k_i is the thermal diffusivity of the layer material. The time-dependent temperature increase is given by the theory as:

$$\Delta T_{ave}(\tau) = \frac{P_0}{\pi^{\frac{3}{2}} a \Lambda} D(\tau) \quad (D.4)$$

where P_0 is the total output of power from the sensor, a is the overall radius of the disk, Λ is the thermal conductivity of the sample that is being tested and $D(\tau)$ is a dimensionless time dependent function with:

$$\tau = \sqrt{\frac{t}{\Theta}} \quad (D.5)$$

In this equation t is the time measured from the start of the transient recording, and Θ is the characteristic time defined as:

$$\Theta = \frac{a^2}{k} \quad (\text{D.6})$$

where k is the thermal diffusivity of the sample.

Now by making a computational plot of the recorded temperature increase versus $D(\tau)$, we obtain a straight line, the intercept of which is ΔT_i and the slope is $\frac{P_0}{\pi^{\frac{3}{2}} a \Lambda}$ using experimental times significantly longer than Δt_i .

Since k and hence Θ are not known before the experiment, the final straight line from which the thermal conductivity is calculated is obtained through a process of iteration. Thus it is possible to determine both the thermal conductivity and the thermal diffusivity from one single transient recording.

Appendix E

Energy Density DoE of Additive Manufacturing Inocnel 718 for Space Rocket application

E.1 Introduction

For SLM process there is a high number of parameters directly linked to the quality of the finished part. It is an important and difficult challenge to understand the physics of this process and to develop a control strategy with more than 50 process parameters [126]. The most common parameters used to optimize the process in SLM are the hatching distance, the scanning speed, and the laser power. All these parameters influence the volumetric energy density that affect the mechanical properties and the surface roughness of the components[126]. Moreover, if the process parameters generate an insufficient energy, some typical defects are produced on the part. For example a low hatch distance results in porosities in the part, and a low laser power associated with a high scanning speed and large layer thickness usually causes the so-called balling phenomenon[126].

Parameters like energy density and scanning strategy, influence the temperature profile during the building process and consequently the resulting hardness. The rapid heating and cooling during the SLM process increase the hardness of AM Inconel™ 718 more than conventional processes [127]. Aim of the research it the investigation on influence of deposition parameters on mechanical hardness structural property of Inconel 718.

E.2 Background - VICKERS test

Known as an extrinsic material property, hardness can be defined as the resistance presented by a material respect to plastic deformation due to the penetration of an indenter tool [128], [129]. Hardness test is non-destructive (or semi-destructive) and hardness measure results to be linearly proportional with mechanical properties of

materials as Young module, tensile strength and yield strength [128], [110]. A good understanding of the relationship between measured hardness values and the mechanical properties would allow for hardness to be used as a predictive tool for mechanical properties and help streamline the qualification and inspection protocols for structural components. The advantage of this method is its applicability to a wide range of materials: metals, ceramics, composite, plastics [130]. Meyer [131] gives an alternative definition of hardness based on the projected area of the impression rather than the surface area. The mean pressure p_m between the surface of the indenter is defined equal to the applied load L divided by the projected area of the indentation A_i . Meyer proposed that this mean pressure should be taken as the measure of hardness. It is referred to as the Meyer hardness. An advantage of the Meyer test is that it is less sensitive, respect to theories that use the effective real area, to the applied load [132].

$$p_m = \frac{L}{A_i} \quad (E.1)$$

Meyer also proposed an empirical relation between the load and the size of the indentation. This relationship is called Meyer's law [131]. Meyer's law range of validity is related to material properties.

$$P = kd^{n'} \quad (E.2)$$

Where:

- P is the applied load [Kg];
- d is the diameter of indentation [mm];
- n' is a material constant related to strain hardening of metal;
- k is a material constant expressing the resistance of metal to penetration;

Vickers test is a perfect application of the Mayer's law. Vickers hardness is related to the measure of the diagonal of the square plastic indentation obtained by a diamond pyramid indenter pressed against the investigated surface with a given load L , after elastic recovery (ISO 6507).

Rockwell [133] and Brinell [134] hardness test, characterised by a conical and a spheroidal indenter respectively, usually require modifying either the load or the indenter at some point in the hardness scale. Because of this a measurement of a high number of specimens with different load cannot be compared. On the other hand, the impressions made by the pyramid indenter are geometrically similar and independent of load making Vickers test, for this study, more suited.

The Standard ISO 6507, applied to perform hardness, was designed for standard fabrication processes. Currently no Standards describe procedures dedicated to Additive Manufactured surface hardness measurements. In [92] a procedure to measure the

material properties of additive manufacturing materials is proposed. For reliable hardness measures, the surface finish state is critical. A flat surface is indicated and for accurate penetration the surface roughness must be minimized according to BS EN ISO 6507. The applicability of ISO 6507 for testing AM materials is linked to the requirements 'to meet surface finish specification'.

Surfaces obtained by means of Additive Manufacturing present a rough surface, and surface roughness changes according to the investigated (side or front with respect to growth direction) surface. In addition to this, the contour layer is not representative of material mechanical properties because of different process parameters. This remarkable difference could cause a high porosity that makes indentation test difficult and measure unreliable. Polishing surfaces allows avoiding this influence from the hardness measurement.

Keist and Palmer [93] demonstrated that Vickers test hardness procedure can be applied for Additive Manufacturing SLM processed materials as Ti-6Al-4V alloys, but it results in a large result scattering due to different phase orientation because of the AM manufacturing process.

E.3 Materials and methods

A Design of Experiment method was planned to evaluate hardness and micro hardness properties of Inconel718 processed by SLM. The particular arrangement of all specimens has been used for evaluating the mechanical properties distribution on the printing platform and the material response to seven different energy densities.

Twenty-eight specimens for hardness testing, made of Inconel718 alloy, were printed by means of a SLM Concept Laser M2 Series printer, with a build volume of 250x250x280 mm (x, y, z), in Inconel718 powder by Carpenter Additive. The chemical composition of the powder is presented in Table 1. Table 2 shows sieve analysis, laser size diffraction, hall flow and apparent density of the powder. The sieve analysis was characterized according to ASTM Standard B214 [135]. Laser scattering particle size analysis is performed to ASTM Standard B822 [136]. The powder hall flow analysis outputs the flow rate (FR), that has been certified as the standard output for hall flowmeter testing techniques, as explained in ASTM Standard B213 [137]. The apparent density is measured according to ASTM Standard B212 [138].

CHEMICAL ANALYSIS

		Units	Min	Max	Result	Approved
C	Carbon	weight %	0	0.08	0.03	Pass
Fe	Iron	weight %	Balance	-	Balance	Pass
N	Nitrogen	weight %	0	0.03	0.01	Pass
O	Oxygen	weight %	0	0.03	0.02	Pass
Cu	Copper	weight %	0	0.3	<0.1	Pass
B	Boron	weight %	0	0.006	<0.001	Pass
Co	Cobalt	weight %	0	1.0	0.1	Pass
Al	Aluminium	weight %	0.20	0.8	0.53	Pass
Ti	Titanium	weight %	0.65	1.15	1.01	Pass
Nb + Ta	Niobium + Tantalum	weight %	4.75	5.50	4.92	Pass
Mo	Molybdenum	weight %	2.80	3.30	3.10	Pass
Ni	Nickel	weight %	50.00	55.00	52.30	Pass
Cr	Chromium	weight %	17.0	21.0	18.9	Pass
S	Sulphur	weight %	0	0.015	0.001	Pass
P	Phosphorus	weight %	0	0.015	0.004	Pass
Si	Silicon	weight %	0	0.35	0.04	Pass
Mn	Manganese	weight %	0	0.35	0.02	Pass

Fig. E.1 Powder Chemical composition

SIEVE ANALYSIS - ASTM B214

	Units	Min	Max	Result	Approved
+63 μm	weight %	0	0	0	Pass
+53 μm	weight %	0	1	0	Pass
+45 μm	weight %	Info Only	-	5.18	Pass

LASER SIZE DIFFRACTION - ASTM B822

	Units	Min	Max	Result	Approved
Dv (10)	μm	Info Only	-	21.7	Pass
Dv (90)	μm	Info Only	-	57.8	Pass
Dv (50)	μm	Info Only	-	35.9	Pass
-5 μm	volume %	0	0	0	Pass
-15 μm	volume %	0	10	1	Pass

HALL FLOW - ASTM B213

	Units	Min	Max	Result	Approved
FR _H	s/50g	Flow	-	14	Pass

APPARENT DENSITY - ASTM B212

	Units	Min	Max	Result	Approved
Bulk Density	g/cm ³	Info Only	-	4.12	Pass

Fig. E.2 Powder properties

The specimens have a cubic shape, with 20 mm edge. Each cube is rotated by an angle of 15 deg on the building platform respect to recoating blade in order to avoid that the force of the blade could cause the part detachment from the building platform [84]. The printing platform is divided in 4 quadrants with 7 specimens in each. Given a polar reference angle θ centered in the center of the platform, this disposition makes possible to evaluate the influence of the polar angle, on the mechanical properties of the specimens, Figure E.3. Each specimen is named with a letter and a number. Letters A, B, C, D indicate 4 different quadrants of the building platform. The numbers from 1 to 7 refer to the different AM process parameters used, and the ones named with the same number are positioned at the same distance from the center of the platform.

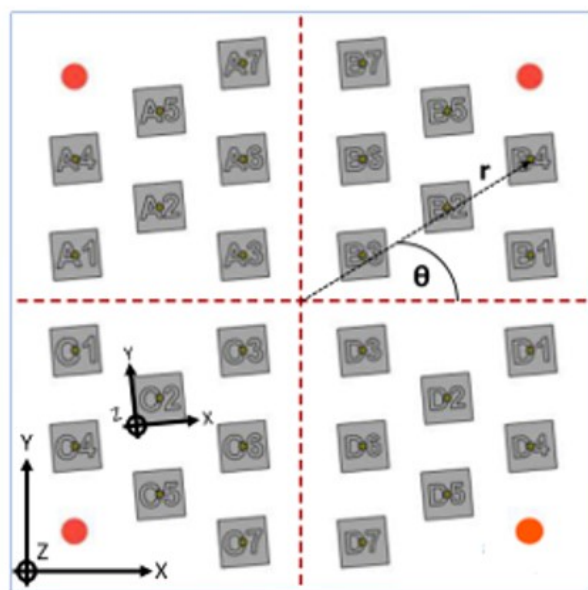


Fig. E.3 Building platform and coordinate system

In specimen manufacturing, the main process parameters used for the body and contour of the part are listed in Figure E.4.

Body	Layer thickness [mm]	0,03
	Spot Size [mm]	0,15
	Trace Width [mm]	0,105
	Overlap Factor [mm]	0,7
	Power [W]	192
Contour	Spot size [mm]	0,15
	Beam compensation [mm]	0,075
	Contour Speed [mm/s]	1600
	Hatch Zone Border [mm]	0,065

Fig. E.4 Main body and contour process parameters

In the investigated case study, the modified process parameters are the laser power and the scanning speed. The processing parameters values included in the DOE range around the values indicated by the printer supplier for Inconel 718 (192 W laser power and 600 mm/s scanning speed). The DoE parameters (laser power, scanning speed and energy density) of every specimen are indicated in Figure E.5. A pure nitrogen inert gas has been used for the painting chamber requirements and a silicon cluster is used for the powder bad deposition.

Specimen number	Laser Power [W]	Scanning speed [mm/s]	Energy density [J/mm ³]
1	192	400	152,38
2		600	101,59
3		800	76,19
4	230	500	146,03
5		600	121,69
6		700	104,31
7		900	81,13

Fig. E.5 DoE process parameters

The scanning strategies used to melt each layer affects the properties of the specimen, because of the different thermal gradients generated. The main scanning strategies includes zig-zagging tracks, arrays of parallel stripes, spirals, contours from the external edges to the center of the part [139], [140]. In this study the scanning pattern chosen is called “island scanning”. The advantages of this strategy are that it shortens the scan vector and reduces the residual stress [85], [83], [86]. This strategy divides each layer into smaller islands that are scanned in a random order, maintaining perpendicular the scanning vectors of the neighboring islands. While printing subsequent layers, the islands are shifted in both x and y directions [83]. A scheme of the strategy can be seen in Figure E.6.

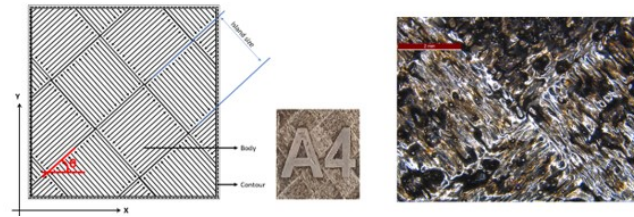


Fig. E.6 Island scanning strategy

SLM process parameters affect material density and consequently the material properties [141]. It is known that four main parameters can be combined in the Energy Density (ED): Laser Power [P], Scanning Speed v [mm/s], Layer Thickness d [mm] and Hatch Distance h [mm] [142] (Figure E.7). ED expresses the amount of energy delivered per unit volume of powder deposited and it is defined as follows [143]:

$$ED = \frac{P}{vdh} \left[\frac{J}{mm^3} \right] \quad (E.3)$$

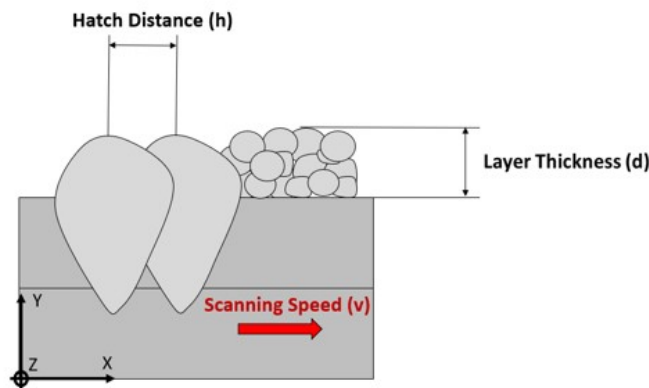


Fig. E.7 ED parameters

ED is related to density, porosity and defect formation mechanism [141]. In this research, the relative density of each specimen is measured with an Archimedes' scale and presented in Figure E.13 and Figure E.14.

The Inconel™ 718 under investigation is a weldable nickel superalloy, able to improve its strength properties mainly by precipitation hardening phases and solid-solution

hardening effect of the refractory metal elements as niobium (Nb) and molybdenum (Mo) in a nickel-chromium based matrix. Depending on the manufacturing methods and heat treatment, different types of precipitates (γ' , γ'' , δ), carbides (MC, M₆C, M₂₃C₆) and secondary phases can be present inside the microstructure. The precipitation of the secondary phases is induced by heat treatment in the temperature range of 620 °C-760 °C. For such a metallurgical reaction to properly take place, the aging constituents (Al, Ti, Nb) must be dissolved in the matrix. Nickel-based alloys are popular for their high temperature corrosion resistance and excellent mechanical strength at elevated temperature are the general characteristics because Inconel™718 is so popular. To evaluate the effects of a standard thermal treatment [144], hardness test was performed on thermal treated specimens too. The treatment has been performed with a simple industrial oven without pressure and atmosphere controls (Figure E.8). The chart presented in Figure E.9 shows the temperature vs time treatment cycle.



Fig. E.8 Thermal treatment furnace with specimens

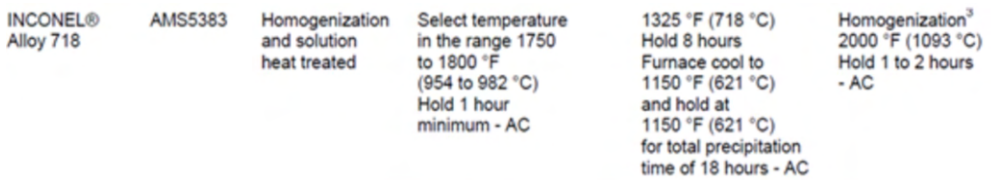


Fig. E.9 Thermal treatment cycle

Once fabricated, each coupon was removed from build plate using a band saw. The Average Surface Roughness (Ra) was 9,6 m, with a standard deviation of 1,5 m. Because contour parameters of all DoE specimens do not change (only body parameters changes) the average Ra is independent from the difference samples' process parameters. The sample preparation was performed by means of machining removal, for XY plane tests, of the down-skin (Figure E.10) and, for the XZ/YZ plane, of the Contour Layer skin. Mechanical polishing with a sander machine (Grit size 320, 800, 2500) and water coolant. The average surface roughness (Ra) of the polished specimens is 0,06 m, standard deviation 0,04 m. This procedure assure that the hardness analysis is performed respect to the in-skin material in order to avoid uncommon behaviour due to the contour-skin, up-skin or down-skin, especially after the non-controlled atmosphere heat treatment.

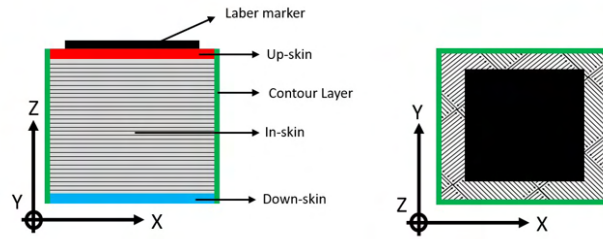


Fig. E.10 Sample preparation

E.4 Hardness testing

Hardness and micro-hardness have been evaluated at the DIMEAS Laboratory of Politecnico di Torino. The used durometer is an INOVATEST NEMESIS 9000 integrated with the IMPRESSIONS™ tester control and workflow software. The used micro-durometer is an INNOVATEST NOVA 130 also integrated with the IMPRESSIONS™ tester control and workflow software. Data acquisition is obtained according to Standard EN ISO 65074. Two different surfaces of every sample were tested and 5 repetition for each measuring configuration were acquired at room temperature; the average of the 5 measures was assumed as the hardness value. Indent sizes were measured using the machine implemented software (impressions©) with a manual selection of 4 vertices.



Fig. E.11 Example of indentation print

Additive Manufacturing processes provide different mechanical properties between the printing base plane (xy plane) and the building job direction (z). Hardness was evaluated in both planes: horizontal slices (xy-plane) and vertical cross-sections (xz or yz plane). Figure E.12 shows a schematic representation of measured surfaces. Difference between bottom, centre and top location of the plane analysed respect to X, Y or Z axe has not been considered: for XY plane only the bottom one, close to the support that links the specimens to the platform, has been tested. For YZ/XZ plane a random contour one has been selected. Different studies reported a homogeneity hardness distribution from the bottom to the top of the specimens respect to the printing direction [145]. On the other hand others show that the hardness decreases through the build height [146]. The higher hardness at the bottom of the builds was attributed to enhanced precipitation hardening due to the repetitive heating cycles experienced by the bottom region of the builds during the AM process [147].



Fig. E.12 Measured surface

The xy plane analysed in the present paper in the bottom slice of the specimen close to the machine printing platform. It is the xy surface the closest to supports used to link the specimen to the machine printing platform. The 5 indentations are located in the centre [130] (inside a 5 mm radius circle) of the analysed surface because of the better stability of the sample while load is applied.

Due to large literature available on hardness data for Inconel™ 718 processed by SLM technology [148],[11],[149],[150],[151],[152],[97] Vickers test was chosen. A preliminary study has been performed to choose a correct load able to perform the lower possible standard deviation linked to the largest available plastic deformation.

E.5 Results

E.5.1 Density measurements

The results of relative density measurements are reported in Figure 8. Density ranges from 96,96% to 100,08%. In Figure E.13 and E.14 the plot of the relative density vs the ED of the different specimens is reported.

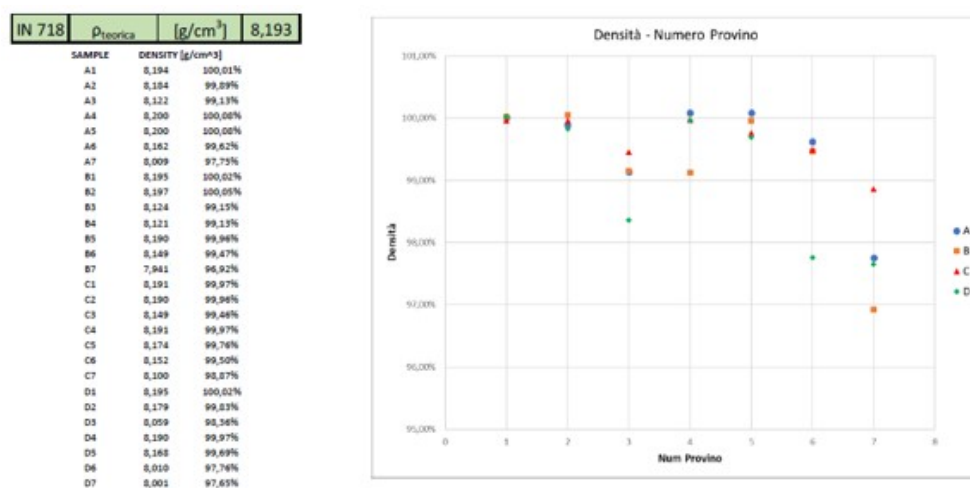


Fig. E.13 Relative density vs ED

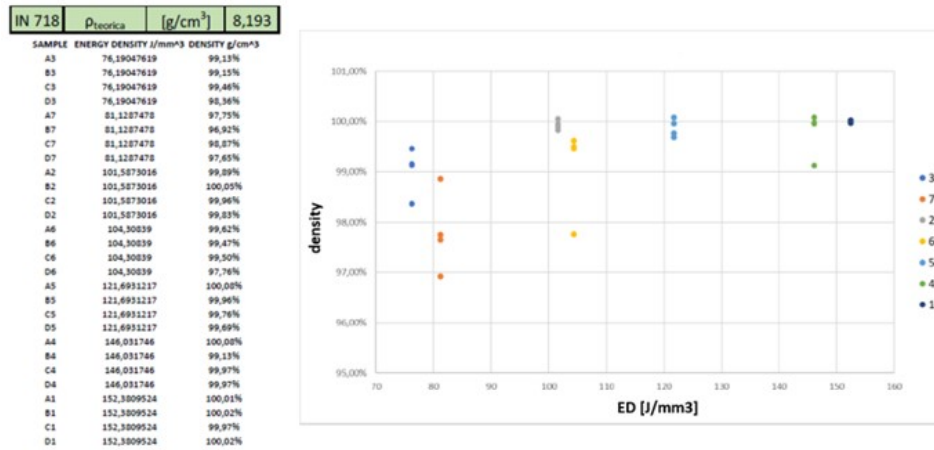


Fig. E.14 Relative density vs ED

E.5.2 Preliminary hardness measurements

Preliminary hardness testing results are plotted in Figure E.15 for different applied loads, run on A1 specimen on two different surfaces, parallel and perpendicular to deposition direction. In the same plot the data scattering, i.e. standard deviation, is reported. It can be observed that increasing the load decreases the scattering as the effect of local roughness is averaged according to increasing area of the imprint. HV20 has been identified as the optimal method for hardness properties because of low standard deviation in Hardness measurements on both surfaces.

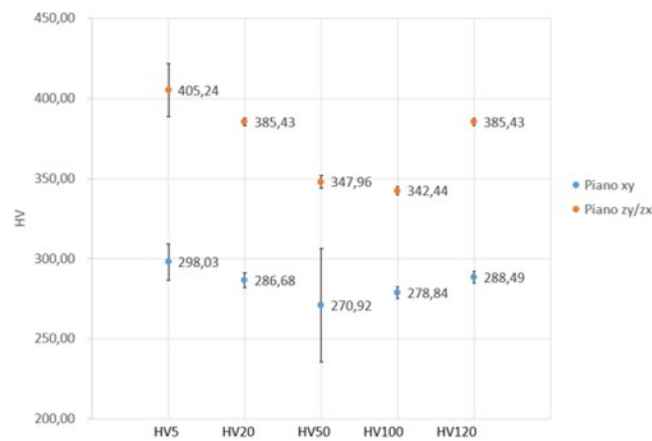


Fig. E.15 Preliminary hardness testing results

The experimental results presented in Figure E.15 reveal that DoE's specimens exhibit a strong non asymptotic Indentation Size Effect (ISE). For hardness test, this phenomenon was not expected because the elastic deformation is negligible respect to the plastic one. However, the specimens' majority shows an ISE effect. In particular it is possible to identify, for lower loads, an ISE and, for higher loads, a Reverse Indentation Size Effect (RISE). On the other hand, for general micro- and nano-hardness testing, the ISE effect is present and often it is a dominant aspect of the study [153],[148]. This particular non asymptotic Indentation Size Effect (combination between ISE and RISE)

it is probably due to the particular arrangement and movement of dislocation in materials produced by SLM Additive Manufacturing processes.

E.5.3 Hardness results: as built specimens

The results of the hardness data processing of the as-built specimens are reported in Figure E.16 with a common [154] representation that shows the hardness value respect to the printing platform for both, XY and ZY/ZX planes. The values represent the average of the 5 measures evaluated on every specimen both on the x-y surface and on the perpendicular ones (x-z/x-y planes). The average measures are reported related to the position on the platform where specimens were manufactured, a coloured palette is also applied. Referring to the x-y plane results, the hardness ranges from 279 HV (C3 specimen) to 304 HV (D1 specimen). On this plane, there is not a great variation in terms of hardness by changing the process parameters and the platform quadrant. Referring to the vertical direction (x-z or y-z plane), the measured hardness range is wider. The average hardness ranges from 288 (A7 specimen) to 402 HV (A5 specimen).

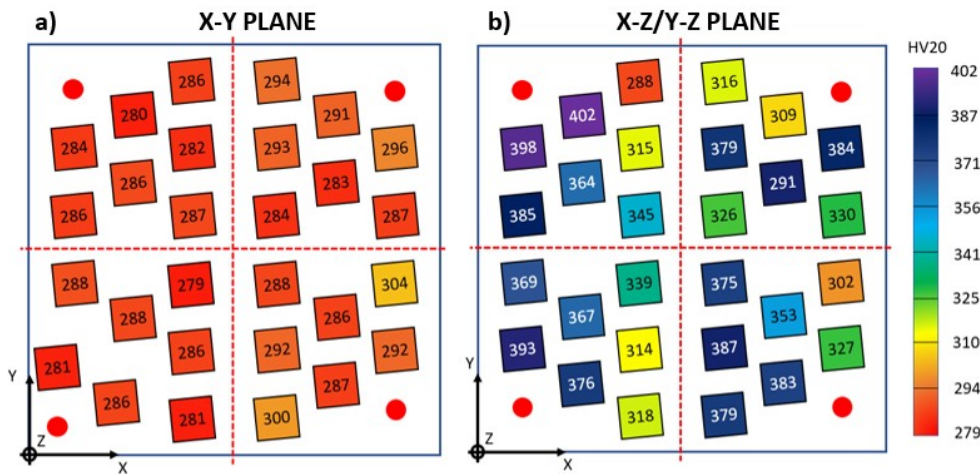


Fig. E.16 Color scale-based hardness representation for as-build specimens: 1a) x-y plane; 1b) x-z or y-z plane

If the hardness measured on the two surfaces are compared, in Figure E.17 the colored specimens have the same hardness on the x-y and x-z/y-z direction. The specimens are defined then isotropic if the hardness value measured on one surface is included in the standard deviation range of the other. Furthermore, the different colors distinguish the 4 different quadrants of the platform. On the A Quadrant, the only isotropic specimen is A7, whose hardness is 286 HV on the x-y plane and 288 HV on the x-z/y-z plane. On the B quadrant, the isotropic specimen is B2, whose hardness value is 283 HV on the x-y plane and 291 HV on the x-z/y-z plane. The last isotropic specimen is on the D quadrant. It is the D1 specimen, that presents a hardness value of 304 HV on the x-y plane and of 302 HV on the x-z/y-z plane. On the C quadrant no specimen can be considered isotropic.

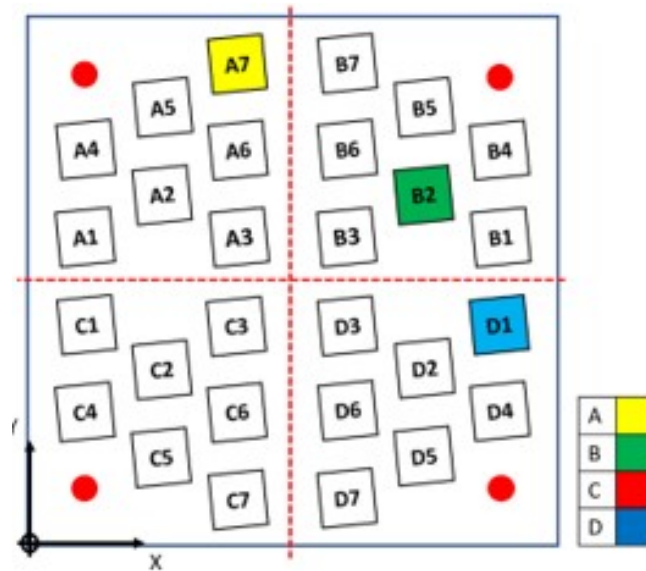


Fig. E.17 Specimens isotropy: as-build samples

In Figure E.18 the specimens printed with the same process parameters, but in different quadrants, showing the same hardness are pointed out. The different colors represent the different process parameters and the analysis refers on both x-y and z-x/z-y planes. Referring to the specimens described by number 1, all the specimens have different hardness values. The specimens described by number 2 have the same hardness values on the quadrant A and C (A2 and C2 specimens), measuring respectively 286, 288 HV (x-y plane) and 364, 367 HV (x-z/y-z plane). The number 3 specimens have the same hardness on the A quadrant (A3) and on the C quadrant (C3). A3 and C3 specimens' hardness measure respectively 287 HV and 279 HV on the x-y plane and 345 HV and 339 HV on the x-z/y-z plane. The number 4 specimens have the same hardness on all the quadrants, except from quadrant D. Respectively, the A4, B4, C4 specimens' hardness measure 284 HV, 296 HV, 281 HV on the x-y plane and 398 HV, 384 HV, 393 HV on the x-z /y-z plane. The number 5 specimens have the same hardness on the C and D quadrant. C5 and D5 measure 286 HV and 287 HV on the x-y plane and 376 HV and 383 HV on the x-z/y-z plane. The number 6 specimens have the same hardness on A and C quadrants. Respectively, the A6 and C6 specimens' hardness measure 282 HV, 286 HV on the x-y plane and 314 HV, 315 HV on the x-z/y-z plane. Finally, number 7 specimens have the same hardness on the B and C quadrant. Respectively, B7 and C7 measure 294 HV, 281 HV on the x-y plane and 316 HV, 318 HV on the x-z/y-z plane.

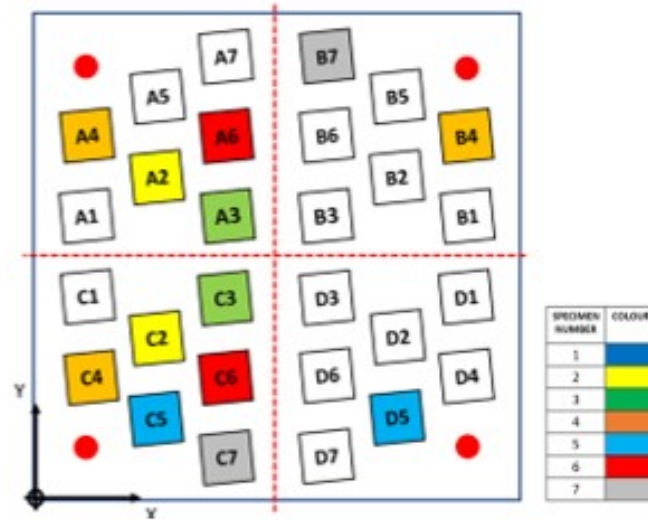


Fig. E.18 Similitude between different quadrants: as-build specimens

E.5.4 Hardness results: heat treated specimens

In Figure E.19, E.20 and E.21 the corresponding results are reported for heat treated specimens. In Figure E.19 the average hardness measurements are reported, obtained on x-y surface (left) and y-x and x-z surfaces. Heat treated specimens present a greater overall hardness HV20 value.

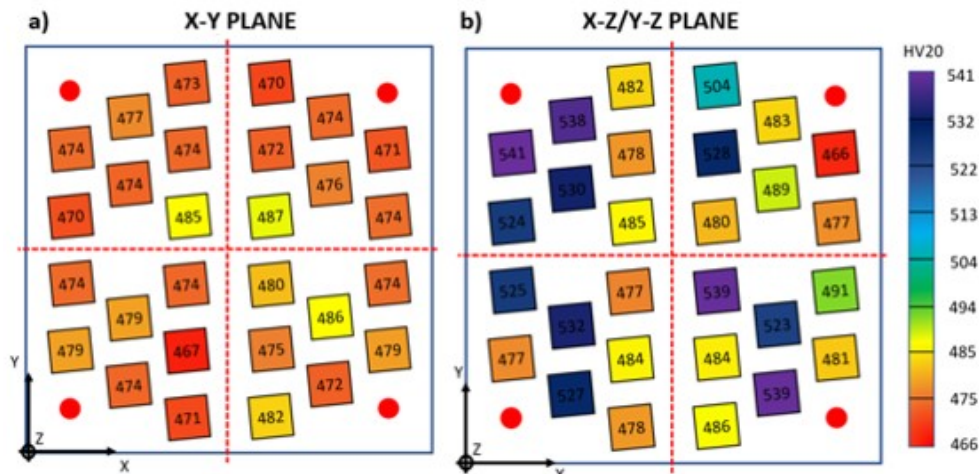


Fig. E.19 Color scale-based hardness representation for heat treated specimens: 1a) x-y plane; 1b) x-z or y-z plane

Respect to the x-y plane results, the hardness ranges from 467 HV (C6 specimen) to 487 HV (B3 specimen). On this plane, on the same way presented for the as-build specimens, the variation in terms of hardness by changing the process parameters is close to be negligible respect to all the platform quadrant. Referring to the vertical direction (x-z or y-z plane), there is a higher hardness variation than the horizontal one. The average hardness ranges from 481 (D4 specimen) to 541 HV (A4 specimen).

The material isotropy on the build platform after heat treatment is presented in Figure E.20. The heat treatment effect can be clearly in Figure E.20: 15 specimens that can be considered very close to isotropy, respect to only 3 for the as-build previous presented case. In addition to this all quadrants have at least 3 isotropic samples.

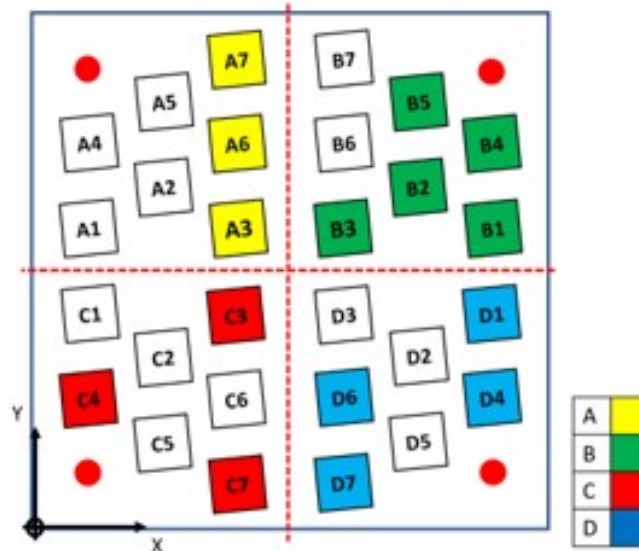


Fig. E.20 Specimens isotropy: heat treated samples

Figure E.21 The specimens described by number 1 have the same hardness values on the quadrant A and C (A1 and C1), measuring respectively 470, 474 HV (x-y plane) and 524, 525 HV (x-z/y-z plane). The number 2 specimens have the same hardness on the A quadrant and on the C quadrant (A2 and C2). A2 and C2 specimens' hardness measure respectively 474 HV and 479 HV on the x-y plane and 530 HV and 532 HV on the x-z/y-z plane. Specimens number 3 have the same hardness on all the quadrants, except from quadrant D. Respectively, the A3, B3, C3 specimens' hardness measure 485 HV, 487 HV, 474 HV on the x-y plane and 485 HV, 480 HV, 477 HV on the x-z /y-z plane. The number 4 specimens have the same hardness on the C and D quadrant. C4 and D4 measure 474 HV and 472 HV on the x-y plane and 527 HV and 539 HV on the x-z/y-z plane. The number 5 specimens have the same hardness on A,C and D quadrants. Respectively, 477 HV, 474 HV and 472 on the x-y plane and 538 HV, 527 HV and 539 on the x-z/y-z plane. Specimens number 6 present same hardness value on all quadrants except for quadrat B. Respectively, for x-y plane the hardness value is 474 HV, 467 HV, 475 HV and for x-z/y-z plane 478 HV, 474 HV, 474 HV. Specimens number 7 have the same hardness on the A, C and D quadrant. Respectively, 473 HV, 471 HV, 482 HV on the x-y plane and 482 HV, 478 HV, 486 HV on the x-z/y-z plane.

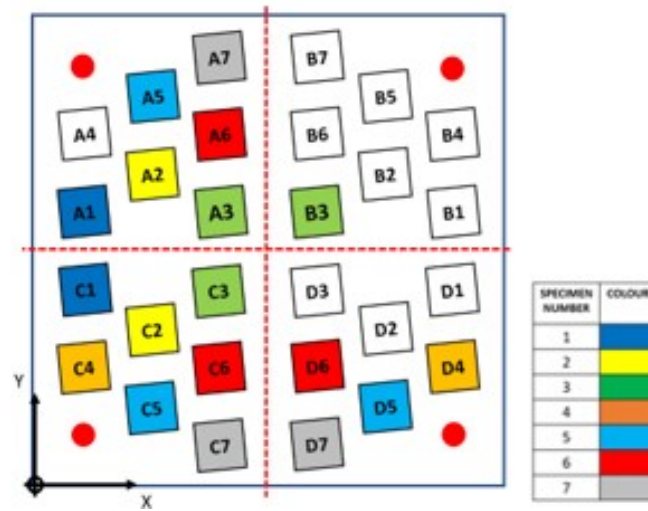


Fig. E.21 Similitude between different quadrants: heat treated specimens

E.6 Discussion

E.6.1 As build specimens

The present test campaign shows that the energy density modifies hardness properties of Inconel 718 with a remarkable effect to the ZX/ZY plain and a negligible on to the XY plane. It is known that input energy density in AM process modifies the temperature profile during additive manufacturing and therefore the resulting hardness [148]. In particular increase in the input energy decreases the Nb that phase need to shows up with a consequently modification of hardness [147].

In addition, this study shows that the analysed plane has the major influence on the mechanical properties in all specimens for A, B, C, and D platform areas. However, while tensile [153], fatigue crack growth [155] and Low Cycle Fatigue [153] properties of XY and ZX/ZY specimens are different, a negligible difference for hardness in planes parallel and perpendicular to the building direction has been reported in different studies [147],[155],[145].

A first clear analysis of results presented in SECTION AA can be performed respect to the influence of the printing process parameters. It is possible to prove that plane XY shows negligible hardness variation between specimens printed in the same area with different process parameters (Figure E.22). On the other side, plane ZX/YX has a strong dependence from printing parameters (Figure E.23).

All XY specimens with same process parameters in all 4 areas present a high similarity hardness. Therefore, it is possible to state that plane XY mechanical properties are not influenced by the position of the component on the platform and from the process printing parameters. For almost all mechanical application it is strongly required that a component do not behave in a different way if they are printed in A, B, C or D platform areas. A clear example is the behaving of specimens A2, B2, C2 and D2 (same

parameters, different platform position) that present an almost perfect repeatability of XY hardness value. On the other hand (Figure E.23) ZX/ZY hardness value do not shows a good repeatability in all different A, B, C, and D areas of the printing platform. For instance the behaving of specimens A2, B2, C2 and D2 (same parameters, different platform position) do not figure out am acceptable repeatability of hardness value.

The present study shows another remarkable behaviour of ZX/ZY plane mechanical properties: centre, respect to the perimeter, of the printing platform do not shows a better repeatability of hardness value from experimental tests. Normally standard AM processes have a good repeatability in the centre of the platform because the laser beam is more perpendicular to the platform and therefor there is a better relation between coded processes parameters and real ones measured during the printing processes.

All as build specimens, except A7, B2 and D1, have a strong anisotropy because of the notable important difference between hardness measurement respect to XY and ZX/ZY planes. To better understand the behaving of mechanical property analysed in this DoE study hardness vs energy density representation is proposed in Figure xx for all A, B, C, and D platform areas. As-build specimens presents a general increase of hardness respect to the energy density raising. Plane XY has not a particular dependence from the energy density. All for platform areas present same hardness with no changes with the energy raising. On the other hand, plane ZX/ZY shows a strong dependence from the energy density: the more energy density increases the more Vickers hardness value rises. This is true for all platform areas A, B and C, but not for D.

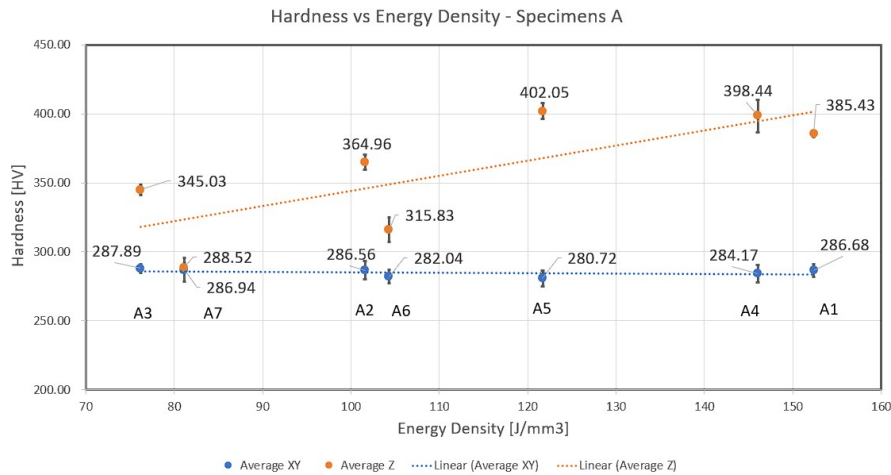


Fig. E.22 Hardness vs Energy Density - Specimens A

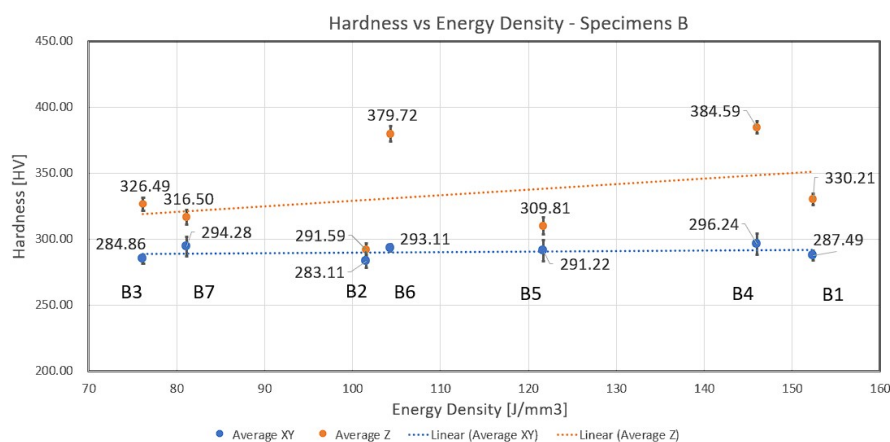


Fig. E.23 Hardness vs Energy Density - Specimens B

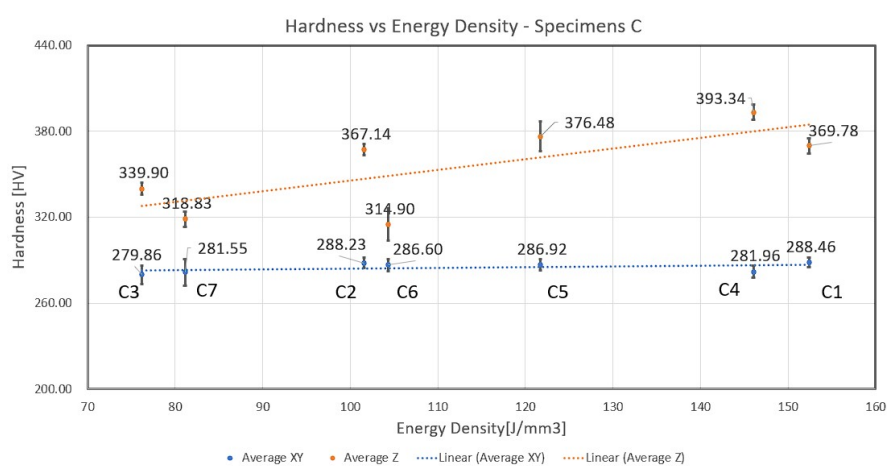


Fig. E.24 Hardness vs Energy Density - Specimens C

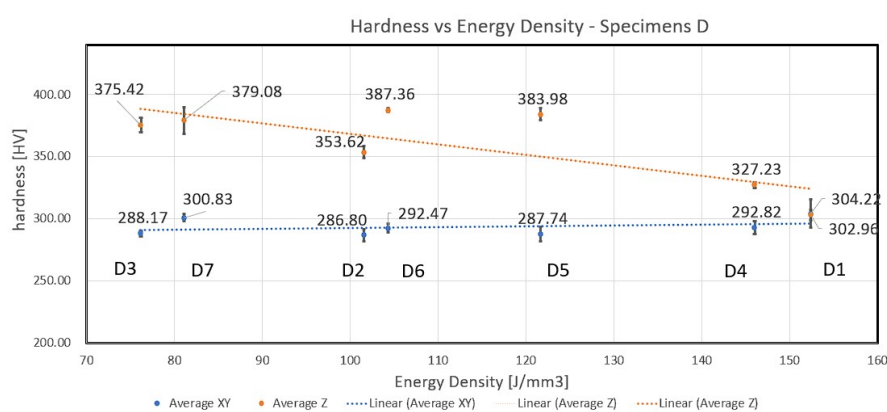


Fig. E.25 Hardness vs Energy Density - Specimens D

E.6.2 Heat treated specimens

Heat treated specimens present a general higher hardness value in both, XY and ZX/ZY planes. This is a common properties transformation for Inconel 718 post heat treatment

[152], [156]. In addition it is present a better mechanical properties homogeneity all around the platform (Figure E.19).

The maximum value of hardness for as built specimens is 304 HV20 and 402 HV20, respectively for XY plane and ZX/ZY one. The maximum value of hardness for heat treated specimens is 487 HV20 and 541 HV20, respectively for XY plane and ZX/ZY one. The heat treatment reduce the maximum hardness gap between different planes of the material under study form 99 to 54: this particular result shows that, in order to achieve a better isotopy behavior, it is necessary to introduce a strong microstructure modification via a heat treatment: normally [156] no melting pool, better grain links and especially no grain size difference between XY and ZX/ZY plane are responsible a better mechanical isotropy of the AM Inocel 718.

Figure 5 is a representation of the better isotropy of specimens after heat treatment: the as built test campaign present only 3 (out of a total of 28) isotropy simples (Figure E.18) versus 15 after the treatment process. Therefore, it is possible to state that the heat treatment can perform a strong mechanical modification to more than 50% of specimens.

In addition to a better isotropy behavior, the heat treatment process introduces a good platform repeatability. It is possible to understand, by analyzing Figure 6 respect to Figure E.18, that the number of specimens that can be considered with similar hardness value between A, B, C and D areas evolve from a number of 13 for the as build study, to a number of 18.

The difference between hardness value respect to the energy density is drastically reduced by the heat treatment. Figure XX shows that all A, B, C and D both, XY and ZX/ZY samples, are slightly influenced by an increasing of the energy density.

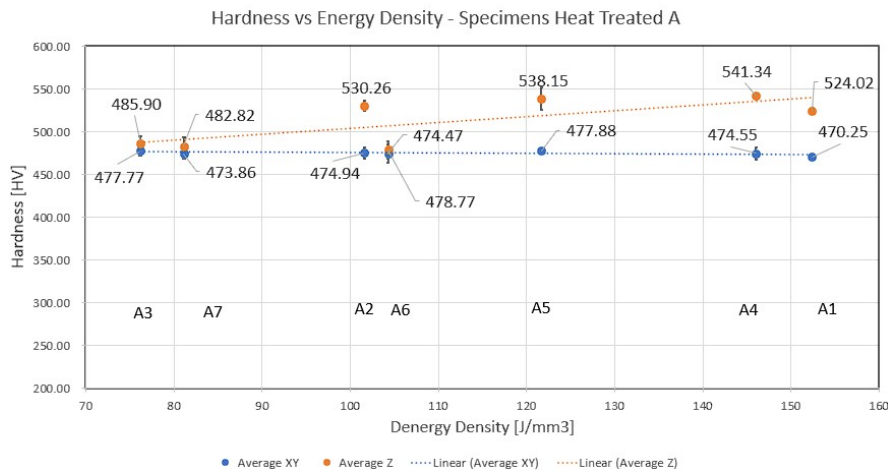


Fig. E.26 Hardness vs Energy Density - Specimens heat treated A

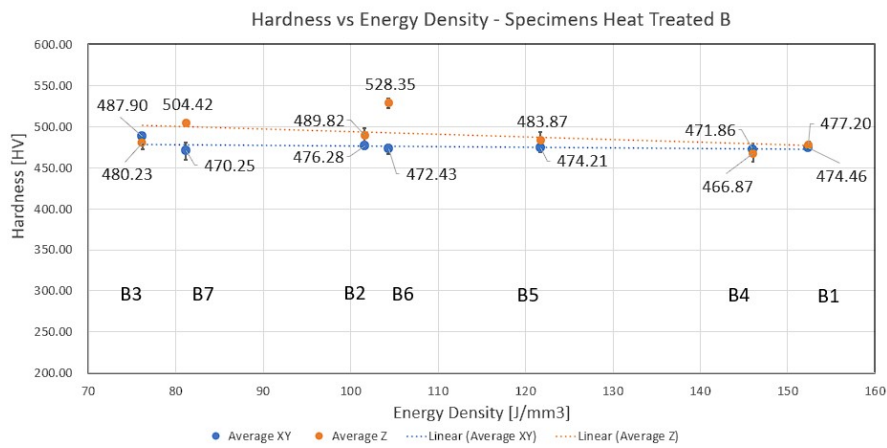


Fig. E.27 Hardness vs Energy Density - Specimens heat treated B

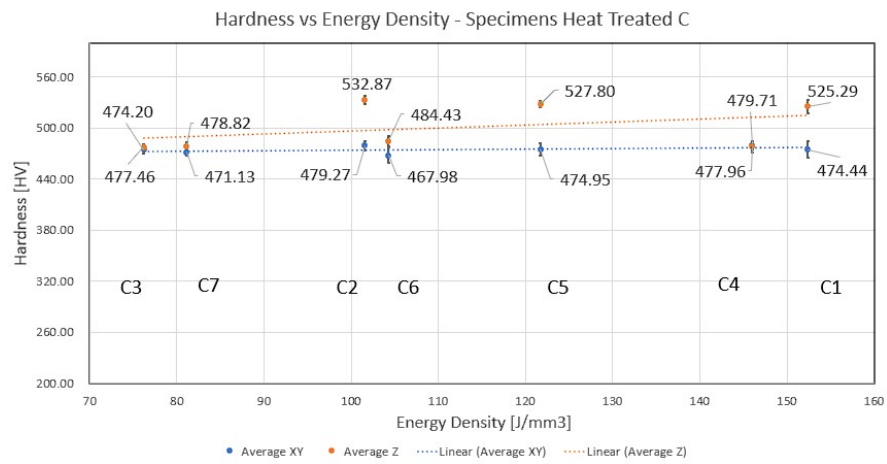


Fig. E.28 Hardness vs Energy Density - Specimens heat treated C

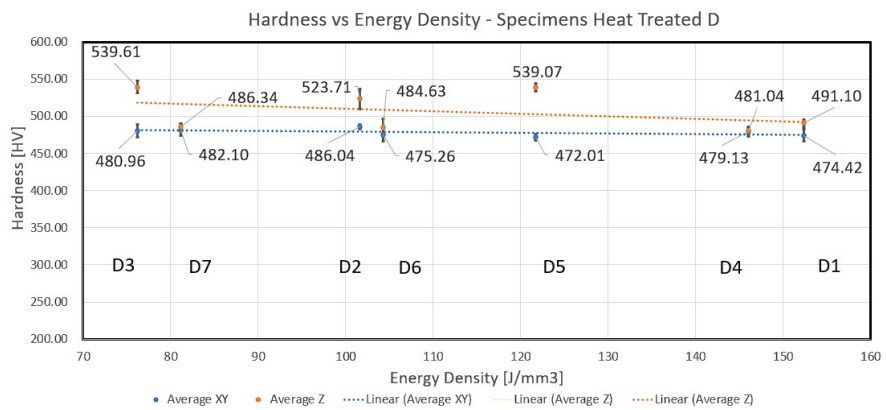


Fig. E.29 Hardness vs Energy Density - Specimens heat treated D

Appendix F

Hardness and Micro-hardness full results

A full presentation of hardness value is presented in Figure ?? and Figure ??, form specimen A and B respectively.

	Operatore	Tipologia di Prova	Macchinario	Numero Prova	Year	Month	Day	Method	Risultato	Scala	Obiettivo	d1	d2	Indenter	Forza	MEDIA	DEVIAZIONE STANDARD
PIANO XY	Matteo Crachi	Durezza	@ INNOVATEST Nemesis 9000	1	2021	novembre	17	Vickers - UNI EN ISO 6507	175.73	HV20	2.5x	0.4594	0.4594	HV	20 (196.1 N)	175.08	1.58
	Matteo Crachi	Durezza	@ INNOVATEST Nemesis 9000	2	2021	novembre	17	Vickers - UNI EN ISO 6507	174.6	HV20	2.5x	0.4574	0.4644	HV	20 (196.1 N)		
	Matteo Crachi	Durezza	@ INNOVATEST Nemesis 9000	3	2021	novembre	17	Vickers - UNI EN ISO 6507	173.95	HV20	2.5x	0.4609	0.4626	HV	20 (196.1 N)		
	Matteo Crachi	Durezza	@ INNOVATEST Nemesis 9000	4	2021	novembre	17	Vickers - UNI EN ISO 6507	177.27	HV20	2.5x	0.4591	0.4557	HV	20 (196.1 N)		
	Matteo Crachi	Durezza	@ INNOVATEST Nemesis 9000	5	2021	novembre	17	Vickers - UNI EN ISO 6507	177.27	HV20	2.5x	0.4557	0.4591	HV	20 (196.1 N)		
	Matteo Crachi	Durezza	@ INNOVATEST Nemesis 9000	6	2021	novembre	17	Vickers - UNI EN ISO 6507	166.33	HV20	2.5x	0.4696	0.4748	HV	20 (196.1 N)		
	Matteo Crachi	Durezza	@ INNOVATEST Nemesis 9000	7	2021	novembre	17	Vickers - UNI EN ISO 6507	168.81	HV20	2.5x	0.4696	0.4679	HV	20 (196.1 N)		
	Matteo Crachi	Durezza	@ INNOVATEST Nemesis 9000	8	2021	novembre	17	Vickers - UNI EN ISO 6507	181.36	HV20	2.5x	0.4504	0.454	HV	20 (196.1 N)		
	Matteo Crachi	Durezza	@ INNOVATEST Nemesis 9000	9	2021	novembre	17	Vickers - UNI EN ISO 6507	178.05	HV20	2.5x	0.458	0.4548	HV	20 (196.1 N)		
	Matteo Crachi	Durezza	@ INNOVATEST Nemesis 9000	10	2021	novembre	17	Vickers - UNI EN ISO 6507	177.25	HV20	2.5x	0.4557	0.4592	HV	20 (196.1 N)		
PIANO ZX (oppure ZY)	Operatore	Tipologia di Prova	Macchinario	Numero Prova	Year	Month	Day	Method	Risultato	Scala	Obiettivo	d1	d2	Indenter	Forza	MEDIA	DEVIAZIONE STANDARD
	Matteo Crachi	Durezza	@ INNOVATEST Nemesis 9000	1	2021	novembre	17	Vickers - UNI EN ISO 6507	153.09	HV20	2.5x	0.5009	0.4835	HV	20 (196.1 N)	153.64	7.87
	Matteo Crachi	Durezza	@ INNOVATEST Nemesis 9000	2	2021	novembre	17	Vickers - UNI EN ISO 6507	137.61	HV20	2.5x	0.5322	0.5061	HV	20 (196.1 N)		
	Matteo Crachi	Durezza	@ INNOVATEST Nemesis 9000	3	2021	novembre	17	Vickers - UNI EN ISO 6507	158.08	HV20	2.5x	0.487	0.4818	HV	20 (196.1 N)		
	Matteo Crachi	Durezza	@ INNOVATEST Nemesis 9000	4	2021	novembre	17	Vickers - UNI EN ISO 6507	153.65	HV20	2.5x	0.4922	0.4904	HV	20 (196.1 N)		
	Matteo Crachi	Durezza	@ INNOVATEST Nemesis 9000	5	2021	novembre	17	Vickers - UNI EN ISO 6507	153.63	HV20	2.5x	0.5026	0.4801	HV	20 (196.1 N)		
	Matteo Crachi	Durezza	@ INNOVATEST Nemesis 9000	6	2021	novembre	17	Vickers - UNI EN ISO 6507	150.94	HV20	2.5x	0.4957	0.4957	HV	20 (196.1 N)		
	Matteo Crachi	Durezza	@ INNOVATEST Nemesis 9000	7	2021	novembre	17	Vickers - UNI EN ISO 6507	164.52	HV20	2.5x	0.4817	0.4678	HV	20 (196.1 N)		
	Matteo Crachi	Durezza	@ INNOVATEST Nemesis 9000	8	2021	novembre	17	Vickers - UNI EN ISO 6507	146.77	HV20	2.5x	0.4887	0.5166	HV	20 (196.1 N)		
	Matteo Crachi	Durezza	@ INNOVATEST Nemesis 9000	9	2021	novembre	17	Vickers - UNI EN ISO 6507	163.93	HV20	2.5x	0.4835	0.4679	HV	20 (196.1 N)		
	Matteo Crachi	Durezza	@ INNOVATEST Nemesis 9000	10	2021	novembre	17	Vickers - UNI EN ISO 6507	154.17	HV20	2.5x	0.4991	0.4818	HV	20 (196.1 N)		

Fig. F.1 Hardness full results - Specimen A

	Operatore	Tipologia di Prova	Macchinario	Numero Prova	Year	Month	Day	Method	Risultato	Scala	Obiettivo	d1	d2	Indenter	Forza	MEDIA	DEVIAZIONE STANDARD
PIANO XY	Matteo Crachi	Durezza	@ INNOVATEST Nemesis 9000	1	2021	novembre	20	Vickers - UNI EN ISO 6507	158.09	HV20	2.5x	0.4835	0.4852	HV	20 (196.1 N)	163.58	3.42
	Matteo Crachi	Durezza	@ INNOVATEST Nemesis 9000	2	2021	novembre	20	Vickers - UNI EN ISO 6507	166.32	HV20	2.5x	0.473	0.4714	HV	20 (196.1 N)		
	Matteo Crachi	Durezza	@ INNOVATEST Nemesis 9000	3	2021	novembre	20	Vickers - UNI EN ISO 6507	166.34	HV20	2.5x	0.4696	0.4748	HV	20 (196.1 N)		
	Matteo Crachi	Durezza	@ INNOVATEST Nemesis 9000	4	2021	novembre	20	Vickers - UNI EN ISO 6507	162.72	HV20	2.5x	0.4783	0.4765	HV	20 (196.1 N)		
	Matteo Crachi	Durezza	@ INNOVATEST Nemesis 9000	5	2021	novembre	20	Vickers - UNI EN ISO 6507	164.49	HV20	2.5x	0.4748	0.4749	HV	20 (196.1 N)		
	Matteo Crachi	Durezza	@ INNOVATEST Nemesis 9000	6	2021	novembre	20	Vickers - UNI EN ISO 6507	159.8	HV20	2.5x	0.4922	0.4713	HV	20 (196.1 N)		
	Matteo Crachi	Durezza	@ INNOVATEST Nemesis 9000	7	2021	novembre	20	Vickers - UNI EN ISO 6507	170.71	HV20	2.5x	0.4661	0.4661	HV	20 (196.1 N)		
	Matteo Crachi	Durezza	@ INNOVATEST Nemesis 9000	8	2021	novembre	20	Vickers - UNI EN ISO 6507	165.73	HV20	2.5x	0.4696	0.4765	HV	20 (196.1 N)		
	Matteo Crachi	Durezza	@ INNOVATEST Nemesis 9000	9	2021	novembre	20	Vickers - UNI EN ISO 6507	155.29	HV20	2.5x	0.4887	0.4887	HV	20 (196.1 N)		
	Matteo Crachi	Durezza	@ INNOVATEST Nemesis 9000	10	2021	novembre	20	Vickers - UNI EN ISO 6507	166.33	HV20	2.5x	0.4696	0.4748	HV	20 (196.1 N)		
PIANO ZX (oppure ZY)	Operatore	Tipologia di Prova	Macchinario	Numero Prova	Year	Month	Day	Method	Risultato	Scala	Obiettivo	d1	d2	Indenter	Forza	MEDIA	DEVIAZIONE STANDARD
	Matteo Crachi	Durezza	@ INNOVATEST Nemesis 9000	1	2021	novembre	20	Vickers - UNI EN ISO 6507	150.95	HV20	2.5x	0.4853	0.5061	HV	20 (196.1 N)	157.34	5.44
	Matteo Crachi	Durezza	@ INNOVATEST Nemesis 9000	2	2021	novembre	20	Vickers - UNI EN ISO 6507	154.17	HV20	2.5x	0.4888	0.4922	HV	20 (196.1 N)		
	Matteo Crachi	Durezza	@ INNOVATEST Nemesis 9000	3	2021	novembre	20	Vickers - UNI EN ISO 6507	144.6	HV20	2.5x	0.4991	0.5131	HV	20 (196.1 N)		
	Matteo Crachi	Durezza	@ INNOVATEST Nemesis 9000	4	2021	novembre	20	Vickers - UNI EN ISO 6507	159.78	HV20	2.5x	0.4748	0.4887	HV	20 (196.1 N)		
	Matteo Crachi	Durezza	@ INNOVATEST Nemesis 9000	5	2021	novembre	20	Vickers - UNI EN ISO 6507	152.03	HV20	2.5x	0.4817	0.5061	HV	20 (196.1 N)		
	Matteo Crachi	Durezza	@ INNOVATEST Nemesis 9000	6	2021	novembre	20	Vickers - UNI EN ISO 6507	151.97	HV20	2.5x	0.4835	0.5045	HV	20 (196.1 N)		
	Matteo Crachi	Durezza	@ INNOVATEST Nemesis 9000	7	2021	novembre	20	Vickers - UNI EN ISO 6507	150.42	HV20	2.5x	0.4905	0.5026	HV	20 (196.1 N)		
	Matteo Crachi	Durezza	@ INNOVATEST Nemesis 9000	8	2021	novembre	20	Vickers - UNI EN ISO 6507	151.97	HV20	2.5x	0.4887	0.4993	HV	20 (196.1 N)		
	Matteo Crachi	Durezza	@ INNOVATEST Nemesis 9000	9	2021	novembre	20	Vickers - UNI EN ISO 6507	150.95	HV20	2.5x	0.487	0.5043	HV	20 (196.1 N)		
	Matteo Crachi	Durezza	@ INNOVATEST Nemesis 9000	10	2021	novembre	20	Vickers - UNI EN ISO 6507	156.38	HV20	2.5x	0.4835	0.4905	HV	20 (196.1 N)		

Fig. F.2 Hardness full results - Specimen B

A full presentation of micro-hardness value is presented in Figure F.3 and Figure F.4, form specimen A and B respectively.

	Operatore	Tipologia di Prova	Maccinario	Numero Prova	Year	Month	Day	Method	Risultato	Scala	Obiettivo	d1	d2	Indenter	Forza	MEDIA	DEVIAZIONE STANDARD
PIANO XY	Matteo Crachi	Micro Durezza	@ INNOVATEST Nemesis 9000	1	2021	novembre	17	Vickers - UNI EN ISO 6507	176.77	HV0.2	2.5x	0.0461	0.0455	HV	20 (196.1 N)	199.05	5.34
	Matteo Crachi	Micro Durezza	@ INNOVATEST Nemesis 9000	2	2021	novembre	17	Vickers - UNI EN ISO 6507	179.85	HV0.2	2.5x	0.0457	0.0451	HV	20 (196.1 N)		
	Matteo Crachi	Micro Durezza	@ INNOVATEST Nemesis 9000	3	2021	novembre	17	Vickers - UNI EN ISO 6507	188.44	HV0.2	2.5x	0.0446	0.0441	HV	20 (196.1 N)		
	Matteo Crachi	Micro Durezza	@ INNOVATEST Nemesis 9000	4	2021	novembre	17	Vickers - UNI EN ISO 6507	189	HV0.2	2.5x	0.0441	0.0445	HV	20 (196.1 N)		
	Matteo Crachi	Micro Durezza	@ INNOVATEST Nemesis 9000	5	2021	novembre	17	Vickers - UNI EN ISO 6507	184.63	HV0.2	2.5x	0.0449	0.0448	HV	20 (196.1 N)		
	Matteo Crachi	Micro Durezza	@ INNOVATEST Nemesis 9000	6	2021	novembre	17	Vickers - UNI EN ISO 6507	194.7	HV0.2	2.5x	0.0433	0.044	HV	20 (196.1 N)		
	Matteo Crachi	Micro Durezza	@ INNOVATEST Nemesis 9000	7	2021	novembre	17	Vickers - UNI EN ISO 6507	187.32	HV0.2	2.5x	0.0449	0.0441	HV	20 (196.1 N)		
	Matteo Crachi	Micro Durezza	@ INNOVATEST Nemesis 9000	8	2021	novembre	17	Vickers - UNI EN ISO 6507	200.7	HV0.2	2.5x	0.0429	0.0431	HV	20 (196.1 N)		
	Matteo Crachi	Micro Durezza	@ INNOVATEST Nemesis 9000	9	2021	novembre	17	Vickers - UNI EN ISO 6507	189.59	HV0.2	2.5x	0.0442	0.0442	HV	20 (196.1 N)		
	Matteo Crachi	Micro Durezza	@ INNOVATEST Nemesis 9000	10	2021	novembre	17	Vickers - UNI EN ISO 6507	199.48	HV0.2	2.5x	0.0431	0.0432	HV	20 (196.1 N)		
PIANO ZX (oppure ZY)	Operatore	Tipologia di Prova	Maccinario	Numero Prova	Year	Month	Day	Method	Risultato	Scala	Obiettivo	d1	d2	Indenter	Forza	MEDIA	DEVIAZIONE STANDARD
	Matteo Crachi	Micro Durezza	@ INNOVATEST Nemesis 9000	1	2021	novembre	17	Vickers - UNI EN ISO 6507	178.8	HV0.2	2.5x	0.0459	0.0451	HV	20 (196.1 N)	181.98	11.88
	Matteo Crachi	Micro Durezza	@ INNOVATEST Nemesis 9000	2	2021	novembre	17	Vickers - UNI EN ISO 6507	166.48	HV0.2	2.5x	0.0479	0.0465	HV	20 (196.1 N)		
	Matteo Crachi	Micro Durezza	@ INNOVATEST Nemesis 9000	3	2021	novembre	17	Vickers - UNI EN ISO 6507	167.02	HV0.2	2.5x	0.0482	0.0461	HV	20 (196.1 N)		
	Matteo Crachi	Micro Durezza	@ INNOVATEST Nemesis 9000	4	2021	novembre	17	Vickers - UNI EN ISO 6507	194.11	HV0.2	2.5x	0.044	0.0435	HV	20 (196.1 N)		
	Matteo Crachi	Micro Durezza	@ INNOVATEST Nemesis 9000	5	2021	novembre	17	Vickers - UNI EN ISO 6507	184.6	HV0.2	2.5x	0.0448	0.0449	HV	20 (196.1 N)		
	Matteo Crachi	Micro Durezza	@ INNOVATEST Nemesis 9000	6	2021	novembre	17	Vickers - UNI EN ISO 6507	198.3	HV0.2	2.5x	0.0434	0.045	HV	20 (196.1 N)		
	Matteo Crachi	Micro Durezza	@ INNOVATEST Nemesis 9000	7	2021	novembre	17	Vickers - UNI EN ISO 6507	184.08	HV0.2	2.5x	0.0459	0.0438	HV	20 (196.1 N)		
	Matteo Crachi	Micro Durezza	@ INNOVATEST Nemesis 9000	8	2021	novembre	17	Vickers - UNI EN ISO 6507	185.13	HV0.2	2.5x	0.0453	0.0442	HV	20 (196.1 N)		
	Matteo Crachi	Micro Durezza	@ INNOVATEST Nemesis 9000	9	2021	novembre	17	Vickers - UNI EN ISO 6507	180.39	HV0.2	2.5x	0.0463	0.0444	HV	20 (196.1 N)		
	Matteo Crachi	Micro Durezza	@ INNOVATEST Nemesis 9000	10	2021	novembre	17	Vickers - UNI EN ISO 6507	180.87	HV0.2	2.5x	0.0461	0.0445	HV	20 (196.1 N)		

Fig. F.3 Micro-hardness full results - Specimen A

	Operatore	Tipologia di Prova	Maccinario	Numero Prova	Year	Month	Day	Method	Risultato	Scala	Obiettivo	d1	d2	Indenter	Forza	MEDIA	DEVIAZIONE STANDARD
PIANO XY	Matteo Crachi	Micro durezza	@ INNOVATEST Nemesis 9000	1	2021	novembre	17	Vickers - UNI EN ISO 6507	192.44	HV0.2	2.5x	0.044	0.0438	HV	20 (196.1 N)	179.34	8.09
	Matteo Crachi	Micro durezza	@ INNOVATEST Nemesis 9000	2	2021	novembre	17	Vickers - UNI EN ISO 6507	174.74	HV0.2	2.5x	0.0466	0.0455	HV	20 (196.1 N)		
	Matteo Crachi	Micro durezza	@ INNOVATEST Nemesis 9000	3	2021	novembre	17	Vickers - UNI EN ISO 6507	175.26	HV0.2	2.5x	0.0457	0.0463	HV	20 (196.1 N)		
	Matteo Crachi	Micro durezza	@ INNOVATEST Nemesis 9000	4	2021	novembre	17	Vickers - UNI EN ISO 6507	174.74	HV0.2	2.5x	0.0457	0.0465	HV	20 (196.1 N)		
	Matteo Crachi	Micro durezza	@ INNOVATEST Nemesis 9000	5	2021	novembre	17	Vickers - UNI EN ISO 6507	185.56	HV0.2	2.5x	0.0447	0.0448	HV	20 (196.1 N)		
	Matteo Crachi	Micro durezza	@ INNOVATEST Nemesis 9000	6	2021	novembre	17	Vickers - UNI EN ISO 6507	171.81	HV0.2	2.5x	0.0465	0.0465	HV	20 (196.1 N)		
	Matteo Crachi	Micro durezza	@ INNOVATEST Nemesis 9000	7	2021	novembre	17	Vickers - UNI EN ISO 6507	175.76	HV0.2	2.5x	0.0455	0.0463	HV	20 (196.1 N)		
	Matteo Crachi	Micro durezza	@ INNOVATEST Nemesis 9000	8	2021	novembre	17	Vickers - UNI EN ISO 6507	172.79	HV0.2	2.5x	0.0465	0.0462	HV	20 (196.1 N)		
	Matteo Crachi	Micro durezza	@ INNOVATEST Nemesis 9000	9	2021	novembre	17	Vickers - UNI EN ISO 6507	186.77	HV0.2	2.5x	0.0444	0.0448	HV	20 (196.1 N)		
	Matteo Crachi	Micro durezza	@ INNOVATEST Nemesis 9000	10	2021	novembre	17	Vickers - UNI EN ISO 6507	183.54	HV0.2	2.5x	0.0445	0.0454	HV	20 (196.1 N)		
PIANO ZX (oppure ZY)	Operatore	Tipologia di Prova	Maccinario	Numero Prova	Year	Month	Day	Method	Risultato	Scala	Obiettivo	d1	d2	Indenter	Forza	MEDIA	DEVIAZIONE STANDARD
	Matteo Crachi	Micro durezza	@ INNOVATEST Nemesis 9000	1	2021	novembre	17	Vickers - UNI EN ISO 6507	184.08	HV0.2	2.5x	0.0453	0.0445	HV	20 (196.1 N)	175.25	13.12
	Matteo Crachi	Micro durezza	@ INNOVATEST Nemesis 9000	2	2021	novembre	17	Vickers - UNI EN ISO 6507	189.03	HV0.2	2.5x	0.0444	0.0442	HV	20 (196.1 N)		
	Matteo Crachi	Micro durezza	@ INNOVATEST Nemesis 9000	3	2021	novembre	17	Vickers - UNI EN ISO 6507	158.11	HV0.2	2.5x	0.0488	0.048	HV	20 (196.1 N)		
	Matteo Crachi	Micro durezza	@ INNOVATEST Nemesis 9000	4	2021	novembre	17	Vickers - UNI EN ISO 6507	183.52	HV0.2	2.5x	0.0452	0.0448	HV	20 (196.1 N)		
	Matteo Crachi	Micro durezza	@ INNOVATEST Nemesis 9000	5	2021	novembre	17	Vickers - UNI EN ISO 6507	166.61	HV0.2	2.5x	0.0472	0.0471	HV	20 (196.1 N)		
	Matteo Crachi	Micro durezza	@ INNOVATEST Nemesis 9000	6	2021	novembre	17	Vickers - UNI EN ISO 6507	172.77	HV0.2	2.5x	0.0474	0.0453	HV	20 (196.1 N)		
	Matteo Crachi	Micro durezza	@ INNOVATEST Nemesis 9000	7	2021	novembre	17	Vickers - UNI EN ISO 6507	168.5	HV0.2	2.5x	0.0471	0.0467	HV	20 (196.1 N)		
	Matteo Crachi	Micro durezza	@ INNOVATEST Nemesis 9000	8	2021	novembre	17	Vickers - UNI EN ISO 6507	191.83	HV0.2	2.5x	0.0445	0.0434	HV	20 (196.1 N)		
	Matteo Crachi	Micro durezza	@ INNOVATEST Nemesis 9000	9	2021	novembre	17	Vickers - UNI EN ISO 6507	177.28	HV0.2	2.5x	0.0462	0.0453	HV	20 (196.1 N)		
	Matteo Crachi	Micro durezza	@ INNOVATEST Nemesis 9000	10	2021	novembre	17	Vickers - UNI EN ISO 6507	160.72	HV0.2	2.5x	0.0486	0.0475	HV	20 (196.1 N)		

Fig. F.4 Micro-hardness full results - Specimen B

Appendix G

Tensile Test full results

G.1 Tensile Traction test - Room Temperature

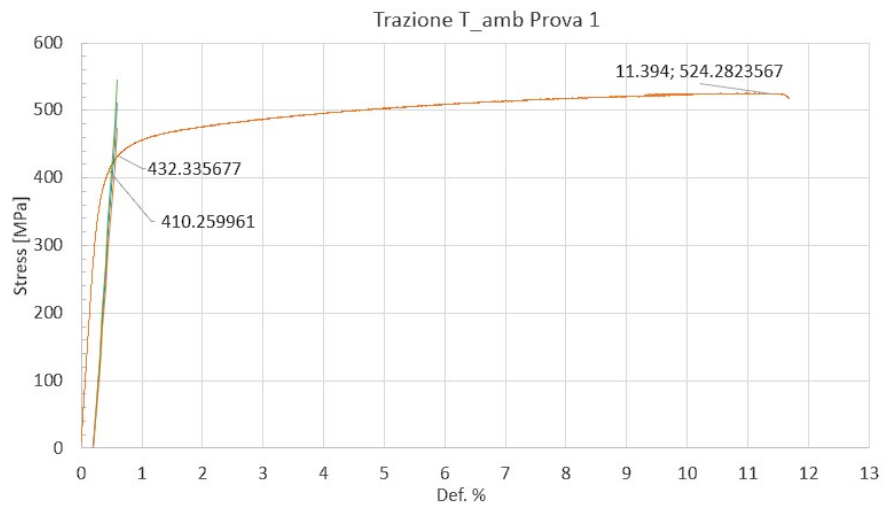
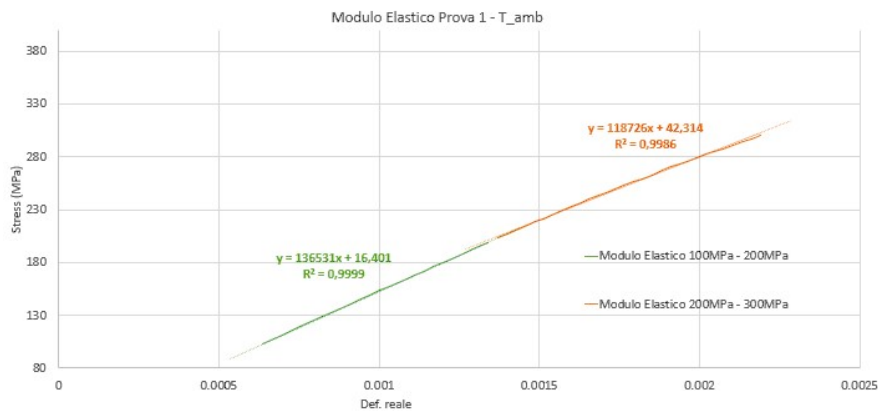
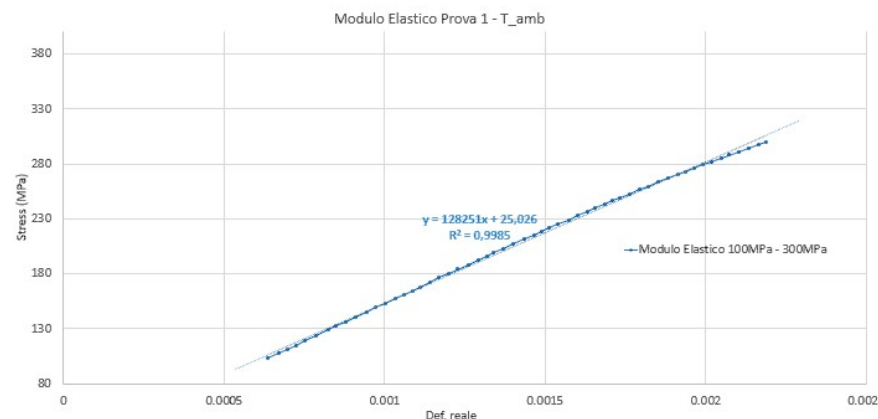


Fig. G.1 Traction Test 1 - Room Temp



(a)



(b)

Fig. G.2 Young Module Traction Test 1 - Room Temp

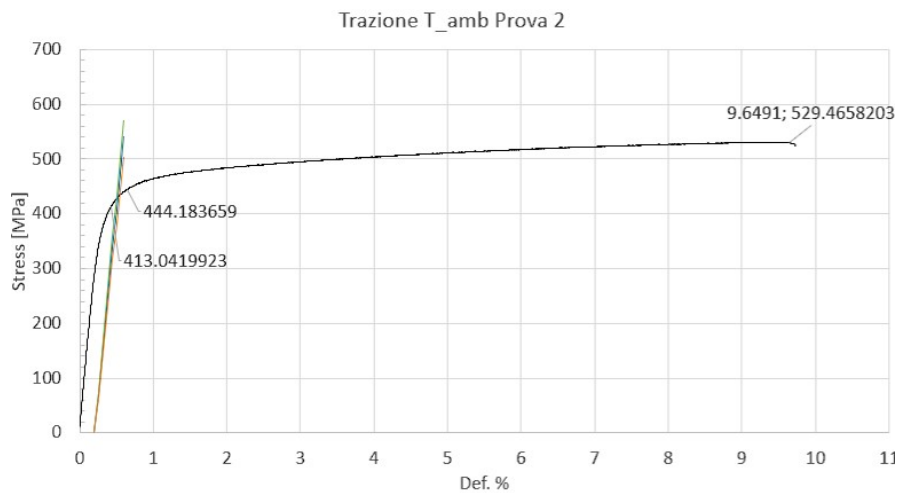
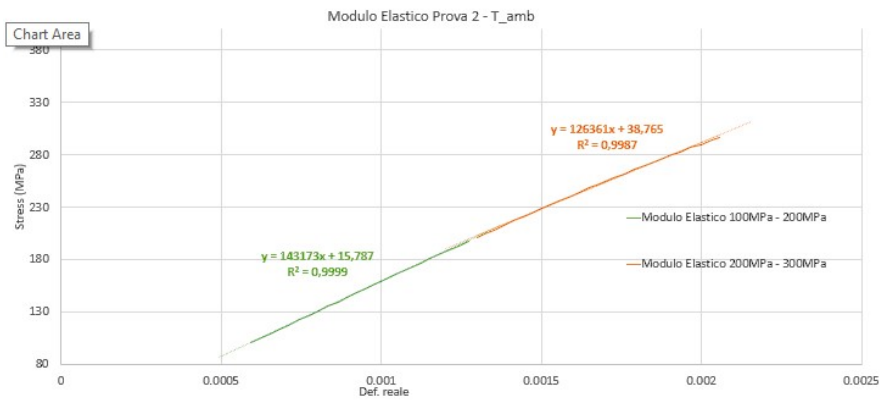
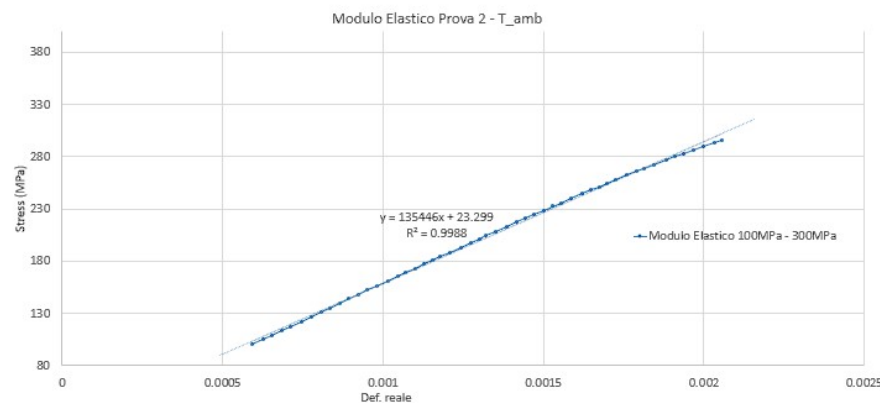


Fig. G.3 Traction Test 2 - Room Temp



(a)



(b)

Fig. G.4 Young Module Traction Test 2 - Room Temp

G.2 Tensile Traction test - 150°C

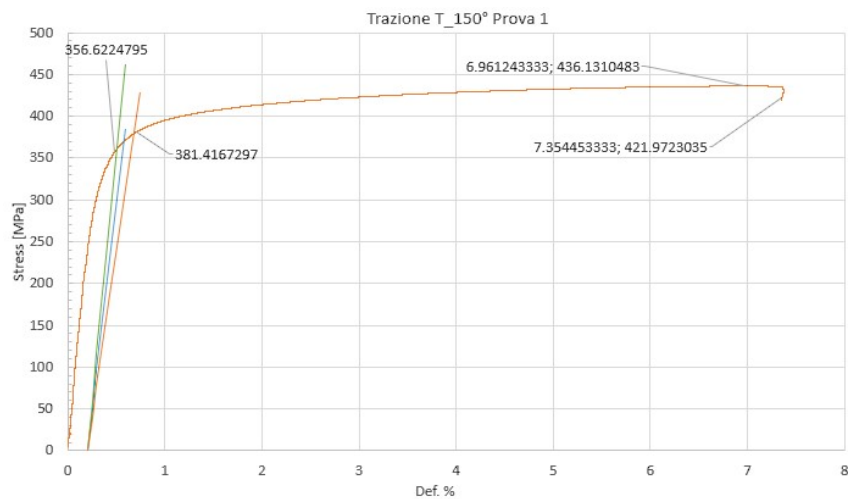


Fig. G.5 Traction Test 1 - 150°C

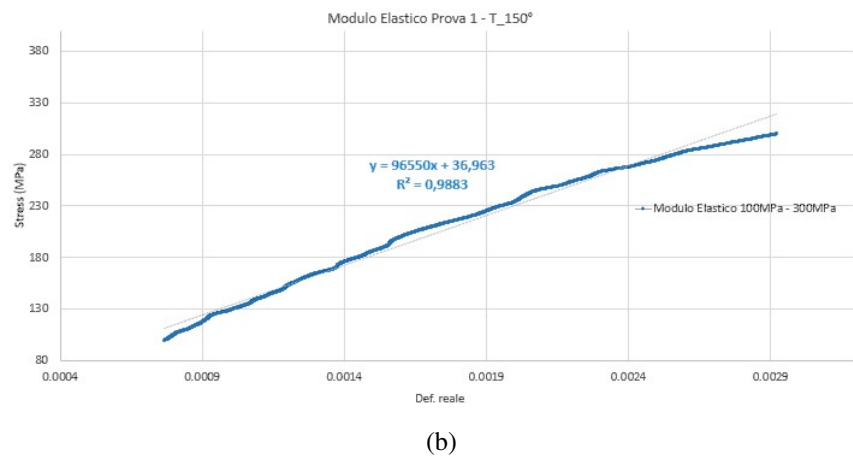
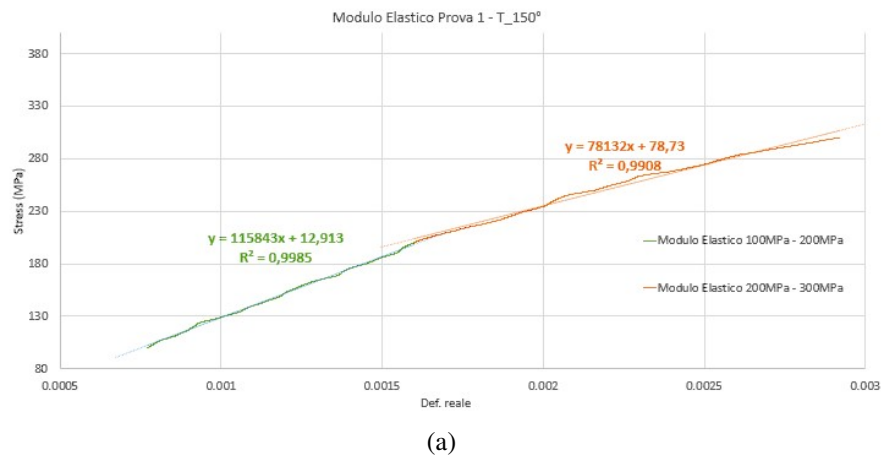


Fig. G.6 Young Module Traction Test 1 - 150°C

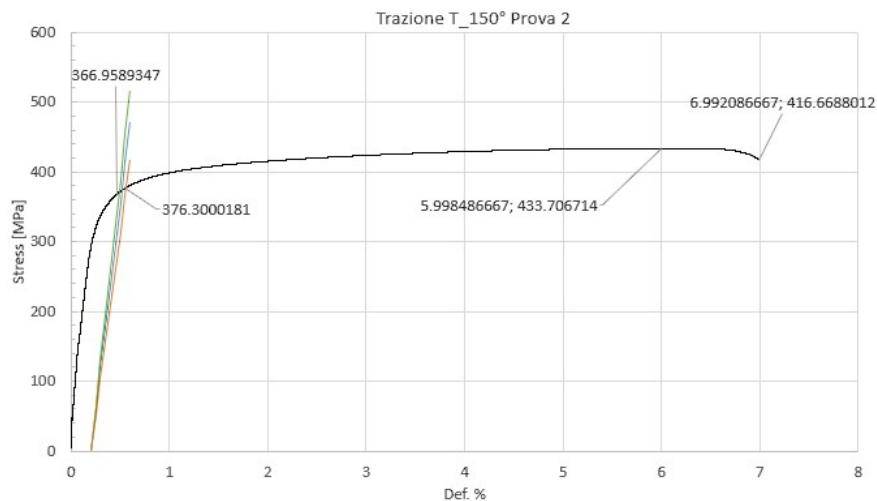
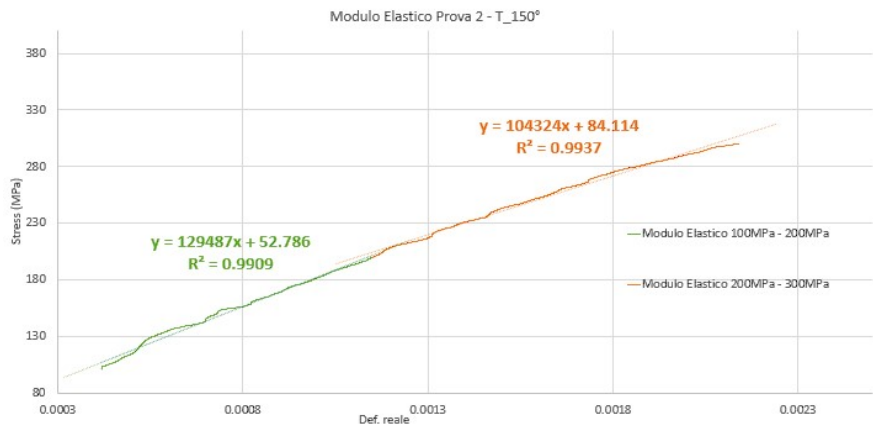
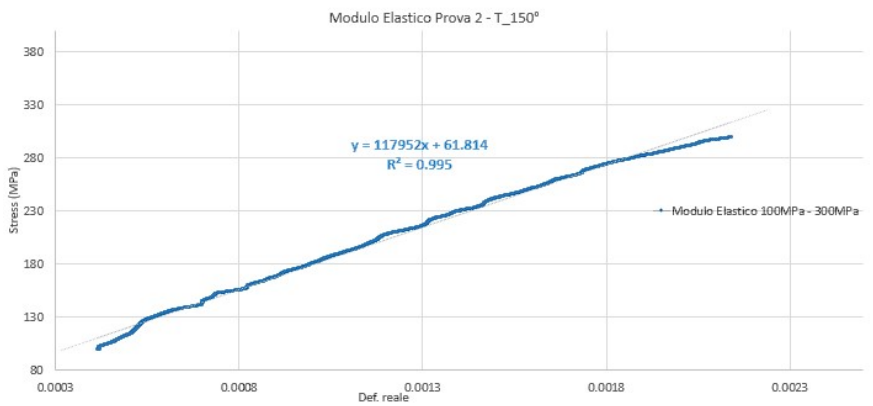


Fig. G.7 Traction Test 2 - 150°C



(a)



(b)

Fig. G.8 Young Module Traction Test 2 - 150°C

G.3 Tensile Traction test - 350°C

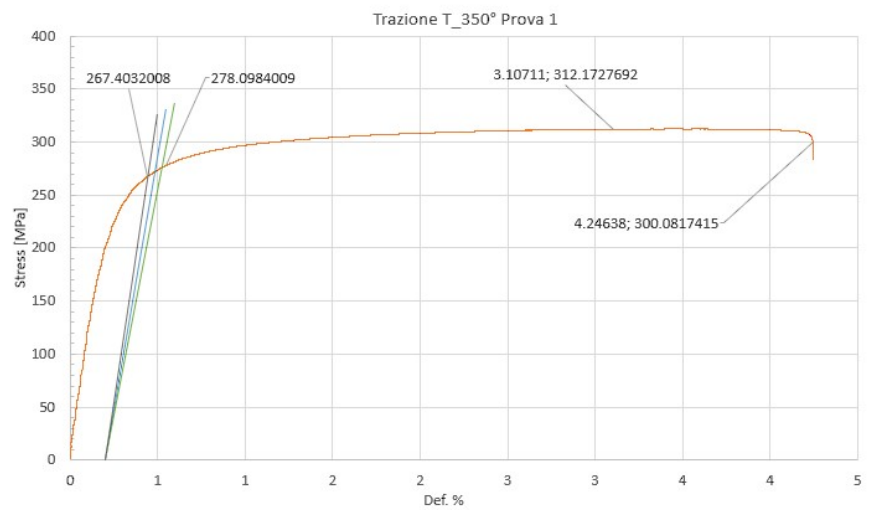
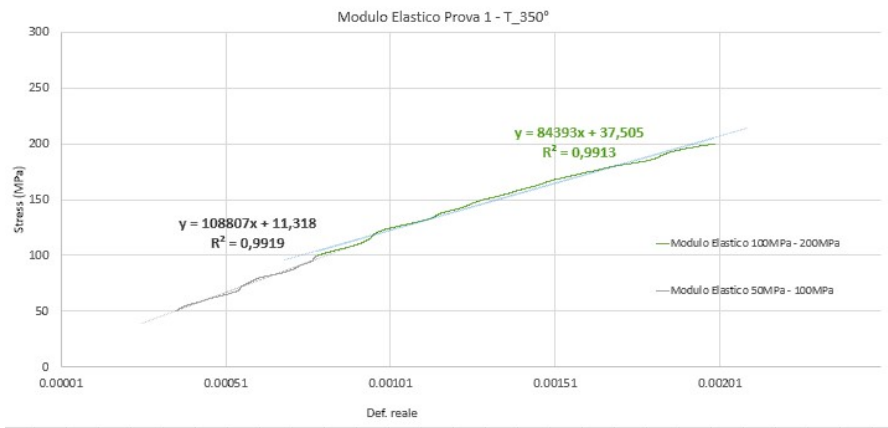
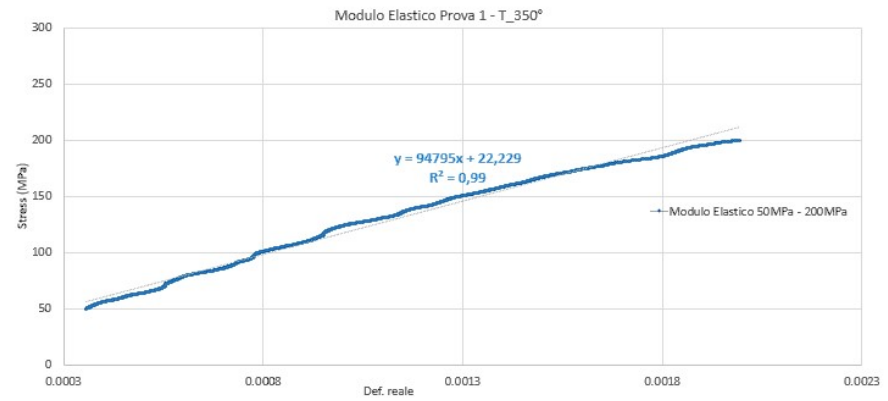


Fig. G.9 Traction Test 1 - 350°C



(a)



(b)

Fig. G.10 Young Module Traction Test 1 - 350°C

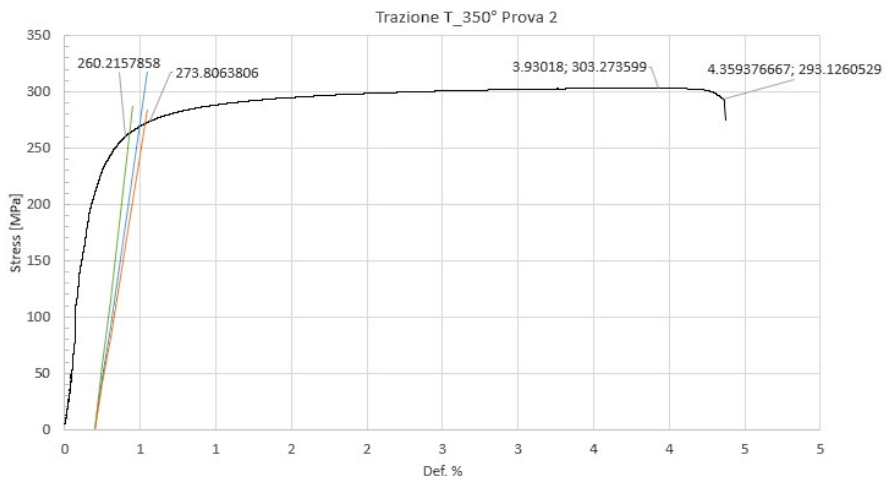
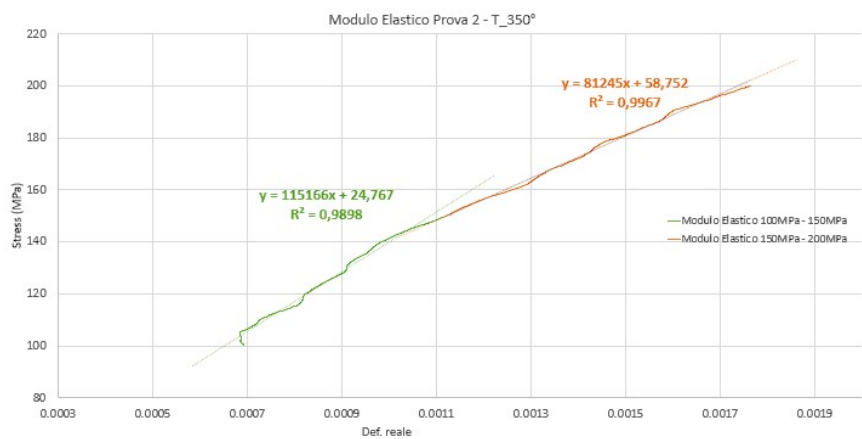
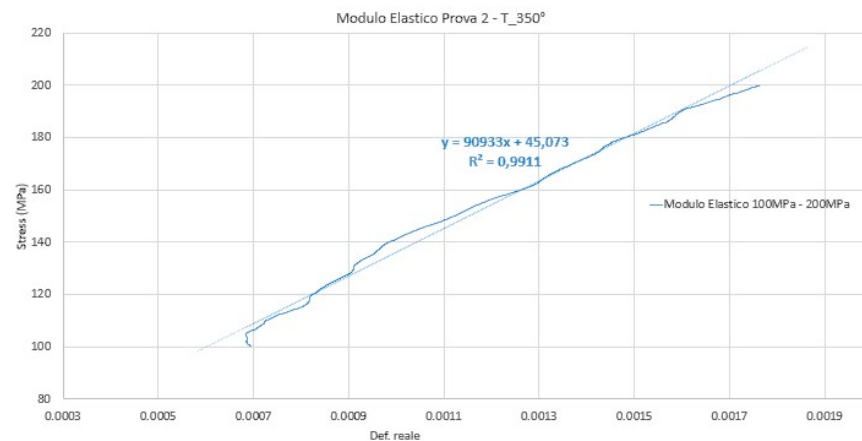


Fig. G.11 Traction Test 2 - 350°C



(a)



(b)

Fig. G.12 Young Module Traction Test 2 - 350°C

G.4 Tensile Traction test - 550°C

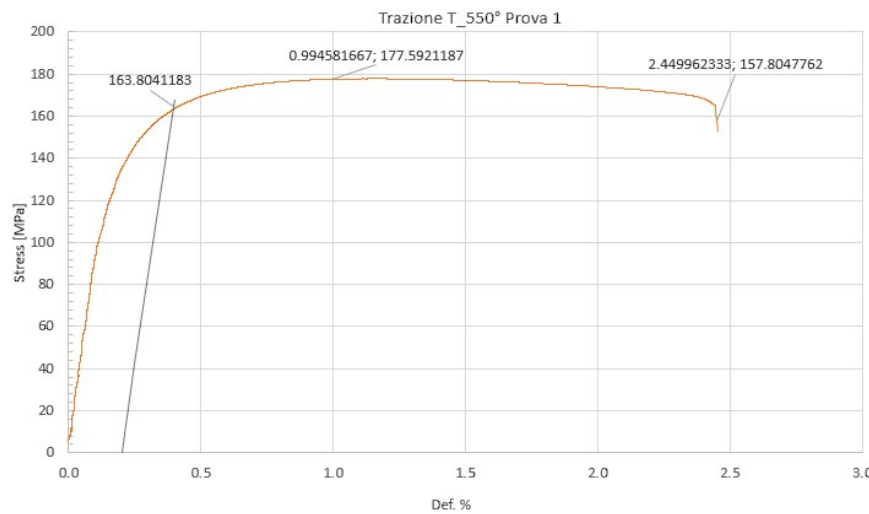
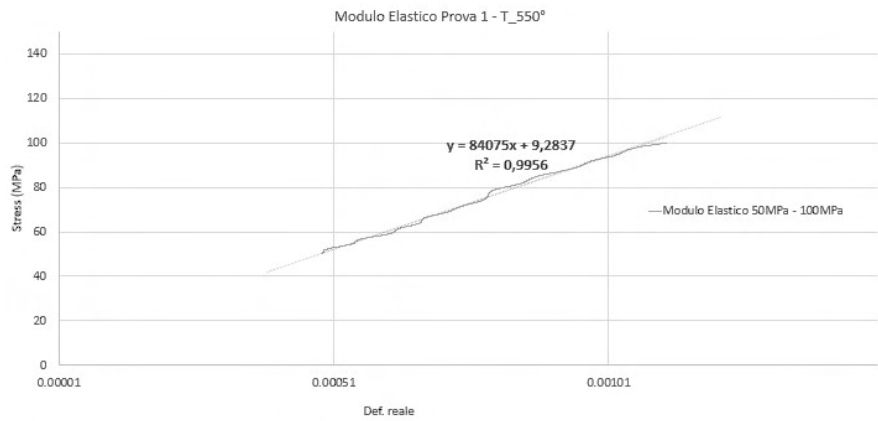


Fig. G.13 Traction Test 1 - 550°C



(a)

Fig. G.14 Young Module Traction Test 1 - 550°C

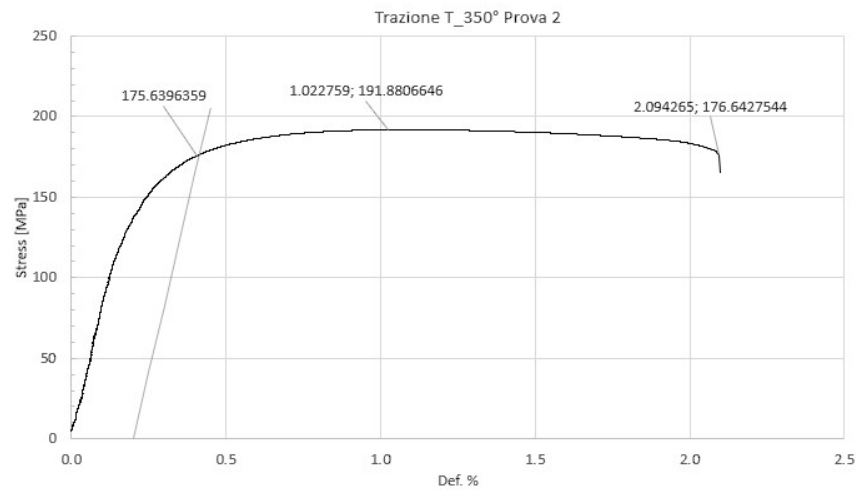
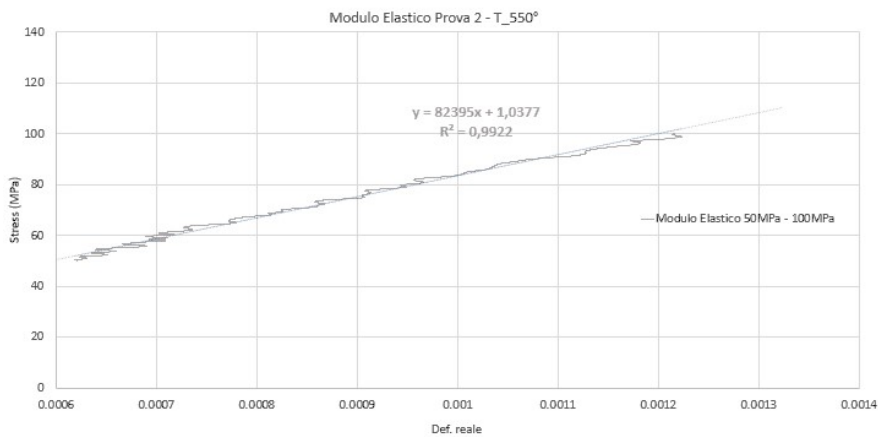


Fig. G.15 Traction Test 2 - 550°C



(a)

Fig. G.16 Young Module Traction Test 2 - 550°C

G.5 Tensile Traction test - 650°C

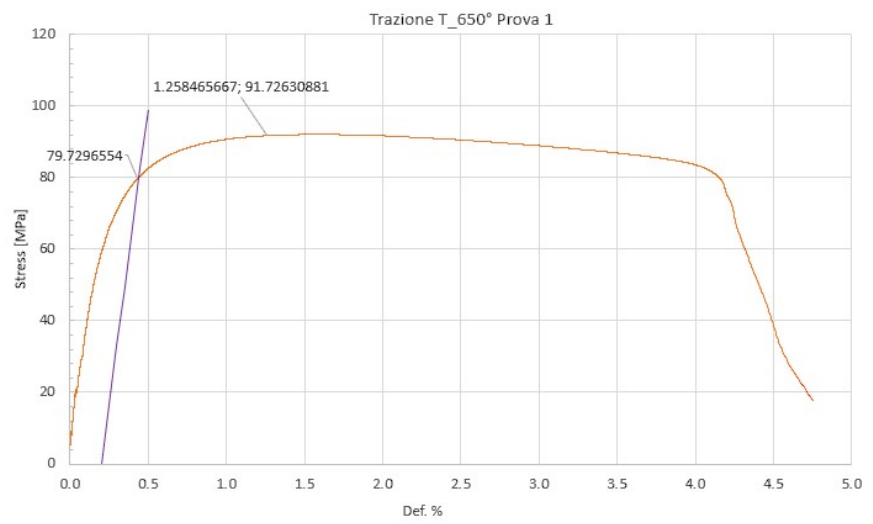
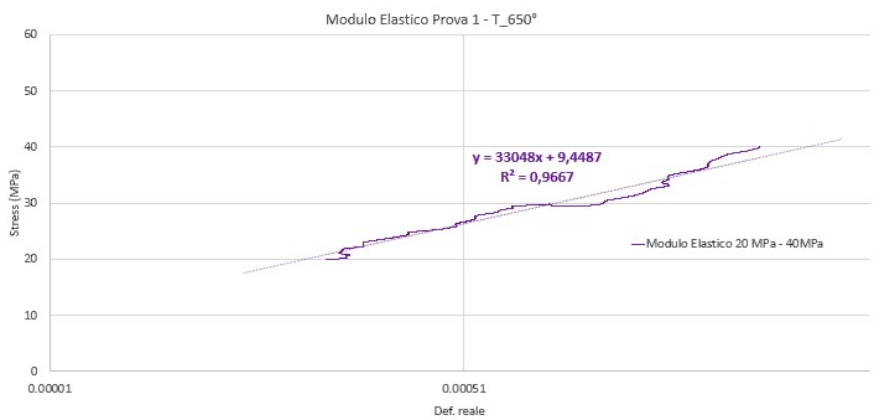


Fig. G.17 Traction Test 1 - 650°C



(a)

Fig. G.18 Young Module Traction Test 1 - 650°C

Appendix H

Tensile Test Ramberg-Osgood relationship calculation procedure

The relationship between stress and strain in the plastic field, i.e. for, can be described by the Ramberg-Osgood law (R.-O: Model):

$$\sigma = K \varepsilon_p^n \quad (\text{H.1})$$

where:

- ε_p is the plastic deformation;
- σ is the stress respect to the applied plastic deformation;
- n is the hardening ratio exponent (material's constant);
- K is the strength coefficient (material's constant);

By expressing the ε_p from Equation H.1 as a function of σ we obtain:

$$\varepsilon_p = \left(\frac{\sigma}{K} \right)^{\frac{1}{n}} \quad (\text{H.2})$$

By expressing the elastic and the plastic deformation, ε_{tot} can be remodelled as:

$$\varepsilon_{tot} = \varepsilon_e + \varepsilon_p = \frac{\sigma}{E} + \left(\frac{\sigma}{K} \right)^{\frac{1}{n}} \quad (\text{H.3})$$

After calculating the actual deformation and stress from the experimental data, the parameters of the R.O. relationship can be derived by formulating the equation for the plastic part in logarithmic terms. In a Log-Log diagram the plastic relationship is presented as a straight line whose angular coefficient is the hardening ratio exponent (n).

$$\log_{10}(\sigma) = \log_{10}(K) + n \log_{10}(\varepsilon_p) \quad (\text{H.4})$$

The strength coefficient (K) is instead calculated at $\epsilon_p = 1$. In reality, no structural engineering material achieves such a high plastic deformation: the value is purely theoretical.

$$\log_{10}(\sigma) = \log_{10}(K) \quad (\text{H.5})$$

From the Log-Log chart it is possible to evaluate $\log_{10}(\sigma)$ and therefore K :

$$K = 10^{\log_{10}(\sigma)} \quad (\text{H.6})$$

H.1 Ramberg-Osgood model VS real deformation-real stress curve

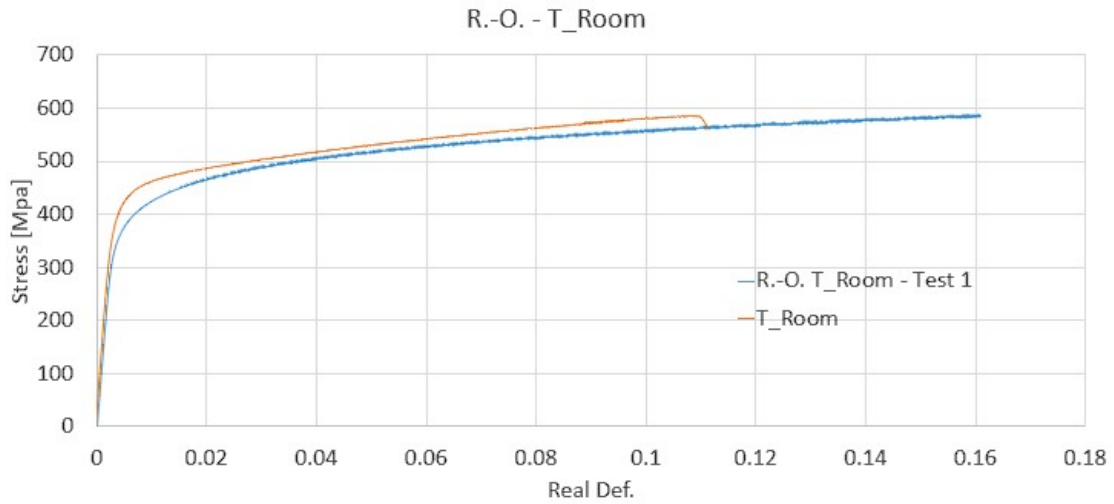


Fig. H.1 Ramberg - Osgood model - Test 1 Troom

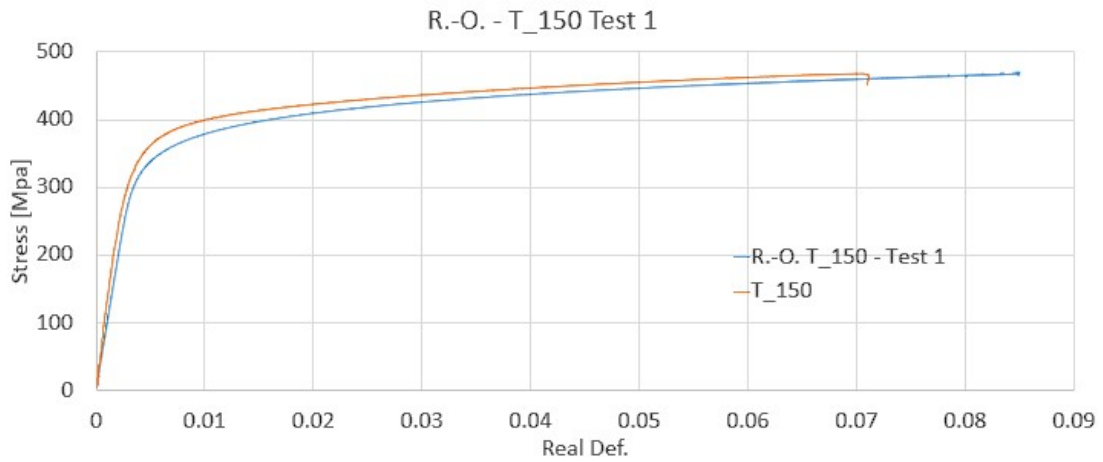


Fig. H.2 Ramberg - Osgood model - Test 1 T150

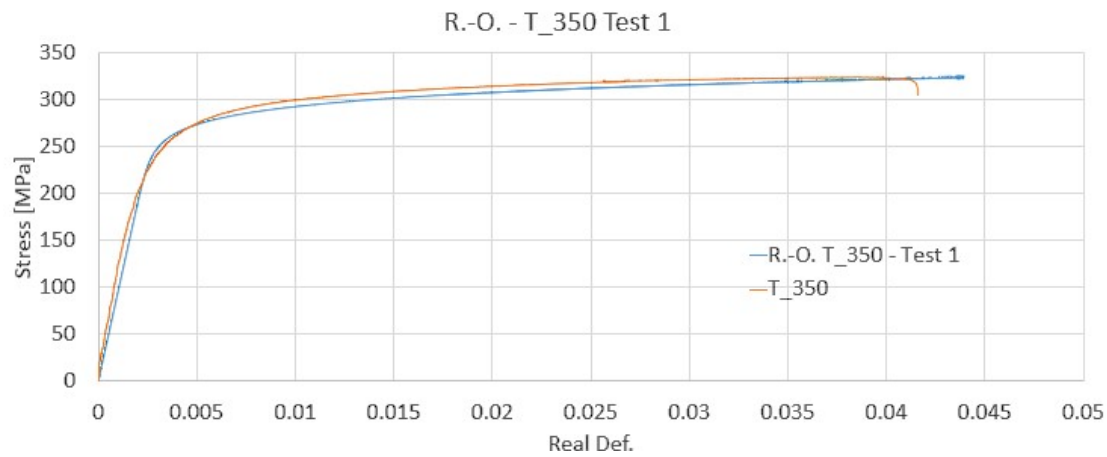


Fig. H.3 Ramberg - Osgood model - Test 1 T350

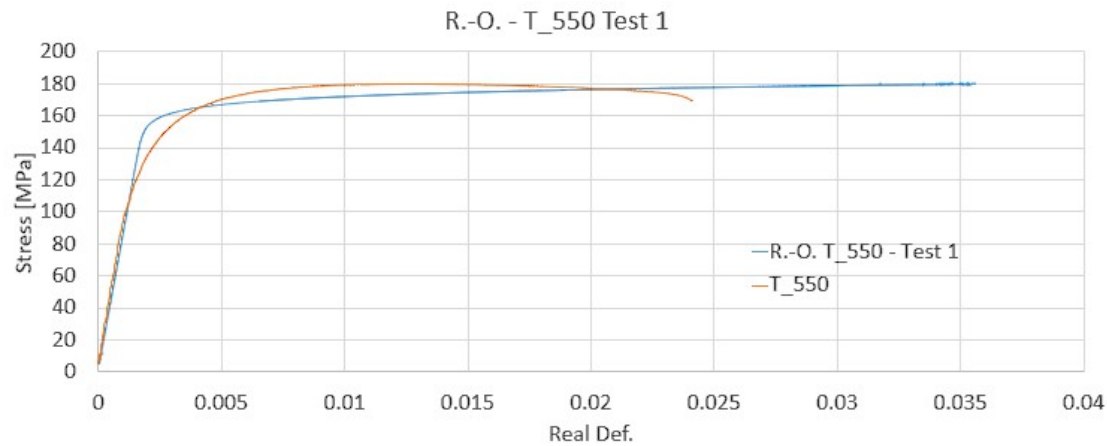


Fig. H.4 Ramberg - Osgood model - Test 1 T550

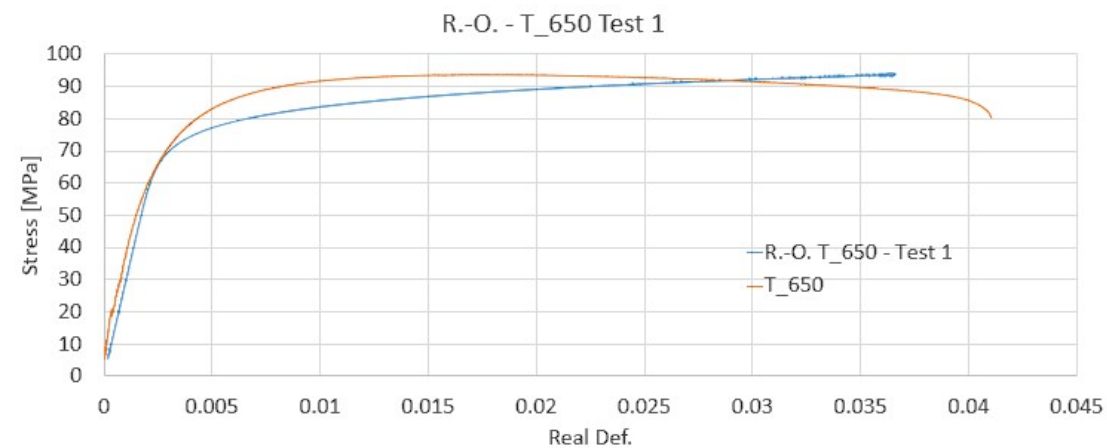


Fig. H.5 Ramberg - Osgood model - Test 1 T650

H.2 Log-Log Ramberg-Osgood relationship chart

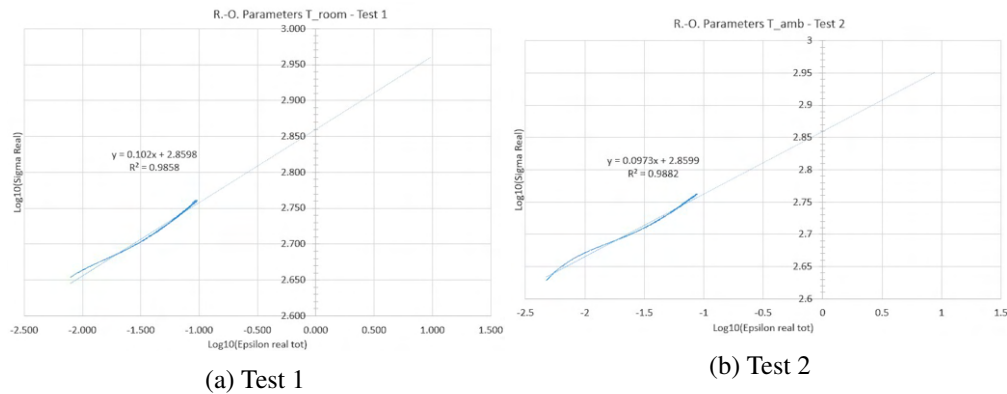


Fig. H.6 Ramberg-Osgood relationship - T room

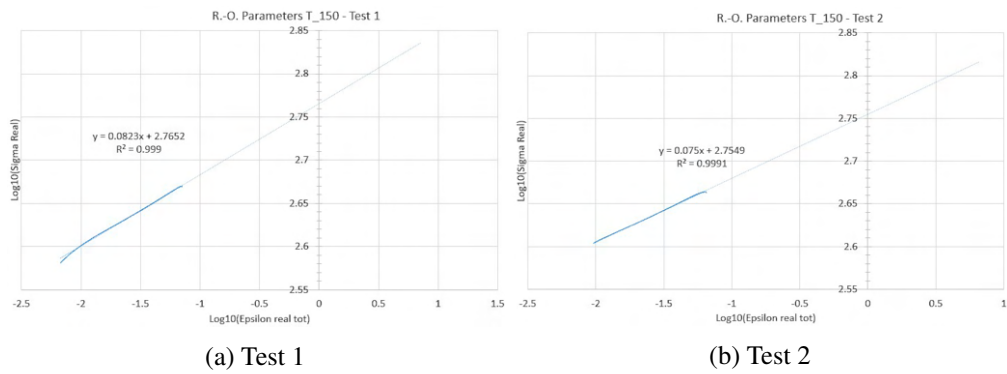


Fig. H.7 Ramberg-Osgood relationship - T 150°C

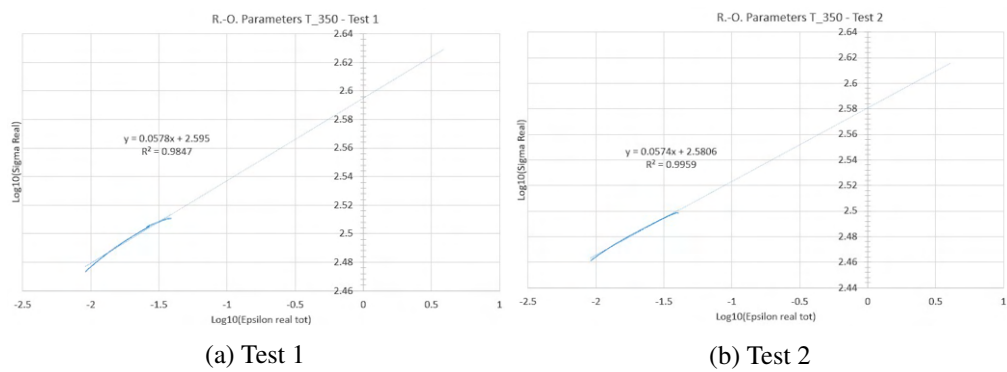


Fig. H.8 Ramberg-Osgood relationship - T 350°C

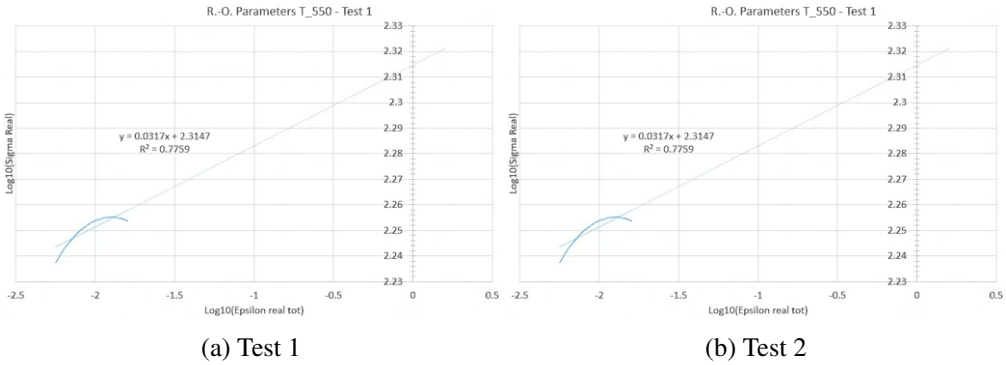


Fig. H.9 Ramberg-Osgood relationship - T 550°C

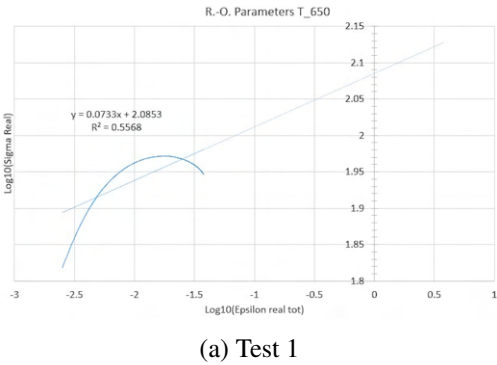


Fig. H.10 Ramberg-Osgood relationship - T 650°C

Appendix I

Compression Test Young Module calculation procedure

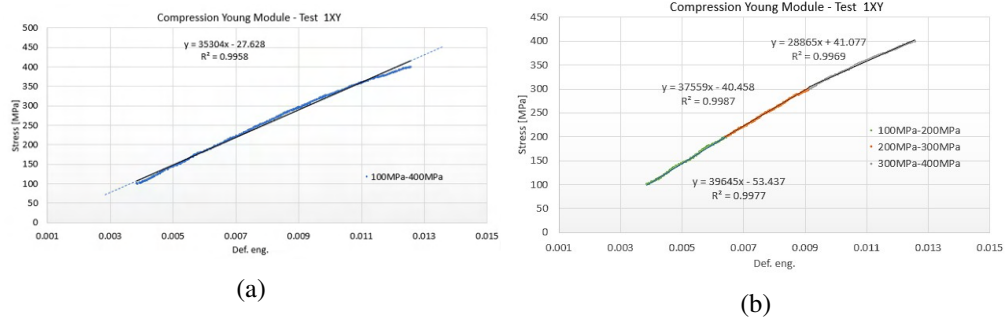


Fig. I.1 Young Module XY - test 1

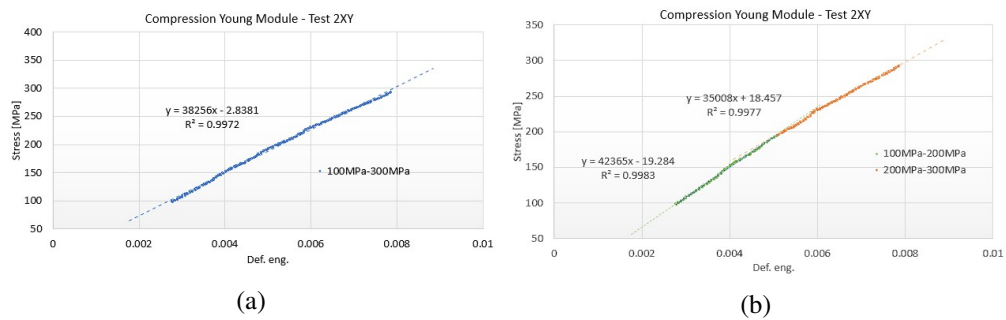
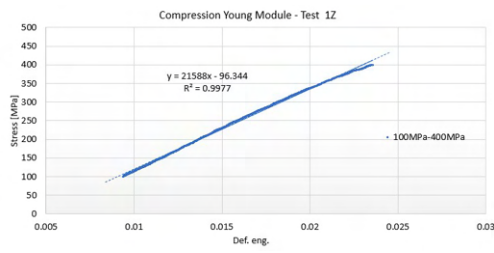
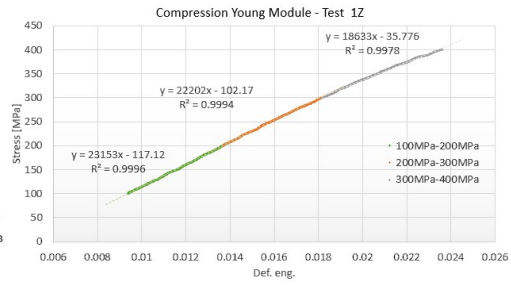


Fig. I.2 Young Module XY - test 2

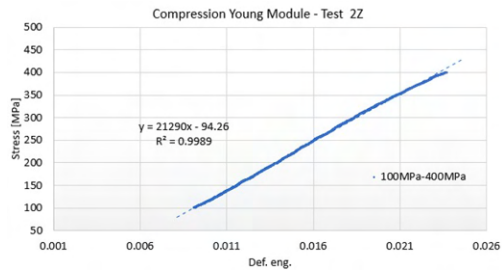


(a)

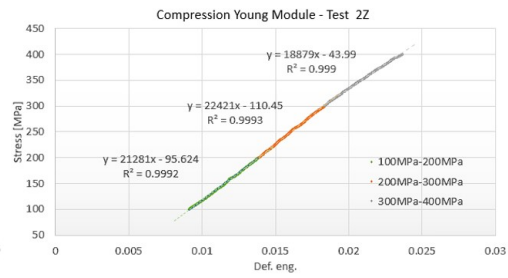


(b)

Fig. I.3 Young Module Z - test 1



(a)



(b)

Fig. I.4 Young Module Z - test 2

Appendix J

Ramberg - Osgood Cycling curve relationship

The procedure is the same presented on appendix H. Results of first fitting curves are presented in Figure J.1.

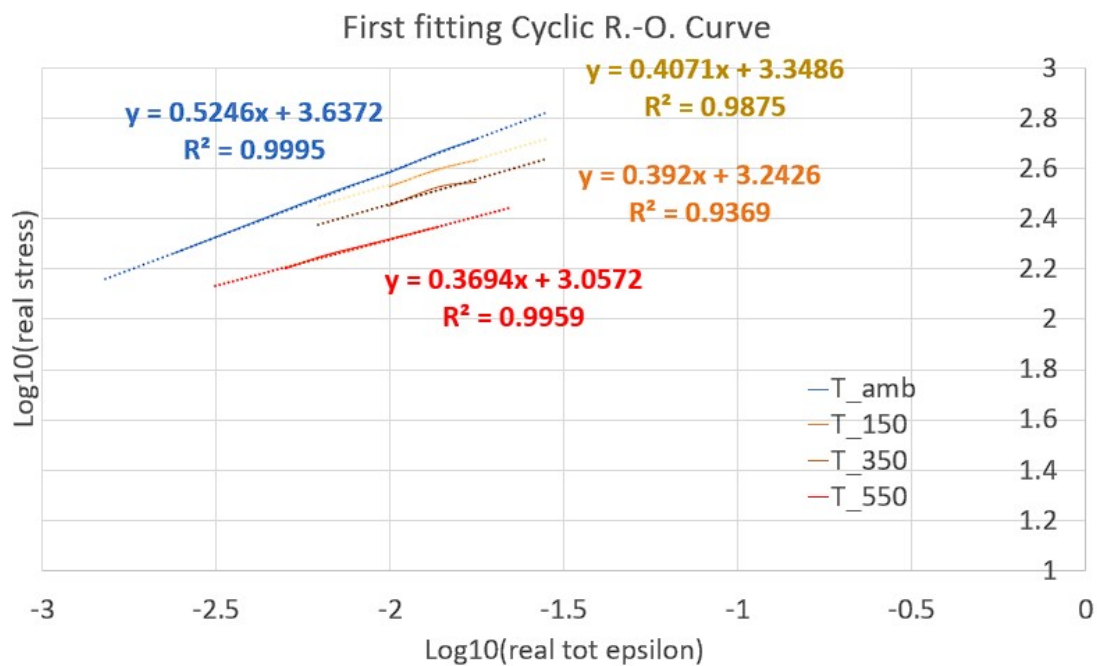


Fig. J.1 Ramberg - Osgood cycling model - First parameters attempt

However no PFC real replication behavior was achieved (Table J.1), therefore a second manual modification has been performed (Table J.2), with very good results.

Ramberg - Osgood Cycling curve relationship - First attempt Parameters

	K'	n'
Room	4265.79	0.52
150°C	2187.76	0.40
350°C	1737.8	0.39
550°C	1122.01	0.36

Table J.1 Ramberg - Osgood Cycling curve relationship - First attempt Parameters

Ramberg - Osgood Cycling curve relationship - Correct Parameters

	K'	n'
Room	4265.79	0.48
150°C	2187.76	0.37
350°C	1737.8	0.37
550°C	1122.01	0.35

Table J.2 Ramberg - Osgood Cycling curve relationship - Correct Parameters

Appendix K

Coffin - Manson parameters

The procedure is the same presented on appendix H. Results of first fitting curves are presented in Figure K.1.

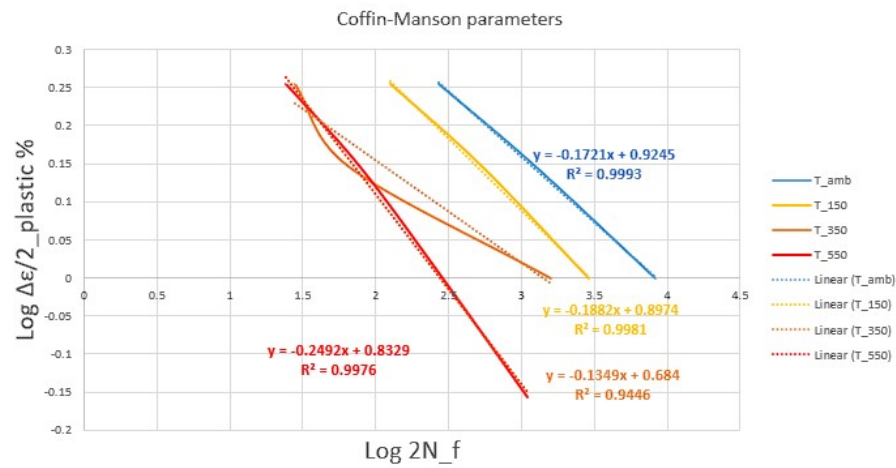


Fig. K.1 Coffin - Manson Log-log parameters